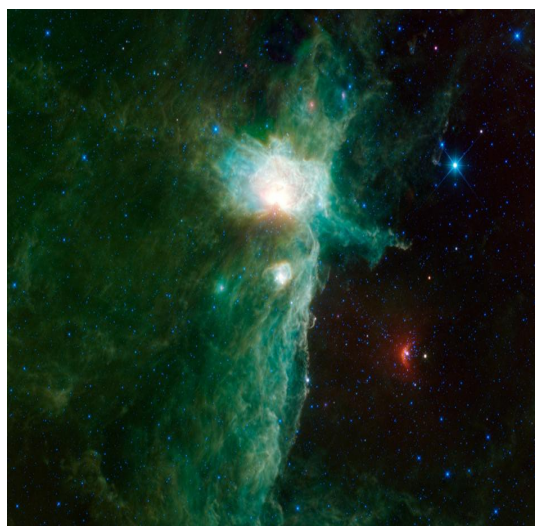


On the variability of young massive stars



Guilherme Domingos Carvalho Teixeira

Programa doutoral em Física MAP-fis
Departamento de Física e Astronomia
2018

Orientador

M. S. Nanda Kumar
Investigador
Instituto de Astrofísica e Ciências do Espaço

Coorientador

Mário J. P. F. G. Monteiro
Professor Associado
Faculdade de Ciências da Universidade do Porto





Todas as correções determinadas pelo júri, e só essas, foram efetuadas.

O Presidente do Júri,

Porto, ____ / ____ / ____

P

S

O

Acknowledgements

I thank my supervisors for their guidance, and my collaborators for the helpful discussions. I would also like to thank my host institution, CAUP (Centro de Astrofísica da Universidade do Porto) and IA (Institute of Astrophysics and Space Sciences).

The work presented in this thesis was funded by the PhD fellowship PD/BD/113478/2015 funded by FCT (Portugal), and the fellowship IA 2018-36-BIM. I would also like to acknowledge the support provided by IDPASC-Portugal program (PD/24/2013).

Above all I thank my family for their support throughout this entire work. I couldn't have reached this point without any of you.

Guilherme Teixeira

Resumo

As estrelas de grande massa são uma pequena fração de todas as estrelas formadas na galáxia ($\sim 1\%$) mas, apesar disto, são o principal responsável pela evolução galáctica. Apesar da sua importância, há perguntas sem resposta no que toca aos seus processos de formação. Uma das principais questões diz respeito a como elas ganham a sua massa e quão importante é o papel da acreção no seu processo formativo? Nós exploramos esta questão procurando por sinais de acreção actualmente a decorrer, especificamente através da variabilidade espectral e fotométrica dos nossos alvos.

Para esse fim, neste projecto, usamos espectros da estrela do tipo O σ OriA, obtidos através do espectrógrafo PARAS para determinar a sua variabilidade em curtos espaços de tempo (entre algumas horas até alguns dias) usando uma versão modificada do método de Variação Temporal Espectral. Testamos este método com observações do NARVAL de conhecidas estrelas variáveis do tipo O e B. Apesar de o método funcionar na amostra de teste descobrimos que, o sinal-sobre-ruído das observações do PARAS não é alto o suficiente para permitir a confirmação de uma detecção ou não-detecção de variabilidade. Propomos novos protocolos de observação para detectar variabilidade espectral em estrelas do tipo O baseando-nos nestes resultados.

De seguida usamos duas amostras de candidatos a objectos estelares jovens massivos (MYSOs) de modo a determinar se estes são fotometricamente variáveis no infra-vermelho próximo utilizando dados do censo VVV. Usamos dados das 'pawprints' do VVV para construir duas bases de dados, após o pós-processamento adicional de todos os dados do VVV. Identificamos as fontes MYSO nessa base de dados e procedemos a fazer uma análise das curvas de luz (LCs) e do periodograma Lomb-Scargle. As LCs foram classificadas de acordo com a sua periodicidade e morfologia. Também ajustamos as suas distribuições espectrais de energia (SED) a modelos de objectos estelares jovens. O catálogo de candidatos MYSO variáveis resultante dá um vislumbre sem precedentes para possíveis processos de acreção a influenciar as magnitudes observadas no infravermelho próximo, tal como previsto pelos modelos de acreção não-constante. Observações de seguimento destes MYSOs variáveis podem ser usados para explorar mais a natureza de acreção nestes objectos.

Abstract

Massive stars are a small fraction of all stars formed in the galaxy ($\sim 1\%$) but, in spite of this, they are the major engine driving galactic evolution. Despite their importance, there are still unanswered questions in their formation processes. One of the main questions is how do they gain their mass and how big of a role accretion plays in their formation process? We look into this question by looking for signs of ongoing accretion, specifically in spectral and photometric variability.

To that end, in this project, we use spectra of the O-star σ OriA taken from the PARAS spectrograph to determine if it is variable in short time-spans (a few hours to days) using a modified version of the Temporal Variance Spectrum method. We test this method with NARVAL observations from known variable O and B stars. We find that although the method works in the test sample, the SNR of the PARAS observation is not high enough to allow a confirmation of detection or non-detection of variability. Based on this findings we propose new observational protocols to detect spectral variability in O-stars.

We then use two samples of massive young stellar objects candidates in order to determine if they are photometrically variable in the NIR using data the VVV survey. We used the VVV pawprint data to build two databases, after performing some additional post-processing to the entire VVV data. We identified the MYSO sources in that database and performed a light-curve (LCs) and Lomb-Scargle periodogram analysis. The LCs were classified according to their periodicity and morphology. We also fitted their spectral energy distributions (SED) to models of young stellar objects. The resulting catalog of variable MYSO candidates gives an unprecedented look into possible accretion processes influencing observed NIR magnitudes as predicted by models of non-constant accretion. Follow-up of these variable MYSOs can be used to further explore the nature of accretion in these objects.

Key-words

Young stellar objects, Massive stars, variability, photometry, spectroscopy.

Contents

1	Introduction	27
1.1	Star formation Primer	27
1.1.1	Observational constraints of high-mass star formation	28
1.1.2	High-mass star formation	30
1.1.3	On the nature of accretion in YSOs	31
1.1.4	Observational signatures of High Mass star variability	32
1.2	Techniques to examine variability	33
1.2.1	Photometry	33
1.2.2	Spectroscopy	34
1.2.3	Asteroseismology	35
1.3	The impact of new facilities: an age of Big Data	36
1.4	Aims	37
1.4.1	Spectroscopic variability of a young O star: case Study	37
1.4.2	Studying photometry variability in MYSOs	38
1.4.3	Adapting to Big Data	38
1.4.4	Matching observations to stellar models	39
2	Exploration of the spectroscopic variability in SigmaOriA	40
2.1	Observations	42
2.1.1	Line list	45
2.2	Measuring spectral variability	46
2.2.1	The cross correlation function	46
2.2.2	Bisector method and Line profile variations	47
2.2.3	Smoothed Temporal variance spectrum analysis	49
2.2.4	Testing known variable stars	51
2.3	Results	52
2.3.1	Frequency determination	53
2.3.2	Regarding the confidence of the results	56

2.4	The way forward	59
3	The VVV survey (a Big Data challenge)	60
3.1	The VVV survey	60
3.2	Processing of the pawprint photometry	61
3.3	Construction of the ancillary databases	63
3.3.1	Robust statistical indicators: IQR and MAD	64
3.4	Building the LC pipeline	65
3.4.1	Photometric errors from observing conditions	66
3.4.2	Concerning non-linearity errors	68
3.4.3	Are the errors affected by the chosen target fields?	69
3.4.4	Periodograms, false alarm probability, and their aliases	70
3.5	Data products and the way forward	71
4	The photometric variability of MYSOs	73
4.1	Defining target sample	75
4.1.1	EGO sample	76
4.1.2	Non-EGO sample	77
4.2	Computing and fitting SEDs	78
4.3	Results	80
4.3.1	Variable sources	80
4.3.2	LC classes	81
4.3.3	SEDs	87
4.4	Discussion	90
4.4.1	On the presence of other signposts of High-mass Star formation . . .	92
4.4.2	SEDs	95
4.5	Conclusions	98
5	Summary and Future Work	99
5.1	Spectroscopic variability	99
5.2	Photometric Variability	100
5.3	Future prospects of variability research	101
5.4	The challenging nature of Big Data and the need for adaptation	102
A	Additional materials	113
A.1	Tables	113

A.2	Figures	133
A.2.1	LCs	133
A.2.2	SEDs	154
 B Publications		 168
B.1	Thesis publications	168
B.1.1	Refereed	168
B.1.2	Catalogs	168
B.2	Additional Publications	168
B.2.1	Refereed	169
B.2.2	Proceedings	169
B.2.3	Catalogs	169

List of Tables

2.1	Main characteristics of the used instruments.	43
2.2	Summary of the test sample.	43
2.3	Summary of observed nights.	44
2.4	Summary of SNR.	45
2.5	Summary of the studied lines.	46
2.6	Results of the test sample.	51
2.7	Frequencies and amplitude of the variability by line.	57
3.1	Summary of the CASU photometry flags.	62
4.1	Summary of the target samples	78
4.2	Used filters and apertures for building the SEDs.	79
4.3	Source coordinates, photometric data and variability	81
4.4	Observed parameters of LC classes, for both EGO and non-EGO samples.	81
4.5	SED results by mass bin.	89
4.6	EGO and non-EGO MYSO candidates with nearby methanol masers.	94
4.7	Summary of the median fit parameters, for both EGO and non-EGO samples divided by periodicity.	95
A.1	Input data to build the SEDs.	114
A.2	Results of the weighted averaging of the fit SEDs.	124

List of Figures

1.1	The four stages of protostellar evolution. SED distributions (left panels) corresponding to the different protostar+disk configurations (right panels). From Isella (2006).	29
1.2	The linewidth relation for the Central Molecular Zone of the galactic center measured for four molecules. Filled symbols correspond to structures which do not contain higher level structures. Open symbols correspond to structures that do contain higher level structures. From Shetty et al. (2012).	31
1.3	Example of the type of line-profile variability found in a sample of O stars and B supergiants from a spectroscopic time-series. [Right panels] Variability in the first and third moments of the line-profile (center), and the two parameters defining the line-broadening (right). Quoted numbers indicate the mean value, standard deviation, minimum and maximum values, respectively. All quantities in km s^{-1} except for $\langle v^3 \rangle$ (in $10^4 \text{ km}^3 \text{ s}^{-3}$). [Left panel] Three characteristic profiles having $\langle v^3 \rangle = 0$ (black) and maximum negative/positive skewness (red and blue, respectively). From Simón-Díaz (2015).	35
1.4	Data volumes from existing and upcoming telescopes: Very Large Telescope (VLT), Sloan Digital Sky Survey (SDSS), Visible and Infrared Telescope for Astronomy (VISTA), Large Synoptic Survey Telescope (LSST), and Thirty Meter Telescope (TMT). From Kremer et al. (2017).	36
1.5	Different runtime obtained using large scale astronomical data with n training and m test examples. The solid black lines represent the speed up of the buffer k-d tree using 4 GPUs over brute-force and multi-core k-d tree based traversal using 4 cores/ 8 hardware threads. From Kremer et al. (2017).	37
2.1	Simple schematic of an echelle grating cross-dispersion. From <i>Wikipedia</i> .	41

2.2	Zoomed Part of the raw Image showing Echelle orders of the Th-Ar spectra on both the Fibers (Star Fiber and Calibration Fiber) between 3700 Å and 6800 Å. From Chakraborty et al. (2010).	44
2.3	. Construction of a Cross-Correlation Function by correlating a template binary mask. From Melo (2001).	47
2.4	The CCFs for each day of month M1(left panels), and the difference from the median CCF (left panels). Day M1D1(top), M1D2(center), and M1D3(bottom) are shown. The dark line in the CCF plots corresponds to the median CCF of the month.	48
2.5	(TVS) $_N^{1/2}$ (top),($smTVS$) $_N^{1/2}$ (middle) normalized by unity and mean line profile (bottom) of the line He I $\lambda 4471$ Å in the spectra of λCep . Filter width S is 0.2 Å. The horizontal line corresponds to the significance level 0.001. From Kholtygin & Sudnik (2016).	50
2.6	Variability of H_α for $\sigma Ori E$ on the night of 28 of November of 2007. Plotted are the variability of the line in velocity space (top left), the differences between consecutive observations (bottom left), the TVS (top right), and the smTVS (bottom right). On the TVS and smTVS plots, the dotted, dashed and full black lines correspond, respectively to the 1- σ , 2- σ , and 3- σ of the TVS.	52
2.7	LPVar of H_α for m2 each line corresponds to a combination of all observations of each day.	53
2.8	TVS (top) and smTVS (bottom) of H_α for M1. The dotted, dashed and full black lines correspond, respectively to the 1- σ , 2- σ , and 3- σ of the TVS.	54
2.9	Comparison of the H_α and He $_{5875}$ lines. From left to right and top to bottom we have a comparison of their amplitudes, EWs, and FWHM. The bottom right plot present the changes in EWs of each line over in each observation (blue dots are H_α and green dots are He $_{5875}$. The observations are M1D1, M1D2, M1D3, M2D3, M2D5, M2D6, M2D7, M3D1, M3D2, M3D3, M3D4, M3D5, M3D6.	55
2.10	The smTVS of the lines which showed larger variations in m1. From left to right and top to bottom H_α , H_β , He_{4471} , and He_{5875} . The dotted, dashed and full black lines represent, respectively, 1-,2-, and 3- σ of the TVS.	56
2.11	The BIS+ as a function of measured RV from the CCFs of M1. Each point represents the combined spectra of 6 consecutive observations from each day. This combination was made in order to increase the SNR.	58

3.1	VVV survey area.	61
3.2	Mock-up of a pawprint showing the moon (left) and exposure map for a filled tile(right). In the exposure map, dark green = 1, light green = 2, magenta = 3, red = 4, yellow = 6, in units of the single-pawprint exposure time.	63
3.3	Scheme of the created databases highlighting the key which connects them.	64
3.4	IQR of a distribution.	65
3.5	LC of an eruptive event. Top panel shows the LC of the source, the error bars represent $MAD(\Delta S_{i_{mjd}})$, the bottom plot shows the RGB image of the source using the Spitzer IRAC 3.6 μm , IRAC 4.0 μm , and the 24 μm MIPS band as blue, green and red, respectively. The VVV source is indicated by the blue circle and the green cross represents the MIPS co-ordinates. The contours of the RGB are in the interval of [Peak-5 σ , Peak] from the ATLASGAL observation at 850 μm . From Teixeira et al. (2018).	67
3.6	Annuli used to determine the photometric errors.	68
3.7	Histogram showing the systematic errors using the vicinity of each source. The red curve represents the case where we only consider the stellar sources with ± 1 mag around our targets. The blue curve represents the case where we consider all stellar sources in the vicinity of our targets.	69
3.8	Systematic errors as a function of the magnitude of each target. The red points represents the case where we only consider the stellar sources with ± 1 mag around our targets. The blue points represent the case in which we consider all stellar sources in the vicinity of our targets. From Teixeira et al. (2018).	70
4.1	Example SEDs. From left to right, SEDs for three different objects of similar masses at Stages I, II, and III of evolution. From top to bottom, objects have masses ~ 0.2 , ~ 2 , and $\sim 20 M_{\odot}$ objects. Each plot shows 10 SEDs, one for each inclination (solid lines), the input stellar photosphere for each model (dashed lines). From Robitaille et al. (2006).	75
4.2	Same SEDs as in Fig. 4.1, the different contribution to the SEDs are shown: the star (blue), the disk (green), and the envelope (red). From Robitaille et al. (2006)	76

- 4.3 Some of the clearer LCs, periodic (left column) and aperiodic (right column). Each figure shows the LC of the source, error bars represent $\text{MAD}(\Delta S_{i_{mjd}})$. The vertical axis represents the variability from the median normalized by $\text{max}(|K_i - \text{median}(K)|)$. From Teixeira et al. (2018). 82
- 4.4 Prototypical LPV-yso sources: Top panel for each figure shows the LC of the source, error bars represent $\text{MAD}(\Delta S_{i_{mjd}})$, the left middle panel shows the corresponding periodogram in logarithmic scale (also plotted are the 99%, 95%, and 90% false probability levels, respectively: the green dot-dashed line, the cyan full line, and the red dashed line), the bottom left panel shows the phase-folded light curve of the source using the best period fitted (also shows the corresponding value in days), the bottom right plot shows the RGB image of the source using the Spitzer IRAC 3.6 μm , IRAC 4.0 μm , and the 24 μm MIPS band as blue, green and red, respectively. The VVV source is indicated by the blue circle and the green cross represents the MIPS co-ordinates. The contours of the RGB are in the interval of [Peak-5 σ , Peak] from the ATLASGAL observation at 850 μm . From Teixeira et al. (2018). 83
- 4.5 Prototypical STV sources: Top panel for each figure shows the LC of the source, error bars represent $\text{MAD}(\Delta S_{i_{mjd}})$, the left middle panel shows the corresponding periodogram in logarithmic scale (also plotted are the 99%, 95%, and 90% false probability levels, respectively: the green dot-dashed line, the cyan full line, and the red dashed line), the bottom left panel shows the phase-folded light curve of the source using the best period fitted (also shows the corresponding value in days), the bottom right plot shows the RGB image of the source using the Spitzer IRAC 3.6 μm , IRAC 4.0 μm , and the 24 μm MIPS band as blue, green and red, respectively. The VVV source is indicated by the blue circle and the green cross represents the MIPS co-ordinates. The contours of the RGB are in the interval of [Peak-5 * σ , Peak] from the ATLASGAL observation at 850 μm . From Teixeira et al. (2018). 84
- 4.6 LC of a dipper event. Colors and symbols are the same as in Fig. 4.4. From Teixeira et al. (2018). 85
- 4.7 Typical Fader event. Colors and symbols are the same as in Fig. 4.4. From Teixeira et al. (2018). 86

4.8	LC of the example of a low-amplitude eruptive event. Colors and symbols are the same as in Fig. 4.4. From Teixeira et al. (2018).	87
4.9	Grid of SEDs for our prototypical sources. The dark line corresponds to the best fit model. The grey lines correspond to other $\chi^2 - \chi_{best}^2 < 3$ models. From Teixeira et al. (2018).	91
4.10	Diagram of the circumstellar structure surrounding the non-EGO (left) and EGO (right) objects. In the non-EGO case, the central protostellar source is surrounded by a spherical shell of circumstellar material which has still not evolved to a disk, the spherical shell is inhomogeneous since there are some local over-densities in the interior of the circumstellar gas. In EGOs, the polar areas are being cleared by outflow or jet emission from the central source, leading to a more unobstructed view of the source by the observer. .	91
4.11	Histogram of ΔK divided by sample and periodicity. EGO and non-EGO sources are shown, respectively, on the right and left plots. From Teixeira et al. (2018).	92
4.12	Mass versus envelope-accretion rate for the fitted SEDs of EGO and non-EGO sources, in logarithmic scale. EGO, non-EGO, periodic, and aperiodic, are plotted at the top left, top right, bottom left, and bottom right, respectively. From Teixeira et al. (2018).	96
4.13	HR diagram for our sources. Symbol size corresponds to different mass bins, as shown in the legend, where $M = M_{\star}/M_{\odot}$. The dashed lines(from bottom to top) are the PMS tracks for 1, 2 , 3, 4, 5, 6, and 7 M_{\odot} , the filled line is the ZAMS. Blue and red symbols are, respectively, EGOs and non-EGOs. From Teixeira et al. (2018).	97
A.1	LC of the source, with error bars representing $MAD(\Delta S_{i_{mjd}})$, periodograms (also plotted are the 99%, 95%, and 90% false probability levels, respectively: the green dot-dashed line, the cyan full line, and the red dashed line), the phase-folded LC using the best period fitted, the RGB image of the source using the Spitzer IRAC 3.6 μm , IRAC 4.0 μm , and the 24 μm MIPS band as blue, green and red, respectively. The VVV source is marked by the blue circle and the green cross represents the MIPS coordinates. The contours of the RGB are in the interval of [Peak-5 σ , Peak] from the ATLASGAL observation at 850 μm	134
A.2	Continuation of Fig. A.1.	135

A.3	Continuation of Fig. A.1.	136
A.4	Continuation of Fig. A.1.	137
A.5	Continuation of Fig. A.1.	138
A.6	Continuation of Fig. A.1.	139
A.7	Continuation of Fig. A.1.	140
A.8	Continuation of Fig. A.1.	141
A.9	Continuation of Fig. A.1.	142
A.10	Continuation of Fig. A.1.	143
A.11	Continuation of Fig. A.1.	144
A.12	Continuation of Fig. A.1.	145
A.13	Continuation of Fig. A.1.	146
A.14	Continuation of Fig. A.1.	147
A.15	Continuation of Fig. A.1.	148
A.16	Continuation of Fig. A.1.	149
A.17	Continuation of Fig. A.1.	150
A.18	Continuation of Fig. A.1.	151
A.19	Continuation of Fig. A.1.	152
A.20	Continuation of Fig. A.1.	153
A.21	Continuation of Fig. A.1.	154
A.22	The fitted SEDs with the best fit model in the black line, the grey lines are other $\chi^2 - \chi_{best}^2 < 3$ models, data points, upper, and lower limits are, respectively, circles, inverted triangles, and triangles.	155
A.23	Continuation of Fig. A.22.	156
A.24	Continuation of Fig. A.22.	157
A.25	Continuation of Fig. A.22.	158
A.26	Continuation of Fig. A.22.	159
A.27	Continuation of Fig. A.22.	160
A.28	Continuation of Fig. A.22.	161
A.29	Continuation of Fig. A.22.	162
A.30	Continuation of Fig. A.22.	163
A.31	Continuation of Fig. A.22.	164
A.32	Continuation of Fig. A.22.	165
A.33	Continuation of Fig. A.22.	166
A.34	Continuation of Fig. A.22.	167

List of Abbreviations

CTTS	Classical T Tauri Stars
EGO	Extended Green Object
EW	Equivalent width
HMSF	High-mass Star Formation
IR	Infrared
LPVar	Line profile variations
LPV-yso	Long Period Variables
LTE	Local Thermodynamical Equilibrium
MS	Main-sequence
MYSO	Massive Young Stellar Objects
NIR	Near Infrared
NLTE	Non Local Thermodynamical Equilibrium
PLP	Protostellar Luminosity Problem
PMS	Pre-main sequence
SED	Spectral Energy Distribution
SNR	Signal-to-noise ratio
STV	Short Timescale Variable
VALD	Vienna Atomic Line Data
VVV	Vista Variables in the Via Lactea
YSO	Young Stellar Objects
ZAMS	Zero-age main sequence

Chapter 1

Introduction

Massive stars ($\geq 8M_{\odot}$) are crucial elements for galactic evolution. They are responsible for the chemical enrichment of the interstellar medium, they can trigger or quench star formation in molecular clouds and, despite their relative small numbers ($< 1\%$ of all stars in the galaxy), they generate $\sim 20\%$ of the total galactic luminosity.

Given this important role, it is essential to study and understand the mechanisms and processes which govern their short ($< 10\text{Myr}$) and violent lives. Some of the largest gaps in our knowledge of their life-cycle concern the topic of how do massive stars form and how to they accrete their large masses. Because they are few in number and evolve rapidly, by the time they become visible, they are already in the main-sequence, even though still accreting. There is some discussion if these stars even have a proper pre-main sequence phase.

This thesis work aims at studying one aspect of the initial stages of massive stars, namely variability, which is strongly related to accretion processes. This work uses both spectral and photometric methods to study variability in these stars. The unprecedented nature of this work serves as a blueprint for future research of the topic.

1.1 Star formation Primer

Stars form in dense cores, deeply embedded in molecular clouds (Stahler & Palla, 2005). These giant clouds of molecular hydrogen collapse when their self-gravity overcomes the effects of rotation, turbulence, magnetic fields, and thermal pressure (Stahler & Palla, 2005; Kippenhahn & Weigert, 1990). Initial spherical collapse models (Larson, 1969) considered that material would completely fall into the forming protostar, not taking into account that the conservation of angular momentum would act to form circumstellar disks. Nowadays, these models have become more complex, in order to explain observations of disks, such as those visible in classical T-Tauri stars (CTTS).

Later works (Adams et al., 1987; Lada, 1987; André, 1994) have found that low-mass (sun-like) protostars can be divided into four classes based on their spectral energy distribution (SED). These range from Class 0 to Class III, where the former is at the birth-line and the latter close to the zero-age main-sequence (ZAMS). These protostellar classes can be summarized as such (see Fig. 1.1):

- Class 0, where the central core begins spherical collapse, and with peak emission in sub-millimeter wavelengths. Molecular jets and outflows are driven by these objects;
- Class I objects, have peak emission occurring in the far infrared wavelengths, while the jets and outflows are optically visible due to shocked gas. Most observed radiation is still re-emission from the disk;
- Class II objects have peak emission in the near-infrared (NIR) wavelengths, the scale height of the disk is now small when compared with its radius, most jet/outflow activity has subsided.
- Class III objects are mostly emitting in the optical range, the anemic disk is almost exhausted, and accretion has stopped.

For stars with masses greater than $20 M_{\odot}$, the Kelvin-Helmholtz time (thermal adjustment timescale) is inferior to the formation time (free-fall time), therefore, the star becomes fully radiative while it is still accreting, . Considering that the radiative pressure produced at this stage is enough to stop accretion it should be impossible to form stars of masses $\geq 60M_{\odot}$ (Larson & Starrfield, 1971). This problem is one of the many currently plaguing high-mass star formation theories since it directly contradicts the observational fact that there are stars with masses higher than $60 M_{\odot}$. Modern numerical models (Krumholz et al., 2005, 2009; Kuiper et al., 2010) have addressed these issues concluding that there is no upper limit to the formation of massive stars (Krumholz (2015) in the formation of very high mass stars).

1.1.1 Observational constraints of high-mass star formation

High-mass stars are rare, as stars with masses higher than $15 M_{\odot}$ account for $\sim 0.1\%$ of all stars formed in the galaxy (Miller & Scalo, 1979), and are also short-lived, with lifetimes less than 10 Myr (Salaris & Cassisi, 2005). Given their scarcity and short lifespans we only observe a reduced number of these stars within the solar vicinity and most of them are already well within their main-sequence phase. The limited number of young observable

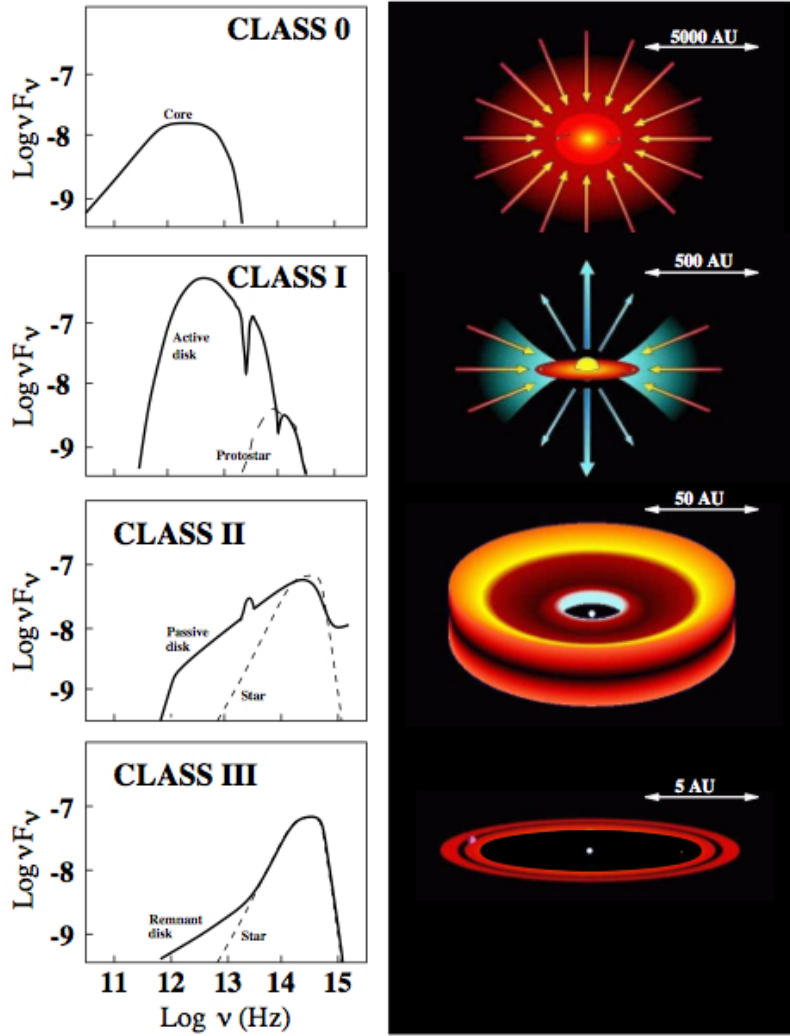


Figure 1.1: The four stages of protostellar evolution. SED distributions (left panels) corresponding to the different protostar+disk configurations (right panels). From Isella (2006).

stars in the solar neighborhood is a huge factor limiting our current knowledge of high-mass star formation.

To study young massive stars we have to look to distances further than 400 pc, where we find the closest O-star, in the Orion Nebula. The large distances severely limit the level of detail which can be observed. Given that high-mass stars are usually found in massive star clusters, crowding and confusion become a huge source of observational problems (Krumholz, 2015b), particularly because they increase the aforementioned large distances and lower resolutions issues.

Typical regions of massive star formation are greatly extinguished by interstellar dust, making observations on the visual wavelength ranges extremely difficult. Interstellar extinction redshifts stellar radiation into higher wavelengths where the flux will be lost to

atmospheric absorption and re-emission, further increasing the confusion factor of the observations.

Finally, the luminosity of high-mass stars is such that their intense radiation quickly destroys their surrounding environment. Therefore, the signposts of early evolution are erased without trace.

We can conclude that the current high-mass star formation (HMSF) studies are severely under-sampled observationally. Hydro-dynamic simulations and radiative transfer models have tried to successfully simulate HMSF but there is not, up to now, enough evidence to constrain these models.

1.1.2 High-mass star formation

Stars form inside giant molecular clouds (GMCs), molecular gas clouds with typical surface densities of $\sim 0.1 - 1 \text{ g cm}^{-2}$, typical masses of a few thousand M_{\odot} , and radius of $\sim 1 - 2$ pc. Observations of molecular clouds have shown that two empirical power-law relations, known as "Larson's Relationships", govern the physics of GMCs in equilibrium. The first is a relation between the mass and radius of a molecular cloud, the second Larson relationship links the linewidth of the emission line and the radius the cloud (Larson, 1981; Shetty et al., 2012). Figure 1.2 shows the linewidth-size relationship for four molecules, it is apparent that for smaller scale structures the dispersion in velocities is also smaller.

High-mass star formation occurs inside massive cores of $\sim 0.1\text{pc}$ in radius and $\sim 100 M_{\odot}$, that are usually turbulent.

The timescales involved in forming a 10-100 M_{\odot} star are ~ 100 kyr, an order of magnitude smaller than low-mass star formation. An even bigger discrepancy is in the timescales governing the thermal evolution of the stars. The thermal evolution timescale of a star, known as the Kelvin-Helmholtz time (t_{kh}), is given by:

$$t_{kh} = \frac{GM_{\star}^2}{R_{\star}L_{\star}} \quad (1.1)$$

where G is the gravitational constant, M_{\star} is the mass of the star, R_{\star} is its radius and L_{\star} is the current luminosity of the star.

If we consider a sun-like star, in its zero-age main-sequence, we would have a Kelvin-Helmholtz timescale of ~ 50 Myr. In the case of a protostar, of sun-like mass, the $R_{\star}L_{\star}$ is almost 100 times greater, which leads to a $t_{kh} \sim 100$ kyr. If we perform a similar calculation to a 50 M_{\odot} star in its ZAMS, with a typical radius of 10 R_{\odot} and $3.5 * 10^5 L_{\odot}$, we obtain a thermal timescale of ~ 20 kyr, whereas the free-fall time is $\sim 10^5$ yrs. Therefore, high-mass

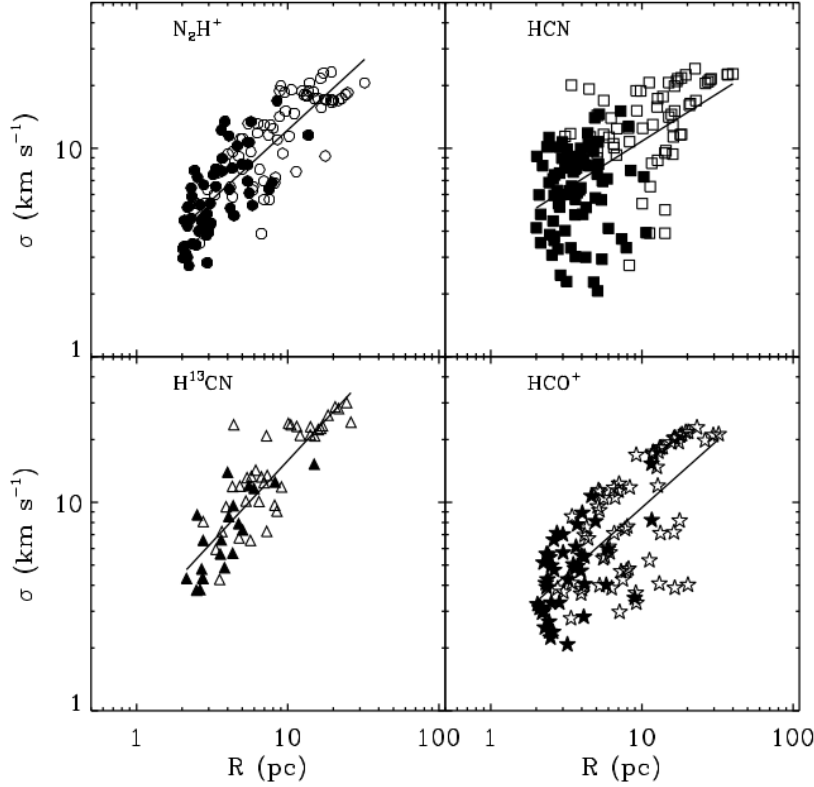


Figure 1.2: The linewidth relation for the Central Molecular Zone of the galactic center measured for four molecules. Filled symbols correspond to structures which do not contain higher level structures. Open symbols correspond to structures that do contain higher level structures. From Shetty et al. (2012).

stars will reach thermal equilibrium while still forming, and, ultimately, it can be said they reach the main-sequence while still accreting. As a reminder it should be noted that the formal definition of a main-sequence star is that the star has achieved hydrostatic and thermal equilibrium (Stahler & Palla, 2005). The nature of accretion in high-mass stars is yet to be studied. It will be indirectly addressed through the work here.

1.1.3 On the nature of accretion in YSOs

The paradigm of accretion in young stellar objects (YSO) shifted from a model of constant mean accretion rate to that favoring short events of intense accretion (Vorobyov & Basu, 2006, 2015; Zhu et al., 2009). This paradigm shift required, in order to address the issue of the ‘protostellar luminosity problem’ (Kenyon et al., 1990; Kenyon & Hartmann, 1995; Dunham et al., 2014). There are two main sources for contributing to the total luminosity received from a protostar: the protostellar structure and instantaneous accretion rate. It is complicated to distinguish the overall contributions from each. Nevertheless, it has been

observed that the total luminosity of protostars tend to be an order of magnitude smaller than otherwise expected. This is known as the protostellar luminosity problem (PLP) (Kenyon et al., 1990; Kenyon & Hartmann, 1995; Dunham et al., 2014).

An easy way to solve the PLP is to distribute the accretion luminosity into short periods or bursts, in which the photometric luminosity is high, while retaining a low luminosity during the remainder of the time. This scenario naturally predicts that YSOs will be variable.

A variety of models including turbulent or competitive accretion, accretion regulated by core, disk, and feedback, are invoked to understand the deviation from the idealized case of an isothermal sphere (Kenyon et al. (1990), McKee & Offner (2010), Myers (2010), Vorobyov & Basu (2008), Dunham & Vorobyov (2012), Dunham et al. (2014) and references therein). However, most of these models share the variable accretion component, albeit differing at various mass regimes. The accumulated observational evidence appears to favor variable accretion instead of constant mean scenarios (Dunham et al., 2014). Photometric variability of YSOs can be related to their natal environment, accretion physics or a combination of both (Contreras Peña et al. (2017), Kesseli et al. (2016), Meyer et al. (2017) and references therein). Some of the variability can be caused by cold and hot spots formed on the surface of the YSO by in-falling material from the disc. Dust clumps in the stellar medium surrounding the YSO can cause variable extinction of star-light as it passes along the observers line of sight (e.g. Herbst & Shevchenko (1999), Eiroa et al. (2002) among others).

Therefore, the way to truly settle the question of the PLP is through observational evidence. It is necessary to look for tracers of ongoing accretion, either in the spectra or in the brightness of these young high mass objects. Our aim is to study this phenomena in MYSOs.

1.1.4 Observational signatures of High Mass star variability

The best way to observe changes in or around any star is to look for differences in the light reaching any given detector, be it a human eye, a photographic plate, or a CCD. Changes in circumstellar environment or even in stellar structure affect both the amount and nature of the light-wave reaching us.

In the low-mass regime, there are two well-known examples of highly variable YSOs: FUors (FU Orionis) and EXors (EX Lupi). These high amplitude photometric variables

are the result of variable accretion lasting, respectively from a few years to a few months. These objects are known to be low-mass YSOs, although similar counterparts in the higher mass range have been found (Kumar et al., 2016; Caratti o Garatti et al., 2017). Kumar et al. (2016) studied highly variable light curves (LCs) of massive young stellar objects (MYSOs) candidates from the Vista Variables in the Via Lactea (VVV) survey (Minniti et al., 2010), arguing that they were signposts of ongoing episodic accretion. Photometric and spectroscopic variability in a $20 M_{\odot}$ MYSO was used by Caratti o Garatti et al. (2017) to conclude that disk-mediated accretion bursts are a common mechanism across stellar masses. ALMA observations were used by Hunter et al. (2017) as evidence that sudden accretion is responsible for the growth of a massive protostar. These findings suggest that episodic accretion may be a common mechanism in star formation, independent of mass. Computational models predict luminous flares in MYSOs, which are morphologically similar to FUors and EXors (Meyer et al., 2017). So, is this the same phenomena observed at different scales? This question can only be answered by increasing the number and detail of both photometric and spectroscopic observations of MYSOs.

1.2 Techniques to examine variability

1.2.1 Photometry

The basic principle of photometry is to count the photons, i.e., the brightness that reaches the detector using a well determined wavelength filter. This information can be used in different ways to determine stellar properties. For example, combining the brightness of different filters we can obtain the value of stellar colors which can give an idea of the evolutionary stage of a star. Furthermore, and of particular relevance to the work performed during this thesis, measuring the brightness of a source over multiple epochs results in a measurement of brightness variability over time. Such changes can be used to infer stellar structure variations, circumstellar changes or even properties of the interstellar medium.

The study of time varying photometry is a powerful source of information. With the development of better and more precise instrumentation, the detection of smaller variations has allowed astronomers to better quantify and qualify stellar phenomena. A significant number of large time-domain surveys have, as a consequence, taken place, including wide-field optical imaging surveys (e.g. GAIA Perryman (2005)). The exploration of variability in the infrared and NIR has started to become more important nowadays as these wavelength bands are more indicated to deal with the problem of interstellar

extinction. Such bands are also helpful in studying YSOs and MYSOs since these tend to still be embedded in highly extinct regions, and sometimes still surrounded by remnants of their primordial giant molecular cloud (GMC). The VISTA variables in the Via Lactea (VVV) survey (Minniti et al., 2010) was created to study photometric variability in the NIR.

1.2.2 Spectroscopy

The spectra of O-stars suffers from several phenomena which hinder its study. Particularly, the lack of sharp absorption lines in the spectra led to the realization that stellar rotation couldn't be the only mechanism behind the observed broadening. In order to explain this, several authors proposed that the broadening was caused by an effect that they referred to macroturbulent broadening (Struve, 1952; Conti & Ebbets, 1977; Howarth et al., 1997). Simón-Díaz et al. (2010) performed measurements of the non-rotational component and concluded that it was not produced by any large scale turbulent motions.

In Aerts et al. (2009), the so-called pulsational hypothesis was revived. According to this hypothesis it is possible to explain macroturbulence in massive stars by as a collective pulsational velocity broadening due to gravity modes (Aerts et al., 2009; Simón-Díaz et al., 2010). Although the presence of such pulsational components has been confirmed in the case of B dwarfs and giants, it is yet to be explored in the case of O-type stars.

Macroturbulent broadening and its link to line-profile variability has been explored in Simón-Díaz (2015). As we can see in Fig. 1.3 the line-profile does exhibit variability but the overall shape of the profile appears to remain constant. The approach delineated by Simón-Díaz is interesting but their observational strategy was designed to search for long-period variations. In fact, using this long-period variability studies Simón-Díaz was even able to determine the presence of spectroscopic trinnaries in Sigma-Ori (Simón-Díaz et al., 2011).

Recent studies of spectral variability in O-stars have shown several long-period physical effects with multiple degrees of complexity. These studies have looked into spectral observations taken throughout periods of years and the role which effects like macroturbulence have in line-broadening (Simón-Díaz & Herrero, 2014; Simón-Díaz et al., 2014; Simón-Díaz, 2015). In recent years there has been a revival of the so-called pulsational hypothesis which suggests that macroturbulence in massive stars can be explained by a collective pulsational broadening, a consequence of asteroseismic gravity modes (Aerts, 2015). So far, these studies have considered long-period variability but they have not

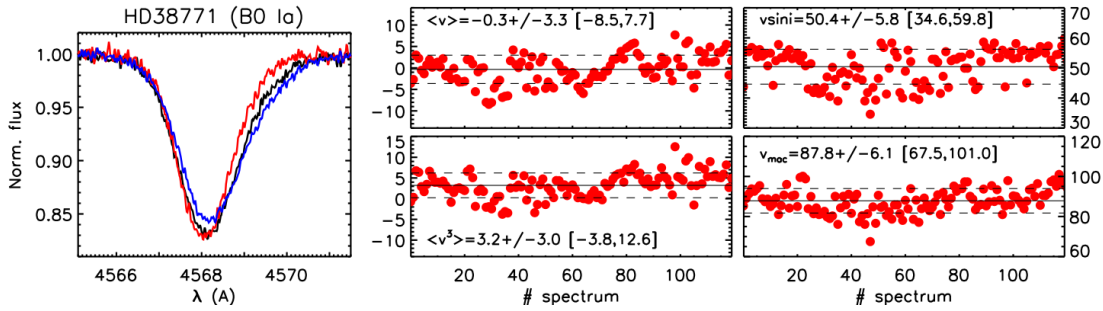


Figure 1.3: Example of the type of line-profile variability found in a sample of O stars and B supergiants from a spectroscopic time-series. [Right panels] Variability in the first and third moments of the line-profile (center), and the two parameters defining the line-broadening (right). Quoted numbers indicate the mean value, standard deviation, minimum and maximum values, respectively. All quantities in km s^{-1} except for $\langle v^3 \rangle$ (in $10^4 \text{ km}^3 \text{ s}^{-3}$). [Left panel] Three characteristic profiles having $\langle v^3 \rangle = 0$ (black) and maximum negative/positive skewness (red and blue, respectively). From Simón-Díaz (2015).

contemplated short-period variability in the context of young O-stars.

1.2.3 Asteroseismology

One of the most powerful tools used to study stellar physics is Asteroseismology. The theoretical concept supporting asteroseismology is that the different oscillations modes observed on the stellar surfaces probe their interiors at different depths (Christensen-Dalsgaard, 2008).

Presently asteroseismology in O-stars has been performed mostly with data from satellite-based missions like CoRoT, Kepler, MOST among others. The limited number of these stars in the fields of these satellites and the difficulties linked to mode identification have kept the number of O-stars studied quite small. One of the ways to overcome the mode identification problems is to use high-resolution spectroscopy as an observational tool (Aerts, 2015; Christensen-Dalsgaard, 2008).

Asteroseismology can be used both with spectral or photometric variability, because the technique studies oscillations through a period or frequency analysis. While it has been used successfully in a myriad of cases, its application to O stars remains an issue. The difficulties inherent to time dependent spectral variations expanded upon above, i.e., broadened lines, lack of absorption lines, to name a few, limits the effectiveness of high-resolution spectroscopy to this end. Furthermore, the level of photometric precision required to apply asteroseismology to MYSO observations is, currently, a distant goal. The most promising avenue of inquiry is, therefore, the detection of spectral variability

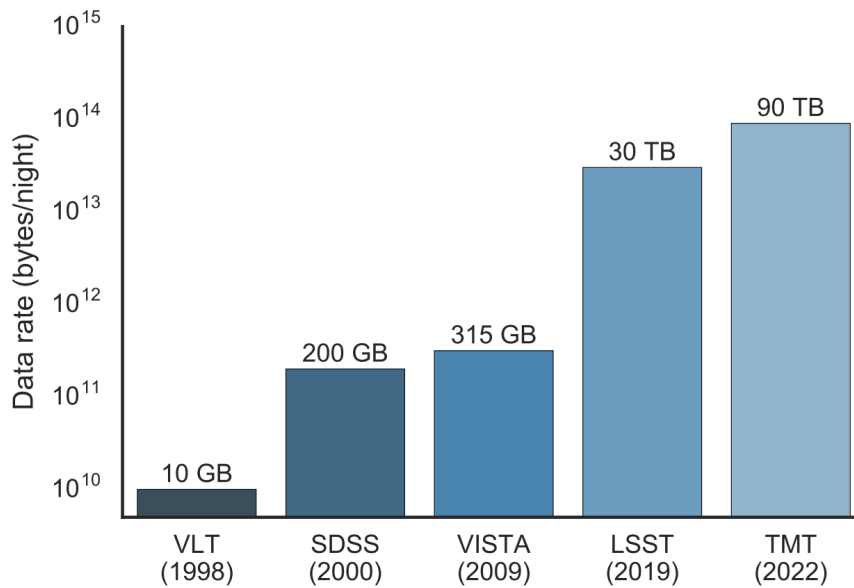


Figure 1.4: Data volumes from existing and upcoming telescopes: Very Large Telescope (VLT), Sloan Digital Sky Survey (SDSS), Visible and Infrared Telescope for Astronomy (VISTA), Large Synoptic Survey Telescope (LSST), and Thirty Meter Telescope (TMT). From Kremer et al. (2017).

using the most precise spectrographs available. If such variations exist, the subsequent frequency analysis might be used to identify asteroseismic modes.

1.3 The impact of new facilities: an age of Big Data

Finally, it is important to devote some time to the ongoing change in astronomical studies resulting from the increasing volume of data available to astronomers. Figure 1.4 shows the amount of data produced nightly with different telescopes, and projecting the expected volume of some upcoming facilities. In the span of two decades the volume of data produced by single telescope facilities has increased four orders of magnitude (Kremer et al., 2017).

Such an increase requires the use of very different approaches to coding. The challenges presented by this increase call for astronomers to develop and use strategies from the realm of computer sciences and engineering. It is no longer efficient for an individual astronomer to spend their time producing small scripts which, while being effective when used for a small subset of data, become processor-heavy and time-consuming when applied to larger data sets. As a way to drive this point home, Fig. 1.5 shows how adapting a k-d tree search structure, which cannot be parallelized for graphical processing units (GPUs), can result in vastly different computational times.

The failure of "brute force" approaches to coding requires astronomers, and other

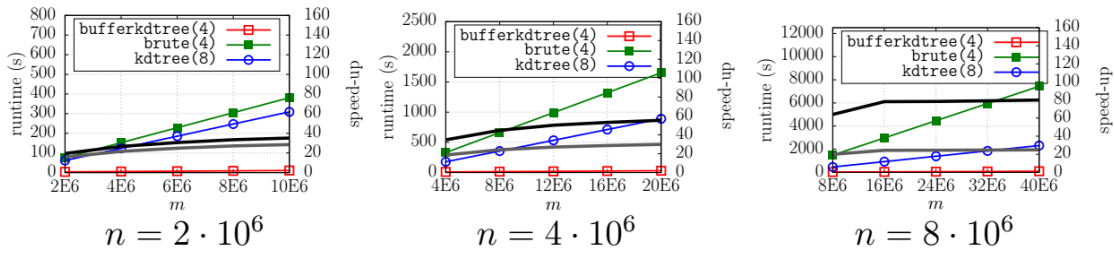


Figure 1.5: Different runtime obtained using large scale astronomical data with n training and m test examples. The solid black lines represent the speed up of the buffer k-d tree using 4 GPUs over brute-force and multi-core k-d tree based traversal using 4 cores/ 8 hardware threads. From Kremer et al. (2017).

scientists, to be evermore dependent on parallel computing, computational clusters, and requires any individual scientist to have code optimization in mind when creating coding frameworks for their individual tasks.

Most computational approaches are effective when dealing with 'small' datasets, however, large volumes of data and information require a high degree of computational optimization. The day-to-day coding, developed by individual astronomers for personal use fails, when faced with the large data.

1.4 Aims

The major aim of this work is to study signposts of ongoing accretion in HMSF and MYSOs. Our approach is, therefore, two-fold: 1- explore the use of high-resolution spectroscopy to detect variability in a young O-star and, if possible, obtain some of its asteroseismic data; 2 - use newly available time-series of NIR photometric data to detect variability on MYSOs.

While either of these two can give rise to a single thesis by itself, the fact is that, given the exploratory nature of the first approach, it was deemed necessary to have a backup plan. Also, both of these approaches are complementary, in the sense that we are moving towards earlier stages of massive stellar evolution. The first of these approaches is exploratory in nature, requiring the development and adaptation of techniques used in other studies.

1.4.1 Spectroscopic variability of a young O star: case Study

Our initial goal was to use high-resolution spectroscopy to study short-period variability in stellar spectra of young massive stars. An asteroseismic analysis of these objects would

allow us to peer into the physics at play in young massive-stars, observe any ongoing star formation, and constrain the relevant physical processes. It was expected that such an analysis would also lead us to pinpoint the origin of these phenomena.

In our opinion a observational strategy based on the study of short-period variability in young O-stars could help to further the understanding of these enigmatic objects. Short-period variations might be signposts of such phenomena as ongoing accretion, stellar activity, disk-star interactions among others. Our detailed high-resolution spectral observations would therefore allow to constrain theoretical aspects and improve current massive star formation models.

The intended approach was to use observations repeated throughout several nights to study short-period variability. Furthermore, exploring these short-period pulsations and attempt to isolate any signals that might be present there. The analysis of such signals could be of extreme value in a path towards an asteroseismic view of young high-mass stars.

In tandem with this goal we also explored the vast photometric data of the VVV project since its wavelength coverage (NIR) results in the study of younger objects.

1.4.2 Studying photometry variability in MYSOs

The aim of the photometric analysis was to obtain the light curves of MYSOs contained in the VVV survey data and identify the ones which presented variability. To this purpose we reprocessed pawprint photometry, thus reducing the photometric noise, and used a combination of catalog information to match the correct MYSO candidates in the VVV.

There were two additional objectives of this study: a) to classify observed light-curves according to their variability; b) analyze them for periodicity.

Considering the large data volume of the VVV survey (over 6 million stellar sources with more than 60 observations per source over 5 years), the reprocessing of pawprint information was a Big Data problem, requiring the use of different coding techniques and structure.

1.4.3 Adapting to Big Data

The use of the VVV survey required a change of approach to the data analysis techniques and coding to better reflect the large volume of data present in the data set. Since one of the goals of this work was to study photometric variability in the VVV, in order to identify variable sources using the best possible version of its photometry the pawprint

data available had to be reprocessed.

Therefore, part of this project required the development of computational codes to reprocess the pawprint data and use it to build two databases while computing some auxiliary queryable information.

1.4.4 Matching observations to stellar models

As a final goal, it was decided that the focus should be on physical characteristics of the studied sources. In order to accomplish this, the extensive nature of the photometric data available in several catalogs was used, using well-known SED models of PMS stars and χ^2 minimization techniques. Analysis of these characteristics, and the type and duration of the observed variability can indicate what are the causes which trigger these variations, additionally it provides an extra verification of their MYSO nature.

Chapter 2

Exploration of the spectroscopic variability in SigmaOriA

The search of spectral variability in massive O stars, as described in the introduction, requires an in-depth study of high-resolution stellar spectra.

The spectrum of O stars can be difficult to study given the extreme physical properties of these stellar objects which impact any observed lines. Given their high effective temperatures (T_{eff}), of the order of > 10000 K, only a small number of distinct absorption lines in the visible and near-infrared wavelength bands are observed. Their spectra are dominated by H I and He I lines (Gray, 2005). Furthermore, these stars are fast-rotators with projected rotational velocities, $v \sin i$, of the order of 100 km s^{-1} . Such high velocities result in large line-broadening. The level of broadening is such that strong absorption lines are highly blended with weak lines (Gray, 2005).

Studies have been made to observe and characterize line-variability in O-stars. Sudnik & Henrichs (2016) and Martins et al. (2015) have reported, respectively, the presence of short-lived prominences and line variability in several observed lines (e.g. H_{α}). Although spectral variability in some O-stars has been an established fact for the past three decades the physical processes behind the variability are far from being understood, and there is still debate regarding the presence of periodicity in this variability (Fullerton et al., 1996; Sudnik & Henrichs, 2016; Markova et al., 2011).

The presence of non-radial pulsations can cause surface variability which, in turn, will result in spectral variability of lines. Another triggering mechanism for variations is the presence of magnetic spots which lead to a non-homogeneous surface (Martins et al., 2015). When the stellar surface is not isotropic, as is the case in the vicinity of magnetic spots, the surface brightness varies along the stellar surface, which will propagate into the photosphere.

Nowadays, the use of echelle spectrographs (see Fig. 2.1) has become common-place.

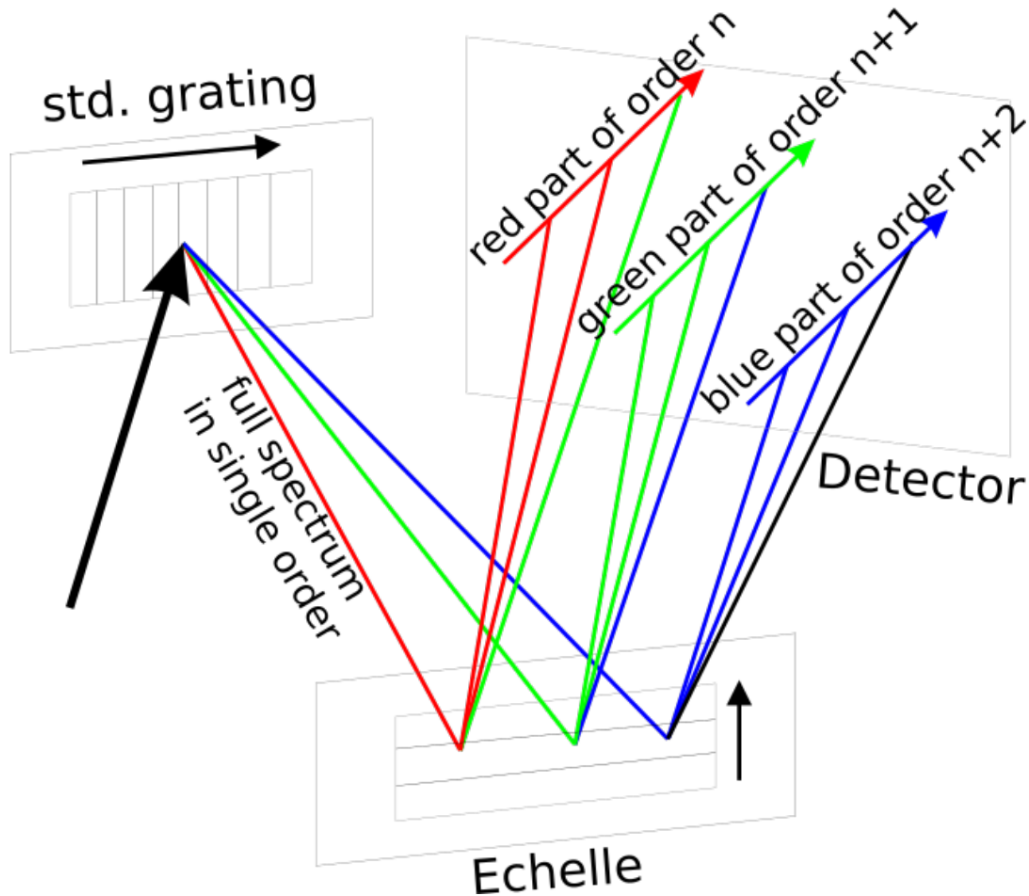


Figure 2.1: Simple schematic of an echelle grating cross-dispersion. From *Wikipedia*.

They are an offshoot of spectrographs named from their use of an echelle grating. They allow to record high-resolution spectra while, at the same time, covering large wavelength ranges. The combination of two perpendicular dispersion elements allows this extra coverage. One of these, usually an high-dispersion grating, is responsible for providing the high-resolution, while the other element, which is known as a cross-disperser, will disperse them into orders.

Therefore, in order to study the observability of spectral variations in O stars, using the capabilities of ever more present high-resolution spectrographic facilities, we started an observational campaign. The target chosen for this work was Sigma Orionis AB, or σ OriAB, located in the heart of the σ Ori cluster.

σ OriAB, which had long been thought to be a visual binary system, has been recently confirmed as a triple system (Simón-Díaz, 2015; Schaefer et al., 2016). It is now known to be composed by σ OriB and a spectroscopic binary σ OriA (with components Aa and Ab). The components of the binary are, respectively an O9.5 and an early-type B star. There has been some discussion about the masses, distances and ages to these in the more recent

literature. Simón-Díaz (2015) estimates the masses of, respectively σ OriAa, σ OriAb, and σ OriB as 20 ± 1 , 14.6 ± 0.8 , and $13.6 \pm 1.1 M_{\odot}$, while Schaefer et al. (2016) computed their masses to be 16.99 ± 0.2 , 12.81 ± 0.18 , and $11.54 \pm 1.15 M_{\odot}$. This discrepancy might be a product of the evolutionary models used, in fact although the age of the σ Ori cluster has been estimated to be between 2 and 3 Myr, the ages determined for the different components of σ AB by Simón-Díaz (2015) were, respectively, 0.3, 0.9, and 1.5 Myr which does not match the expected range, and is therefore being researched at the moment.

Despite the discrepancies of the modeled ages, the spectra of σ OriAa and σ OriAb are compatible with main sequence stellar atmospheres. The orbital parameters determined by Simón-Díaz (2015) and Schaefer et al. (2016) are in close agreement, with a period between the spectroscopic binary of $P \sim 143$ days, and $P \sim 58400$ days for the visual binary σ OriAB. The distance to the system has been computed as $d = 387.51 \pm 1.32$ pc by Schaefer et al. (2016), reducing the previous Hipparcos based estimates which were plagued by large uncertainties since the target is sometimes saturated in Hipparcos frames. σ OriAa is a fast rotator with an approximate rotational velocity of $v \sin i$ of $\sim 135 \text{ km s}^{-1}$ (Simón-Díaz, 2015).

Our choice of target is a result of the relative young age of the σ OriA spectroscopic binary, which makes it possible for it to still be accreting from the surrounding circumstellar medium. Finally, the relatively small distance makes it an optimal target for our study.

Section 2.1, explains the two datasets used in this work, i.e., the test and observational datasets used. The variability tools used are summarized in Sec. 2.2. The results are shown and discussed in Sec. 2.3, while in Sec. 2.4 we briefly address the way forward.

2.1 Observations

The data, composed of observations taken with different high-resolution echelle spectrographs, and used for this work can be separated into one of two sets: test data, composed of high (≥ 200) signal-to-noise (SNR) NARVAL observations of OB stars taken from its archive¹; and the study data composed of time sensitive PARAS observations of σ OriAB (Chakraborty et al., 2010). Some of the main characteristics of these instruments can be found in table 2.1.

The targets used for testing the adopted analysis methodology were: σ OriE, HD34078, 15Sgr, ζ Oph, and λ Ceph, respectively, B2, O9.5, O9.7, O9.2, and O6.5 stars at different

¹<http://tblegacy.bagn.obs-mip.fr/narval.html>

Table 2.1: Main characteristics of the used instruments.

Instrument	Resolution	Wavelength Range	Echelle Grating	Telescope
		nm	g mm^{-1}	m
PARAS	67000	[370, 860]	31.6	1.2
NARVAL	65000	[370, 1000]	79	2

Table 2.2: Summary of the test sample.

Star	Spec. Type	Number of observations	SNR
$\sigma Ori E$	B2	62	250
HD34078	O9.5	47	250
HD167264	O9.7	28	250
ζOph	O9.2	16	250
λCep	O6.5	40	250

evolutionary stages. Table 2.2 summarizes the spectral type, number of observations, mean SNR, and exposure times of these stars. The data was obtained directly from the NARVAL archive and used without additional processing.

The observations of $\sigma Ori AB$ were obtained with the 1.2m Telescope at Mt. Abu, India, using the high resolution echelle spectrograph PARAS (Chakraborty et al., 2010). PARAS covers the wavelength range [3700, 8600] Å, split into 92 orders, but given their efficiency, only the range [3800, 6900], or 67 orders are used for RV studies (see Fig.2.2). Consecutive orders overlap ~ 10 Å on each wing of a given order. A summary of the observations can be found at table 2.3. The target was observed over a total of 14 days, split in 3 periods over 3 distinct months.

The spectra was reduced using the PARAS reduction pipeline (Chakraborty et al., 2010; Roy et al., 2010), and additional post-processing was performed with a custom Python code in order to perform the wavelength calibration, barycentric correction and to extract the different orders. Each order was blaze-corrected.

Throughout the remainder of this chapter M1, M2, and M3 will be used, respectively for January 2015, February 2016, and March 2016. During three days in M1, the target was observed throughout the full night with exposures of 600s, giving a coverage of ~ 8 h, a total of 47 observations. The dataset of M1 is highly important as it should allow the detection of variations in periods of ≤ 8 h. In months M2 and M3 the exposure time was doubled but the target was only observed at the beginning and end of the night, for a

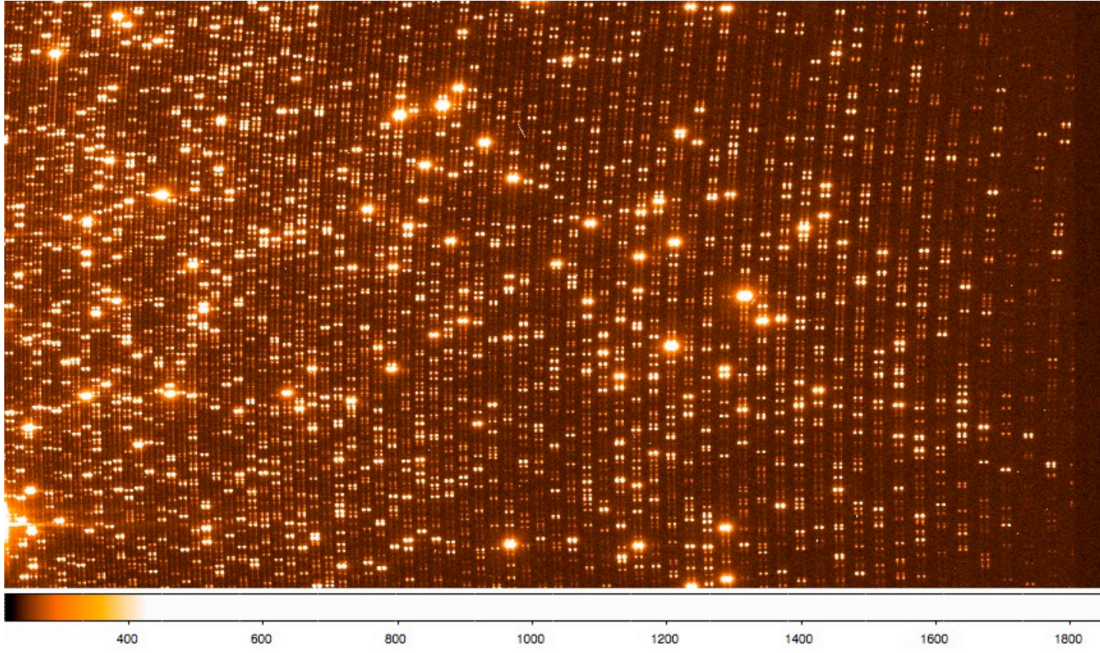


Figure 2.2: Zoomed Part of the raw Image showing Echelle orders of the Th-Ar spectra on both the Fibers (Star Fiber and Calibration Fiber) between 3700 Å and 6800 Å. From Chakraborty et al. (2010).

Table 2.3: Summary of observed nights.

day	Identifier	MJD	Exptime(s)	# exposures	SNR
2015-01-17	M1D1	57039	600	15	~ 40
2015-01-18	M1D2	57040	600	18	~ 40
2015-01-19	M1D3	57041	600	14	~ 40
2016-01-03	M2D3	57390	1200	2	~ 50
2016-01-04	M2D4	57391	1200	2	~ 50
2016-01-05	M2D5	57392	1200	3	~ 50
2016-01-06	M2D6	57393	1200	2	~ 50
2016-01-07	M2D7	57394	1200	3	~ 50
2016-02-01	M3D1	57419	1200	2	~ 50
2016-02-02	M3D2	57420	1200	2	~ 50
2016-02-03	M3D3	57421	1200	1	~ 50
2016-02-04	M3D4	57422	1200	1	~ 50
2016-02-05	M3D5	57423	1200	1	~ 50
2016-02-06	M3D6	57424	1200	1	~ 50

Table 2.4: Summary of SNR.

# of combined exposures	base exptime(s)	Median SNR
1	600	~ 40
1	1200	~ 50
2	600	~ 56
2	1200	~ 75
6	600	~ 96

total of 12 and six observations of 1200s, respectively.

Given the measured signal to noise ratio (SNR) of our observations, $SNR \leq 50$, groups of consecutive observations were combined, whenever possible. Groups of two and six observations were attempted, improving the SNR to ≤ 96 . Given the nightly coverage, groups of six observations were only possible in the case of month M1. For months M2 and M3 the two nightly observations were combined increasing the SNR to ≤ 75 (see Table 2.4).

2.1.1 Line list

O-stars have a small number of absorption lines in the visible wavelength range, as most elements in these stars are ionized (Gray, 2005). Therefore, line-lists taken from Vienna Atomic Line Database (VALD) (Piskunov et al., 1995; Kupka et al., 1999; Ryabchikova et al., 2015) were combined with synthetic spectra obtained from the POLLUX database (Palacios et al., 2010) in order to determine which lines could give a bigger information content.

Lines in the PARAS spectral range, [3800, 6900Å], with line depth $\geq 30\%$ of the flux were selected. Next, these lines were compared with the observed spectra and only those outside the order-overlap region were kept. This selection minimizes issues resulting from the lack of flux in the wings of orders.

Given that the target is a fast rotating star, its absorption lines are broadened and often blended with telluric absorption lines. Since these blends are capable of inducing variation in the stellar spectra, it was important to also select absorption lines with a small amount of telluric contamination, and to keep track of it using the appropriate atmospheric models.

After careful study, the final list of selected lines was assembled, with a total of seven absorption lines, composed of several H and He transitions. The full list is presented in

Table 2.5: Summary of the studied lines.

Identifier	Center Wavelength	Element
H_α	6563	H I
H_β	4861	H I
H_γ	4341	H I
He_{4026}	4026	He I
He_{4471}	4471	He I
He_{4712}	4712	He I
He_{5875}	5875	He I

Table 2.5.

2.2 Measuring spectral variability

In order to qualify and quantify the presence of variability, the choice of spectral indicators is key. Following a review of literature, the techniques chosen to perform this exploratory study were: the cross-correlation function (CCF), the temporal variance spectrum (TVS), the bisector method, and a modified variant of the TVS.

2.2.1 The cross correlation function

The CCF of a spectra combines the information content of multiple spectral lines by shifting a binary mask in velocity space and summing the flux in velocity bins. It is given by the following equation :

$$CCF(v) = \sum_i A[\lambda(i)].M[\lambda(i)(1 + v/c)].w_i \quad (2.1)$$

where v is the velocity shift, $A[\lambda(i)]$ is the spectrum intensity at wavelength $\lambda(i)$, $M[\lambda(i)(1 + v/c)]$ is the mask shifted by a Doppler effect, and w_i is the weight of the spectral line (Pepe et al., 2002). A visual representation of this technique can be observed in 2.3.

CCF usage is more advantageous when a large number of spectral lines are available which allows a significant reduction of the noise contribution by a factor of \sqrt{N} , where N is the number of lines used in the binary mask (Figueira, P. private communication). In spite of the reduced number of lines in O-stars, there is still value in using a CCF for their study.

The left panels in Fig. 2.4 (discussed in more detail in Sec. 2.3) show the computed

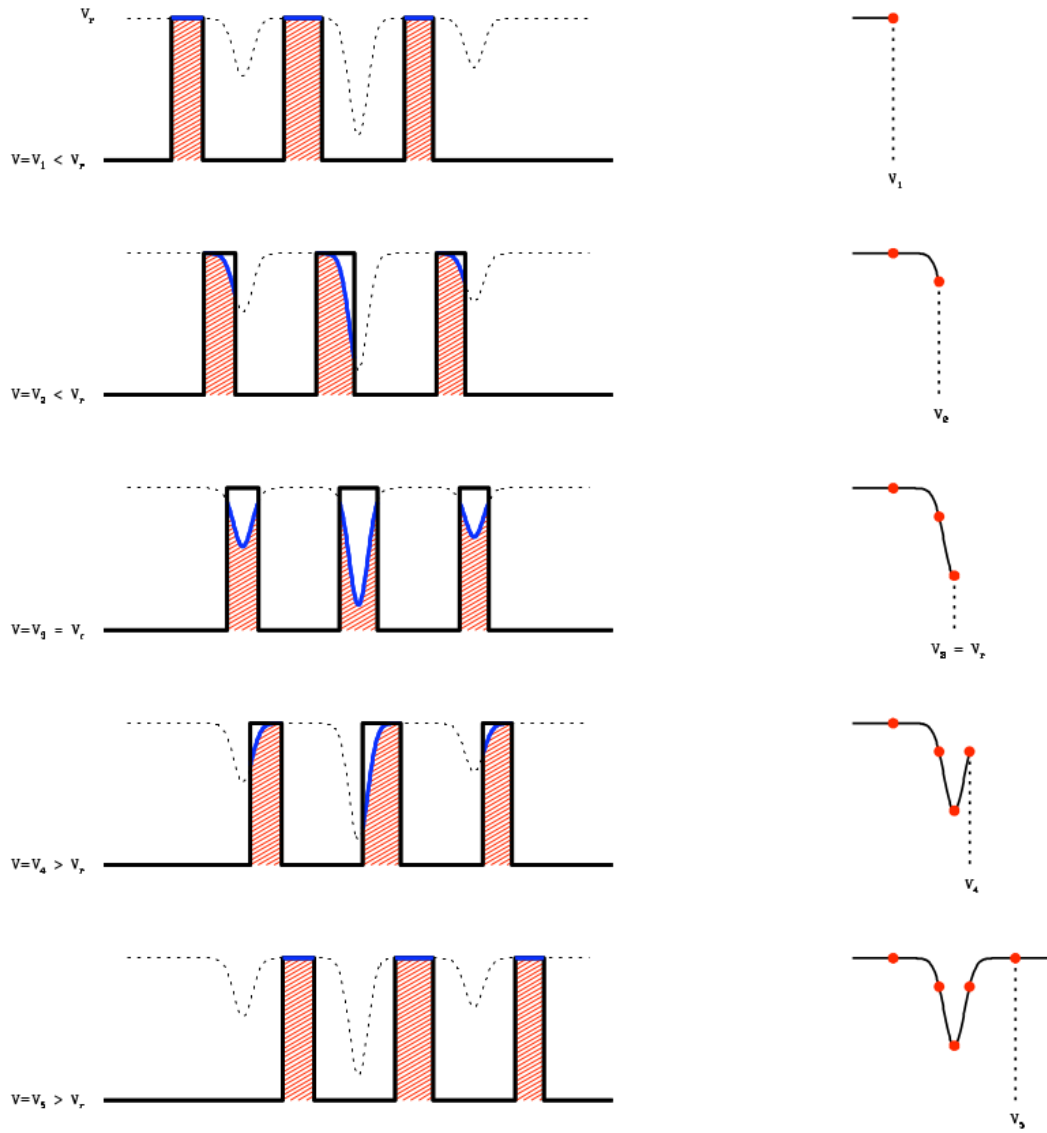


Figure 2.3: . Construction of a Cross-Correlation Function by correlating a template binary mask. From Melo (2001).

CCFs for M1. These were obtained from median combined spectra (see previous section for more details). The small number of available lines made this method inefficient and let us to explore other spectral variability indicators.

2.2.2 Bisector method and Line profile variations

Line profile variations (LPVar) result from several physical processes acting on the spectral lines. LPVars, are the observable element of changes in the stellar atmosphere itself but these can be the result of diverse processes such as stellar activity, the presence of companions, surface inhomogeneities (Fullerton et al., 1996; Martins et al., 2015) to name a few.

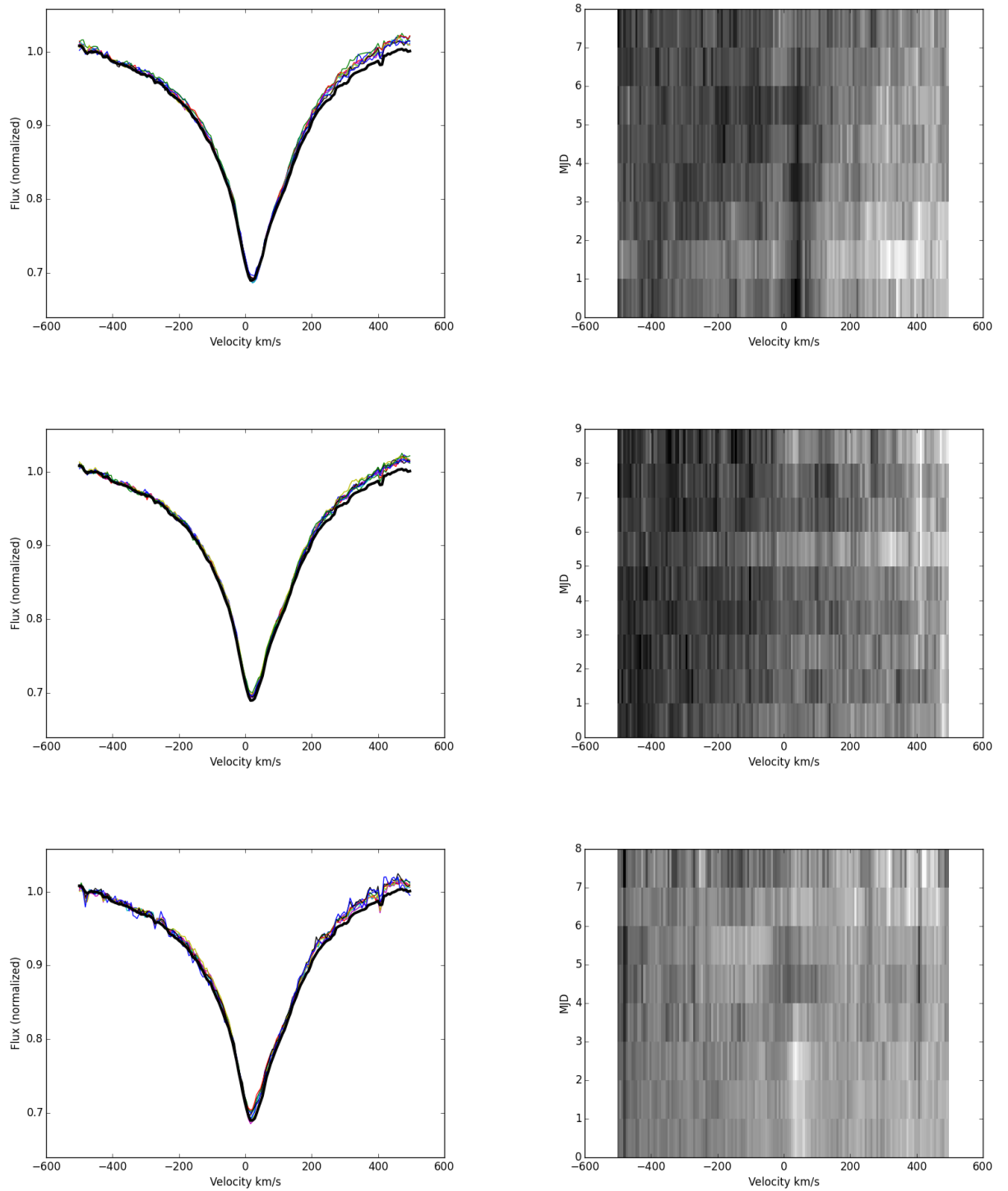


Figure 2.4: The CCFs for each day of month M1(left panels), and the difference from the median CCF (left panels). Day M1D1(top), M1D2(center), and M1D3(bottom) are shown. The dark line in the CCF plots corresponds to the median CCF of the month.

The study of LPVar concerns the measurement of changes in spectral lines over multiple observations. These variations can be changes in line-depth or equivalent widths, skewness of the spectral lines, the slope of the bisector, among others. Even though there are different metrics which can be used to characterize LPVars, the main ones usually focus on the changes to the bisector of absorption lines (Aerts et al., 2010; Figueira et al., 2013).

Following the findings of Figueira et al. (2013), in this work we used multiple independent LPVar indicators: the bisector inverse slope (*BIS*), with two extra parameterizations, *BIS*⁺ and *BIS*⁻, the *V_{span}*, the ΔV , and the *V_{asy}*. The *BIS* is the difference between the midpoint of the CCF at the top (average midpoint between 60% – 90% of flux) and at the bottom of the line (average midpoint between 10% – 40% of flux). The *BIS*⁺ and *BIS*⁻ are, respectively the maximum and minimum leverage cases of the *BIS*, considering narrower bands than usual at different heights. The *V_{span}* measures the difference between two gaussian RV fits of the CCF, a fit considering the upper part of the CCF and another considering the bottom part. This indicator has proven more reliable than the *BIS* for low SNR cases. The ΔV indicator corresponds to the difference between the central RV and the RV obtained from fitting a gaussian, and represents RV shifts which can be explained by line asymmetries. The *V_{asy}* is yet another indicator which compares the average information content on the blue wing with the average information content on the red wing of a given spectral line.

2.2.3 Smoothed Temporal variance spectrum analysis

Another useful technique, which quantifies changes in spectra over time is known as temporal variance spectrum analysis (TVS). Using TVS, for each spectrum, the differences between it and the median combined spectra are summed. To obtain it, the following equation is used:

$$TVS_j = \frac{1}{N_f - 1} \sum_{i=1}^{N_f} d_{ij}^2 \quad (2.2)$$

where N_f are the degrees of freedom, i is the spectrum and d_{ij} is the matrix of residual spectra (Fullerton et al., 1996).

The TVS can determine if the observed variation of a spectra is above the noise level. So, it can be used to flag interesting lines which merit further study.

The SNR of a spectra is known to impact the usefulness of the TVS (Fullerton et al., 1996), with marginal detections for $SNR \leq 100$. It is also sensitive to other phenomena, such as cosmic rays, telluric emission, to name a few. Given that the sensitivity of TVS

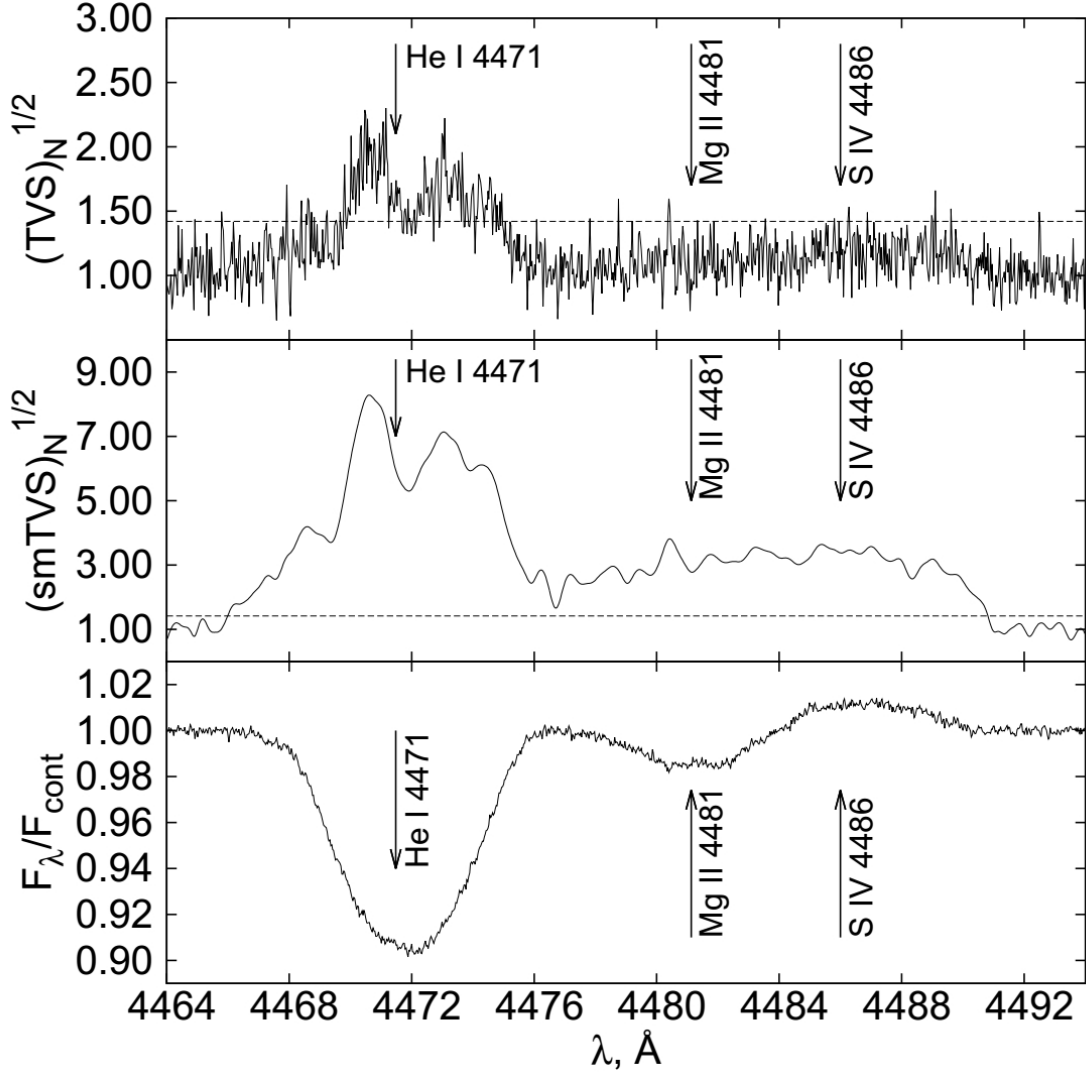


Figure 2.5: $(TVS)_N^{1/2}$ (top), $(smTVS)_N^{1/2}$ (middle) normalized by unity and mean line profile (bottom) of the line He I $\lambda 4471$ Å in the spectra of λCep . Filter width S is 0.2 Å. The horizontal line corresponds to the significance level 0.001 . From Kholtygin & Sudnik (2016).

depends on so many different factors, and the low SNR of the spectra used in this work, a modified version of the TVS was used, in order to detect variability.

Kholtygin & Sudnik (2016) introduced a modified form of the TVS, the smoothed temporal variance spectrum (smTVS). This method differs from the TVS since it uses a pre-smoothing with a gaussian filter. The main reason for its development was to detect line profile variations in spectra with low SNR. It has been shown to be effective to detect profile variations of amplitudes less than one percent of the continuum (see Fig. 2.5). For further details see Kholtygin & Sudnik (2016).

Table 2.6: Results of the test sample.

Star	Number of observations	SNR	Variability
<i>σOriE</i>	62	250	Y
HD34078	47	250	Y
HD167264	28	250	N
<i>ζOph</i>	16	250	Y
<i>λCeph</i>	40	250	Y

2.2.4 Testing known variable stars

The indicators presented throughout this section, were applied to the test sources. Given the high SNR of the test sample observations, these provide a best case scenario for observing conditions. The variability of stars in the test sample has been well-studied in the literature. Table 2.6 summarizes the test sources and the obtained results. Figure 2.6 shows one of the most variable targets in the test sample, σ OriE, a known variable. Variability was recovered in tested stars known to be variables, particularly in three lines: H_{α} , He_{5876} , and He_{4471} . Additionally, this battery of tests has shown that variability is clearer if there is a full night coverage of observations. So, detection of spectral variability requires both high SNR and also a large number of consecutive observations throughout a night.

For the test sample sources which are considered to be variable stars, the tools confirmed their variability nature. Analysis of the non-variables also resulted in confirming their lack of variability. We can conclude that, for sources in the test sample, the proposed methodology works. All that remained was to apply the method to the σ OriAB observations.

Given the broad nature of the stellar lines present in the spectra of these stars, a question arises: how to deal with telluric line contamination coming from our atmosphere? In order to attempt to measure the impact that these can have in the measured variability we used atmospheric models, from the TAPAS tool (Bertaux et al., 2014) to extract a model for the same airmass and atmospheric conditions present at the time of the observations. We then use these atmospheric lines to create a mask to clean our spectra. We found that in the case of lines as broad as ours, the impact of these tellurics wasn't significant to our chosen measurements, i.e. the skewness of the spectral lines. Given this lack of impact in our test cases, we decided to proceed without the correction. We were consistent in this choice for all stars in our samples. Therefore, any observed variability

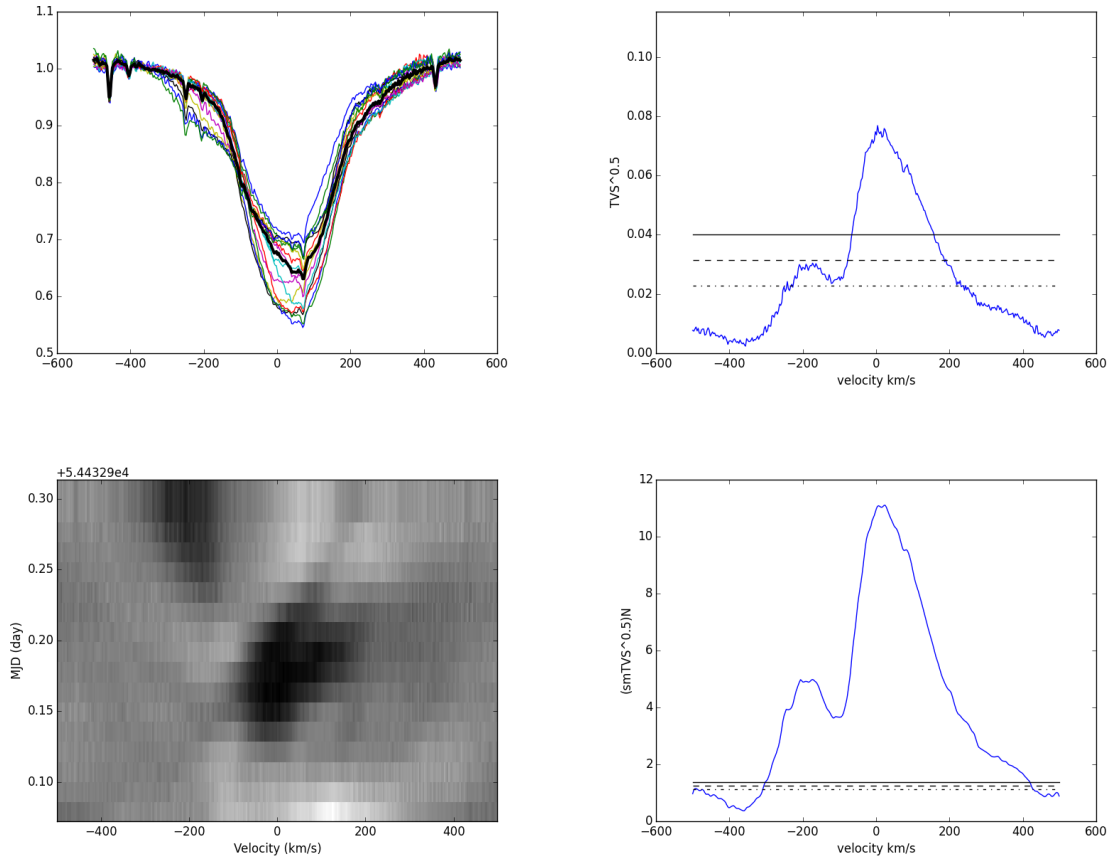


Figure 2.6: Variability of H_α for $\sigma Ori E$ on the night of 28 of November of 2007. Plotted are the variability of the line in velocity space (top left), the differences between consecutive observations (bottom left), the TVS (top right), and the smTVS (bottom right). On the TVS and smTVS plots, the dotted, dashed and full black lines correspond, respectively to the $1-\sigma$, $2-\sigma$, and $3-\sigma$ of the TVS.

is not explained by telluric lines in the spectra.

2.3 Results

Groups of two consecutive exposures were median combined and used to produce the CCF of our line-list. Figure 2.4 shows the CCFs produced for month M1 and a grayscale representation of the difference between each observation and the median CCF of the month. The region displaying greater changes is close to the center of the line, which corresponds to the radial velocity of the target.

The H_α line is one of the lines showing larger variations both throughout and between different nights. Figure 2.7 shows the variations H_α between the days of m2, while Fig. 2.8 shows the TVS and smTVS for M1. There is a clear peak around $\sim 30 \text{ km s}^{-1}$. The

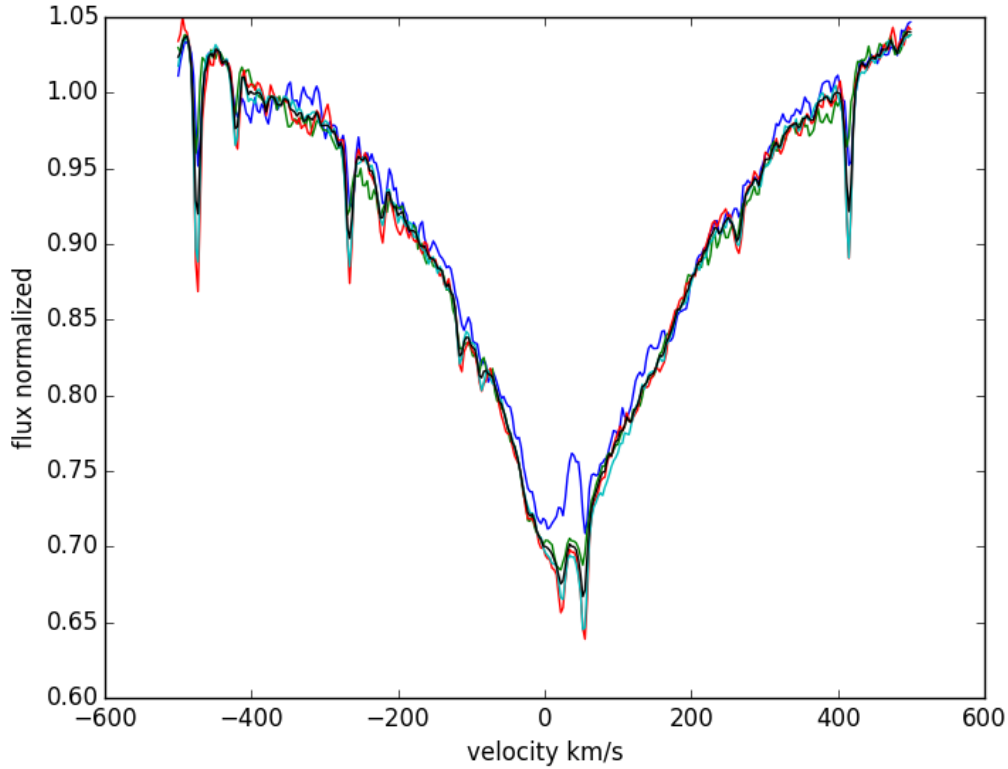


Figure 2.7: LPVar of H_{α} for m2 each line corresponds to a combination of all observations of each day.

same behavior is present in the TVS and smTVS of m2 and m3.

Possible correlations between H_{α} and He_{5875} were explored using four variables: line amplitude, line equivalent width, full width at half-maximum, and time. The EW of these two lines appears to be anti-correlated, while the amplitude and FWHM do not appear to have any correlation, see Fig. 2.9.

The smTVS plots also show that H_{α} , H_{β} , and He_{4471} appear to peak around the 30 km s^{-1} velocity, while the He_{5875} line appears to have a stronger component close to the -10 km s^{-1} (see Fig. 2.10). The smTVS plot of He_{5875} has multiple peaks around the center of the line, an indication of the high variable nature of its core.

Since the observations of M1 appear to show a degree of variability, it was important to quantify it. For that purpose, a frequency analysis was performed.

2.3.1 Frequency determination

In order to study the frequency of variations in the observed lines, the FAMIAS software (Zima, 2008) was used. One of the main features of this code is the ability to use multiple observations to obtain underlying cyclic phenomena.

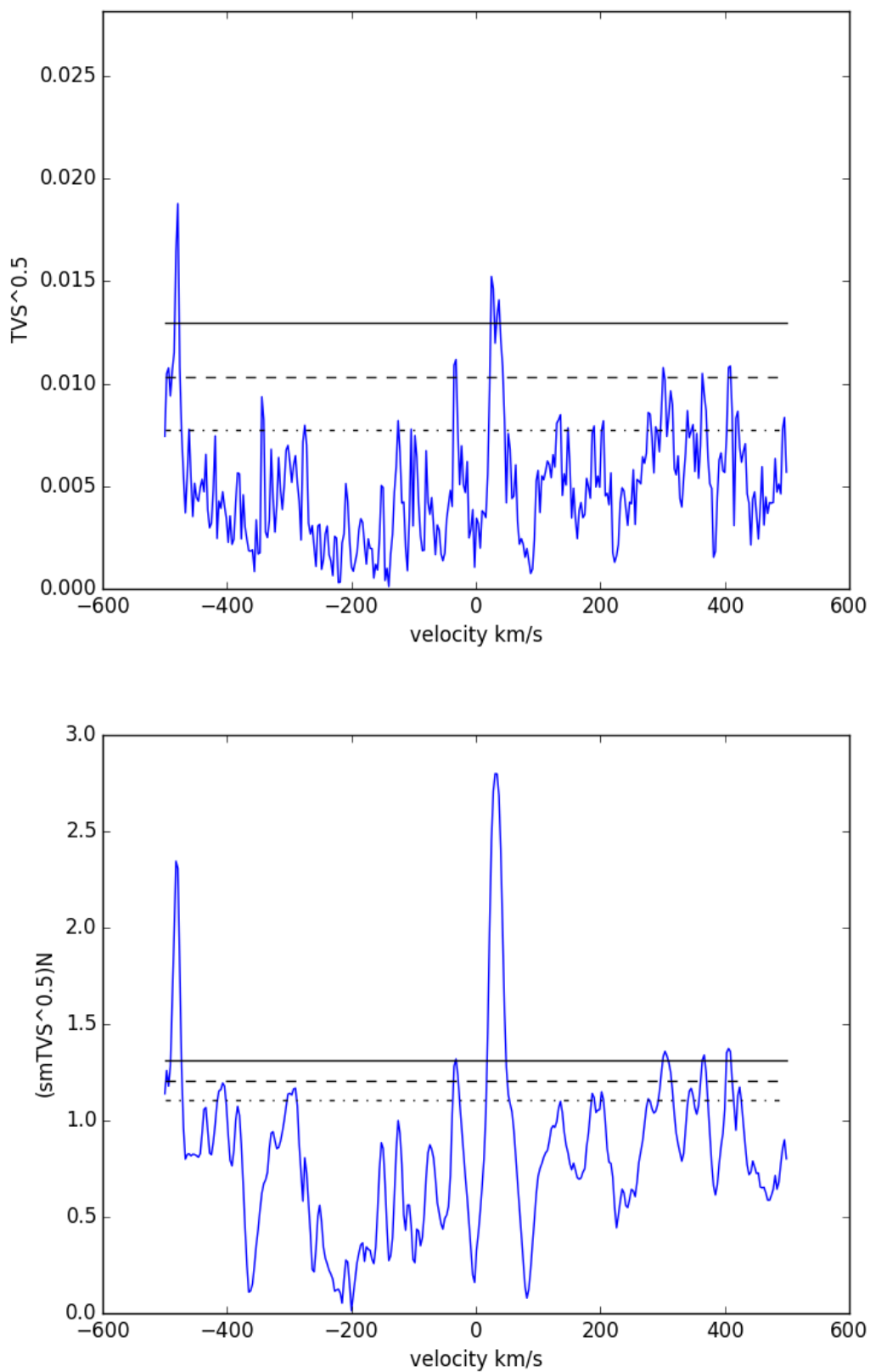


Figure 2.8: TVS (top) and smTVS (bottom) of H α for M1. The dotted, dashed and full black lines correspond, respectively to the 1- σ , 2- σ , and 3- σ of the TVS.

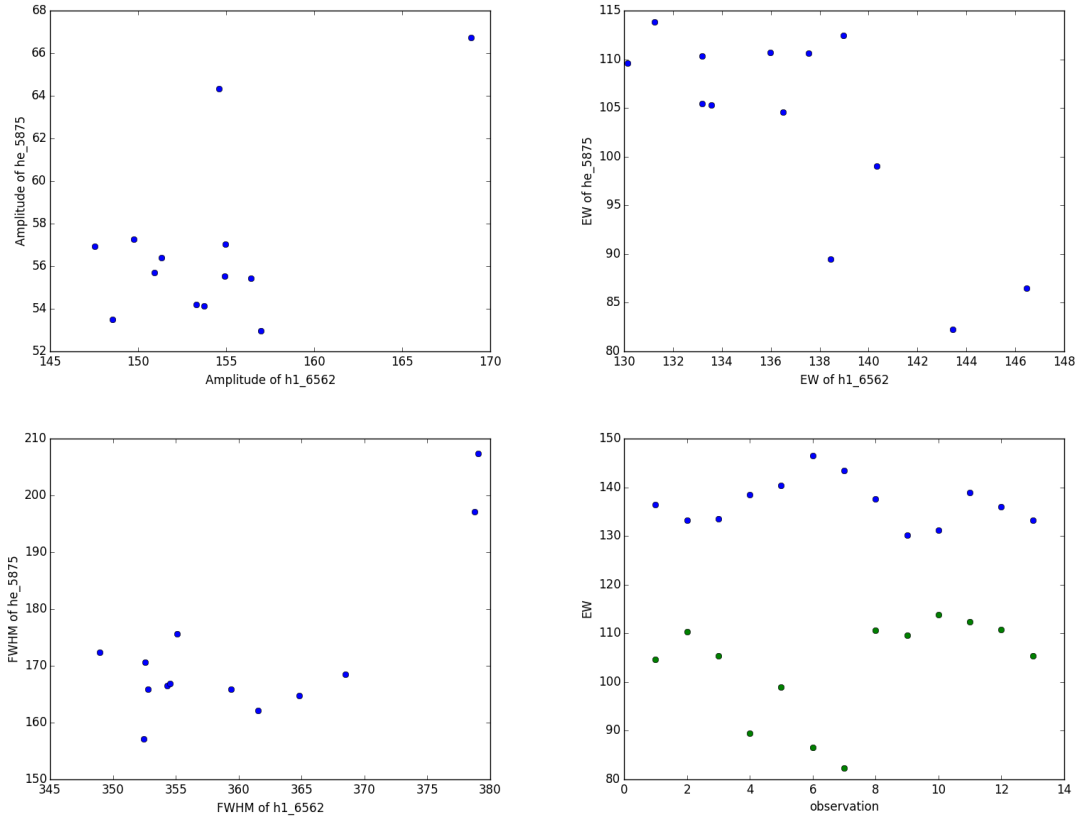


Figure 2.9: Comparison of the H_α and He_{5875} lines. From left to right and top to bottom we have a comparison of their amplitudes, EWs, and FWHM. The bottom right plot present the changes in EWs of each line over in each observation (blue dots are H_α and green dots are He_{5875}). The observations are M1D1, M1D2, M1D3, M2D3, M2D5, M2D6, M2D7, M3D1, M3D2, M3D3, M3D4, M3D5, M3D6.

The software was applied to individual lines and the frequency for each month of observation was computed, using the SNR as a weight factor. There is a big difference in coverage between the observations of M1 and the subsequent months. As such, the resulting frequencies from M1 are likely more reliable than the others, given the larger number of consecutive observations through the nights, so, these are more sensitive to transient phenomena.

Table 2.7 shows a summary of the frequencies obtained by analyzing the third moment of each line in the different sets of months. The third moment, which corresponds to the skewness of a line, has been shown to be strongly correlated with the macroturbulent velocity (Simón-Díaz, 2015). Focusing on the results of M1, most observed frequencies are between 3 and 5 cycles per day, which means a variability lasting between 8 and 4 hours. Such variability can be caused by high-order g-mode frequencies (which tend to last from a few hours to a few days), although it is also possible that these variations can be caused

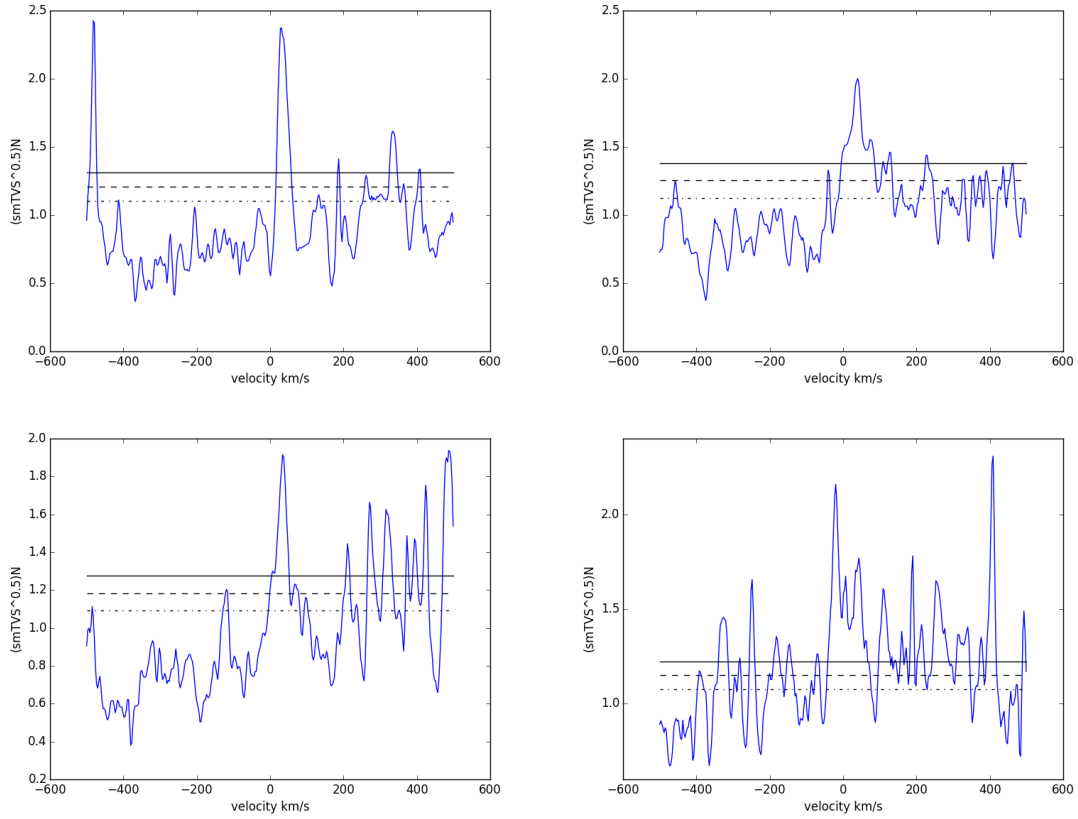


Figure 2.10: The smTVS of the lines which showed larger variations in m_1 . From left to right and top to bottom H_α , H_β , He_{4471} , and He_{5875} . The dotted, dashed and full black lines represent, respectively, 1-,2-, and 3- σ of the TVS.

by other photospheric phenomena, such as large prominences. It is clear that there is high variability of the observed frequencies between different months for some lines but, given the lack of sufficient time coverage of both M2 and M3, the frequencies obtained in these months should be taken with skepticism.

2.3.2 Regarding the confidence of the results

There are two major issues which call into question the results presented above. First, the presence of the binary companion, which could be the origin of any detected variability, and, second, and most importantly, the low SNR of the observations which introduces uncertainty in the LPVar tools.

2.3.2.1 Activity or companion?

Given the complexity of the $\sigma Ori AB$ stellar system and the major difficulties of observing the spectra of O-stars, it was important to discard the possibility that the observed variability is not caused by the presence of the binary component.

Table 2.7: Frequencies and amplitude of the variability by line.

Line	month	frequency(max) (c d^{-1})	amplitude $\text{km}^3 \text{s}^{-3}$
H $_{\alpha}$	M1	3.31085	233381
H $_{\alpha}$	M2	2.17648	758325
H $_{\alpha}$	M3	2.62377	262817
H $_{\beta}$	M1	2.85104	273366
H $_{\beta}$	M2	46.0657	321948
H $_{\beta}$	M3	5.22773	221607
H $_{\gamma}$	M1	3.26486	351102
H $_{\gamma}$	M2	8.50674	1106830
H $_{\gamma}$	M3	0.49505	735063
He $_{4026}$	M1	0.45985	682541
He $_{4026}$	M2	42.2352	347185
He $_{4026}$	M3	22.6931	587515
He $_{4471}$	M1	3.31088	270105
He $_{4471}$	M2	32.9823	632329
He $_{4471}$	M3	0.49505	383043
He $_{4713}$	M1	2.30496	8738.63
He $_{4713}$	M2	41.6515	11290
He $_{4713}$	M3	17.1584	8892.76
He $_{5875}$	M1	5.15021	281340
He $_{5875}$	M2	3.89278	1817970
He $_{5875}$	M3	0.49505	533551

The observed variability has associated lifetimes ranging from a few hours up to a day and the inner binary companion of $\sigma Ori AB$ has a period of ~ 143 days. Therefore, changes should be noticeable over the period of a few weeks, not over a few hours/days.

Nevertheless, in order to rule out the possibility of a binary-induced variability, line-profile variability techniques were used. It is common to disentangle activity from other sources of RV variability (e.g. planetary companion), by determining if there is a correlation between the values of line-profile indicators. The bisector inverse slope (BIS), the Bi-Gauss and the velocity asymmetry V_{asy} have been shown to be able to distinguish between activity-induced variability or an RV-shift caused by a nearby component (Figueira et al.,

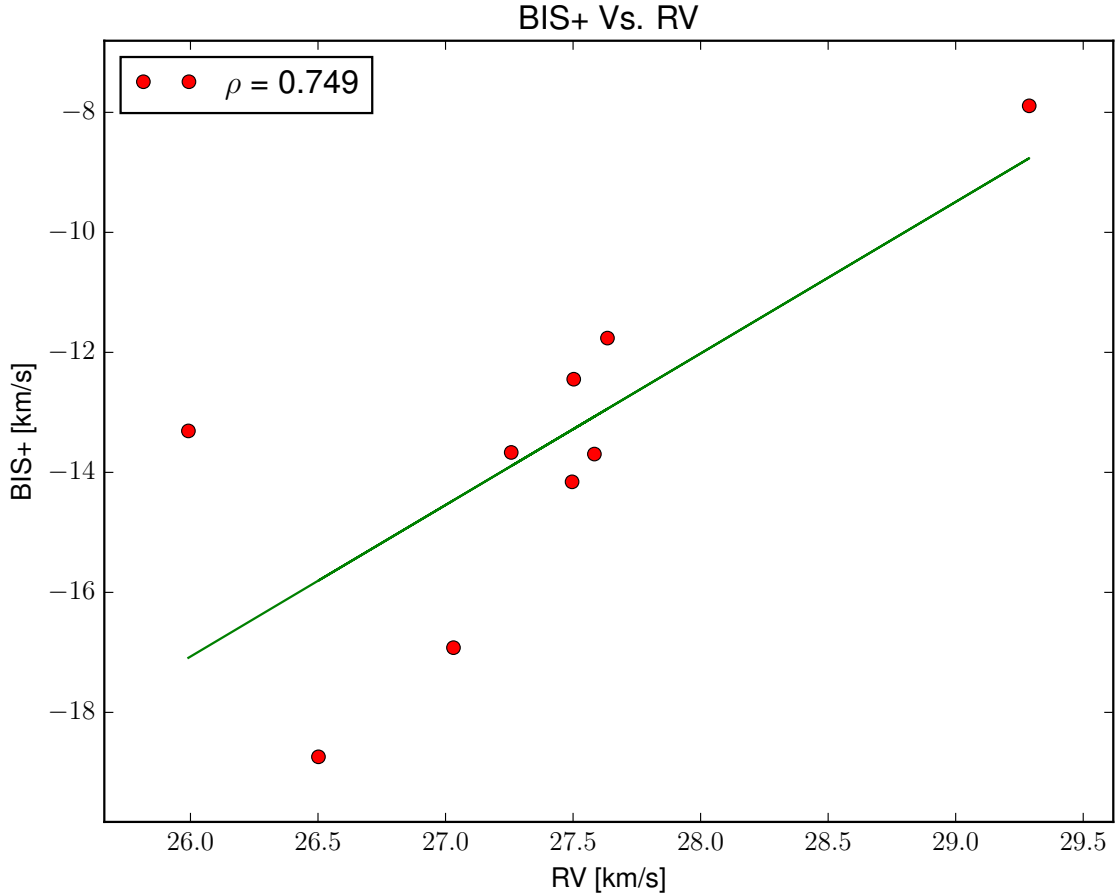


Figure 2.11: The BIS+ as a function of measured RV from the CCFs of M1. Each point represents the combined spectra of 6 consecutive observations from each day. This combination was made in order to increase the SNR.

2013).

This diagnosis was first used on the CCF of the first month to check that the variations of the CCF were not dominated by a RV-signal from the spectroscopic companion. The BIS+ is presented in Figure 2.11. The BIS+ method was chosen given its usefulness in cases of low SNR observations (Figueira et al., 2013). Given the apparent correlation, with a Pearson coefficient of 0.749050, between the measured RV and the value of the BIS+ we can conclude that the CCF profile variations are not being caused by an orbital companion but most likely by a stellar activity component (Figueira et al., 2013).

2.3.2.2 SNR and observing strategies

The results presented in this work suffer from the low-SNR of the observations. Most LPVar tools, with a few exceptions (e.g. smTVS), were created for, and depend on, high-SNR, since noise can mimic signatures of variability. Furthermore, attempts to increase

the SNR of observations depend on median combination of the spectra, resulting in loss of some of the temporal resolution. An increase of the SNR would help to improve the level of confidence in the results. This point is clear given the corroboration obtained with the test sample, as it was comprised of high SNR observations.

Both sample spectra (i.e. $\sigma Ori AB$ and test stars) point the way forward: to detect variability in O-stars on an half-day (or smaller) time-scale it is paramount to have multiple observations during the same night, repeated over consecutive nights. Even when dealing with an highly variable star, such as $\sigma Ori E$, the best detections are for those days with large number (> 10) of consecutive observations throughout the night. While nights with ≤ 4 observations, spread over the entire night, still showed some variability, it was not possible to successfully quantify it even in such an extreme variable star.

2.4 The way forward

Using several LPVar tools we have examined spectroscopic observations of $\sigma Ori AB$. We have detected some variations in the H_α and He_{5875} lines with periods between 4 and 8 hours. The source of variability is unlikely to be the binary companion. The low SNR of the spectra requires additional higher-SNR (~ 250) observations, with an large number of consecutive observations (> 10), throughout the same night, and preferentially made during consecutive nights.

The method used in this study has detected signs of variability in the spectra of $\sigma Ori AB$. While this is an important result given the link between variability and ongoing accretion, the SNR of the observations used was not enough to fully explore and disentangle the source of this variability and test the pulsational hypothesis. More high-SNR, time-sensitive observations are required to understand the causes of spectral variability of this young star.

Since the data lacked enough SNR for our purposes, we implemented a complementary approach based on a photometric study of variability. To that effect, we pursued a collaboration in the context of the VVV survey. This required an understanding of the expertise needed to deal with the large volume of data available in the survey.

Chapter 3

The VVV survey (a Big Data challenge)

As outlined in Chapter 1, modern day astronomy has an abundance of data, particularly from high-cadence surveys which attempt to observe all objects in large sections of the sky (e.g. Gaia, VVV, to name a few). The large volume of data produced by such surveys requires us to adapt typical data reduction techniques (Kremer et al., 2017).

The VVV survey has given an unprecedented time coverage, in the NIR, to a significant area of the galaxy (Minniti et al., 2010). This coverage is what makes our work, of looking for variability in MYSOs, possible. While the VVV data is made available in the VSA (Cross et al., 2012) we chose instead to use pawprint data for our work. This decision was made on the basis that we think that pawprint data can provide better photometric quality than tile data, given their sharper image profiles and better calibrations.

This chapter summarizes the computational work performed on the VVV data, which can be divided into the following steps:

- Reprocessing the data of VVV pawprints
- Building the LCs and quantifying their errors
- Computing the periodograms of the LCs

3.1 The VVV survey

The VVV survey covered 520 deg^2 area of the inner Galactic bulge (see Fig. 3.1), over a period of five years (from 2010 to 2014), to deliver multiple epoch photometric observations in the NIR passbands ($0.9\text{-}2.5 \mu\text{m}$) (Minniti et al., 2010). The data is available publicly at the Cambridge Astronomical Survey Unit (CASU) and at the VSA (Cross et al., 2012).

The wide-field camera, composed by 16 detectors produces, in each exposure, a gap-filled image, known as a 'pawprint' (see Fig. 3.2). In order to fill in these gaps the VVV team adopted a strategy of partially overlapping and dithering multiple 'pawprints'. A

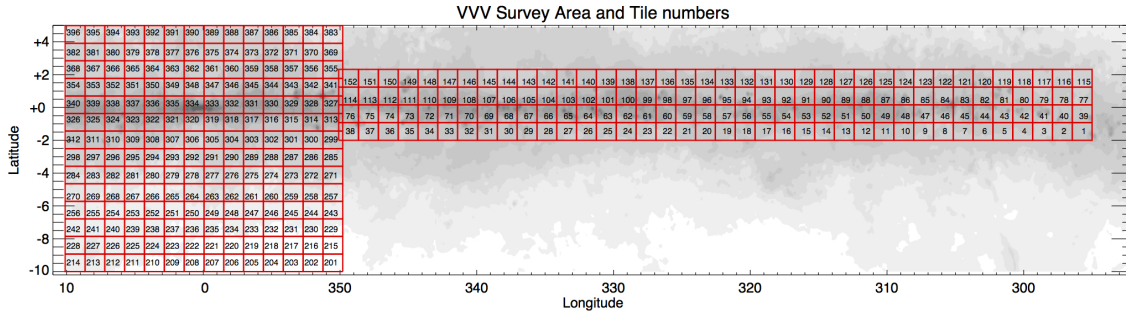


Figure 3.1: VVV survey area.

total of six, slightly offset observations, are made at each pointing resulting in a 'tile', a composite image covering 1.501 deg^2 of the sky (Minniti et al., 2010). With the exception of the edges (with data from a single 'pawprint'), the other regions of each 'tile' have data from at least two 'pawprints', to a maximum of six for regions where all 'pawprints' overlap (see Fig. 3.2). A single 'pawprint' is the basic product of any observation, therefore, it tends to have better photometric and seeing information given the sharper image profiles and calibrations when compared with those of the combined 'tile'.

So, we decided to mine the 'pawprint' data, since we expect it to have a better quality than 'tile' data. Nevertheless, this data required additional reprocessing before it could be properly explored.

3.2 Processing of the pawprint photometry

One of the difficulties of using 'pawprint' data was to match the sources throughout multiple 'pawprints' and epochs. In order to perform this task, we used a source matching method similar to the one presented in Smith et al. (2018). Given that the survey used similar pointing coordinates for different pawprints (within $20''$) throughout the entire survey, it is possible to identify sets of coincident pawprints. Each set has been observed in different epochs, so there are variations of observing conditions within each set. The natural consequence of this is that not all sources may be detected at all epochs.

For each set of 'pawprints', groups of epochs 90 days apart were identified. In each of these groups, a 'master epoch' was identified, this is the observation with the best seeing and which also has a source count higher than the median for the group. Between 'master epochs' of consecutive groups, sources are matched using a radius of $1''$, then the same matching strategy is applied between each 'master epoch' and the respective group of epochs. This approach retains any source which has only a single detection in one of the 'master epochs'. For additional details I refer the reader to Smith et al. (2018).

Table 3.1: Summary of the CASU photometry flags.

Flag	Classification
1	Galaxy
0	Noise
-1	Stellar
-2	Probably stellar
-3	Probable galaxy
-7	Bad pixel within 2" aperture
-9	Saturated

Furthermore, the pawprint photometry used was one of the standard CASU products (Lewis et al., 2010), namely aperMag2, which corresponds to an aperture photometric radius of $r = 1/\sqrt{2} * 1''$, and has been shown to result in more reliable magnitudes for objects in crowded fields (Lucas et al., 2008). The classification flags for the photometry are also the standard CASU schema, and are shown in Tab. 3.1.

For each 'pawprint', the calibration procedure followed by CASU which can be summarized in the following steps:

- Using the flatfield exposures, the detectors are normalized to the same gain
- A cross-matching procedure is done between the 2MASS catalog and the detected sources in each VISTA detectors
- The 2MASS magnitudes of these sources are transformed into the VISTA photometric system using the color equations
- The zeropoint of the detector is defined as the offset between the median 2MASS and VISTA magnitudes
- A median of all detectors is determined to be the total zeropoint, while the scatter is also written into the FITS header as the error in the zeropoint
- A final step takes into account differences between the 16 detectors which are measured in a monthly basis.

In order to reduce the scatter level in short-period variations, we have chosen to bin all data for each source using a small time interval (≤ 0.5 days) as our binning window. While this provides a reduction of the level of scatter it also prevents the detection of variability

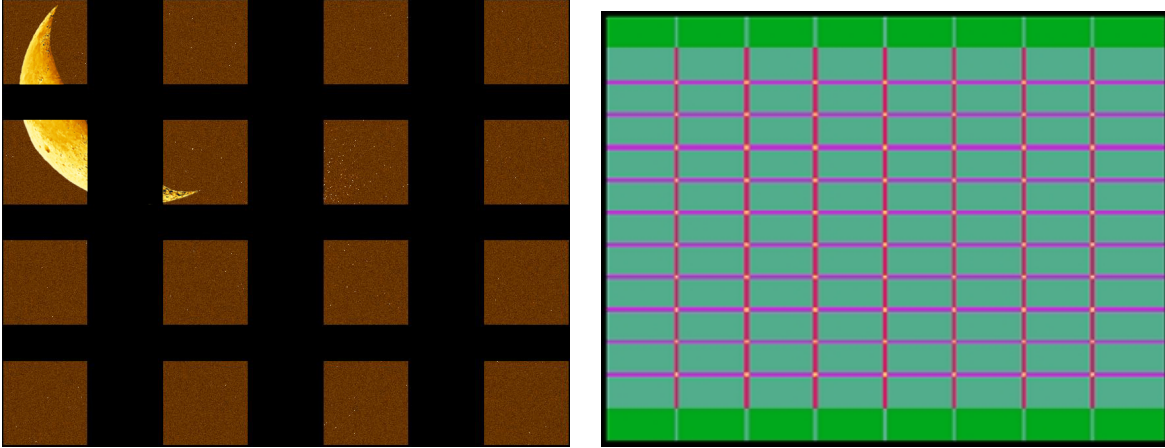


Figure 3.2: Mock-up of a pawprint showing the moon (left) and exposure map for a filled tile(right). In the exposure map, dark green = 1, light green = 2, magenta = 3, red = 4, yellow = 6, in units of the single-pawprint exposure time.

in shorter timescales. The photometric sensitivity improves as a factor of the number of observations binned, scaling as \sqrt{n} , where n is the number of binned observations. Since the final product of the matching and binning processes will have small photometric errors ($K_{err} \leq 0.05$ mag), it will allow the detection of low-level photometric variability. In order to handle the large volume of processed data, we had to build two ancillary databases.

3.3 Construction of the ancillary databases

The advantage of splitting the results into two databases is that, by using a specialized programming language, such as SQL, the database is quickly queryable for a set of sky coordinates. Big Data astronomy can only become relevant if we, astronomers, can successfully adapt tools, which, until recently, were the purvey of sciences such as Computer Science to our needs.

The results of the processed pawprints were split into two different databases: varSource and varDetection. For each entry in the varSource database, we determined, an unique identification, median coordinates in the ICRS, median magnitude in the K-band, the Median Absolute Deviation (MAD), the the standard deviation, the Inter-Quartile Range (IQR), the number of pawprints in which the source was observed, the number of total observed epochs, the modal class, and the number of epochs classified with each flag. The varDetection database, which is connected to varSource using the unique identifications, contains the photometric information for each source at each epoch. Structurally it contains the source id (corresponding to the id in varSource), the K-band magnitude, the photometric class, and the modified Julian date (MJD) of the observation (see Fig. 3.3) .

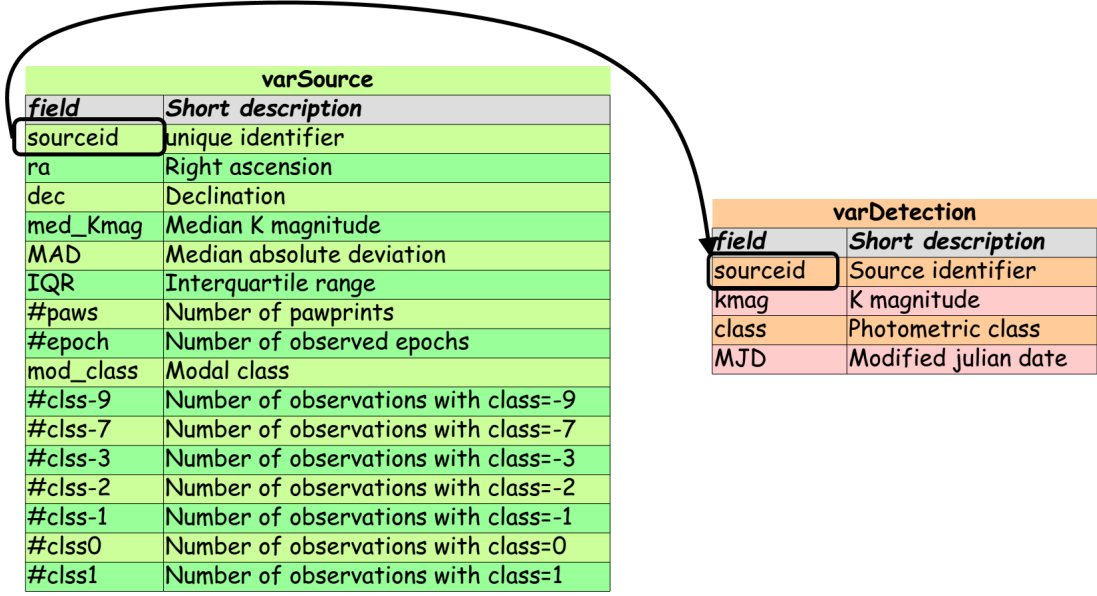


Figure 3.3: Scheme of the created databases highlighting the key which connects them.

Each source has, in this database, on average between 60-240 entries.

The median of the co-ordinates and magnitude, and the modal class were computed for all pawprint observations. A few robust statistical indicators were also computed so that it is possible to pick up variable sources easily.

3.3.1 Robust statistical indicators: IQR and MAD

In order to measure the amplitude and dispersion of the variability, the MAD and IQR were computed, which are well established robust statistical indicators (Hampel , 1974; Upton et al., 1996; Sokolovsky et al., 2017). Both parameters are largely insensitive to outliers, unlike the standard deviation. Therefore, an inherently variable source will be well traced by an high value of MAD or IQR.

The median of the absolute differences between a data-point and the median is known as MAD and is computed by:

$$MAD = median(|K_i - median(K)|) \tag{3.1}$$

in which, K_i is an observation and K represents all the observations. The amplitude between the third (Q3) and first quartiles (Q1) of a distribution, or IQR (see Fig. 3.4) can be calculated by the difference:

$$IQR = Q3 - Q1 \tag{3.2}$$

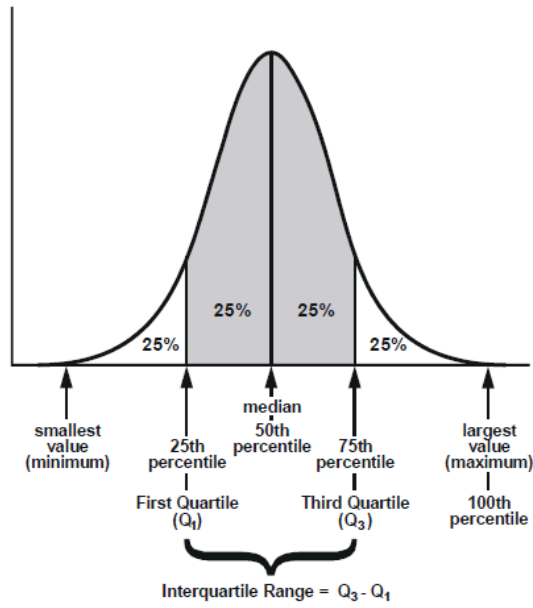


Figure 3.4: IQR of a distribution.

The robustness of these two indicators has made their use ubiquitous in the study of LCs (Sokolovsky et al., 2017).

The big advantage of introducing the IQR and MAD quantities into the ancillary databases is that it introduces a method to select potentially interesting targets for further study. While the process of creating the databases is computationally intensive, once those initial computations were done, no further calculations were necessary to perform queries around a given set of coordinates or with preselected conditions. The databases could, therefore, be explored more easily.

As the databases were built, the next step was to develop a computational code which would take the information of each source and quickly build a LC. While the steps necessary to build any single LC could be performed with a simple Python code, our project required an additional degree of complexity which could take into account dealing with a large number of sources simultaneously.

3.4 Building the LC pipeline

Assembling a LC for any target can be summarized by the following steps:

1. Query a set of coordinates and search radius on the databases.
2. Build a list with all sources that match our query.
3. Exclude all sources with a modal class = -9, i.e. saturated.

4. Build a LC for all non-saturated observations using the difference from median ($K_{median} - K_{mag_i}$).
5. Compute a Lomb-Scargle Periodogram.
6. Compute the period with the maximum power and use it to build a phase-folded LC.

The above procedure was automatized by a custom-made Python code, which could then be applied to multiple sources in order to obtain their LCs. Figure 3.5 exemplifies one such LC(top panel). The only problem remaining with this approach was how to quantify the errors in measurements of the photometry of any given target at a certain epoch. Among the major sources of error the measurements are subject to we list, in no particular order : poor seeing, improper photometry, poor observing conditions, flat fields errors, and detector non-linearity.

Poor seeing tends to make sources appear wider in the 'pawprints', thus leading to loss of flux when using the same photometric apertures. Observing conditions can also have other impacts, since the atmosphere is NIR bright, humidity can disperse more light from the detector. Some of the detectors have different sensitivities throughout, leading to flatfield and sky frames which are not fully uniform, and show some point-like objects. Furthermore, detector non-linearity becomes an issue for brighter sources, as photon counts will be less reliable the closer to saturation a pixel gets, while, for fainter sources the distinction between what is noise and signal is an issue.. In order to attempt to minimize and quantify these possible sources of error, we performed a series of tests and corrections.

3.4.1 Photometric errors from observing conditions

Most sources of error mentioned above, i.e., bad seeing, improper photometry, atmospheric conditions, should also affect other stars surrounding the main target. Therefore, we tried to minimize their contribution by using the other stars in the vicinity of each source. A selection of any stellar sources (class = -1) in an area defined between an annulus $r=1''$ and $r=60''$ was made (see Fig. 3.6). The typical number of sources obtained by this criteria is $\sim 200 - 100$. This selection excludes sources within $r < 1''$. For each source S_i , we computed the difference ($\Delta S_{i_{mjd}}$) from the median magnitude value ($\widetilde{S}_{i_{mjd}}$). The photometric deviation of an individual epoch, when compared with all epochs, can be represented by the median value of the difference for all sources in the annulus $\Delta \widetilde{S}_{i_{mjd}}$.

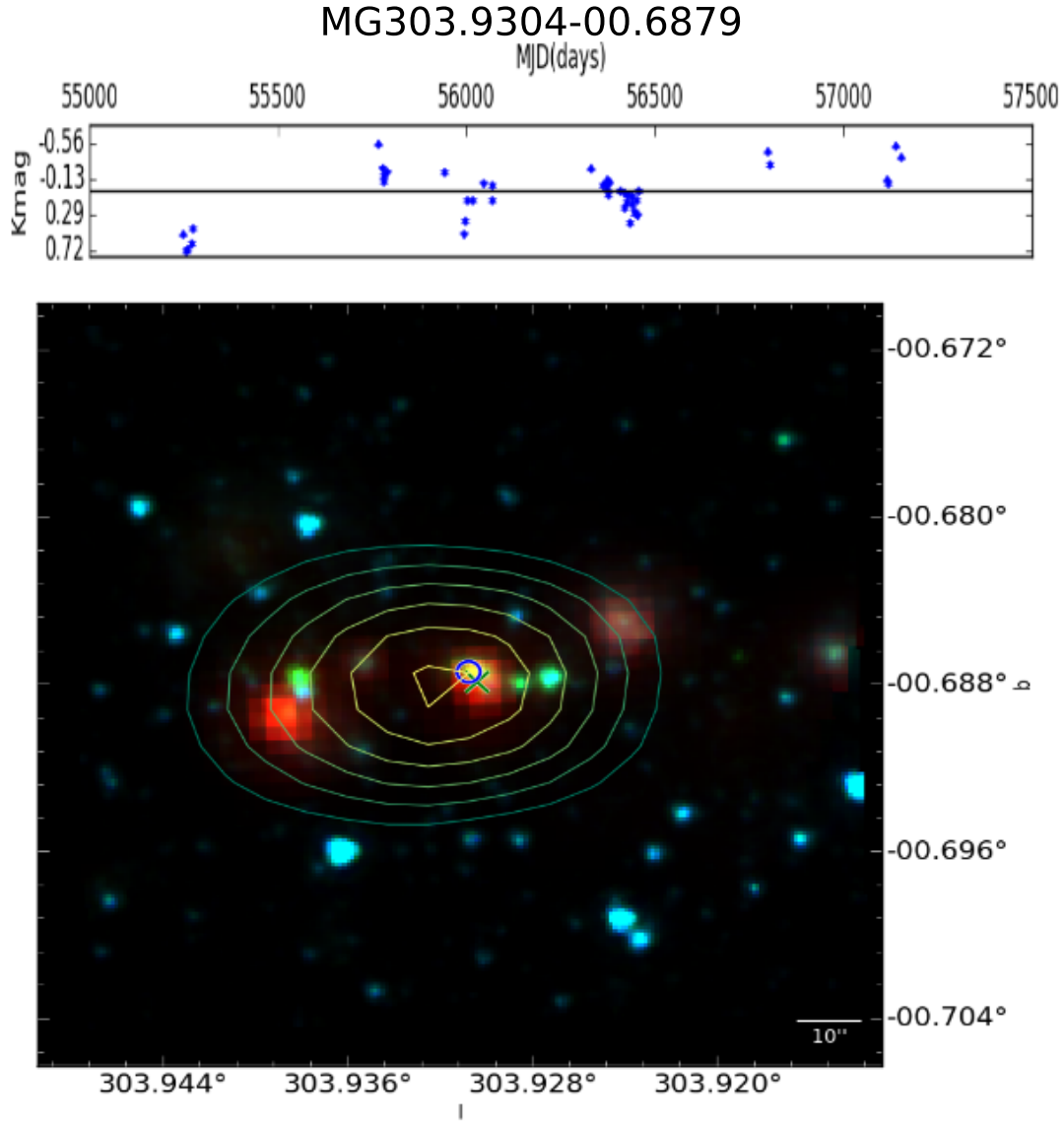


Figure 3.5: LC of an eruptive event. Top panel shows the LC of the source, the error bars represent $\text{MAD}(\Delta S_{i_{mjd}})$, the bottom plot shows the RGB image of the source using the Spitzer IRAC 3.6 μm , IRAC 4.0 μm , and the 24 μm MIPS band as blue, green and red, respectively. The VVV source is indicated by the blue circle and the green cross represents the MIPS co-ordinates. The contours of the RGB are in the interval of $[\text{Peak}-5\sigma, \text{Peak}]$ from the ATLASGAL observation at 850 μm . From Teixeira et al. (2018).

The corrected LC is produced by adding that offset to $S_{i_{mjd}}$. For any given epoch, the 1σ error in the vicinity of the target can be approximated by the MAD of the deviations for all stars in the vicinity, $\text{MAD}(\Delta S_{i_{mjd}})$. This error is plotted as error bars in each LC (see Fig. 3.5). This test addresses cases where the sources of error affects all stars in $r \leq 1'$, but it fails to account for non-linearity and SNR issues which affect sources of different magnitudes differently.

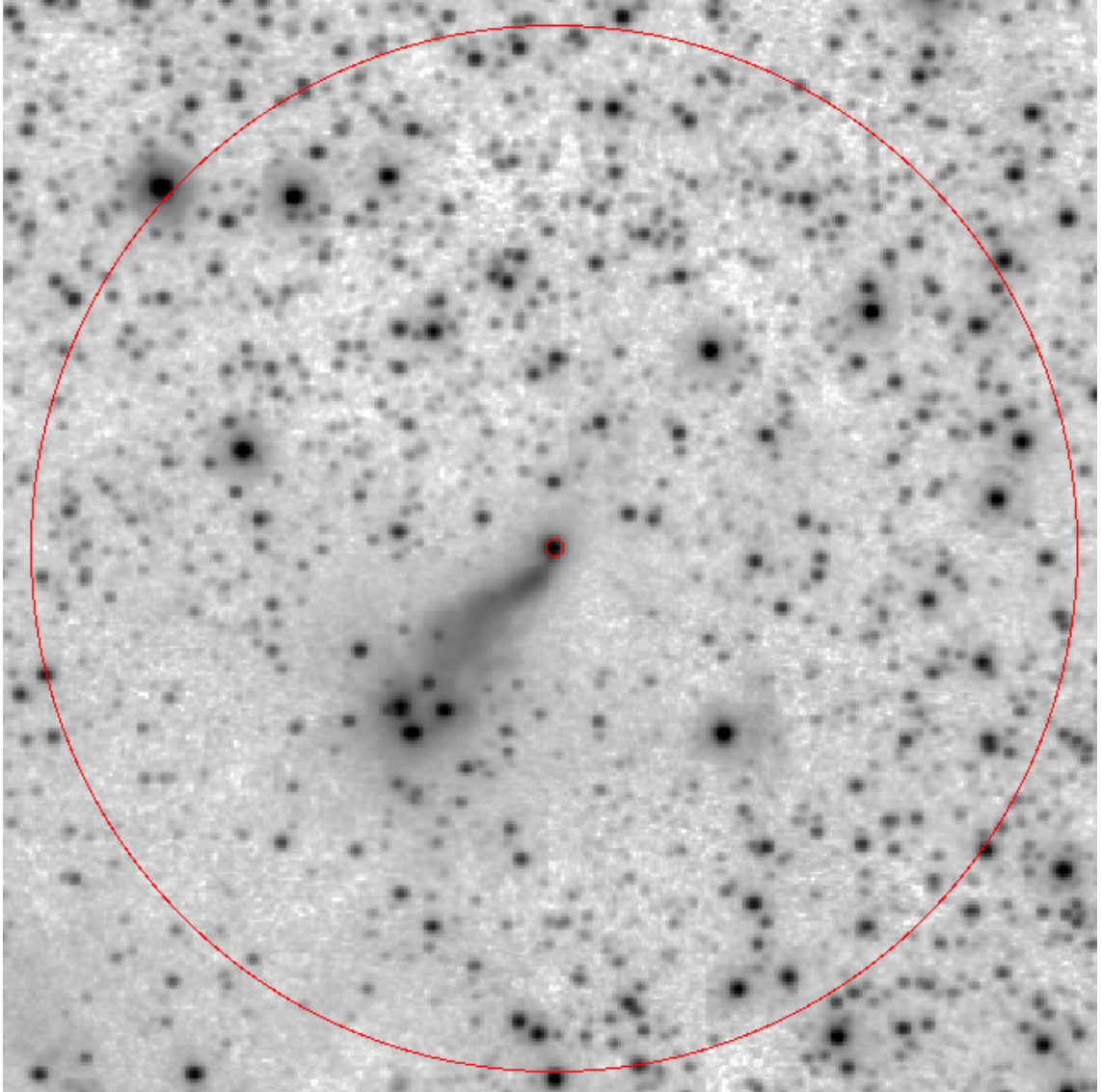


Figure 3.6: Annuli used to determine the photometric errors.

3.4.2 Concerning non-linearity errors

The previous test addresses systematic sources of error which affect all sources equally. But it fails to account for detector non-linearity and SNR issues which are known to be magnitude-dependent. Therefore, a case can be made that by choosing all the stellar sources, regardless of their magnitude, we can be underestimating our errors, which will be dominated by the low signal-to-noise ratio sources in the $60''$ radius. Although for most candidate variables this will not be problematic, the dominant source of noise for brighter candidate variables ($K_s < 11.5$ mag) is the detector non-linearity.

The same experiment as detailed above (sources in the annulus $1'' \leq r \leq 60''$) was performed for stellar sources of comparable magnitude to the target, i.e. ± 1 mag. This selection criteria effectively decreased the number of valid sources by a factor of ten for

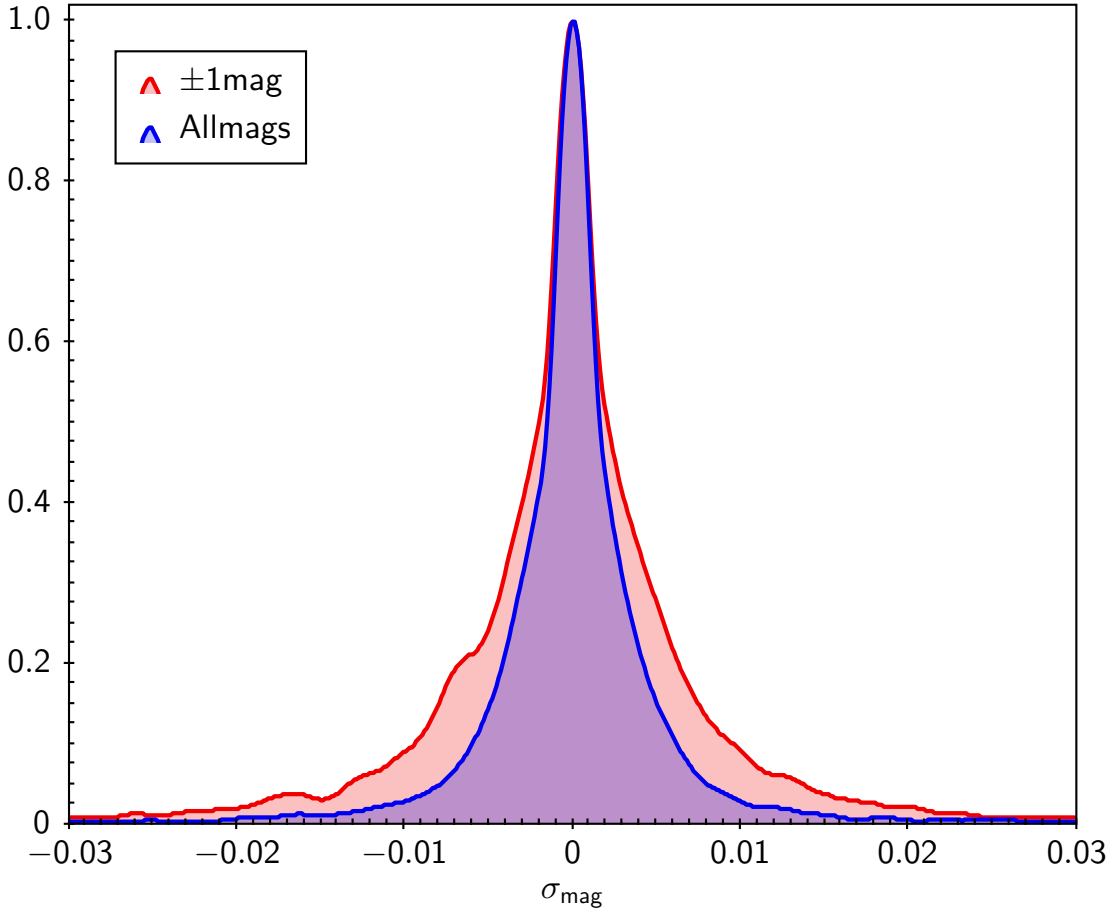


Figure 3.7: Histogram showing the systematic errors using the vicinity of each source. The red curve represents the case where we only consider the stellar sources with ± 1 mag around our targets. The blue curve represents the case where we consider all stellar sources in the vicinity of our targets.

brighter targets. The results of this test are shown in Fig. 3.7 and 3.8. The median error obtained if we use all neighbors or the magnitude limited neighbors, the 1σ goes from ~ 0.0018 to $K_s \sim 0.0031$ mag. Although there is an increase in the errors, they are still below the typical errors obtained from the 1σ errors of the target fields.

3.4.3 Are the errors affected by the chosen target fields?

While in the previous subsections we justified our adopted errors as being representative of observing conditions and detector non-linearity, there is one final consideration to take, the selected targets are all found in known star forming regions, most of which are deeply embedded in dark clouds, begging the question: can the reduced number and non-uniform distribution of sources introduce a form of uncertainty? Furthermore, the known variability of YSOs can lead to the presence of multiple variable sources inside the $60''$ radius.

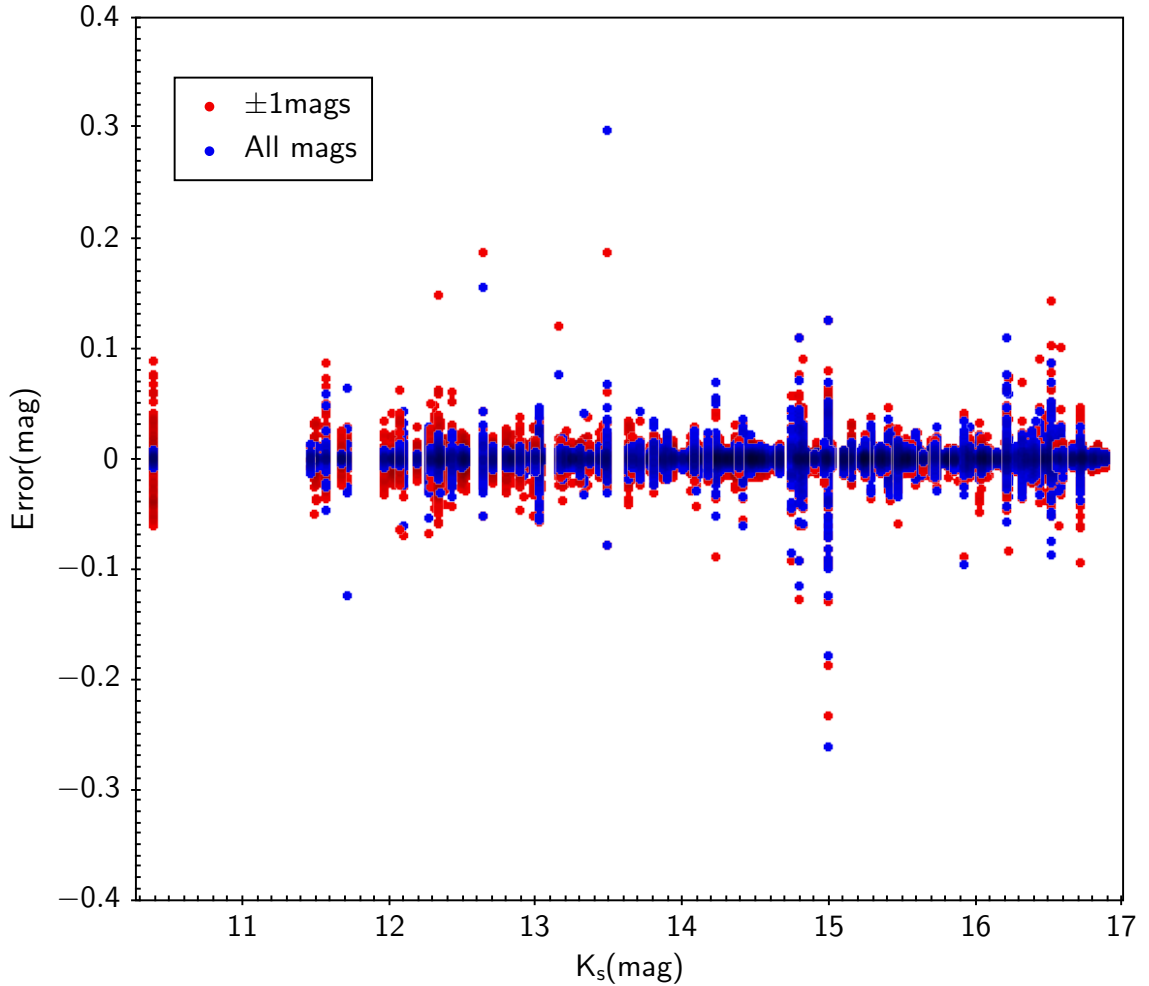


Figure 3.8: Systematic errors as a function of the magnitude of each target. The red points represents the case where we only consider the stellar sources with ± 1 mag around our targets. The blue points represent the case in which we consider all stellar sources in the vicinity of our targets. From Teixeira et al. (2018).

The impact of this selection bias needs to be quantified. With that in mind, we performed the following experiment: instead of using the sources inside an annulus around our target, we took the sources inside the same area ($1 < r < 60''$) but centered in a random coordinate at a distance $\sim 5'$ away. Using the same methodology as described in the previous subsection we found a field variability consistent with the $\text{MAD}(\Delta S_{i_{mjd}})$ computed in the vicinity of star forming regions.

3.4.4 Periodograms, false alarm probability, and their aliases

Next, the the Lomb Scargle(LS) periodogram was computed, in order to detect periodicities hidden in the LC variability. While producing a LS periodogram, which allows the identification of the maximum power frequency component, its interpretation is not

straightforward. As such, Scargle (1982) introduced the false alarm probability (FAP) to isolate the signals into those resulting from noise, and those which are real. The caveat of the FAP is that its predictive power decreases when noise is correlated, errors are non-Gaussian, and variability is highly non-sinusoidal. For the periodogram of each target, the 90%, 95%, and 99% FAP levels were computed.

The FAP addresses a specific concern: the probability that a peak of a given magnitude can be produced by a signal without any periodic component. This is quite different from determining if the signal is periodic with the corresponding observations (VanderPlas, 2017).

As shown in the literature, a given periodicity can produce harmonics of itself as a result of binning, observational window, and noise. These harmonics appear as additional peaks, or aliases, in the periodograms (VanderPlas, 2017). In order to mitigate this effect, an additional verification step was added, which attempted to determine if the measured frequencies were real or if they were aliases. The highest peak and the 10 higher-power peaks were identified. The measured frequencies were searched for aliases between each of the 10 higher-power peaks. This verification searched for: a) multiples in the frequency range; b) multiples in the period range; c) solving the equation:

$$f_i = f_t + n * f_w \tag{3.3}$$

where the frequency of the alias (f_i), depends on the true frequency (f_t), an integer (n), and a frequency window (f_w). The used frequency windows were 1 year (0.0027 day^{-1}), 1 day (1 day^{-1}), and a sidereal day (1.0027 day^{-1}), since for Earth based telescopes these are the most common aliases (VanderPlas, 2017).

3.5 Data products and the way forward

We have detailed in this chapter all the preliminary work and testing which was performed to obtain our working data and method. A large part of our work was spent in this stage. After reprocessing the entire pawprint photometry, and computing indicators of variability, such as, the IQR and MAD, we built and prepared a database with that information. Additionally, we coded tools to plot, on the fly, LCs of any given target and to quantify the photometric error at any given epoch considering nearby sources with similar magnitudes. Finally, our code also computes the periodicity of a given LC using Lomb-Scargle periodograms.

One of the major advantages of the ancillary databases and codes created is that they can be applied to any study of variability in different samples/evolutionary stages using

the wealth of information of the VVV survey. Therefore, we applied the products created in this chapter to pursuit our main objective: the study of variability in selected samples of MYSOs.

Chapter 4

The photometric variability of MYSOs

The paradigm of star formation has shifted from a model where each young stellar object (YSO) undergoes a process of constant accretion to a model favoring low-level accretion punctuated by short events of intense accretion (Vorobyov & Basu, 2006, 2015; Zhu et al., 2009). Among the possible causes for photometric variability of YSOs are conditions and changes in their natal environment, accretion physics or a combination of both (Contreras Peña et al. (2017), Kesseli et al. (2016), Meyer et al. (2017) and references therein). Material from the circumstellar disc, while falling onto the YSO, can form cold and hot spots, thus leading to some of observed variability. Variable extinction of star-light can be caused by dust clumps in the stellar medium as they pass along the observers line-of-sight.

Some of the most impressive examples of high-amplitude photometric variability, caused by variable accretion are FUors (FU Orionis) and EXors (EX Lupi). These are transient phenomena which can last, respectively, from a few years to a few months. Both FUors and EXors are low-mass YSO phenomena but, recently, higher-mass range counterparts have been observed (Kumar et al., 2016; Caratti o Garatti et al., 2017). Kumar et al. (2016) identified a sample of highly variable objects in the VVV survey to be Massive Young Stellar Objects (MYSOs) and argued that they were signposts of ongoing episodic accretion. Caratti o Garatti et al. (2017) used observations of spectroscopic and photometric variability of a $20M_{\odot}$ MYSO to conclude that, across stellar masses, disk-mediated accretion bursts were a common mechanism. Further evidence that sudden accretion is responsible for the growth of a massive protostar was also observed by Hunter et al. (2017) using ALMA observations. This preponderance of evidence suggests that episodic accretion is a mass-independent common mechanism of star formation. In fact, computational models of MYSOs, also predict the existence of luminous flares in their evolution, with similar morphologies to those of FUors and EXors (Meyer et al., 2017).

This discovery of a dozen highly variable MYSOs by Kumar et al. (2016), raises

the question of what is the overall nature of their variability. Therefore, the following study examines the presence of variable phenomena in known Extended Green Objects (EGOs) (Cyganowski et al., 2008) and IR sources, deeply embedded in clumps identified by the APEX Telescope Large Area Survey of the Galaxy (ATLASGAL) (Schuller et al., 2009). We can use the point source photometry to examine the variability of these sources since they represent unbiased large samples of point-like massive young stellar candidates. Although known Red MSX Sources (RMS) and ultra compact HII (UCHII) regions are important MYSO samples, their study requires larger aperture photometry of extended objects to examine variability, which we postpone to a different study.

The use of point source photometry requires targets to be point-like in MIPS observations, to have signposts associated with high-mass star formation and, that they are also point-like in the NIR K_s band.

The SED of a source measures the energy emitted by it at different wavelengths. When dealing with blackbody radiation, the peak of emission can be determined by Wien's Law, and the area under the curve follows Stephan-Boltzmann's law, connecting the total energy output to the blackbody temperature.

The grid of precomputed SED models created by Robitaille et al. (2006), and the subsequent SED fitting tool (Robitaille et al., 2007) have been successfully used in the literature to determine the physical properties of YSOs using photometric observations. The grid of models was computed using radiative transfer codes, dust and gas geometries, dust properties, to name a few of the parameters used. The fitting tool uses whatever photometric data available and searches the model grid using a χ^2 minimization technique. The more data a given source has, the more constrained the model can be. The tool only obtains directly a luminosity and temperature, the remaining parameters (e.g. age, mass) are derived from the evolutionary tracks.

The 200000 models made available in Robitaille et al. (2006) cover multiple ranges of evolutionary stages, from deeply embedded protostars to a stage where the star is surrounded by an optically thin disk. Typical model SEDs from this grid, are shown in Fig. 4.1. Figure 4.2 shows the different contributions of each component to the overall SED. Different convolved filters were also obtained so that it is a relatively easy task to use photometry from different sources. The newer versions of this code also allow the user to convolve custom filters not included in the original program (Robitaille et al., 2007). As reported initially by Robitaille et al. (2006), it should be clear that Mid-IR filters are an efficient way to separate YSOs from photospheres, and if wavelengths larger than $\sim 20\mu\text{m}$ are added to NIR and MIR fluxes, it becomes easier to distinguish between

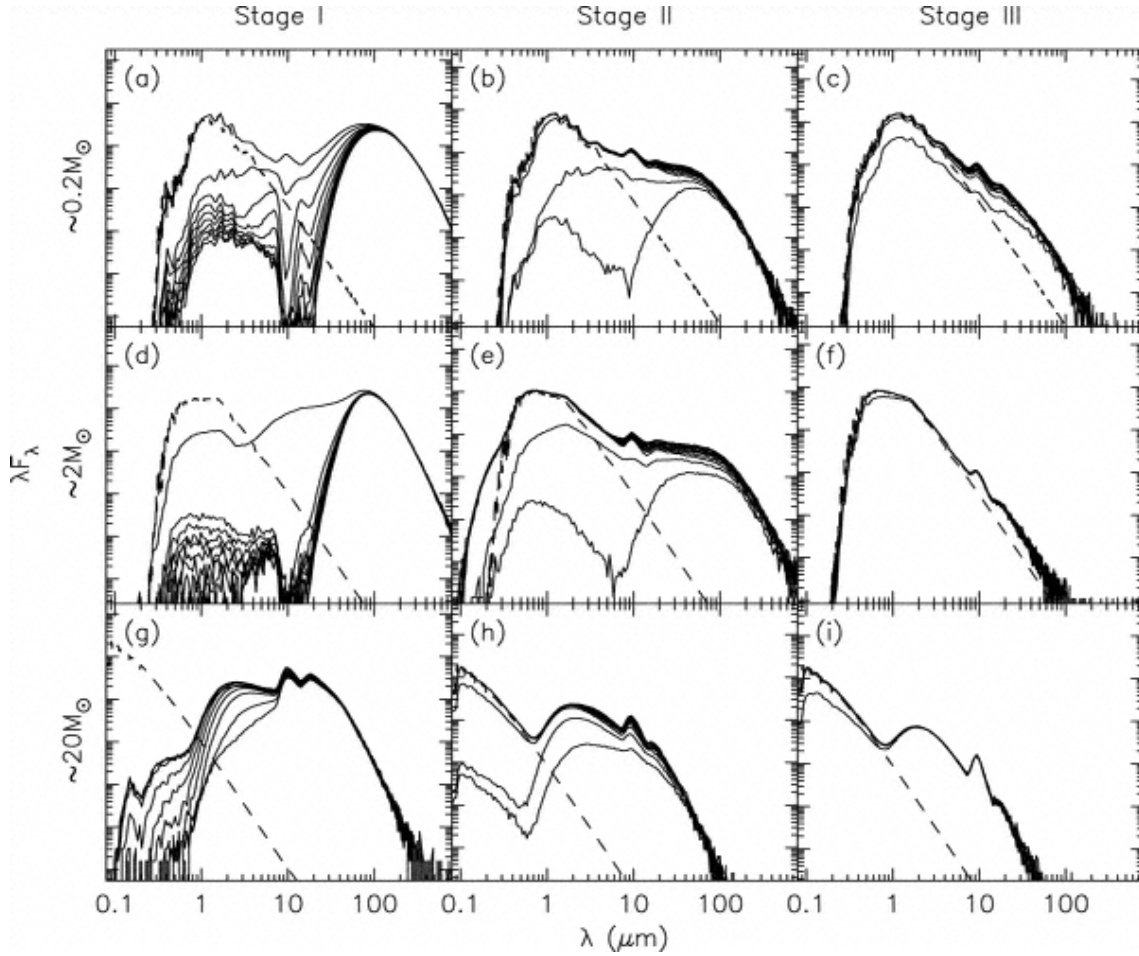


Figure 4.1: Example SEDs. From left to right, SEDs for three different objects of similar masses at Stages I, II, and III of evolution. From top to bottom, objects have masses ~ 0.2 , ~ 2 , and $\sim 20 M_{\odot}$ objects. Each plot shows 10 SEDs, one for each inclination (solid lines), the input stellar photosphere for each model (dashed lines). From Robitaille et al. (2006).

multiple evolutionary stages of YSOs.

The work shown in this chapter is divided into the following steps:

- Sample definition
- Computing and fitting SEDs
- Analysis of the results and implications to HMSF

4.1 Defining target sample

Three different and highly complimentary surveys, covering much of the same area at different wavelengths (from $\sim 1.2 - 870 \mu\text{m}$) were used to pinpoint the candidate MYSOs: MIPS GAL (Carey et al., 2009), ATLAS GAL (Schuller et al., 2009), and VVV (Minniti et al., 2010). We chose to focus our work in MYSO sources which represent two early

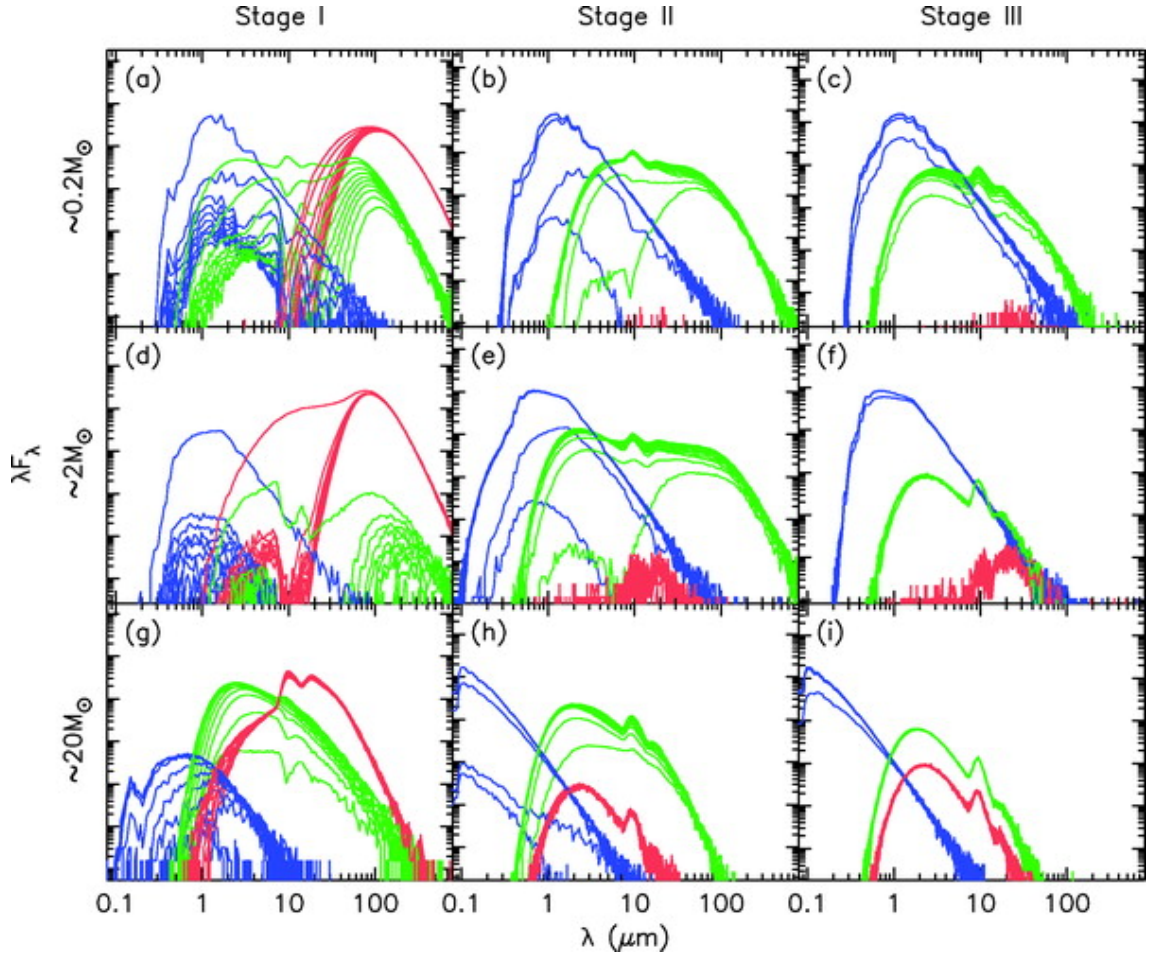


Figure 4.2: Same SEDs as in Fig. 4.1, the different contribution to the SEDs are shown: the star (blue), the disk (green), and the envelope (red). From Robitaille et al. (2006)

evolutionary phases of massive stars; a) driving sources of EGOs, on a phase of actively ejecting mass, b) luminous MIPS 24 μm point sources embedded in ATLASGAL clumps which likely haven't begun to produce outflows (hereafter, non-EGOs).

4.1.1 EGO sample

EGOs, are sources which show an extended emission on the Spitzer 4.5 μm band (IRAC 2) and lack such extended emission in the adjacent 3.6 μm and 5.8 μm bands. The H_2 , and CO lines, which are excited by the interaction of outflows and jets with the ISM, are contained in this band. Therefore, when there is excess in this band with respect to the other IRAC bands, it is a clear sign of outflow/jet interaction.

EGOs were initially cataloged by Cyganowski et al. (2008), this catalog was extended by the work of Chen et al. (2013a,b). Without question, EGOs are tracers of outflow activity, common across mass ranges but lower-mass outflows are below the detection threshold of the original GLIMPSE survey used for their classification as EGO (Cyganowski et al.,

2008; Chen et al., 2013b), with the exception of those objects in the closest SFRs. Therefore, EGOs, are considered to be H_2 flows driven by MYSOs (Cyganowski et al., 2008) or MYSO outflow cavities (Takami et al., 2012).

The number of unique EGOs cataloged so far is 270. Given that Cyganowski et al. (2008) used a MIPS $24\ \mu\text{m}$ detection in their original classification, these usually are considered to be the driving source of the outflow. The known EGO positions were queried on the varSource catalog (see Sec. 3.3), to find $2\ \mu\text{m}$ counterparts using two different search radius, $r \leq 1''$ and $r \leq 0.5''$. 187 and 153 driving sources were found for the respective radii. Considering that YSOs with disk and outflow activity tend to be surrounded by NIR circumstellar nebulae, it is possible that such sources appear to be extended sources in the NIR. Therefore, we allowed that detected VVV sources could be photometrically classified as both point-like or extended (80% of detections were point-like). As an additional selection criteria, three color composites (see Fig. 3.5 for an example), were used to confirm if the identified point sources are good representations of an outflow driving source. This examination led to a final EGO sample composed of 153 sources clearly representing $2\ \mu\text{m}$ counterparts of the $24\ \mu\text{m}$ sources, which are presumed to be driving sources responsible for the extended green emission.

4.1.2 Non-EGO sample

We begin with a sample of candidate MYSOs and ask what is the nature of variability in them. Using ATLASGAL, Contreras et al. (2013) and Urquhart et al. (2014) built the Compact Source Catalog (CSC) which identified ~ 10000 dense clumps. The mass, density, and distance to these clumps are provided by Urquhart et al. (2018) and they are believed to represent active sites of high-mass star formation. We define our non-EGO sample by:

- Matching the CSC to MIPS GAL point-like sources in $24\ \mu\text{m}$ band ($r \leq 5''$)
- Matching the resulting catalog with the varSource database ($r \leq 5''$)
- Match results again with varSource ($r \leq 1''$)

Since the dense clumps of CSC are considered to represent active HMSF regions, they can be assumed to host MYSOs. Matching red point-like sources in $24\ \mu\text{m}$ band with the peak emission in the $870\ \mu\text{m}$ band, in the search radius, is a reliable way to define MYSO candidates, as they should be bright in the $24\ \mu\text{m}$ band. This search returned a total of 873 point sources, for purposes of refining our catalog, when multiple matches were returned

Table 4.1: Summary of the target samples

Sample	EGOs	Non-EGOS	Total
‡ of sources	153	448	601

for the same clump, the source with the shortest centroid distance to the CSC coordinates was chosen. Since the MIPS FWHM is equal to $6''$, we searched these 873 targets in the varSource catalog ($r \leq 5''$), finding 574 K_s -band targets. Since these targets had multiple matches in the VVV K_s -band, we constrained our search to $r \leq 1''$, resulting in 2171 sources found in the varSource catalog. We then removed any source with less than ten non-saturated epochs over the entire survey. The resulting catalog contained 367 clumps with a single match and 147 with multiple matches. These multiple matching targets were individually assessed based on their magnitude, color, and centroid distance. The final 448 (367+81) targets are K_s -band point sources and represent the MYSO candidate at the peak of an ATLASGAL clump.

Table 4.1 summarizes the studied samples. The total MYSO sample for our variability study is, therefore, composed of 153 EGO and 448 non-EGO sources, resulting in 601 targets. A part of the EGO sample (66 sources) also lies within ATLASGAL clumps.

4.2 Computing and fitting SEDs

All sources in both our samples can be considered as good representations of MYSOs, based on signs of HMSF and the shallowness of the surveys used. Nevertheless, we chose to analyze their $1.2 \mu\text{m} - 870 \mu\text{m}$ spectral energy distributions (SEDs), in an effort to better understand their nature.

The photometric data used to build the SEDs was obtained by querying online surveys for available near- and far-infrared photometry. In particular, the public archival online data from the 2MASS, SPITZER, ATLASGAL, and Herschel programs was used (Huchra et al., 2012; Carey et al., 2009; Schuller et al., 2009; Pilbratt et al., 2010). The maximum photometric error ($\pm 10\%$) was assumed to be a reasonable upper limit.

In order to model the SEDs of the target sources we used the Python version of the SED fitting tool (Robitaille et al., 2007). Table 4.2 summarizes the bands, filters, wavelengths, and apertures used.

Given the large beam-size of the observations in higher wavelengths (Herschel and ATLASGAL) these were set as upper limits. Even for those sources which are well resolved at $24 \mu\text{m}$, if longer wavelength-emission was to be used, the light tends to come from

Table 4.2: Used filters and apertures for building the SEDs.

Filter	Wavelength (μm)	Aperture ($''$)
J	1.235	3
H	1.662	3
K_s	2.159	3
IRAC1	3.6	4
IRAC2	4.5	4
IRAC3	5.8	4
IRAC4	8.0	4
MIPS24	24	6
PACS70	70	5.6
PACS160	160	10.7
SPIRE250	250	17
SPIRE350	350	24
SPIRE500	500	35
AGAL870	870	19.2

multiple sources, and sometimes, even small clusters, which is a consequence of their larger beam-sizes. Lower wavelength data was set as data points, but for members of the EGO sample this was not the case. Given that the main characteristic of EGOs is extended emission in the $4.5 \mu\text{m}$ IRAC band, the data from that band was set as an upper limit, since these sources are defined by their excess in that band.

We set up an extinction range of $A_v = 0\text{-}50$ mag for all sources. The initial distance range used for fitting was between $d=1$ kpc and 13 kpc based on the known depth of the ATLASGAL survey. This large range of distances resulted in large uncertainties which were not acceptable for our intended analysis. To mitigate this issue, we used the distances presented in Urquhart et al. (2018), which were available for 105 targets, with an uncertainty of ± 1 kpc. For the remaining 102 sources the fitting procedure was limited to the original distance range ($d=1\text{-}13$ kpc).

In order to perform the final SED fitting we follow the method detailed in Grave & Kumar (2009):

1. Run the SED fitting tool for available observational data (see Tab. A.1)

2. Select all models with $\chi^2 - \chi_{best}^2 < 3$
3. Compute the inverse χ^2 of each model
4. Perform a weighted average for each parameter, where inverse χ^2 is the weight

The full input observational data used to construct the SEDs is shown in Tab. A.1. The results of this fitting procedure will be presented below.

4.3 Results

4.3.1 Variable sources

The LCs of 601 (448 non-EGO + 153 EGO) were visually examined and compared with the source IQR, we consider a source to be variable if its $IQR > 0.05$. This value was determined by performing a visual inspection of the LCs to be associated with having $> 20\%$ of the data-points above the 1σ error of the field.

This variability metric resulted in 51 (of the 448) non-EGO and 139 (of the 153) EGO targets classified as variable sources, totaling 190 (of 601) variable sources. Figure 4.3 presents some of the LCs with distinct variability. The plots of the LCs, phase-folded LCs, periodograms and three-color composite images for each target are also made available in the Appendix. Table 4.3 presents the relevant information concerning the variability of each variable source.

When comparing the highly variable ($\Delta K > 1$ mag) targets found by our method with those discovered by Contreras Peña et al. (2017), only three objects were found to be common to both works. These three sources were already the target of a follow-up study presented by Kumar & Grave (2007). The other highly variable sources were not found in the Contreras Peña et al. (2017) catalog, prompting a question of why this discrepancy existed. Upon visual inspection of their LCs, it was found that they are not highly variable ($\Delta K > 1$ mag) in the 2010-2012 period, which is one of their original selection criteria. Of the three common sources, MG300.3241-00.1985, MG322.4833+00.6447, MG342.3189+00.5876, the spectroscopy of the first one has been studied and it has been classified as a MNor, an object with a mixture of characteristics from FUors and EXors (Contreras Peña et al., 2017).

According to periodogram analysis, it was found that 1 member of the non-EGO sample, and 15 members of the EGO sample, could change their classification if the detected aliases were the true periods, a point which will be expanded in the discussion.

Table 4.3: Source coordinates, photometric data and variability

Source	RA (deg)	DEC (deg)	K_s (mag)	MAD (mag)	IQR (mag)	ΔK_s (mag)	Class	Period (day)
MG303.9304-00.6879	195.10156	-63.54177	15.21	0.15	0.33	1.28	Erup	NA
MG328.0494-00.0487	238.7064	-53.7280	12.28	0.149	0.278	1.83	Fad	NA
MG352.2452-00.0636	261.5178	-35.5005	15.95	0.079	0.166	0.53	STV	29.4
MG354.4384+00.4185	262.5086	-33.4088	14.66	0.091	0.523	0.89	Dip	NA
G309.91+0.32	207.7246	-61.7394	13.65	0.204	0.383	0.81	LPV-yso	545.9
G335.59-0.29	247.7437	-48.7308	13.16	0.097	0.348	0.61	low-Erup	NA
G351.78-0.54	261.6775	-36.1536	14.46	0.06	0.12	0.38	STV	18.3
G343.50-0.47	255.3267	-42.8267	15.38	0.10	0.18	0.86	LPV-yso	1156.3

Table 4.4: Observed parameters of LC classes, for both EGO and non-EGO samples.

LC classification	EGO	non-EGO	Total
Periodic	90 (~ 65%)	21 (~ 41%)	111
Aperiodic	49 (~ 35%)	30 (~ 59%)	79
LPV-yso	53 (~ 38%)	9 (~ 18%)	62
STV	37 (~ 27%)	12 (~ 23%)	49
Dipper	15 (~ 11%)	5 (~ 10%)	20
Fader	13 (~ 9%)	5 (~ 10%)	18
Eruptive	21 (~ 15%)	20 (~ 39%)	41

4.3.2 LC classes

Light curves were then classified based on their overall morphology and periodicity. We followed a classification scheme similar to the one used by Contreras Peña et al. (2017). The behavior and morphology of the LCs, can represent a connection with an underlying physical process.

As such, the classification scheme divides LCs into: a) Long Period Variables (LPV-yso); b) Short Timescale Variable (STV); c) Faders; d) Dippers and ; e) Eruptive. With LPV-yso and STVs belonging to a larger category of periodic variables while the remaining classes (Faders, Dippers, and Eruptive) are part of the aperiodic variable group. In the following text we provide short definitions of each different class.

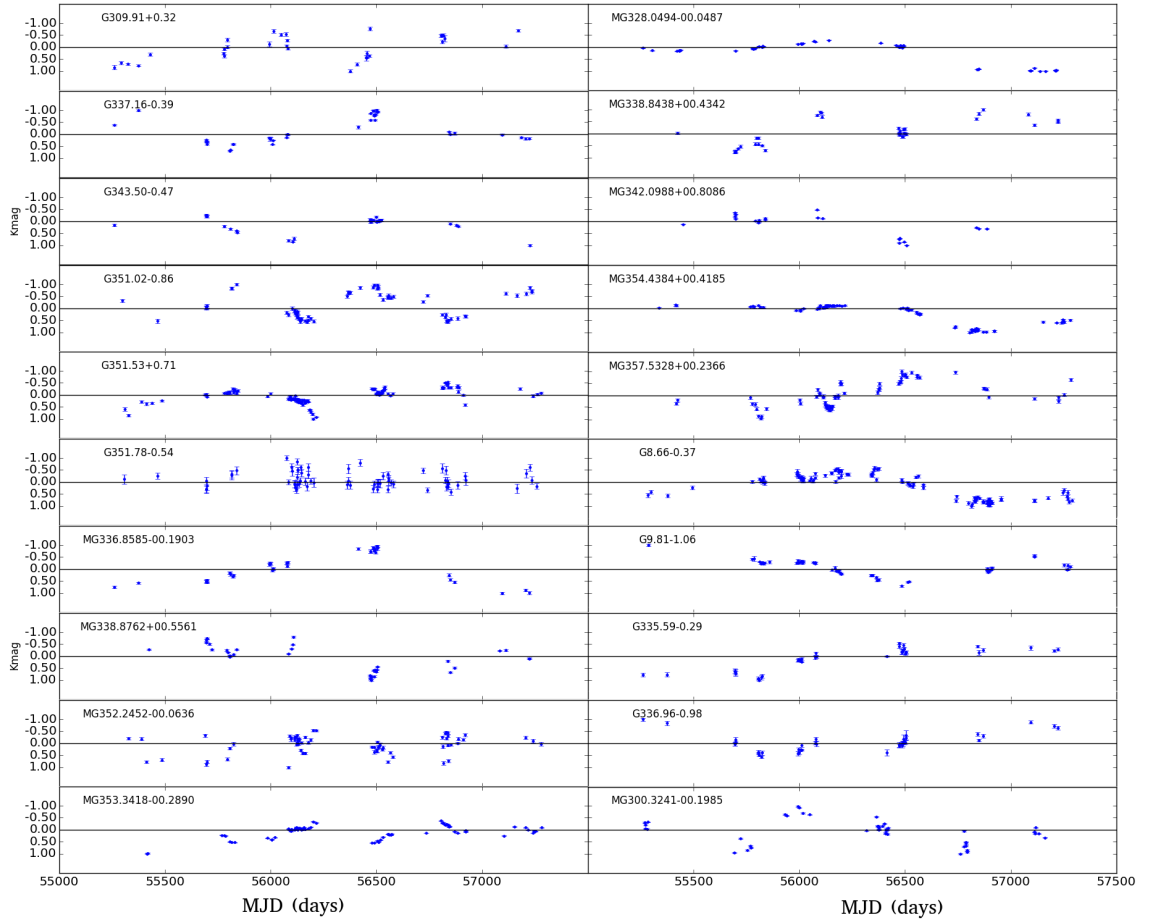


Figure 4.3: Some of the clearer LCs, periodic (left column) and aperiodic (right column). Each figure shows the LC of the source, error bars represent $MAD(\Delta S_{i_{mjd}})$. The vertical axis represents the variability from the median normalized by $\max(|K_i - \text{median}(K)|)$. From Teixeira et al. (2018).

4.3.2.1 Long Period Variables-yso

LPV-yso have, by definition, long periods ($P > 100$ days). These periods are larger than the typical rotational periods of the inner-disc orbits of YSOs ($P < 15$ days) or stellar rotation, so, LPVs are most likely caused by circumstellar dust.

For an example of two prototypical LPV-yso, see Fig. 4.4, showing G309.91+0.32 and G343.50-0.47, which have periods of ~ 545 and ~ 1156 days, respectively. Both sources have periodograms showing peaks well above the 99% FAP level and no aliases were found for either source.

4.3.2.2 Short Term Variables

STVs are another class of periodic variables, exhibiting characteristically shorter periods ($P < 100$ days) than LPV, or which vary over short timescales with no apparent pe-

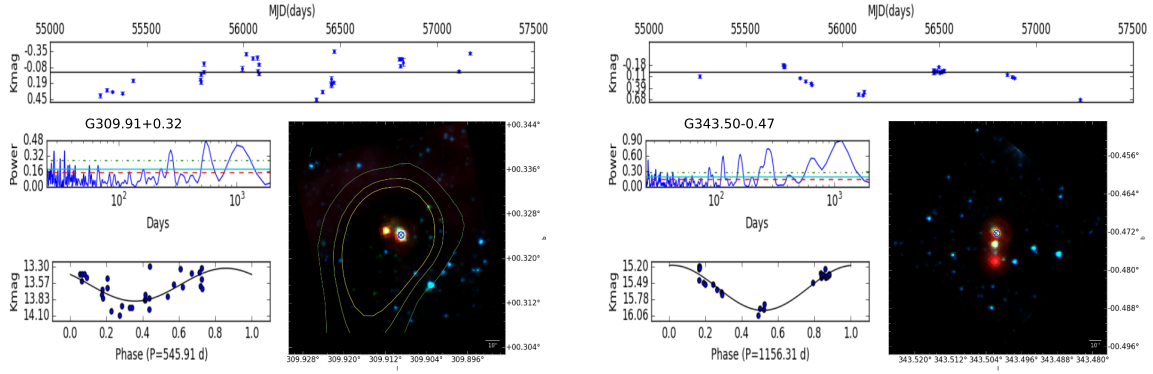


Figure 4.4: Prototypical LPV-yso sources: Top panel for each figure shows the LC of the source, error bars represent $\text{MAD}(\Delta S_{i_{mjd}})$, the left middle panel shows the corresponding periodogram in logarithmic scale (also plotted are the 99%, 95%, and 90% false probability levels, respectively: the green dot-dashed line, the cyan full line, and the red dashed line), the bottom left panel shows the phase-folded light curve of the source using the best period fitted (also shows the corresponding value in days), the bottom right plot shows the RGB image of the source using the Spitzer IRAC 3.6 μm , IRAC 4.0 μm , and the 24 μm MIPS band as blue, green and red, respectively. The VVV source is indicated by the blue circle and the green cross represents the MIPS co-ordinates. The contours of the RGB are in the interval of $[\text{Peak}-5\sigma, \text{Peak}]$ from the ATLASGAL observation at 850 μm . From Teixeira et al. (2018).

riodicity. Variations over periods larger than the stellar rotation or inner disc orbits ($15 < P < 100$), can be explained by obscuration from a circumbinary disc or as an effect of variable accretion (Contreras Peña et al., 2017; Bouvier et al., 2003). The two prototypes of STVs, shown in Fig. 4.5, present typical periods of 29 and 18 days, with neither source presenting aliases in their periodograms.

4.3.2.3 Faders

The typical Fader-class LC either shows a slow decline in brightness over time or a constant luminosity followed by a sharp decrease sustained over a year, it is an aperiodic variation. Two usual explanations for the Fader behavior are: a) the end of an active accretion phase, i.e., return to quiescent phase; b) a long lasting extinction increase. Figure 4.7 shows a typical fader LC, it should be noted that although there appears to be a small periodic signal present until MJD 56500, it is followed by a massive decrease in its brightness.

4.3.2.4 Dippers

A LC showing dimming events lasting between a few months up to a few years, followed by a return to normal brightness, is normally classified as a Dipper. It is important to

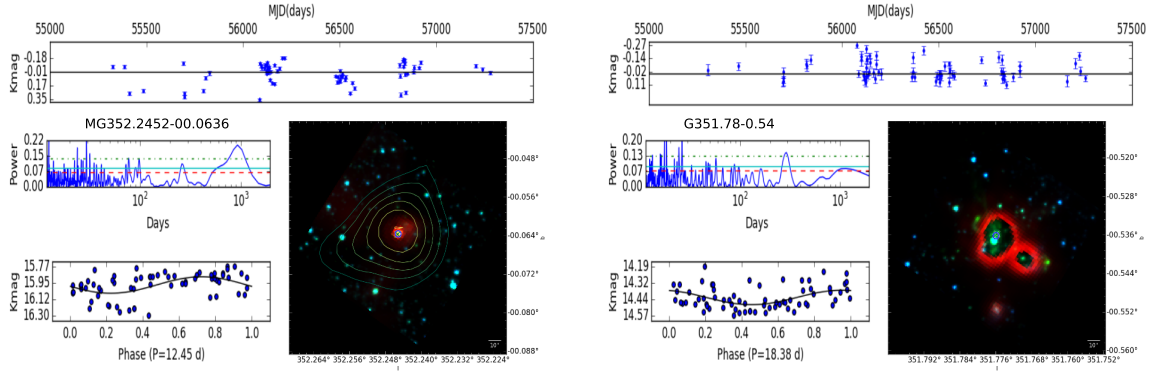


Figure 4.5: Prototypical STV sources: Top panel for each figure shows the LC of the source, error bars represent $\text{MAD}(\Delta S_{i_{mjd}})$, the left middle panel shows the corresponding periodogram in logarithmic scale (also plotted are the 99%, 95%, and 90% false probability levels, respectively: the green dot-dashed line, the cyan full line, and the red dashed line), the bottom left panel shows the phase-folded light curve of the source using the best period fitted (also shows the corresponding value in days), the bottom right plot shows the RGB image of the source using the Spitzer IRAC $3.6 \mu\text{m}$, IRAC $4.0 \mu\text{m}$, and the $24\mu\text{m}$ MIPS band as blue, green and red, respectively. The VVV source is indicated by the blue circle and the green cross represents the MIPS co-ordinates. The contours of the RGB are in the interval of $[\text{Peak}-5 * \sigma, \text{Peak}]$ from the ATLASGAL observation at $850\mu\text{m}$. From Teixeira et al. (2018).

emphasize that while the same terminology exists within the YSOVAR project (Morales-Calderón et al., 2011), it is used there to classify shorter-lived phenomena, on the scales of hours to days. In contrast, the dipper classification here refers to changes occurring in time-scales ranging from of a few weeks up to a few years. The dipper morphology is often connected with extinction increases from variations in the circumstellar and interstellar material. The morphological characteristics of both LCs of dippers and faders are so similar that if we took a snapshot of a dipper event without the return to normal brightness it could easily be confused with a fader LC. While Contreras Peña et al. (2017) has shown that the color-color diagrams of faders and dippers are different, in this work such data was not available. As such, both fader and dipper classes are both used based only on the morphology of their LCs. The typical dipper LC can be seen in Fig. 4.6, a non-variable source through most of the VVV observational epochs, it suffers a drop in brightness which is almost recovered in its entirety about 750 days later.

4.3.2.5 Eruptive

LCs with an aperiodic morphology, presenting outburst and increases in brightness lasting between months and year or, in a few cases, only a few weeks define our final class,

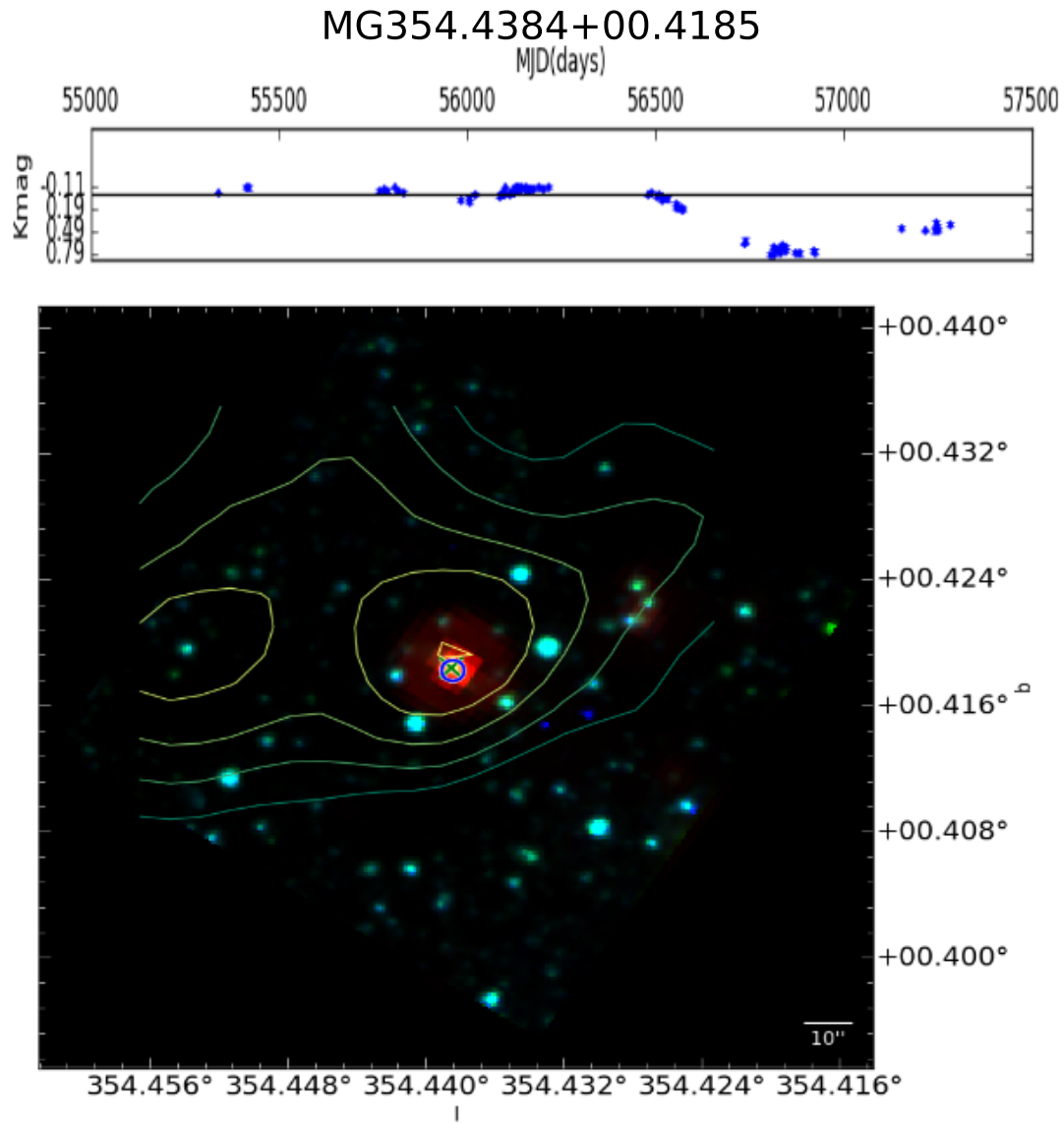


Figure 4.6: LC of a dipper event. Colors and symbols are the same as in Fig. 4.4. From Teixeira et al. (2018).

eruptive variables. The behavior of their brightness corresponds to luminosity increases, a consequence of ongoing accretion. The classic examples for eruptive LCs are FUors and EXors but these are the most extreme forms of this behavior. Given the large amplitude of variability within this group, an additional subdivision of the eruptive class was created. Following a scheme proposed by Medina et al. (2018), 'low amplitude eruptives' are sources with eruptive behavior but with small amplitudes ($\Delta K < 1.0$ mag). This subclass is important to underline the difference between them, FUors and EXors, as there is a possibility that a low amplitude eruptive LC in the K_s band can correspond to an high-amplitude variable source (FUor or EXor), for the right combination of disk geometry and extinction.

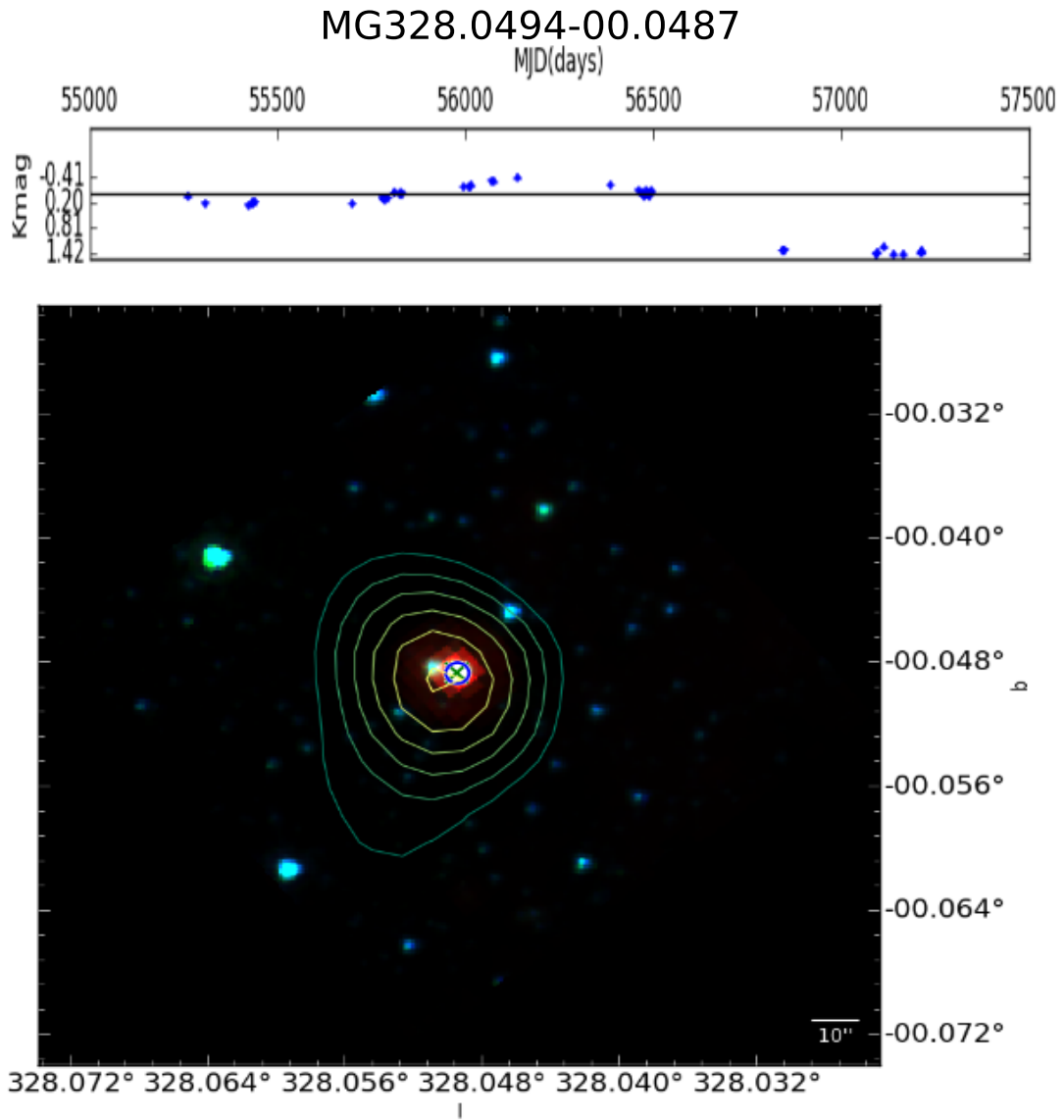


Figure 4.7: Typical Fader event. Colors and symbols are the same as in Fig. 4.4. From Teixeira et al. (2018).

The low-amplitude eruptive subclass was used in this work only as a reference for following studies but is otherwise ignored for the purposes of our analysis, i.e. the eruptive subclass is considered as a single class with no subclasses.

Figure 3.5 and 4.8 presents two clear examples of two different eruptive behaviors. The first, MG303.9304-00.6879, features multiple stages of increased brightness dominated by two large amplitude changes over a period of years. While the second, G335.59-0.29, is a low-amplitude variable showing a LC which has a brightness increase which was maintained over a period of years.

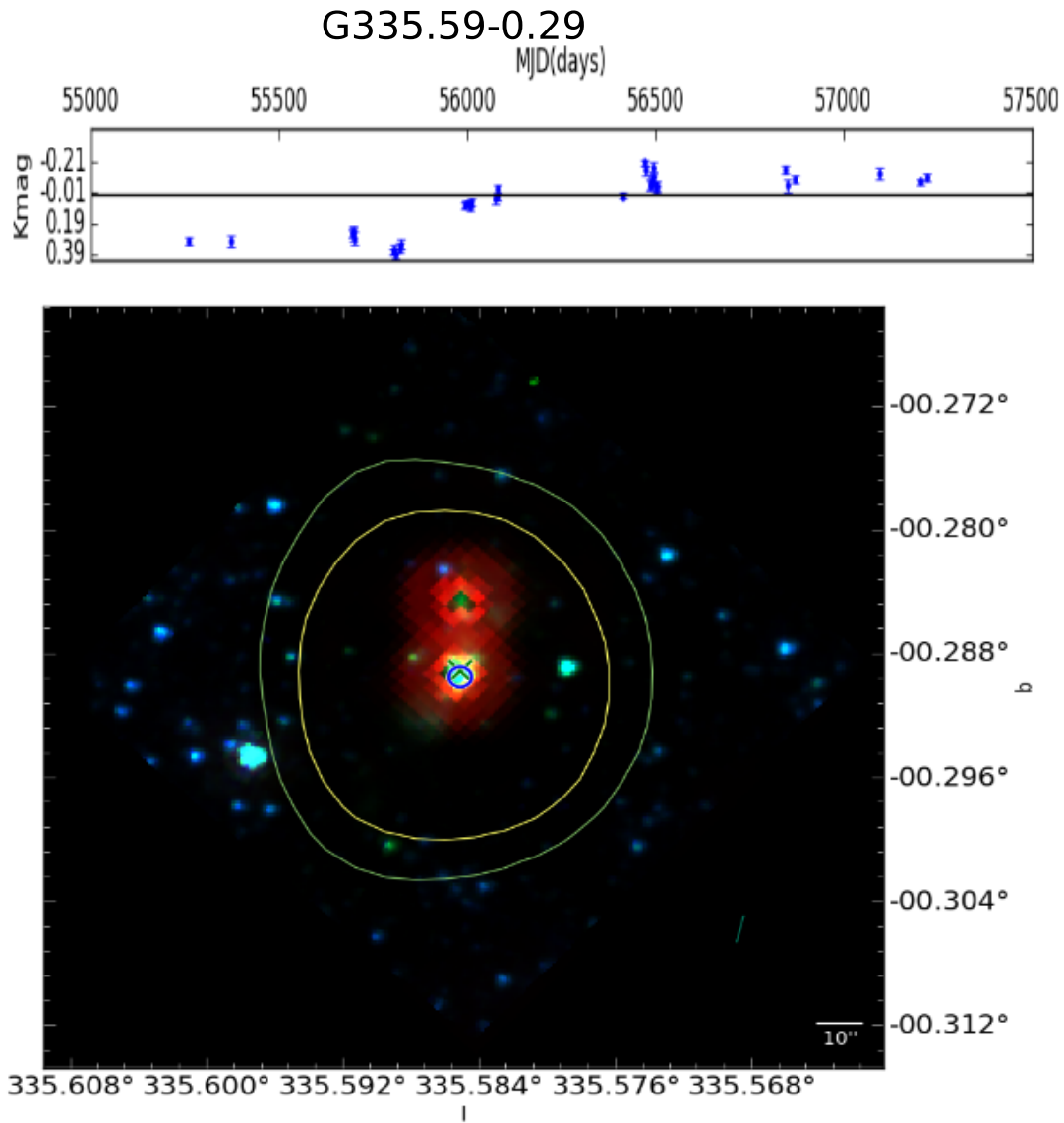


Figure 4.8: LC of the example of a low-amplitude eruptive event. Colors and symbols are the same as in Fig. 4.4. From Teixeira et al. (2018).

4.3.3 SEDs

One of the ultimate goals of the SED fitting was to test the MYSO nature of variable sources. The YSO models of Robitaille et al. (2006) were used to constrain the properties of the targets. Table A.2 summarizes results of the fitting method. Although this table contains 190 entries, one per variable source, only a subset (105) have reasonable uncertainties. As mentioned above, these are the 105 sources with known distances. Using the full distance ranges, some fitted sources, appeared to have sub-stellar masses. This effect is, presumably, caused by the unknown distances and not the true nature of the sources, given that other signposts of high-mass star formation are more reliable than the

uncertainty in distance. Furthermore, this point is supported by the large errors obtained for these objects.

Figure 4.9 presents the SED plots for the different variable sources used as examples of different LC classes, on Sec. 4.3.2. These portray masses going from 1.84 to 10.30 M_{\odot} , luminosities in the range of 57 and 6918 L_{\odot} , and evolutionary ages between 10^4 and 10^6 yrs. The plots show that the SEDs peak close to the $100\mu\text{m}$, a reddened emission consistent with light which has been absorbed and re-emitted by dust and gas in the disk and envelope of the MYSOs.

In order to explore the SED results, these were grouped using different mass bins, which roughly slice sources into low, intermediate, and high-masses (see Tab. 4.5). Roughly $\sim 35\%$ of sources were well adjusted by models in the 4-8 M_{\odot} range, while about 6% are in the $\geq 8 M_{\odot}$ bracket. Most sources ($\sim 60\%$) fall into the $M < 4M_{\odot}$ group.

Table 4.5 summarizes the SED results by listing various properties of the sources grouped in mass ranges roughly separating the low, intermediate, and high-mass sources. It is observed that about $\sim 35\%$ of the targets are modeled in the 4-8 M_{\odot} range and only 6% represent $\geq 8 M_{\odot}$ objects. A large fraction ($\sim 60\%$) are fitted with YSO models representing sources with $M < 4M_{\odot}$.

Sources occupying the 4-8 M_{\odot} bracket show a few hundred solar luminosities, envelope accretion in the order of $\sim 10^{-4} M_{\odot} \text{ yr}^{-1}$, and disc accretion approximately $\sim 10^{-6} M_{\odot} \text{ yr}^{-1}$. The high-mass sources are mostly composed of EGOs (10), with only one non-EGO. The MYSO models which fit these SEDs are similar to the ones shown in Grave & Kumar (2009). Of these 11 objects, four of them show both 6.7 GHz class II and 95 GHz class I methanol maser emission. Sources fitted as intermediate mass are divided into 45 EGOs and 21 non-EGOs, while for low-mass these are 87 EGOs and 25 non-EGOs.

Table 4.5: SED results by mass bin.

M	Sources	L	L	\dot{M}_{env}	\dot{M}_{env}	\dot{M}_{disk}	\dot{M}_{disk}	$A_{V_{circum}}$	$A_{V_{circum}}$
(M_{\odot})	(%)	(L_{\odot})	(L_{\odot})	($M_{\odot} \text{ yr}^{-1}$)					
Range	Ratio	Range	Median	Range	Median	Range	Median	Range	Median
$M < 4$	~ 59	[4.0E-1,9.0E2]	5.0E1	[0,4E-4]	1.3E-5	[-8E-3,4E-5]	2E-7	[6E-1,6E5]	74
$4 \leq M < 6$	~ 21	[8.8E1,1.2E3]	2.9E2	[0,4E-4]	7.8E-5	[-4E-2,9E-6]	6E-7	[2E0,2E4]	56
$6 \leq M < 8$	~ 14	[2.9E2,5.1E3]	9.3E2	[0,6E-4]	2.0E-4	[-2E-1,3E-5]	2E-6	[5E0,1E5]	66
$8 \leq M$	~ 6	[1.3E3,3.7E4]	3.0E3	[1E-4,4E-3]	2.8E-4	[-1E0,4E-6]	-2E-3	[4E1,4E5]	228

4.4 Discussion

The different incidence of variability on the EGO and non-EGO implies that these two are different populations with 139 of 156 (91%) and 51 of the 433 (12%) variable sources, respectively. This discrepancy between the target variability in the two samples can be explained by the fact that EGOs are associated with outflows or outflow cavities. By definition they should be more active by definition than members of the non-EGO sample which are deeply embedded inside clumps. This leads to the conclusion that variability and outflow activity are highly correlated phenomena.

While the non-EGO sample is composed only by sources classified as stars by the pipeline, members of the EGO sample were allowed to be classified as non-stellar (*class*=1). This somewhat relaxed criteria is justified, as EGOs tend to be extended objects in Spitzer $4.5 \mu\text{m}$, and are associated with outflows and cavities. To test if the variability discrepancy was indeed a result of photometric classification, the *class*=-1 selection criteria was applied to the EGO sample. Out of the remaining 30 EGO sources, 23 ($\sim 80\%$) were found to be variable, a larger ratio than the one for non-EGOs. Therefore, the different ratio of variable objects cannot simply be explained as a result of a sample selection criteria bias.

The ratios of periodic variables in the EGO and non-EGO samples, with 64% and 41%, respectively, shown in Tab. 4.4, again reinforce the idea of two different evolutionary stages/ populations. One of the possible explanations of the observational differences is a compound effect of both line of sight (LOS) and evolutionary stage. The objects on the non-EGO sample are inside clumps, so there is no clear LOS to the central source and aperiodic fluctuations from the dense, inhomogeneous circumstellar shell or core are more likely observed. Along polar regions, the circumstellar envelope of EGOs will be cleared by the associated outflows. The cavity will be less inhomogeneous, and a periodic central source or, more likely, the reflection of the flickering source will be observed. Figure 4.10 is an illustrative scheme of the two situations (not to scale). The non-EGO source (Fig. 4.10 a), surrounded by the spherical envelope of circumstellar molecular gas, will show non-periodic variations in the LC caused by regions of over- or under-density. There will be a clearer LOS observing a EGO source (Fig. 4.10 b), as a result of outflows/jets disrupting the circumstellar environment, one of the sources of non-periodic variability.

It can be seen from Fig. 4.11 that the amplitude range of variation in non-EGOs is roughly twice as much as that of EGOs. This reinforces the idea that non-EGO variable sources are relatively more embedded objects when compared to EGOs. A quick analysis of Fig. 4.11 can lead to the suspicion that the higher ratio of periodicity in the EGO

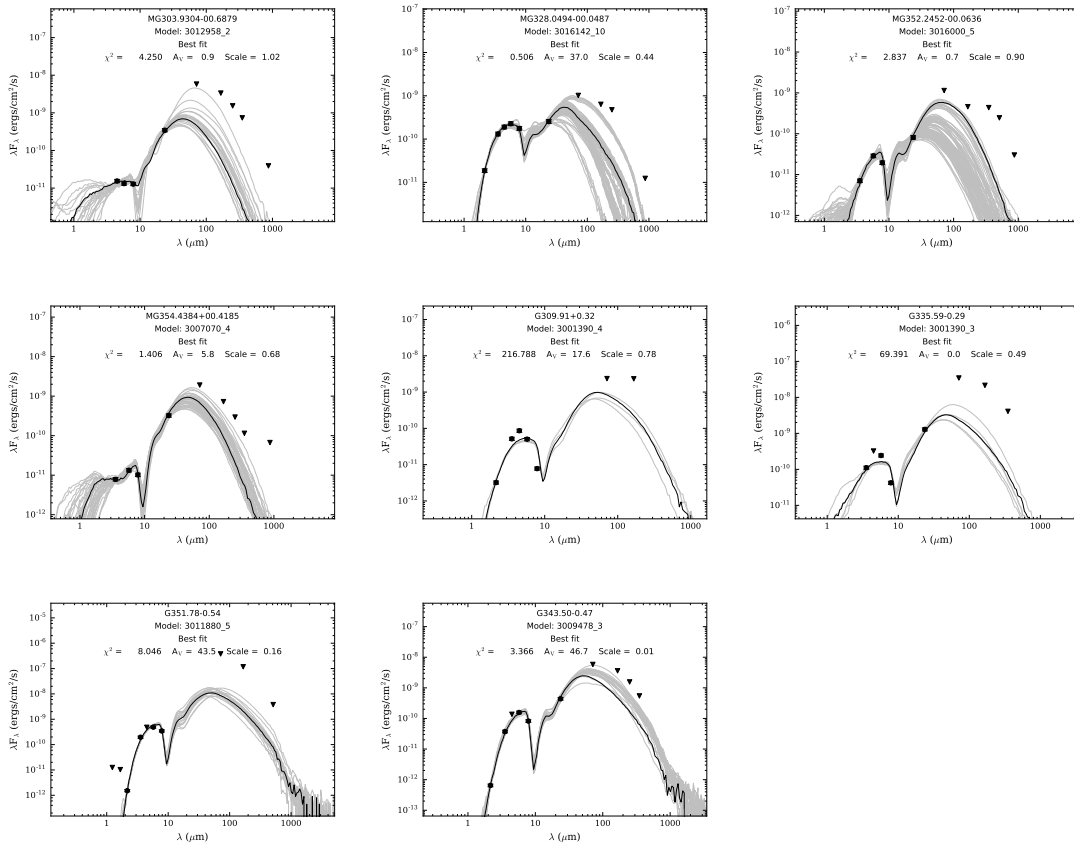


Figure 4.9: Grid of SEDs for our prototypical sources. The dark line corresponds to the best fit model. The grey lines correspond to other $\chi^2 - \chi_{best}^2 < 3$ models. From Teixeira et al. (2018).

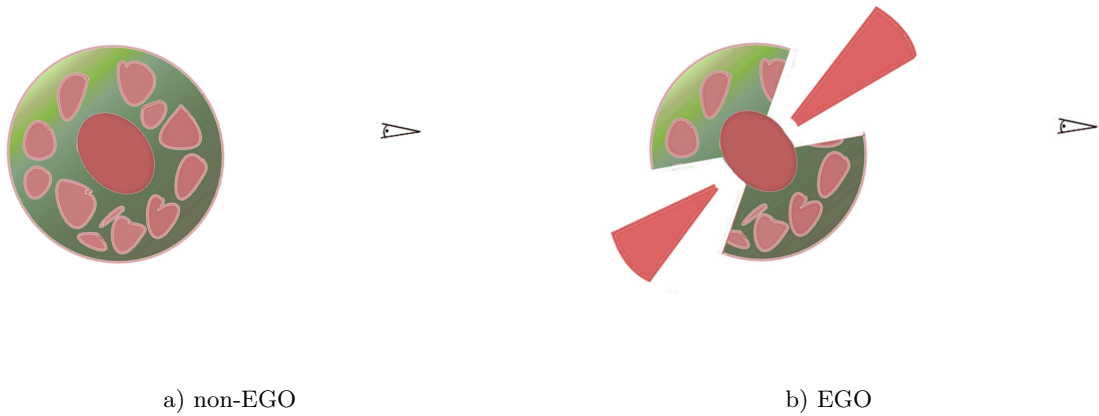


Figure 4.10: Diagram of the circumstellar structure surrounding the non-EGO (left) and EGO (right) objects. In the non-EGO case, the central protostellar source is surrounded by a spherical shell of circumstellar material which has still not evolved to a disk, the spherical shell is inhomogeneous since there are some local over-densities in the interior of the circumstellar gas. In EGOs, the polar areas are being cleared by outflow or jet emission from the central source, leading to a more unobstructed view of the source by the observer.

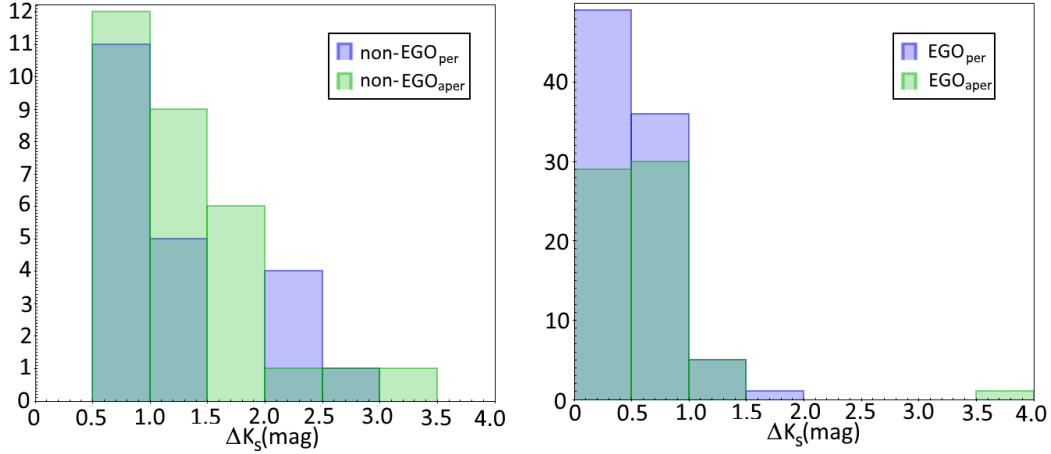


Figure 4.11: Histogram of ΔK divided by sample and periodicity. EGO and non-EGO sources are shown, respectively, on the right and left plots. From Teixeira et al. (2018).

sample is a result of the lower amplitude LCs, since there is a known link between them. This premise was tested selecting only EGO members with $\Delta K \geq 0.5$ mag. 39 (57%) periodic and 29 (43%) aperiodic sources were found while for $\Delta K < 0.5$ mag, there are 50 (74%) periodic and 18 (26%) aperiodic sources. Lower amplitude LCs favor periodicity as expected but these do not fully account for the different prevalence of periodicity between the two samples.

A randomly chosen source from the EGO sample is more likely to be variable than a random non-EGO source. We propose that this is a result of one main effect, the evolutionary stage of objects on each sample. In fact, this can be thought of as resulting from a selection bias, as EGOs will likely have ongoing outflow events while such conditions may not be expected from ATLASGAL cores.

Studying the aliases among the frequencies of highest power, found that five non-EGO ($\sim 9\%$), and 22 ($\sim 15\%$) EGO targets had such aliases. One ($\sim 2\%$) non-EGO would change classification, from LPV-yso to STV, while 15 ($\sim 10\%$) of the EGOs could change between LPV-yso and STV. It should be noted that none of the sources would be reclassified from periodic to aperiodic given that a periodic classification is a result of both LC morphology and period length.

4.4.1 On the presence of other signposts of High-mass Star formation

Looking at the surrounding environment of the sources it is possible to get further clues about their current evolutionary stage. The vicinity of the targets was examined for the presence of other signposts of high mass star formation by querying the SIMBAD online

tool (Wenger et al., 2000) in a $20''$ radius around them.

According to the query, the non-EGO sample has 19 sources classified as YSO candidates, furthermore, 5 sources were classified as AGB candidates, and 9 targets had class II masers (see Table 4.6). While, for the EGO sample targets, 5 were candidate AGBs, 63 had close-by ATLASGAL cores, and 23 had class II masers (see Table 4.6).

Methanol masers have long been associated with High-Mass star formation, therefore, it can be claimed, with a high-degree of confidence that the sources with nearby methanol maser emission, $r \leq 5''$ are, indeed, very likely High-Mass Protostellar cores (Caswell et al., 2010; Chambers et al., 2014; Urquhart et al., 2013). While class I methanol masers can be produced also by jets from low-mass YSOs, class II are only produced by massive outflow activity (de Villiers et al., 2015). Table 4.6 also shows the detection of class I methanol maser for cases where class II methanol masers have been detected as well. Of the 32 sources with nearby class II masers, 30 are either in the EGO sample or have nearby EGOS. This serves to reinforce the association of MYSO outflows and class II methanol masers.

The nearby class II methanol masers of two member of the EGO sample, G351.78-0.54 and G298.26+0.74, were studied for variability by Goedhart et al. (2014). While the former is an highly variable maser, the latter does not show any signal above the instrumental noise. The link between maser and MYSO photometric variability is an interesting avenue of research which we hope to explore in future works.

Finally, the search for other signposts of star formation revealed that the 28 ($\sim 17\%$) EGOS, appear to have close-by HII regions, while only one non-EGO target presents an HII region. This can be taken as further evidence for the evolutionary stage of the targets.

A small note should be made concerning the completeness of the samples. The criteria for selecting non-EGOS: $24 \mu\text{m}$ MIPS sources matching ATLASGAL CSC objects ($r < 5''$), can miss the most luminous sources in the clumps. These can be offset $r > 5''$, leading us to miss many MYSOs in the regions. It is, therefore, a rather important point that the selection cut used is a conservative approach to obtaining good MYSO candidates. It would be a valuable complement to the work presented here if a more careful search of the CSC was performed, in order to find the most luminous FIR sources.

The differences of observed variable LCs between the samples lead to the question: can the different behaviors be explained by the nature of the sources themselves? But, in order to answer this question, it is imperative to further understand the physical parameters of the sources. Therefore, to determine these parameters, we should to look for results from the SED fitting procedure.

Table 4.6: EGO and non-EGO MYSO candidates with nearby methanol masers.

Source	$K_{\sim}mag$ (mag)	IQR (mag)	Distance (kpc)	Class	ClassII Maser	ClassI Maser
MG003.5016-00.2020	16.07	0.23	5.0	Erup	Y	
MG006.9222-00.2512	14.38	0.26	3.0	Erup	Y	Y
MG332.3652+00.6046	14.17	0.09	2.7	Fad	Y	Y
MG333.0294-00.0149	15.24	0.18	4.0	Dip	Y	N
MG339.2939+00.1387	15.63	0.41	4.8	STV	Y	
MG339.5843-00.1282	13.16	0.16	2.6	Dip	Y	Y
MG345.5764-00.2252	15.33	0.3	7.9	Erup	Y	
MG352.6040-00.2253	15.38	0.22	7.6	Erup	Y	
MG358.4604-00.3929	16.03	0.16	5.0	LPV-yso	Y	Y
G9.62+0.20	14.38	0.11	5.2	STV	Y	Y
G6.19-0.36	14.52	0.09	5.1	STV	Y	Y
G5.62-0.08	15.43	0.07	5.1	LPV-yso	Y	Y
G359.44-0.10	14.99	0.13		LPV-yso	Y	Y
G358.84-0.74	13.82	0.12	6.8	LPV-yso	Y	Y
G358.46-0.39(b)	15.45	0.16	2.9	STV	Y	Y
G358.39-0.48	13.93	0.19	2.4	Erup	Y	Y
G358.26-2.06	12.26	0.08	3.0	Fad	Y	
G355.54-0.10	14.08	0.15	3.0	LPV-yso	Y	Y
G355.18-0.42	14.98	0.08	1.2	Erup	Y	Y
G353.46+0.56	13.18	0.1	11.2	LPV-yso	Y	Y
G352.63-1.07	14.56	0.14	0.9	STV	Y	Y
G352.58-0.18	15.62	0.09	5.1	LPV-yso	Y	
G352.13-0.94	12.79	0.1	2.3	LPV-yso	Y	Y
G351.78-0.54	14.46	0.12	0.7	STV	Y	Y
G351.69+0.17	14.91	0.05	12.1	STV	Y	
G351.38-0.18	15.8	0.07	5.6	STV	Y	N
G351.16+0.69	10.4	0.15	1.8	STV	Y	Y
G350.52-0.35	15.02	0.17	3.1	Erup	Y	N
G350.36-0.07	14.31	0.09	11.2	Fad	Y	
G2.54+0.20	12.71	0.09	4.0	LPV-yso	Y	N
G2.14+0.01	13.03	0.03	11.2	Non-var	Y	
G0.09-0.66	13.87	0.08	8.2	STV	Y	Y

Table 4.7: Summary of the median fit parameters, for both EGO and non-EGO samples divided by periodicity.

Parameter	EGO	non-EGO	Periodic	Aperiodic
ΔK_s (mag)	0.52	1.02	0.58	0.69
Period (days)	312	416	126	-
M (M_{\odot})	3.2	3.8	3.2	3.6
\dot{M} ($M_{\odot} yr^{-1}$)	4E-5	6E-6	4E-5	2E-5
\dot{M}_{disk} ($M_{\odot} yr^{-1}$)	3E-7	7E-7	3E-7	6E-7
L (L_{\odot})	125	212	125	190
Age (Myr)	5.0	5.6	5.0	5.0
T (K)	4841	7795	4857	5990
$A_{V_{circum}}$	61	125	71	54

4.4.2 SEDs

The dependence between fitted mass and envelope accretion rate is shown in Fig. 4.12. With the exception of a few outliers, there is a clear correlation between higher mass and accretion rate. This is an expected result, a product of the way the SED models were constructed and has been widely known to be a limitation of the SED model grid (Robitaille et al., 2006). Nevertheless, an analysis of the relation between mass and envelope accretion using different groupings revealed some interesting behaviors. EGO sources have envelope accretion rates one order of magnitude larger than non-EGOs, roughly the same relation between periodic and aperiodic sources. This is not a surprise, considering that EGOs are dominated by periodic sources and non-EGOs by aperiodic sources, as shown in the differences between top and bottom panels of Fig. 4.12. Aperiodic sources, i.e. dippers, faders, and eruptives, are thought to represent objects with low-levels of accretion which undergo bursts of intense accretion. This behavior helps to explain the smaller envelope accretion rate fitted to these classes.

As shown in Robitaille et al. (2006), the age, mass, and accretion rates resulting from the model grid and SED fitting have known correlations and are model dependent. The most reliable parameters resulting from the SED fitting tool are, therefore, luminosity and temperature. Given the barely populated parameter space of high-mass objects in the model grid, differences in luminosity and temperature can be used to choose between models. In an attempt to limit the bias consequence from model grid, the following analysis uses extensively those two parameters: luminosity and temperature.

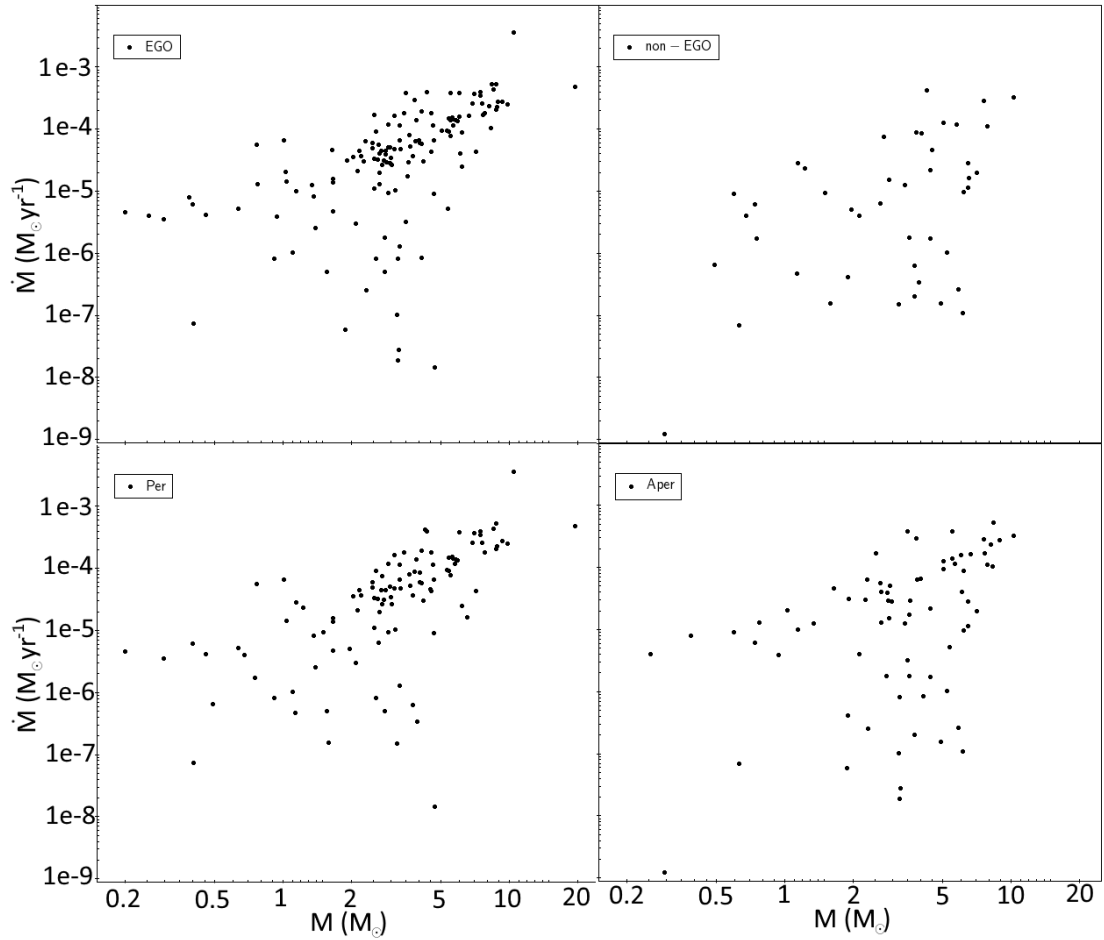


Figure 4.12: Mass versus envelope-accretion rate for the fitted SEDs of EGO and non-EGO sources, in logarithmic scale. EGO, non-EGO, periodic, and aperiodic, are plotted at the top left, top right, bottom left, and bottom right, respectively. From Teixeira et al. (2018).

The results from fitted YSO models were combined with those of Chapter 4, i.e. periodicity, variability, and class. There is no apparent correlation between different modeled parameters (luminosity, temperature, mass to name a few) and the amplitude of variation. In an effort to fully explore the parameter space, the luminosity and temperature of variable sources was used to plot the HR diagram of the targets, as shown in Fig. 4.13. PMS evolutionary tracks from Siess et al. (2000) were over-plotted, as well as the ZAMS curve. An analysis of the HR diagram reveals that, for all mass bins, EGOs tend to be more concentrated closer to birth-line positions. It would be negligent to overlook that a majority of EGO driving sources appear modeled by low- and intermediate-mass stars. This apparent contradiction between sample selection and modeled mass can be explained if we consider that these are very young objects and precursors to high-mass stars, which are lower mass objects accreting material throughout more than half their life until finally

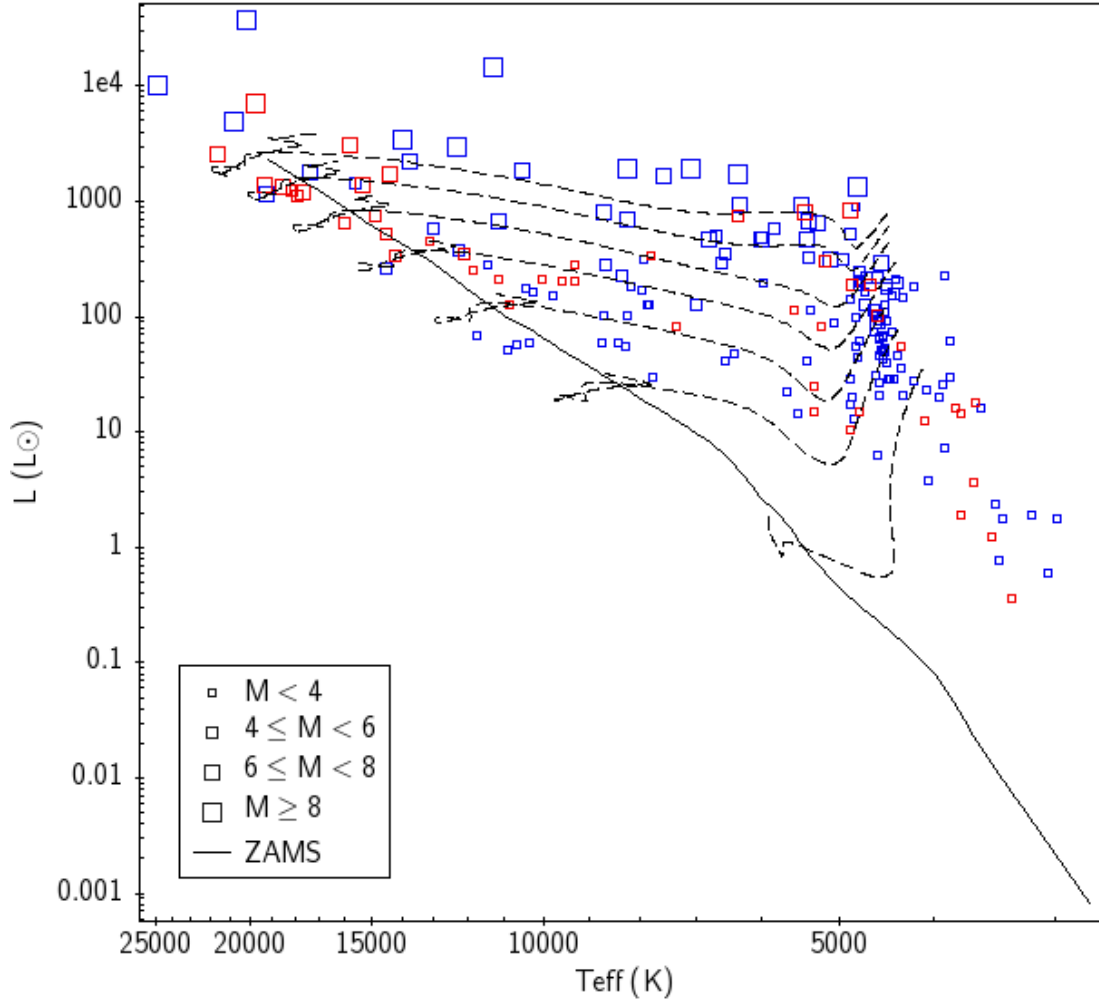


Figure 4.13: HR diagram for our sources. Symbol size corresponds to different mass bins, as shown in the legend, where $M = M_{\star}/M_{\odot}$. The dashed lines (from bottom to top) are the PMS tracks for 1, 2, 3, 4, 5, 6, and 7 M_{\odot} , the filled line is the ZAMS. Blue and red symbols are, respectively, EGOs and non-EGOs. From Teixeira et al. (2018).

contracting and beginning the main sequence. Furthermore, the position of sources in the diagram shows consistency between modeled mass and that of the PMS track.

Recent works, in particular those of Hosokawa et al. (2010), postulate that high-mass stars are bloated objects, and are thought to be pulsationally unstable or go through a period of significant pulsations on their way to settle on the ZAMS (Inayoshi et al., 2013). Furthermore, eruptive variable behavior recurs more frequently in the earlier stages of stellar PMS (Contreras Peña et al., 2017). The HR diagram shows non-EGOs, particularly the higher-mass ones occupying an area close to the ZAMS. These objects are more embedded and have larger ΔK_s than EGOs. These objects, closer to the ZAMS are candidate sources to test the bloated and pulsating young massive stars.

Considering that (Hosokawa et al., 2010) postulated that high-mass protostars become

bloated while under a burst of accretion, the eruptive sources occupying the ZAMS might be an indication of such an event. Most eruptive variables ($\sim 70\%$) occupy either the birth-line or ZAMS evenly split. Given the expected presence of a large envelope in objects on the birth-line, it is possible to conclude that variability in most MYSOs are a result of envelope accretion.

4.5 Conclusions

This study as shown unequivocally that variability is a common characteristic of MYSOs. The higher rate of variable objects in the EGO sample leads to a strong implication between accretion-driven outflow phenomena and observed photometric variability.

The catalog which was created during this study is a valuable tool for follow-up studies as it has increased the number of known variable MYSO candidates (~ 13) by one order of magnitude (~ 190). It can be combined with studies of other wavelength observations (e.g. maser observations) to further explore accretion-driven variability.

Chapter 5

Summary and Future Work

Among the various successes of this body of work we can count: the quantification of photometrically variable EGOs, an analysis of the overall periodic nature of their variability, the evolutionary difference between EGOs and other MYSOs variable candidates, the production of a catalog of variable MYSOs, obtaining an observational guideline to observe spectral variability in young high-mass stars, and testing a methodology to confirm that variability.

This thesis had a set of ambitious goals, with some of these being high-risk. We review here some of the valuable information that we were able to extract from the proposed exploratory work in the thesis proposal, even when the goals were not fully reached as had been hoped.

5.1 Spectroscopic variability

$\sigma Ori AB$ was observed using the high-resolution PARAS spectrograph- These observations were taken during multiple nights, several times per night or, two-three times per night over the course of a week. The analysis of the spectra showed some variations in the H- α and He_5875 lines with periods between 4 and 8 hours. The detections are too close to the noise level to be conclusive. A binary companion cannot explain them.

Using archival data of known variable O and B stars, we were able to successfully test our methodology and approach. The way our codes were designed and our experiment idealized, we were able to detect spectral variability in known variable stars. Upon further examination we were able to determine that the main difference between our $\sigma Ori AB$ and the archival data was the lower SNR of the $\sigma Ori AB$ observation. So our methodology has been validated and allowed us to determine observational constraints that future observing runs should have.

The best way to determine whether $\sigma Ori AB$ presents variability is to perform fur-

ther observations. An idealized observational campaign of $\sigma Ori AB$ would be performed in a high-resolution, stable spectrograph in the optical bands. Exposures times should be such as to ensure a minimum $SNR \sim 250$. And multiple observations should be done per night over a few consecutive nights. Ideally, the number of nightly observations should be $n > 10$. A campaign following the above constraints would be able to either confirm our tentative findings of spectral variability or show them to be noise.

It is clear that the current level of instrumentation has now reached the point where the study of spectral variability in massive O-stars is possible. The question of whether short-term spectral variability is present in young O-stars can now be answered with the right observational strategy, and our work can serve as a roadmap for future proposals. Furthermore, following the examples of other mass ranges, spectral variability can be used to infer the presence of asteroseismic modes in these stars.

The presence of ongoing accretion in young O-stars could be one of the explanations for any observed spectral variability in these timescales. Alternatively, as observed in some Be stars, sometimes the winds can form massive coronal mass ejections which would then fall back on to the stellar surface. This phenomena should be visible in the form of variability traveling through the different lines at different times given that each line probes the stellar atmosphere at different heights.

In the future, observational proposals of young massive O-stars, can use this work as a support tool to develop a good observing strategy.

5.2 Photometric Variability

This study has investigated the nature of near-infrared variability in MYSOs, focusing on the driving sources of EGOs and luminous $24 \mu\text{m}$ point sources coinciding within $5''$ of the massive star forming clumps mapped at $870 \mu\text{m}$ by ATLASGAL. The search led us to examine the K_s -band light-curves of 601 point sources.

- 190 sources (139 EGOs and 51 non-EGOs) were found to be variable with an $IQR > 0.05$ and $\Delta K_s > 0.15$. 111 and 79 of these objects are classified as periodic + aperiodic, respectively.
- The $2\mu\text{m}$ - $870\mu\text{m}$ spectral energy distribution of the variable point sources were assembled and fitted with YSO models. 47 and 6 sources were modeled as $\geq 4 M_\odot$ and $\geq 8 M_\odot$, respectively.

- On an HR diagram, most lower mass EGO sources concentrate along a putative birth-line.
- A high rate of detectable variability in EGO targets (139 out of 153 searched) implies that near-infrared variability in MYSOs is closely linked to the accretion phenomenon and outflow activity.

Further to the discovery of a dozen high-amplitude variable MYSOs (Kumar et al., 2016), this is the first large scale systematic study of near-infrared variability in MYSOs. The variable sources identified in this work are excellent targets with which to undertake follow-up studies to understand the circumstellar environment of MYSOs in detail.

The observed variability of these multiple MYSO sources, raises two major questions: a) is it connected with the current evolutionary status? b) is it observable at other wavelengths.

While there are some promising results involving some of the maser sources studied by Goedhart et al. (2014), a more extensive campaign can further probe the wavelengths presenting greater variability.

Given the results presented and the prevalence of periodic EGOs, a follow-up observational study might help to explain their periodic nature. It would also be an interesting exercise to predict the future magnitude of these periodic sources and try to match the prediction to observations. This comparison could help settle some of the cases where there is some ambiguity in the LC periodograms.

A follow-up study trying to determine the LCs of all Goedhart et al. (2014) maser sources and comparing them to the maser LC is ongoing.

5.3 Future prospects of variability research

The study of variability in young massive stars is of vital importance to the study of accretion in massive stars. After summarizing the main results of this thesis, we want to devote some time to discuss what we see as the way forward for the topic and the field.

A new generation of higher-resolution and more stable spectrographs is emerging both in the optic (e.g. ESPRESSO) and the NIR (e.g. SPIRou). These instruments, when coupled with good observing strategies will allow the detection, or lack thereof, of spectral variability in young massive stars. This technique can be powerful, especially in the NIR, as it allows to probe deeper into SF regions and, therefore, to study younger stars. In order to take full advantage of these facilities, researchers should be specific in their proposals regarding the time and SNR constrains in which these observations should take place.

On the other hand, we have barely scratched the surface of the extended photometric datasets produced by surveys such as VVV. The greatest difficulty, in this context, is identifying reliable MYSO target candidates. Maser variability studies tend to have large beam-sizes, a problem which is prevalent in most larger wavelengths observations. So, there should be an effort to distinguish which sources in the area corresponding to the large-wavelength beam-size are in fact young MYSOs, either by using spectroscopic classification or by using color-color diagrams. Once a suitable identification of the MYSO sources responsible for the observed masers is performed, their photometric variability should be studied. Recent testing has also suggested that using larger aperture photometry from the VVV (aperMag3, aperMag4, aperMag5) might be more suitable for MYSO targets as they tend to be extended in the NIR. If a source is found to be periodically variable, a determination of the period allows the planning of follow-up observations. A well-determined periodicity enables a prediction of brightness at the time of the follow-up observation, thus validating or invalidating the determined period.

Recent works, such as Pieringer et al. (2019), show the importance of improving machine learning methods which highlight interesting sections of LCs presenting significant variability. These types of machine learning techniques have the advantage of, potentially being, applicable to large datasets such as the VVV survey. In particular, the research of young massive stars, will be able to make use of increased data-sets and, using these new machine learning techniques, answer the question of the nature of accretion in these objects. Finally, we expect that within the next decade, these advances, can finally answer the question of how massive stars gain their masses.

5.4 The challenging nature of Big Data and the need for adaptation

A recurring theme throughout this work is that big data problems and tools which, until recently, were restricted to computer sciences, are becoming commonplace in astronomy research. A cursive knowledge of programming is no longer sufficient for astronomers to perform data reduction and analysis, so astronomy curricula need to include more computer science-based courses, such as data handling, database structure and coding to name a few. Until recently, simple coding strategies were sufficient since, regardless of code-efficiency, computation times tended to be small as a result of the small size of the datasets used in astronomy. But such codes will need to be re-engineered because of the larger volume of data resulting from recent large surveys and high-resolution instrumen-

tation.

It is no longer efficient for each astronomer to develop and optimize codes on an individual level. Recent community efforts to produce and share codes (e.g. the Astropy team) try to address this issue but are not sufficient. If astronomy institutions provide support and funds to dedicated computer scientists and code developers in their research teams, researchers can be left to freely perform data analysis/research full-time.

We can confidently look to a very positive and exciting future in scientific research. The Big Data era has arrived, and with it, the promise of long-sought out answers which can only be obtained with large volumes of data.

Bibliography

- Adams, F. C., Lada, C. J., & Shu, F. H. 1987, *ApJ*, 312, 788
- Aerts, C., Puls, J., Godart, M., & Dupret, M.-A. 2009, *A&A*, 508, 409
- Aerts, C., Christensen-Dalsgaard, J., & Kurtz, D. W. 2010, *Asteroseismology*, Astronomy and Astrophysics Library. ISBN 978-1-4020-5178-4. Springer Science+Business Media B.V., 2010, p.,
- Aerts, C. 2015, *IAU Symposium*, 307, 154
- André, P. 1994, *The Cold Universe*, 179
- Audard, M., Ábrahám, P., Dunham, M. M., et al. 2014, *Protostars and Planets VI*, 387
- Bally, J., Aguirre, J., Battersby, C., et al. 2010, *ApJ*, 721, 137-163
- Bernasconi, P. A., & Maeder, A. 1996, *A&A*, 307, 829
- Bertaux, J. L., Lallement, R., Ferron, S., Boonne, C., & Bodichon, R. 2014, *A&A*, 564, A46
- Bouvier, J., Grankin, K. N., Alencar, S. H. P., et al. 2003, *A&A*, 409, 169
- Broos, P. S., Getman, K. V., Povich, M. S., et al. 2013, *ApJS*, 209, 32
- Caratti o Garatti, A., Stecklum, B., Linz, H., Garcia Lopez, R., & Sanna, A. 2015, *A&A*, 573, A82
- Caratti o Garatti, A., Stecklum, B., Garcia Lopez, R., et al. 2017, *Nature Physics*, 13, 276
- Carey, S. J., Noriega-Crespo, A., Mizuno, D. R., et al. 2009, *PASP*, 121, 76
- Castor, J. I., Abbott, D. C., & Klein, R. I. 1975, *ApJ*, 195, 157
- Caswell, J. L., Fuller, G. A., Green, J. A., et al. 2010, *MNRAS*, 404, 1029
- Chakraborty, A., Mahadevan, S., Roy, A., et al. 2010, *Proc. SPIE*, 7735, 77354N

- Chambers, E. T., Yusef-Zadeh, F., & Ott, J. 2014, *A&A*, 563, A68
- Chen, X., Gan, C.-G., Ellingsen, S. P., et al. 2013, *ApJS*, 206, 9
- Chen, X., Gan, C.-G., Ellingsen, S. P., et al. 2013, *ApJS*, 206, 22
- Christensen-Dalsgaard, J. 2008, *IAU Symposium*, 252, 135
- Conti, P. S., & Ebbets, D. 1977, *ApJ*, 213, 438
- Contreras, Y., Schuller, F., Urquhart, J. S., et al. 2013, *A&A*, 549, A45
- Contreras Peña, C. E. 2015, Ph.D. Thesis
- Contreras Peña, C., Lucas, P. W., Minniti, D., et al. 2017, *MNRAS*, 465, 3011
- Contreras Peña, C., Lucas, P. W., Kurtev, R., et al. 2017, *MNRAS*, 465, 3039
- Cross, N. J. G., Collins, R. S., Mann, R. G., et al. 2012, *A&A*, 548, A119
- Csengeri, T., Leurini, S., Wyrowski, F., et al. 2016, *A&A*, 586, A149
- Cyganowski, C. J., Whitney, B. A., Holden, E., et al. 2008, *AJ*, 136, 2391-2412
- de Villiers, H. M., Chrysostomou, A., Thompson, M. A., et al. 2015, *MNRAS*, 449, 119
- Dunham, M. M., & Vorobyov, E. I. 2012, *ApJ*, 747, 52
- Dunham, M. M., Stutz, A. M., Allen, L. E., et al. 2014, *Protostars and Planets VI*, 195
- Eiroa, C., Oudmaijer, R. D., Davies, J. K., et al. 2002, *A&A*, 384, 1038
- Figueira, P. 2010, Ph.D. thesis, University of Geneva, Observatory of the University of Geneva
- Figueira, P., Santos, N. C., Pepe, F., Lovis, C., & Nardetto, N. 2013, *A&A*, 557, A93
- Fullerton, A. W., Gies, D. R., & Bolton, C. T. 1996, *ApJS*, 103, 475
- Goedhart, S., Maswanganye, J. P., Gaylard, M. J., & van der Walt, D. J. 2014, *MNRAS*, 437, 1808
- Grave, J. M. C., & Kumar, M. S. N. 2009, *A&A*, 498, 147
- Gray, D. F. 2005, *The Observation and Analysis of Stellar Photospheres*, 3rd Edition, ISBN 0521851866. , UK: Cambridge University Press, 2005

- Gutermuth, R. A., & Heyer, M. 2015, *AJ*, 149, 64
- Hampel, F. R. 1974 The influence curve and its role in robust estimation, *Journal of the American Statistical Association*, 69 (346) , pp. 383-393
- Hartmann, L., Kenyon, S. J., & Calvet, N. 1993, *ApJ*, 407, 219
- Hayashi, C. 1966, *ARA&A*, 4, 171
- Herbst, W., & Shevchenko, V. S. 1999, *AJ*, 118, 1043
- Heyer, M., Gutermuth, R., Urquhart, J. S., et al. 2016, *A&A*, 588, A29
- Hosokawa, T., Yorke, H. W., & Omukai, K. 2010, *ApJ*, 721, 478
- Howarth, I. D., Siebert, K. W., Hussain, G. A. J., & Prinja, R. K. 1997, *MNRAS*, 284, 265
- Huchra, J. P., Macri, L. M., Masters, K. L., et al. 2012, *ApJS*, 199, 26
- Hunter, T. R., Brogan, C. L., MacLeod, G., et al. 2017, *APJL&A*, 837, L29
- Isella, A. 2006, Ph.D. Thesis, Universita degli Studi di Milano, Milano, Italy
- Inayoshi, K., Sugiyama, K., Hosokawa, T., Motogi, K., & Tanaka, K. E. I. 2013, *APJL&A*, 769, L20
- Kenyon, S. J., Hartmann, L. W., Strom, K. M., & Strom, S. E. 1990, *AJ*, 99, 869
- Kenyon, S. J., & Hartmann, L. 1995, *ApJS*, 101, 117
- Kesseli, A. Y., Petkova, M. A., Wood, K., et al. 2016, *ApJ*, 828, 42
- Kholtygin, A. F., & Sudnik, N. P. 2016, *MNRAS*, 458, 1604
- Kippenhahn, R., & Weigert, A. 1990, *Stellar Structure and Evolution*, XVI, 468 pp. 192 figs.. Springer-Verlag Berlin Heidelberg New York. Also *Astronomy and Astrophysics Library*, 192
- König, C., Urquhart, J. S., Csengeri, T., et al. 2017, *A&A*, 599, A139
- Kremer, J., Stensbo-Smidt, K., Gieseke, F., Steenstrup Pedersen, K., & Igel, C. 2017, [arXiv:1704.04650](https://arxiv.org/abs/1704.04650)
- Krticka, J., & Feldmeier, A. 2018, [arXiv:1807.09407](https://arxiv.org/abs/1807.09407)

- Krumholz, M. R., McKee, C. F., & Klein, R. I. 2005, *APJL&A*, 618, L33
- Krumholz, M. R., Klein, R. I., McKee, C. F., Offner, S. S. R., & Cunningham, A. J. 2009, *Science*, 323, 754
- Krumholz, M. R. 2015, *Very Massive Stars in the Local Universe*, 412, 43
- Krumholz, M. R. 2015, *Notes on Star Formation*, by MarK Krumholz, published as part of the open astrophysics bookshelf <http://open-astrophysics-bookshelf.github.io/>
- Kuiper, R., Klahr, H., Beuther, H., & Henning, T. 2010, *ApJ*, 722, 1556
- Kumar, M. S. N., & Grave, J. M. C. 2007, *A&A*, 472, 155
- Kumar, M. S. N., Contreras Peña, C., Lucas, P. W., & Thompson, M. A. 2016, *ApJ*, 833, 24
- Kupka, F., Piskunov, N., Ryabchikova, T. A., Stempels, H. C., & Weiss, W. W. 1999, *A&A*, 138, 119
- Lada, C. J. 1987, *Star Forming Regions*, 115, 1
- Larson, R. B. 1969, *MNRAS*, 145, 271
- Larson, R. B., & Starrfield, S. 1971, *A&A*, 13, 190
- Larson, R. B. 1981, *MNRAS*, 194, 809
- Lewis, J. R., Irwin, M., & Bunclark, P. 2010, *Astronomical Data Analysis Software and Systems XIX*, 434, 91
- Li, G.-X., Urquhart, J. S., Leurini, S., et al. 2016, *A&A*, 591, A5
- Lucas, P. W., Hoare, M. G., Longmore, A., et al. 2008, *MNRAS*, 391, 136.
- Makin, S. V., & Froebrich, D. 2018, *ApJS*, 234, 8
- Markova, N., Puls, J., Scuderi, S., Simón-Díaz, S., & Herrero, A. 2011, *A&A*, 530, A11
- Martins, F., Marcolino, W., Hillier, D. J., Donati, J.-F., & Bouret, J.-C. 2015, *A&A*, 574, A142
- Martins, F., & Palacios, A. 2017, *A&A*, 598, A56
- Martins, F. 2018, *A&A*, 616, A135

- McKee, C. F., & Offner, S. S. R. 2010, *ApJ*, 716, 167
- Medina, N., Borissova, J., Bayo, A., et al. 2018, arXiv:1806.04061
- Melo, C. H. F. 2001, Ph.D. thesis, University of Geneva, Observatory of the University of Geneva
- Meyer, D. M.-A., Vorobyov, E. I., Kuiper, R., & Kley, W. 2017, *MNRAS*, 464, L90
- Meyer, D. M.-A., Vorobyov, E. I., Kuiper, R., & Kley, W. 2017, arXiv:1710.02320
- Miller, G. E., & Scalo, J. M. 1979, *ApJS*, 41, 513
- Minniti, D., Lucas, P. W., Emerson, J. P., et al. 2010, *New A*, 15, 433
- Morales-Calderón, M., Stauffer, J. R., Hillenbrand, L. A., et al. 2011, *ApJ*, 733, 50
- Myers, P. C. 2010, *ApJ*, 714, 1280
- Ochsenbein, F., Bauer, P., & Marcout, J. 2000, *A&A*, 143, 23
- Ochsendorf, B. B., Cox, N. L. J., Krijt, S., et al. 2014, *A&A*, 563, A65
- Palacios, A., Gebran, M., Josselin, E., et al. 2010, *A&A*, 516, A13
- Pepe, F., Mayor, M., Galland, F., et al. 2002, *A&A*, 388, 632
- Perryman, M. A. C. 2005, *Astrometry in the Age of the Next Generation of Large Telescopes*, 338, 3
- Peters, T., Banerjee, R., Klessen, R. S., & Mac Low, M.-M. 2011, *ApJ*, 729, 72
- Pieringer, C., Pichara, K., Catelán, M., et al. 2019, *MNRAS*, 484, 3071.
- Pilbratt, G. L., Riedinger, J. R., Passvogel, T., et al. 2010, *A&A*, 518, L1
- Piskunov, N. E., Kupka, F., Ryabchikova, T. A., Weiss, W. W., & Jeffery, C. S. 1995, *A&A*, 112, 525
- Puls, J. 2008, *Massive Stars as Cosmic Engines*, 250, 25
- Robitaille, T. P., Whitney, B. A., Indebetouw, R., Wood, K., & Denzmore, P. 2006, *ApJS*, 167, 256
- Robitaille, T. P., Whitney, B. A., Indebetouw, R., & Wood, K. 2007, *ApJS*, 169, 328
- Robitaille, T. P., Meade, M. R., Babler, B. L., et al. 2008, *AJ*, 136, 2413

- Roy, A., Mahadevan, S., Chakraborty, A., Pathan, F. M., & Anandarao, B. G. 2010, *Bulletin of the American Astronomical Society*, 42, 421.07
- Ryabchikova, T., Piskunov, N., Kurucz, R. L., et al. 2015, *Phys. Scr*, 90, 054005
- Salaris, M., & Cassisi, S. 2005, *Evolution of Stars and Stellar Populations*, by Maurizio Salaris, Santi Cassisi, pp. 400. ISBN 0-470-09220-3. Wiley-VCH , December 2005.,
- Scargle, J. D. 1982, *ApJ*, 263, 835
- Schaefer, G. H., Hummel, C. A., Gies, D. R., et al. 2016, *AJ*, 152, 213.
- Schou, J. 2018, arXiv:1806.01055
- Schuller, F., Menten, K. M., Contreras, Y., et al. 2009, *A&A*, 504, 415
- Shetty, R., Beaumont, C. N., Burton, M. G., Kelly, B. C., & Klessen, R. S. 2012, *MNRAS*, 425, 720
- Shu, F. H. 1977, *ApJ*, 214, 488
- Siess, L., Dufour, E., & Forestini, M. 2000, *A&A*, 358, 593
- Simón-Díaz, S., Herrero, A., Uytterhoeven, K., et al. 2010, *APJL&A*, 720, L174
- Simón-Díaz, S., Caballero, J. A., & Lorenzo, J. 2011, *ApJ*, 742, 55
- Simón-Díaz, S., & Herrero, A. 2014, *A&A*, 562, A135
- Simón-Díaz, S., Herrero, A., Sabín-Sanjulián, C., et al. 2014, *A&A*, 570, L6
- Simón-Díaz, S. 2015, *IAU Symposium*, 307, 194
- Smith, L. C., Lucas, P. W., Kurtev, R., et al. 2018, *MNRAS*, 474, 1826
- Sokolovsky, K. V., Gavras, P., Karampelas, A., et al. 2017, *MNRAS*, 464, 274
- Stahler, S. W., & Palla, F. 2005, *The Formation of Stars*, by Steven W. Stahler, Francesco Palla, pp. 865. ISBN 3-527-40559-3. Wiley-VCH , January 2005.
- Struve, O. 1952, *PASP*, 64, 117
- Sudnik, N. P., & Henrichs, H. F. 2016, arXiv:1606.00404
- Takami, M., Chen, H.-H., Karr, J. L., et al. 2012, *ApJ*, 748, 8
- Tan, J. C., Beltrán, M. T., Caselli, P., et al. 2014, *Protostars and Planets VI*, 149

- Teixeira, G. D. C., Kumar, M. S. N., Smith, L., et al. 2018, *A&A*, 619, A41
- Upton, G., Cook, I., 1996, *Understanding Statistics*. Oxford University Press.
- Urquhart, J. S., Moore, T. J. T., Schuller, F., et al. 2013, *MNRAS*, 431, 1752
- Urquhart, J. S., Moore, T. J. T., Csengeri, T., et al. 2014, *MNRAS*, 443, 1555
- Urquhart, J. S., Csengeri, T., Wyrowski, F., et al. 2014, *A&A*, 568, A41
- Urquhart, J. S., K"onig, C., Giannetti, A., et al. 2018, *MNRAS*, 473, 1059
- VanderPlas, J. T. 2017, *arXiv:1703.09824*
- Vorobyov, E. I., & Basu, S. 2006, *ApJ*, 650, 956
- Vorobyov, E. I., & Basu, S. 2008, *APJL&A*, 676, L139
- Vorobyov, E. I., & Basu, S. 2015, *ApJ*, 805, 115
- Wenger, M., Ochsenbein, F., Egret, D., et al. 2000, *A&A*, 143, 9
- Wienen, M., Wyrowski, F., Menten, K. M., et al. 2015, *A&A*, 579, A91
- Zapata, L. A., Leurini, S., Menten, K. M., et al. 2008, *AJ*, 136, 1455
- Zhu, Z., Hartmann, L., & Gammie, C. 2009, *ApJ*, 694, 1045
- Zima, W. 2008, *Communications in Asteroseismology*, 157, 387

Appendix A

Additional materials

The following Appendix materials concern the thesis work and supplement the information presented above. It is subdivided into:

- Tables - Information of the observations, MYSO target summaries, photometric data used to produce SEDs, and the best fitted SEDs
- Figures - includes additional spectral variability plots, the produced LCs, periodograms and color plots, and SEDs

A.1 Tables

This supplement shows the full tables of data of the studied sources. There are two main tables presented here, the photometric information used to produce the SEDs (Tab. A.1), and the parameters of the best fitted SED (Tab. A.2). They are reproduced here for completeness.

Table A.1: Input data to build the SEDs.

Source	J (mJy)	H (mJy)	K_s (mJy)	[3.6] (mJy)	[4.5] (mJy)	[5.8] (mJy)	[8.0] (mJy)	[24] (mJy)	70 (mJy)	160 (mJy)	250 (mJy)	350 (mJy)	500 (mJy)	870 (mJy)
MG002.5577-00.7510				3.73	7.91	10.15	13.15	88.48	931.42	4905.53				1220
MG003.5016-00.2020								53.51						2380
MG006.2185-00.5837			7.18	121.61	224.36	367.37	551.90	3801.94	29697.80	28396.90	26346			4330
MG006.9222-00.2512				20.80	90.98	232.43	329.81	882.17	12654.10	38301.50	53000	45976		8180
MG300.3241-00.1985		0.86	7.18	53.97	123.87	189.28	268.57	712.49	4438.84	11381.30	22095	11587		2280
MG303.9304-00.6879					23.19	25.32	33.84	2739.57	138174	185408	128313	85812		11300
MG305.5101+00.3661			1.82	9.52	22.56	38.40	42.64	162.77	2620.13	7523.15		53309		6680
MG306.1352+00.1330					3.05			172.43	27512.50	60414.60		23380		5290
MG306.5029+00.0731		0.79	7.53	42.01	83.36	115.11	147.32	522.71	2430.10	6373.91	13913			2290
MG313.2760-00.7111				3.71	17.95	31.56	52.66	427.45	4786.08	9590.67	15964			2110
MG317.4777-00.3504			1.71	32.79	66.09	144.51	182.58	707.45	10028.50	32078.80	45655	18946		1210
MG317.5959+00.0527			1.26	26.24	72.34	148.42	198.18	701.04	1180.58	4478.29	19088	22306		2930
MG322.4833+00.6447				1.33	2.35	2.88	2.85	7.93						10110
MG326.7241+00.3552				3.45	12.22	16.30	18.21	85.68	301.20	17519.20		19130	7457	1850
MG326.9250-00.5141				0.98	4.22	13.61	15.53	135.96	7448.96					3660
MG328.0494-00.0487		1.54	13.48	155.94	285.59	435.61	464.15	2018.76	24265.20	35206.80	39668			3590
MG328.6141-00.4657				2.34	6.85	7.99	7.68	22.20	209.66	22135.10				3310
MG331.5722-00.2290			26.30	236.46	565.65	813.39	827.68	1396.53	4782.94	20685.70		26652		4110
MG331.8302+00.0360				14.72	33.06	59.03	82.16	135.46			12790			3840
MG332.1534+00.0069				1.42	3.13	1.90		56.73						3080
MG332.1990+00.5957				13.58	9.67	10.08	13.84	11.19						4840

(To be continued)

Table A.1 (continued)

Source	J (mJy)	H (mJy)	K_s (mJy)	[3.6] (mJy)	[4.5] (mJy)	[5.8] (mJy)	[8.0] (mJy)	[24] (mJy)	70 (mJy)	160 (mJy)	250 (mJy)	350 (mJy)	500 (mJy)	870 (mJy)
MG332.3652+00.6046			2.13	32.22	93.19	178.77	198.73	1093.67			76936	43824	26921	9120
MG332.6662+00.0271				2.16	4.79	7.58	8.34	14.98					6044	890
MG333.0294-00.0149				6.56	16.51	20.89	9.23	292.04	27811.20	41602.20	25085			5120
MG333.2025+00.2940				4.08	15.25	9.06	2.97	305.47	12080.60	21664.80	28060	15920		3440
MG335.2667-00.0151				6.60	25.22	48.03	71.43	226.50	660.41	2015.61				2710
MG335.6100-00.7866					73.07		229.86	1327.16	20213.40	37646	33145	13321		930
MG335.6172-00.2001			3.36	35.27	95.01	214.14	291.25	773.37	1389.56					10300
MG336.8585-00.1903	1.08	2.35	3.87	8.55	14.92	29.81	42.29	62.42		4506.41				6150
MG337.9402-00.5325			6.80	26.80	64.47	69.74	86.75	276.04	2213.37	64023.90				8980
MG338.6328+00.0265	2.95	4.91		126.87	228.32	339.70	406.88	1128.41	8571.15	16042.40	43690			1680
MG338.8438+00.4342				149.47	482.33	920.23	1002.45	3104.07	20310.60	32336.50	34513	15671	6669	1880
MG338.8762+00.5561				13.37	32.85	47.02	45.32	131.98			63243		7043	22130
MG339.2939+00.1387						19.64	55.14	923.61	49686.90	71753.20	74707	46068		2900
MG339.4040-00.4134			3.63	13.90	47.62	98.97	189.44	951.68	6469.26	14827.40				10830
MG339.5843-00.1282			6.69		101.05	144.51	124.01	4038.26	121413	266369	223023	111306	54780	16130
MG342.0988+00.8086				1.75	6.90	10.89	12.21	130.82	1550.22	4390.39	12081	10345		1680
MG342.3189+00.5876				0.67		26.84	61.75	760.19	15318.70	21494.80	27323	14944	8494	1890
MG343.3567-00.4032				1.75	5.11	7.73	9.48	34.81	381.66	4071.62				4780
MG343.4049-00.4007				8.86	25.95	42.53	51.60	153.58	928.84	9710.23			12856	2260
MG345.0737-00.1953			1.39	11.71	16.21	22.18	20.98	8.27			50908			6570
MG345.2198-00.1367				4.59	11.46	15.05	20.62	49.25	316.50	753.48				1790

(To be continued)

Table A.1 (continued)

Source	J (mJy)	H (mJy)	K_s (mJy)	[3.6] (mJy)	[4.5] (mJy)	[5.8] (mJy)	[8.0] (mJy)	[24] (mJy)	70 (mJy)	160 (mJy)	250 (mJy)	350 (mJy)	500 (mJy)	870 (mJy)
MG345.5764-00.2252				4.99	9.69	13.19	9.69	18.08	2030.97	10244.90	30095			4300
MG347.0800-00.3962				20.18	44.44	33.32	13.66	3413.21	87651.20	113690				4920
MG347.7561+00.2323				11.08	22.05	37.73	36.36	71.83	2794.66			35983		6030
MG351.8098+00.6433				61.23	213.67	451.13	397.25	662.58	10945.60	45516.50	81681	44269	26694	18940
MG351.8655-00.2246				3.18	6.04	9.03	6.78	317.35	6178.35	7583.99	19341			2790
MG352.0746-00.3874				1.12	3.84	5.69		90.56	6307.34	15580.70				2630
MG352.2452-00.0636				8.36	31.96	54.99	51.27	642.38	27139.10	25412.50		50847	41630	8720
MG352.6040-00.2253				1.58	6	13.12	9	310.34	12433.80	31817.30	54283	63917		16150
MG353.3418-00.2890			3.88					2732.81	9306.65	16015.40	36109	24237	28484	33570
MG354.4384+00.4185				9.34	30.41	25.56	26.83	2564.40	45320.10	40166	24670	13391		19410
MG354.6995+00.5229								229.57	1076.48	9777.30	30068			4680
MG356.5212+00.2141				38.46	111.42	194.58	225.04	1410.31	4161.91	9780.13	15230	14773	13883	5540
MG357.5328+00.2366			10.08	157.67	435.86	571.61	572.61	2690.73	15212.90	19767	23201	16127		1800
MG358.0590-00.4698				9.42	23.58	36.03	47.32	481.46	1425.39	3442.07		27180		7550
MG358.4604-00.3929					6.40	10.78	4.69	457.07	127315	400983	332122	187402		28970
G9.83-1.05	1.43	1.80	1.12	12.30	19.50	25.30	22.70	220.10						
G9.81-1.06				6.10	25.90	18.50	15.20				9159			
G9.62+0.20				84.30	322.90	675.20	1083.40		177790					
G8.73-0.37	1.27	3.05	3.14	4.20	14.50	20.60	14.40	707.40	26093.90	21879.10				
G8.72-0.36	0.51	1.17	3	11.90	27.90	25.50	13.70	934.70	17224.10	26429.70				
G8.70-0.37	3.01	8.09	10.04	8.80	28.90	46.20	38.60	478.10	9620.31	42757				

(To be continued)

Table A.1 (continued)

Source	J (mJy)	H (mJy)	K_s (mJy)	[3.6] (mJy)	[4.5] (mJy)	[5.8] (mJy)	[8.0] (mJy)	[24] (mJy)	70 (mJy)	160 (mJy)	250 (mJy)	350 (mJy)	500 (mJy)	870 (mJy)
G8.66-0.37	0.45	1.74	8.96	155.20	486.80	784.20	775.90	4595.60	53153.30	61003.30	37794			
G8.27+0.51	2.14	3.24	3.74	12.70	42.70	80.80	75.30	640	25575.10	47433.20	38677	19168		1320
G6.19-0.36	28.53	60.13	23.63	44.40	139.10	159.50	96.60	7064.80	573327	657804	470913	208496	94673	27050
G5.88-1	0.35	1.30	2.76	9.70	20.70	23	12.60	426.20	18341.40	24488.90	21423	22553	9868	5300
G5.62-0.08	2.75	3.69	0.45	1.90	8.20	10.90	1.20	48.40				73421	43526	
G4.89-0.13	1.70	1.79	2.69	11.70	36.30	45	29.70	870.60	27668.30	47441.80	40298			
G4.83+0.23	0.71	3.27	12.10	226.80	523.40	770.32	897.10		435407	360055	200859	89376	34765	10600
G4.63-0.67	3.14	8.97	0.26	10.80	20.40	22.40	18.20	140.10	415.46	10826.50	17460	12163		4180
G359.44+0.10	2.17	2.68	1.43	64.60	250	370.30	229.10		736154	1064810				118900
G358.84+0.74				16.70	29.50	39.20	51.90	1353.60	36006	88604.40	43699	23619		9410
G358.46-0.39(b)			0.44	5.40	16.50	23.90	5.50	142.50	127315	400983	332122	187402	104546	28970
G358.39-0.48			1.79	163.70	432.60	872.70	1570.50		1366660	853627	433860	236659		
G358.26-2.06	0.83	2.84	22.26	136	298.20	346.60	269							
G357.52+0.20			0.81	45.80	109.90	184.90	198.70	794.60	15066	36280.70	42341	35965	24403	7850
G356.37+0.57				21.20	83.70	92	48.40	2918.90	119546	142002	94839	54368		5290
G355.75-0.87	9.61	7.73	5.48	12.30	21.90	29.30	27.30	54.70	383.61	3613.48	5072	9498		
G355.75+0.65				19.10	29	35.10	20.10							
G355.54-0.10	0.74	4.13	7.34	78.90	176.60	298.70	409.70		298411	218012	102269	52536		5420
G355.41+0.10			0.93	19.80	60.80	87.40	58.10	344.70		55819.70	76051			
G355.24+0.37				8.70	25.90	34.60	27.90	684.90	27503.40	41150.10				
G355.19-0.08	1.40	1.85	0.74	23.50	37.20	47.60	33.60	44						

(To be continued)

Table A.1 (continued)

Source	J (mJy)	H (mJy)	K_s (mJy)	[3.6] (mJy)	[4.5] (mJy)	[5.8] (mJy)	[8.0] (mJy)	[24] (mJy)	70 (mJy)	160 (mJy)	250 (mJy)	350 (mJy)	500 (mJy)	870 (mJy)
G355.18-0.42	1.75	2.46	3.07	22.40	114.60	171.70	145.60	1781.40	57761.10	203153	210207	116253	79554	
G354.78+0.83			0.85	22.60	35.40	43.80	51.40	220.40	3511.06	10507.40	14413			
G354.71+0.29	0.99	2.88	6.21	10	19.90	31.10	36.80							15290
G353.58+0.66	0.08	0.15	2.45	36.40	92.20	125.20	125.20	925.50	12030.50	77682.70	76820	41035	23248	11470
G353.46+0.56	0.30	1.10	7.05	78.30	213.10	205.30	155.70		318940	380847				11050
G353.40-0.07	0.56	0.88	1.61	17.10	50.50	58.50	58.70	82.30	2612.60					
G352.63-1.07	0.10	1.52	1	1268.20	3762.40	7861.60	8920.50		1281730					43170
G352.61-0.23	0.14	0.27	0.77	26.20	49.40	56.70	101.20	249	12433.80	31817.30	54283	63917	23433	
G352.60-0.19	2.03	2.81	3.68	14.10	31.50	32.70	27.20		30949.50	53028.60			41328	
G352.58-0.18	0.25	0.98	2.54	15.20	32.30	80.30	155.80		232010	194616	115440			
G352.52+0.77				9.70	20	27.90	26.80	159.10	4605.58					
G352.52+0.76	0.06	0.41	0.46	30.20	51.30	51.80	42.10	1541.10	22437.80	22098.60				
G352.32-0.44	0.35	1.16	19	625.40	1770.80	3265.40	3339.70		1191020	916238	672597	239960		23830
G352.13-0.94	0.32	2.52	13.80	113	365.70	468.60	452.60		266311	259550	150534			
G351.80-0.45			0.17	14.90	35.40	33	15.40		19075.90					35450
G351.78-0.54	5.14	5.70	6.44	232.40	721.20	936.80	910.50		9008490	6513640			644242	
G351.76-0.54				7.80	37.70	54.10	99.60							
G351.69+0.17	1.02	2.29	0.72	39.10	62.40	111.50	151.60	2583.60	75212.60	85038.50	61160			
G351.54-0.57			0.29	29	53.50	87.70	100.70	190.90						
G351.53+0.71	0.12	0.56	1.59	18	47	77.20	90.30	262.70	2529.02					
G351.53+0.70				17.10	86.70	169.90	172.70	1065.10	11067.90					

(To be continued)

Table A.1 (continued)

Source	J (mJy)	H (mJy)	K_s (mJy)	[3.6] (mJy)	[4.5] (mJy)	[5.8] (mJy)	[8.0] (mJy)	[24] (mJy)	70 (mJy)	160 (mJy)	250 (mJy)	350 (mJy)	500 (mJy)	870 (mJy)
G351.38-0.18				16.70	51.30	103.90	152.60	3520.70	49573.10	72878.40	54369	23906		2580
G351.27+1.04	0.23	0.42	1.45	6.80	32.90	73.90	53.30		1149.33					
G351.16+0.69	5.32	49.56	200.78	1433.80	4101.60	4883.70	4673.20							
G351.05-0.39				11.60	24.30	36.90	27.30	49.40		10777.90	16824	12397		
G351.02-0.86				84.50	193.10	278.70	297.60	2641.40	37877.20	51539.60	45848			
G350.75+0.68	0.15	1.76	7.27	38.30	67.20	74	73	3456.20	26490.20	21461.40	13507	8797		
G350.52-0.35	0.53	1.23	4.19	92.20	235.40	509.10	642	2062.60	48195.30					
G350.41-0.07				4.90	11.30	12.20	6.80	31.80	2044.49	21969.60	35733	28924		
G350.36-0.07				9.30	24	18.80	4.70	987.20	56118.30	61175.50	37212	18065		2190
G350.33+0.10	0.76	2.38	8.07	68.90	181.90	488.10	1370.10		832396	739052	420158	161725		
G350.02-0.52				6.80	17.60	29.50	17.80							
G349.64-1.09				0.16	114	340.30	923		142999	193490	167701	77680		
G349.63-1.10(b)	4.14	3.94	3.68	17.50	34.30	45.10	43.80							
G349.63-1.10(a)	0.87	2.91	13.17	41.30	75.80	79.70	60.60							
G349.62-1.11	1.71	1.77	1.76	22.20	65.70	107.60	132.10		2752.99	7217.72				
G349.62-0.20				1.69	5.30	4.10	6.90	97.10	15017.30	24005.10	19841	11182	9563	2020
G348.58-0.92	3.36	3.89	6.10	75.90	216.80	246	154.20	5098.80	191476	214113	210360			28970
G348.17+0.46				14.30	44.40	92	145.90	2432.50	61994.70	111104				12300
G347.08-0.40	0.86	4.80	12.59	51.20	100.70	101.80	51.80	2286.40	87651.20	113690				4920
G344.58-0.02				58	205.80	320	430.10	12302.60	815212	505481	224157	84320		7310
G344.21-0.62	0.26	2.49	16.75	111.50	272.80	358	320	1046.70	18201.30	50127.20				

(To be continued)

Table A.1 (continued)

Source	J (mJy)	H (mJy)	K_s (mJy)	[3.6] (mJy)	[4.5] (mJy)	[5.8] (mJy)	[8.0] (mJy)	[24] (mJy)	70 (mJy)	160 (mJy)	250 (mJy)	350 (mJy)	500 (mJy)	870 (mJy)
G343.78-0.24	0.09	0.52	1.58	23.30	50.30	39.70	15.40	2315.20	52517.10	76811.70				6770
G343.72-0.18(a)	0.79	1.74	11.74	33.60	60.20	55.30	32.60	905.60	17776.40	36648.60	70987			
G343.53-0.51(a)				13.10	62.40	88	75	621.60	11352.90	35043.10	82844	19859		
G343.50-0.47	0.17	0.67	3.85	44.40	204.90	301.20	216.70	3482.40	138502	199245	130416	63516		
G343.50+0.03	3.28	4.46	2.23	12.70	27.40	9.50	31.80	168.60	12338.80	71037.80	73215			
G343.42-0.33	0.09	0.59	4	36.80	74.60	122.40	141.90	298.70	2021.24	5060.20				
G343.40-0.40	0.21	1.71	5.67	17.30	34.50	47.60	40.20	94.40	928.84	9710.23			12856	2260
G343.19-0.08(a)	0.52	4.41	17.80	68.40	146	169.10	193.90	3732.10	34193.70	52532.90	52951	32225	26279	6800
G343.12-0.06	0.10	0.60	1.72	196.20	875.60	1254.90	796.60	19300.20						
G342.15+0.51	0.74	0.73	1.51	6.60	12.40	15.70	16.40	70.50	1420.09		15919	10094	10004	1170
G341.99-0.10			0.78	48.80	162	192.80	89.10	2304	39826.60	58830.50	43078	20185	11807	2870
G341.73-0.97	1.37	1.54	0.39	73.30	213.20	295.70	230.90	1184.90	10332.70	30776.80	36353	22838	16479	
G341.24-0.27				20.80	57.60	60.60	38	1189	62165.40	173692	168839	94719		
G341.23-0.27	13.33	11.75	7.92	6.70	14.20	18.80	13.60	70.30						
G341.20-0.26	0.45	1.62	7.52	23.30	32.30	33.80	15.50	49.40	820.63					
G340.75-1	0.27	1.10	2.99	101.30	239	336.40	552.60	17376	525318	379176				
G339.95-0.54				41.70	140.30	188.40	231.60	7877	399088	435963	285295			13140
G337.30-0.87	2.04	3.72	3.47	56.50	111.20	103.80	38.50	1356.20	74537.20	117284	93897	46990		4120
G337.16-0.39	0.10	0.27	9.74	228.30	536.90	1136.50	2237.20	5589						
G336.96-0.98	0.17	1.38	8.31	27.10	64.60	64.10	42	708.60	26979.10	74832.60	76629			10910
G336.87+0.29			0.18	21.80	66.60	62.10	39.20	612.70	7675.35	23705.50	33553			7430

(To be continued)

Table A.1 (continued)

Source	J (mJy)	H (mJy)	K_s (mJy)	[3.6] (mJy)	[4.5] (mJy)	[5.8] (mJy)	[8.0] (mJy)	[24] (mJy)	70 (mJy)	160 (mJy)	250 (mJy)	350 (mJy)	500 (mJy)	870 (mJy)
G335.59-0.29	0.11	1.20	3.62	132.10	483.80	466.70	111.30	10230	820905	1197480	477395			
G335.43-0.24			0.17	38	298.10	481.70	266.40	2380.30	128964	238070	164135	70651		19760
G334.25+0.07			0.52	8.80	23.40	24.10	8.70	201	17743.50	30110.80	23843	12333		1100
G334.04+0.35	1.56	1.98	3.84	31	101.90	171.80	218.70	2344.90	38882	83179.20	80936	43128	23568	
G332.94-0.69				44.70	215	336.70	354.90	2689.80	341385	452377	314833			11760
G332.91-0.55	1.13	1.90	1.03	14.50	47.40	42.50	8.40	240.20	40389.30	44024.20	46753	28034		4850
G332.81-0.70	0.46	2.40	5.74	63.20	182.20	178.60	180.90	3104.60	82921.10	127274	118693	76167		9360
G332.59+0.04(b)			0.25	7.90	20.50	27.20	41.10	38.10						
G332.59+0.04(a)				3.40	8.80	4.80	6	22.40			29333	9986		1950
G332.58+0.15				7.10	22	24.30	19.20	203.90	16003.50					
G332.56-0.15			0.74	20.70	51	34.60	21.10	782.40	27759.50	76661.80	114352	55331		13110
G332.47-0.52	0.62	2.61	5.58	149.50	420.90	1029.50	1898.50	8610.40	230815	399075				20360
G332.36+0.60	0.12	0.42	1.43	102.20	237.50	368.70	382.80	2216.90			76936	43824	26921	9120
G332.33-0.12	0.42	0.96	1.79	8.10	20.40	26.90	23.70	68.30						2610
G332.28-0.07				9.80	29.20	24.10	14.90	551.90	11479.70	23365.30	52437	65571		
G331.71+0.60	0.89	2.61	6.01	122.50	315.30	421.90	395.80	3720.80	262815	480505				21080
G331.71+0.58	1.81	6.78	8.84	10.70	26.50	16.60	10.60	245.50	97866.60	275609	210021			16380
G331.62+0.53			0.16	47.60	117.20	233.20	444.20	2955.70	79785					
G329.61+0.11	1.24	2.32	3.07	110.80	498.70	880.50	1431.70	8092.80	146103	128545	93253	45750		8010
G329.47+0.52	1.10	2.91	0.36	10.30	28.30	33.70	6.50	1167.90	19074	55495.40	49307			12230
G329.16-0.29	0.89	1.58	1.60	4.30	11.80	16	11.80	106.50	14013.10	58085	68623			4660

(To be continued)

Table A.1 (continued)

Source	J (mJy)	H (mJy)	K_s (mJy)	[3.6] (mJy)	[4.5] (mJy)	[5.8] (mJy)	[8.0] (mJy)	[24] (mJy)	70 (mJy)	160 (mJy)	250 (mJy)	350 (mJy)	500 (mJy)	870 (mJy)
G329.07-0.31(b)	0.26	1.01	2.10	57.50	322.80	795.30	1054.10	6590.20	189204	271610	270278	149892	79840	21390
G329.07-0.31(a)	0.79	2.81	8.15	79.80	277.90	423.40	424.40	4192.30	48243.90	42766.10				
G328.55+0.27	0.61	2.18	11.24	85.10	268.80	368.40	318.40	4483.80	91578.90	108836	73712	33341		4100
G328.14+0.43	0.81	3.89	1.59	64.90	146.90	127.80	23.80	2567.30	156612	153688	98685	43607		7740
G327.89+0.15				10.90	38.60	57.90	43.40	215	26982.10	114346				18650
G327.40+0.44	0.47	1.45	7.32	235.60	876.70	1964.70	2829.90	11960	1355290	1458480	931407	405404	164013	
G327.39+0.20	0.11	1.79	5.27	67.50	196.50	259.90	242.40	3322	160711	318233	238756			11510
G327.30+0.58				24.50	158.80	341.80	364.90	2589.10						
G327.12+0.51	0.39	1.45	15.95	365.30	964.50	2544.50	4347.80	19185.40	1235030	699293	378517	148699		
G326.86-0.67	1.68	2.10	0.77	13	35.80	62.80	13.60	130.90	53020	153152				
G326.80+0.51				3.70	10.20	5.80	6.70	10		5629.10	25416	15808		1850
G326.79+0.38	0.08	1.77	5.79	171	305	348.50	289.10	3762.90	185328	195318	144049			12530
G326.78-0.24	1.36	4.73	27.36	207.50	614.10	1085.60	1415.10	9509.50	220717	270607	221148	94074	41749	11380
G326.65+0.75	1.83	2.13	2.62	40.50	196.80	300.30	218.20	2110.80	56757.40	138162	129254	71528		14420
G326.61+0.80(c)	0.81	4.41	24.95	92.70	162.40	174.20	150.10	1816.60	75746.90	148005	138633			17100
G326.61+0.80(a)				20.20	72.90	115.60	181.70	2248.10	17708.30					
G326.57+0.20	0.78	1.27	1.30	4.40	17.90	25.30	16.80	273.40	37308.40	71863.20	56154	30573		2550
G326.41+0.93	0.25	0.76	2.37	75.70	323.60	468.20	333.40	2551.90	26244.60		266730			
G326.31+0.90	1.20	2.25	4.32	13.50	27.20	36	45.30	68.20	3146.64	9805.79				
G326.27-0.49	0.23	2.07	8.53	147.40	494.50	921.60	784.50	3139.60	80752.10	110188	103871	51766		
G324.19+0.41	0.78	1.15	1.11	25.90	32.20	53	53.70	207	6383.07		61591			9580

(To be continued)

Table A.1 (continued)

Source	J (mJy)	H (mJy)	K_s (mJy)	[3.6] (mJy)	[4.5] (mJy)	[5.8] (mJy)	[8.0] (mJy)	[24] (mJy)	70 (mJy)	160 (mJy)	250 (mJy)	350 (mJy)	500 (mJy)	870 (mJy)
G324.11+0.44	0.14	0.69	4.47	58.90	185.20	207.40	171.30	1537.60	31313.30	56805	58135	31873	26089	6720
G321.94-0.01				18.90	98.30	190.80	173.50	4416.10	262577	497694	382409	204002		
G317.88-0.25	0.12	0.83	3.11	11.40	22.10	19.40	19	17.50	4560.06					10880
G317.87-0.15	0.75	0.96	5.18	6.40	13.10	10.50	8	192.80						
G311.51-0.45	0.99	6.05	3.12	397.10	776	1183.60	1507.70	10139.10	135574	206411	169100	85755	38615	
G309.91+0.32	0.13	2.25	2.32	61.10	129.40	96.70	20.50	581	55899.60	128136				
G305.89+0.02	0.48	1.99	3.49	36.70	120.40	166.40	158.50	3639	275832	407079	286688	130168		11530
G305.82-0.11	0.36	1.08	2.47	15.60	57.50	64.60	50	1062.20	62390.10	153978	184650	86395	47327	8580
G305.62-0.34	3.86	8.96	10.83	15.40	27.10	27.20	19	1082.80	93516.80	103582	64909	27575	11432	1610
G305.57-0.34	1.21	1.42	0.22	20.30	35.90	25	13.30	343.90	17240.10	38088.40	35193	21266		1660
G305.52+0.76	1.05	0.86	1.39	20.70	48.70	55.80	22.80	645.60	20379.90	58633.40	58722	33322		5530
G305.48-0.10	0.39	1.52	11.80	107.80	275.40	358.50	304.10	5052.20	216991	226933	164303	78750		9030
G304.89+0.64	0.92	3.78	1.98	45.70	102.90	165.80	175.10	7645.70	187379	159050	95644	45167	21200	5530
G298.90+0.36	6.80	10.34	12.27	71.70	125.70	160.10	162	3293.10	37075.20	38671.10	23151	25449	12633	
G298.26+0.74	0.21	1.16	24.93	317.10	605.60	648.80	536.30	18226.20			208740	71223	29343	7660
G2.54+0.20	0.07	0.19	5.51	180	365.60	320.70	172	2761.20		62062.30				
G2.14+0.01	0.39	1.81	4.71	21.50	65.80	196.50	310.10		307960	291775	159452	70365	26188	5740
G0.09-0.66			1.88	20.50	76.90	67	19.50	325.30	115667	314354			69898	

Table A.2: Results of the weighted averaging of the fit SEDs.

SOURCE	χ^2	σ_{χ^2}	Av	σ_{Av}	M	σ_M	\dot{M}	$\sigma_{\dot{M}}$	M_{disk}	$\sigma_{M_{disk}}$	\dot{M}_{disk}	$\sigma_{\dot{M}_{disk}}$	L	σ_L	Age	σ_{Age}
			mag		M_{\odot}		$\log(M_{\odot} yr^{-1})$		$\log(M_{\odot})$		$\log(M_{\odot} yr^{-1})$		$\log(L_{\odot})$		$\log(yr)$	
MG358.0590-00.4698	6.98	3.21	12.18	16.83	2.14	1.83	-5.40	-5.67	-1.58	-1.58	-5.63	-1.58	1.91	2.13	4.62	0.95
MG356.5212+00.2141	10.40	2.95	42.94	11.85	3.20	1.69	-6.83	-6.41	-3.54	-2.97	-9.32	-2.97	2.31	2.35	5.98	0.27
MG354.4384+00.4185	7.45	3.72	8.38	9.13	7.87	0.91	-3.96	-4.24	-1.00	-0.74	-5.30	-0.74	2.93	2.58	4.31	0.40
MG352.6040-00.2253	8.75	4.29	39.18	8.79	7.60	0.75	-3.55	-3.70	-1.02	-0.76	-5.57	-0.76	2.91	2.43	4.53	0.45
MG352.2452-00.0636	10.11	2.99	19.40	18.02	5.74	1.85	-3.93	-3.77	-1.08	-0.92	-	-	2.87	2.84	4.27	0.78
MG351.8098+00.6433	10.70	3.01	47.02	6.49	1.89	1.11	-7.23	-6.61	-1.76	-1.87	-6.88	-1.87	1.61	1.84	6.45	0.43
MG347.7561+00.2323	8.34	3.14	44.67	8.74	6.53	0.76	-4.78	-3.77	-1.48	-1.46	-6.15	-1.46	3.15	2.76	6.31	0.38
MG345.5764-00.2252	12.24	2.98	38.91	7.03	4.40	0.53	-5.76	-4.63	-1.40	-1.42	-6.24	-1.42	2.53	2.06	6.42	0.36
MG343.4049-00.4007	8.12	3.22	43.87	10.90	3.19	1.04	-6.99	-6.39	-1.37	-1.37	-6.15	-1.37	2.10	2.45	6.13	0.49
MG343.3567-00.4032	7.19	3.43	29.62	18.85	2.65	2.31	-5.21	-4.93	-1.64	-1.64	-4.95	-1.64	2.44	2.49	4.68	1.61
MG342.3189+00.5876	14.89	3.54	36.44	13.72	1.50	1.46	-5.03	-5.23	-1.46	-1.39	-5.21	-1.39	2.05	2.41	3.92	1.04
MG339.5843-00.1282	7.95	4.27	19.49	9.74	5.03	1.30	-4.03	-3.91	-1.23	-0.99	-6.16	-0.99	2.34	2.15	4.66	0.44
MG339.4040-00.4134	7.38	3.39	41.03	11.66	2.89	2.00	-4.82	-4.85	-1.41	-1.25	-5.16	-1.25	2.52	2.75	4.24	1.12
MG339.2939+00.1387	4.68	2.59	19.03	11.42	4.25	1.45	-3.38	-3.46	-1.98	-1.39	-6.60	-1.39	2.27	2.24	4.63	0.49
MG338.8762+00.5561	8.49	3.07	42.83	12.32	4.49	0.93	-4.33	-3.78	-1.53	-1.40	-5.97	-1.40	2.55	2.19	5.95	0.91
MG338.8438+00.4342	13.24	2.88	32.91	14.51	7.08	2.80	-4.70	-4.54	-0.84	-0.90	-4.61	-0.90	3.49	3.58	5.03	1.30
MG337.9402-00.5325	10.45	3.44	20.44	8.10	3.75	1.62	-6.20	-6.04	-1.75	-1.50	-5.75	-1.50	2.31	2.18	5.74	1.10
MG336.8585-00.1903	16.51	5.28	7.85	4.46	2.75	1.00	-4.13	-3.88	-1.26	-1.38	-6.12	-1.38	1.91	1.56	5.56	1.28
MG335.6172-00.2001	19.97	3.46	18.22	6.90	5.87	1.50	-	-	-1.45	-1.53	-6.37	-1.53	3.09	3.22	6.61	0.19
MG335.6100-00.7866	3.83	2.75	30.28	13.84	4.42	2.17	-4.66	-4.77	-1.42	-1.14	-5.05	-1.14	2.49	2.30	4.16	0.99
MG335.2667-00.0151	10.55	2.89	40.15	14.44	3.94	2.03	-6.47	-6.09	-1.53	-1.74	-5.66	-1.74	2.66	2.67	5.88	1.24
MG333.2025+00.2940	31.24	3.34	5.26	10.71	4.03	1.03	-4.06	-4.18	-1.86	-1.85	-7.30	-1.85	2.01	1.64	4.92	0.36
MG333.0294-00.0149	17.35	2.93	22.88	14.51	5.02	1.06	-3.90	-3.86	-1.26	-1.09	-6.31	-1.09	2.28	1.94	4.80	0.36
MG332.6662+00.0271	8.80	4.05	43.34	9.80	3.40	0.74	-4.90	-4.22	-1.63	-1.50	-6.42	-1.50	2.11	1.93	6.35	0.77
MG332.3652+00.6046	11.46	5.02	27.31	12.65	2.27	2.09	-4.52	-4.30	-1.44	-1.30	-5.16	-1.30	2.15	2.28	3.90	0.96

(To be continued)

Table A.2 (continued)

SOURCE	χ^2	σ_{χ^2}	Av	σ_{Av}	M	σ_M	\dot{M}	$\sigma_{\dot{M}}$	M_{disk}	$\sigma_{M_{disk}}$	\dot{M}_{disk}	$\sigma_{\dot{M}_{disk}}$	L	σ_L	Age	σ_{Age}
			mag		M_{\odot}		$\log(M_{\odot} yr^{-1})$		$\log(M_{\odot})$		$\log(M_{\odot} yr^{-1})$		$\log(L_{\odot})$		$\log(yr)$	
MG332.1990+00.5957	11.72	3.11	5.92	5.79	1.91	0.84	-6.38	-5.87	-2.13	-1.87	-7.60	-7.08	1.02	1.03	5.96	0.34
MG332.1534+00.0069	3.94	2.74	20.62	12.65	1.15	0.86	-4.54	-4.39	-2.33	-1.87	-7.17	-6.23	1.10	1.24	4.95	0.49
MG331.8302+00.0360	8.61	4.14	37.35	12.55	3.81	1.02	-4.05	-3.71	-1.65	-1.47	-6.16	-5.67	2.40	2.43	5.89	1.25
MG331.5722-00.2290	5.70	3.31	38.81	4.88	7.59	0.99	-	-	-1.35	-1.33	-5.85	-5.56	3.41	3.13	6.34	0.18
MG328.6141-00.4657	8.45	2.76	44.71	9.40	1.59	0.90	-6.80	-6.54	-1.87	-1.78	-6.75	-6.51	1.17	1.48	6.02	0.49
MG328.0494-00.0487	10.79	4.66	35.69	5.97	6.20	0.81	-5.01	-4.36	-1.52	-1.31	-6.12	-5.34	3.07	2.61	5.88	0.41
MG326.7241+00.3552	8.40	3.61	25.18	18.68	1.13	1.22	-6.33	-6.35	-2.08	-1.95	-6.48	-6.55	1.40	1.61	4.78	1.59
MG322.4833+00.6447	7.79	4.18	43.27	8.71	1.97	0.99	-5.30	-4.76	-1.85	-1.65	-7.27	-6.86	1.17	1.10	5.67	0.39
MG317.5959+00.0527	15.75	4.56	31.64	10.72	4.97	1.34	-	-	-1.80	-1.73	-7.12	-6.94	2.81	2.75	6.50	0.28
MG317.4777-00.3504	12.50	4.48	32.43	11.45	6.44	1.95	-4.55	-4.42	-0.98	-0.88	-	-	3.24	3.07	4.80	1.21
MG313.2760-00.7111	6.20	3.11	32.70	14.23	1.23	0.90	-4.63	-4.53	-1.54	-1.45	-5.35	-5.20	1.74	2.01	3.74	0.53
MG306.5029+00.0731	11.45	4.04	30.19	7.75	3.75	1.11	-6.69	-6.32	-1.94	-1.76	-6.39	-5.77	2.32	2.64	6.26	0.76
MG305.5101+00.3661	7.49	3.06	40.01	16.52	3.54	1.74	-5.75	-5.27	-1.58	-1.52	-5.64	-5.27	2.33	2.19	5.65	1.34
MG303.9304-00.6879	11.69	3.10	2.72	4.57	10.29	2.05	-3.49	-3.35	-0.86	-0.75	-5.33	-4.88	3.84	3.78	5.01	0.42
MG300.3241-00.1985	17.08	5.65	25.43	6.92	5.88	1.28	-6.58	-5.75	-1.35	-1.31	-6.01	-5.30	3.05	3.16	6.16	0.49
MG006.9222-00.2512	13.50	3.20	49.50	1.55	6.15	1.49	-6.96	-6.32	-1.37	-1.54	-5.84	-5.00	3.12	2.98	6.31	0.52
MG006.2185-00.5837	7.27	4.03	34.95	16.21	6.47	1.38	-4.95	-4.80	-1.21	-0.91	-5.75	-5.08	3.13	2.90	5.43	0.68
G8.27+0.51	20.85	5.72	0.62	0.73	1.16	0.23	-4.49	-4.60	-2.30	-2.12	-5.82	-5.57	1.50	0.84	3.65	0.21
G354.78+0.83	5.82	3.63	26.15	9.37	4.66	0.68	-5.04	-4.80	-1.47	-1.39	-6.22	-5.81	2.35	2.07	5.61	0.60
G354.71+0.29	13.33	3.52	4.85	5.21	7.56	2.38	-3.59	-3.17	-1.05	-0.85	-	-	3.22	3.31	4.59	0.67
G353.58+0.66	9.88	4.65	37.77	6.28	0.91	1.25	-6.09	-6.28	-2.44	-2.03	-7.79	-7.44	1.56	2.02	5.32	0.61
G352.60-0.19	9.03	2.43	14.89	9.81	6.67	1.40	-3.78	-3.36	-1.18	-0.95	-5.66	-5.13	2.85	2.67	5.03	0.95
G352.32-0.44	4.38	2.50	2.54	2.08	8.55	0.91	-3.36	-4.11	-2.15	-1.34	-7.15	-6.28	3.69	3.06	5.21	0.12
G350.41-0.07	14.21	2.91	39.58	12.41	2.67	1.05	-4.70	-4.37	-1.80	-1.63	-6.91	-6.51	1.49	1.04	5.33	0.26
G350.33+0.10	16.04	3.93	10.38	6.32	19.56	4.65	-3.31	-2.95	-1.13	-0.79	-	-	4.57	4.33	4.36	0.73

(To be continued)

Table A.2 (continued)

SOURCE	χ^2	σ_{χ^2}	Av	σ_{Av}	M	σ_M	\dot{M}	$\sigma_{\dot{M}}$	$\log(M_{\odot} yr^{-1})$	$\sigma_{\dot{M}}$	M_{disk}	$\log(M_{\odot})$	$\sigma_{M_{disk}}$	\dot{M}_{disk}	$\log(M_{\odot} yr^{-1})$	$\sigma_{\dot{M}_{disk}}$	L	σ_L	Age	σ_{Age}
			mag		M_{\odot}												$\log(L_{\odot})$		$\log(yr)$	
G350.02-0.52	4.97	2.31	22.62	12.00	6.87	2.24	-3.59	2.24	-3.56	-1.18	-0.90	-	-	-	-	-	2.97	3.00	4.66	0.38
G349.64-1.09	3.63	2.73	16.73	7.73	8.30	1.86	-3.99	1.86	-4.03	-0.95	-0.84	-	-	-	-	-	3.13	2.89	3.82	0.44
G349.62-0.20	6.70	3.27	12.60	7.98	2.92	1.41	-5.03	1.41	-4.55	-2.30	-1.97	-7.65	-7.65	-7.65	-7.65	-7.65	2.01	1.94	5.77	0.87
G344.21-0.62	17.19	2.97	28.98	6.02	4.16	0.79	-4.52	0.79	-4.33	-1.22	-1.04	-6.67	-6.67	-6.67	-6.67	-6.67	2.11	1.75	5.61	0.60
G343.78-0.24	4.76	2.92	1.55	4.43	3.91	0.83	-4.12	0.83	-4.63	-1.93	-1.50	-7.20	-7.20	-7.20	-7.20	-7.20	1.87	1.89	5.26	0.20
G343.53-0.51(a)	9.01	2.94	20.92	17.04	1.03	0.94	-4.85	0.94	-4.78	-1.78	-1.59	-5.58	-5.58	-5.58	-5.58	-5.58	1.40	1.58	3.72	0.67
G343.50+0.03	6.73	3.49	6.73	4.20	2.09	0.53	-5.52	0.53	-5.03	-1.55	-1.53	-7.46	-7.46	-7.46	-7.46	-7.46	1.11	1.07	5.81	0.43
G343.42-0.33	13.29	4.41	34.89	5.75	3.24	0.56	-7.72	0.56	-7.34	-2.17	-2.01	-7.59	-7.59	-7.59	-7.59	-7.59	1.77	1.24	6.35	0.39
G343.19-0.08(a)	14.53	4.56	16.87	8.03	2.66	1.06	-4.40	1.06	-4.24	-1.44	-1.31	-5.94	-5.94	-5.94	-5.94	-5.94	1.84	1.81	4.69	0.47
G342.15+0.51	18.15	3.75	7.74	3.33	5.44	0.65	-4.67	0.65	-4.37	-1.63	-1.68	-6.54	-6.54	-6.54	-6.54	-6.54	2.53	1.93	5.43	0.51
G341.73-0.97	12.27	2.73	34.65	20.10	3.51	1.92	-5.50	1.92	-5.46	-1.80	-1.72	-5.62	-5.62	-5.62	-5.62	-5.62	2.26	2.11	5.15	1.25
G340.75-1.00	14.63	4.56	36.03	9.71	6.16	0.98	-4.06	0.98	-4.10	-1.16	-0.94	-5.88	-5.88	-5.88	-5.88	-5.88	2.66	2.55	4.52	0.64
G336.87+0.29	12.60	3.35	38.96	13.03	6.17	0.94	-4.61	0.94	-4.46	-1.07	-0.99	-6.01	-6.01	-6.01	-6.01	-6.01	2.68	2.40	5.14	0.44
G335.59-0.29	33.02	2.66	0.07	0.16	8.53	0.66	-3.34	0.66	-3.07	-0.88	-0.66	-5.66	-5.66	-5.66	-5.66	-5.66	3.15	2.76	4.53	0.33
G334.25+0.07	38.21	3.56	13.63	12.14	7.44	0.42	-3.24	0.42	-3.19	-0.55	-0.69	-5.46	-5.46	-5.46	-5.46	-5.46	2.78	1.97	4.76	0.31
G334.04+0.35	9.88	4.22	11.94	11.52	3.00	1.22	-4.47	1.22	-4.31	-1.27	-1.12	-5.30	-5.30	-5.30	-5.30	-5.30	2.17	1.92	3.80	0.50
G332.91-0.55	5.54	2.63	2.09	4.51	2.72	1.15	-4.43	1.15	-4.18	-2.03	-1.77	-7.48	-7.48	-7.48	-7.48	-7.48	1.63	1.39	5.28	0.40
G332.59+0.04(b)	5.84	3.67	33.01	5.48	4.12	0.33	-6.08	0.33	-4.78	-1.64	-1.54	-6.28	-6.28	-6.28	-6.28	-6.28	2.41	1.70	6.78	0.25
G332.47-0.52	9.85	2.88	22.13	11.90	6.83	1.48	-3.21	1.48	-3.09	-1.03	-0.87	-	-	-	-	-	3.05	3.10	4.07	0.81
G332.33-0.12	14.25	3.42	25.82	8.78	2.63	1.01	-4.49	1.01	-4.17	-1.45	-1.34	-6.52	-6.52	-6.52	-6.52	-6.52	1.61	1.33	5.40	0.71
G332.28-0.07	8.25	3.10	15.49	11.58	3.85	1.09	-4.20	1.09	-4.07	-1.49	-1.23	-6.40	-6.40	-6.40	-6.40	-6.40	2.04	1.66	4.79	0.36
G331.71+0.58	15.59	3.39	7.64	7.48	7.36	0.59	-3.63	0.59	-3.44	-0.54	-0.56	-5.49	-5.49	-5.49	-5.49	-5.49	2.77	2.22	4.67	0.41
G331.62+0.53	4.87	3.70	15.93	12.23	3.48	1.31	-3.41	1.31	-3.29	-1.01	-0.94	-4.98	-4.98	-4.98	-4.98	-4.98	2.32	2.09	3.75	0.49
G329.47+0.52	8.72	3.93	0.00	0.00	6.14	0.94	-4.16	0.94	-7.40	-0.98	-0.79	-6.95	-6.95	-6.95	-6.95	-6.95	2.57	2.07	4.18	0.20
G329.16-0.29	11.76	4.66	0.95	1.19	2.53	1.23	-3.77	1.23	-3.68	-1.50	-1.45	-6.71	-6.71	-6.71	-6.71	-6.71	1.67	1.46	4.93	0.45

(To be continued)

Table A.2 (continued)

SOURCE	χ^2	σ_{χ^2}	Av	σ_{Av}	M	σ_M	\dot{M}	$\sigma_{\dot{M}}$	M_{disk}	$\sigma_{M_{disk}}$	\dot{M}_{disk}	$\sigma_{\dot{M}_{disk}}$	L	σ_L	Age	σ_{Age}
			mag		M_{\odot}		$\log(M_{\odot} yr^{-1})$		$\log(M_{\odot})$		$\log(M_{\odot} yr^{-1})$		$\log(L_{\odot})$		$\log(yr)$	
G328.55+0.27	12.09	4.34	14.66	11.68	6.09	1.21	-3.77	-3.51	-1.19	-0.91	-	-	2.65	2.31	4.16	0.52
G326.80+0.51	5.68	3.27	25.36	11.00	1.56	0.59	-6.30	-5.65	-2.13	-1.83	-7.65	-7.22	0.80	1.06	5.90	0.32
G326.78-0.24	13.87	4.46	21.18	5.51	5.67	1.32	-3.84	-3.59	-1.10	-0.96	-	-	2.72	2.34	3.85	0.60
G326.65+0.75	85.82	5.93	0.75	0.97	1.57	0.95	-4.61	-4.64	-1.51	-1.44	-5.75	-5.71	1.67	1.44	3.75	0.51
G326.57+0.20	20.91	6.23	1.22	1.11	4.32	1.51	-3.41	-3.37	-1.09	-1.01	-5.43	-4.97	2.27	2.10	4.61	0.35
G326.41+0.93	16.41	3.14	14.72	14.47	1.67	1.58	-4.81	-4.85	-1.61	-1.48	-5.25	-5.09	1.99	2.22	3.66	0.85
G326.31+0.90	8.95	4.07	27.21	4.79	2.58	0.88	-6.09	-5.25	-1.89	-1.72	-6.86	-6.67	1.24	1.27	5.82	0.36
G326.27-0.49	11.61	4.00	19.88	5.46	2.04	1.69	-4.46	-4.23	-1.55	-1.51	-4.33	-4.43	2.36	2.21	3.29	0.26
G324.19+0.41	12.56	2.69	8.41	6.53	3.58	0.72	-4.42	-4.25	-1.44	-1.49	-6.69	-6.52	1.77	1.24	5.24	0.25
G324.11+0.44	10.90	3.41	41.90	8.39	6.07	0.83	-4.39	-3.98	-1.35	-1.15	-5.98	-5.47	2.83	2.47	5.49	0.43
G321.94-0.01	7.83	2.98	21.70	14.56	4.11	1.43	-3.72	-3.43	-1.16	-1.05	-5.46	-5.10	2.30	2.06	4.16	0.46
G317.88-0.25	8.26	4.17	29.00	3.80	2.34	0.62	-6.59	-6.14	-1.93	-1.83	-7.38	-6.93	1.15	0.94	6.20	0.43
G311.51-0.45	7.30	3.04	28.01	13.90	7.12	0.85	-4.37	-3.94	-1.43	-1.03	-	-	3.25	2.83	5.47	0.68
G309.91+0.32	38.03	2.33	0.00	0.02	5.39	0.78	-3.84	-3.57	-1.55	-1.29	-6.60	-6.26	2.36	2.00	4.78	0.35
G305.52+0.76	23.91	3.37	30.16	9.06	2.97	1.06	-4.29	-4.26	-1.67	-1.39	-6.96	-6.61	1.71	1.37	5.04	0.34
MG347.0800-00.3962	3.55	2.71	24.43	12.82	6.87	1.84	-4.72	-4.31	-1.50	-1.11	-6.21	-5.74	3.27	3.37	5.60	.49
MG338.6328+00.0265	6.60	4.30	39.30	9.85	4.89	.87	-6.81	-6.22	-1.62	-1.47	-6.57	-5.83	2.71	2.58	6.20	.41
MG357.5328+00.2366	7.15	3.05	44.32	12.94	5.20	1.48	-5.98	-5.53	-1.74	-1.47	-6.04	-5.40	2.87	2.65	5.78	.80
MG352.0746-00.3874	3.62	2.71	29.75	14.35	.96	.91	-4.79	-4.57	-1.76	-1.60	-6.25	-5.84	1.45	1.90	4.27	.75
MG326.9250-00.5141	7.28	4.32	33.97	14.97	.50	.37	-5.25	-5.10	-1.94	-1.86	-5.44	-5.24	1.17	1.36	3.32	.31
MG002.5577-00.7510	10.33	3.91	24.10	17.55	.75	1.09	-5.76	-5.80	-1.91	-1.55	-6.32	-5.91	1.15	1.85	4.36	1
MG345.2198-00.1367	6.45	3.67	40.61	8.65	2.03	.86	-7.12	-6.76	-1.78	-1.69	-6.63	-6.55	1.50	1.86	6.30	.48
MG351.8655-00.2246	8.30	4.31	20.83	13.17	1.56	.80	-4.68	-4.61	-1.79	-1.53	-6.85	-6.45	1.30	1.09	4.96	.46
MG345.0737-00.1953	13.01	3.67	34.08	3.81	3.92	1.40	-	-	-1.75	-1.83	-5.28	-5.16	2.76	2.84	6.49	.24
MG358.4604-00.3929	10.15	2.39	26.39	20.27	2.49	1.80	-4.23	-4.04	-1.66	-1.24	-6.47	-5.69	1.82	2.03	4.94	.39

(To be continued)

Table A.2 (continued)

SOURCE	χ^2	σ_{χ^2}	Av	σ_{Av}	M	σ_M	\dot{M}	$\log(M_{\odot} yr^{-1})$	$\sigma_{\dot{M}}$	M_{disk}	$\log(M_{\odot})$	$\sigma_{M_{disk}}$	\dot{M}_{disk}	$\log(M_{\odot} yr^{-1})$	$\sigma_{\dot{M}_{disk}}$	L	$\log(L_{\odot})$	σ_L	Age	$\log(yr)$	σ_{Age}
MC342.0988+00.8086	5.58	3.37	18.97	14.94	.30	.28	-5.46	-5.65	-2.20	-2.11	-6.23	-6.14	-6.23	-6.14	.64	.94	3.54	.49			
G327.39+0.20	17.80	4.76	39.33	7.84	6.98	.31	-3.43	-3.83	-1.08	-0.89	-6.04	-5.73	-6.04	-5.73	2.67	2.29	4.79	.32			
G327.12+0.51	15.60	4.10	39.15	7.08	5.50	1.50	-3.43	-3.21	-1.06	-1.02	-5.21	-5.01	-5.21	-5.01	2.68	2.52	4.08	.69			
G343.72-0.18(a)	20.07	3.75	33.11	7.44	3.02	1.06	-4.57	-4.64	-1.78	-1.47	-7.09	-6.72	-7.09	-6.72	1.70	1.24	5.08	.35			
G351.27+1.04	15.29	2.79	31.88	14.11	.58	.70	-5.63	-6.13	-2.04	-1.92	-6.40	-6.56	-6.40	-6.56	1.07	1.32	3.43	1.02			
G340.75-1	17.74	3.77	45.39	6.48	6.72	.57	-4.08	-4.27	-1.32	-0.91	-6.83	-6.61	-6.83	-6.61	2.63	1.88	4.55	.53			
G317.87-0.15	8.91	4	22.67	9.89	1.21	.76	-4.86	-4.77	-2.46	-2.05	-7.54	-7.06	-7.54	-7.06	1.01	.76	5.08	.48			
G350.52-0.35	8.05		49.77		6.37		-	-1.84	-	-	-6.61	-	-6.61	-	3.07	-	6.22				
G358.26-2.06	6.48	3.30	33.41	13.66	5.65	1.01	-3.94	-3.76	-1.17	-1.05	-6.21	-5.91	-6.21	-5.91	2.46	1.98	5.10	.71			
G355.54-0.10	9.05	3.39	43.93	7.15	4.53	1.38	-4.37	-4.14	-1.31	-1.03	-5.83	-5.34	-5.83	-5.34	2.44	2.45	5.25	1.20			
G327.89+0.15	12.66	4.70	35.64	11.39	2.31	.97	-4.19	-4.15	-1.45	-1.28	-6.52	-6.15	-6.52	-6.15	1.65	1.49	5.03	.66			
G350.75+0.68	11.78	3.94	22.44	10.61	3.58	1.10	-4.53	-4.71	-1.51	-1.36	-6.46	-6.08	-6.46	-6.08	1.96	1.54	4.78	.37			
G336.96-0.98	9.85	3.69	29.96	11.21	2.93	1.06	-4.29	-4.19	-1.52	-1.34	-6.74	-6.42	-6.74	-6.42	1.72	1.39	5.04	.33			
G343.50-0.47	9.15	3.97	34.75	11.57	6.61	.45	-3.46	-3.73	-1.06	-0.98	-5.81	-5.42	-5.81	-5.42	2.61	2.15	4.86	.37			
G351.05-0.39	19.11	3.75	45.35	9.80	2.54	.33	-4.95	-4.52	-1.76	-1.83	-7.04	-6.63	-7.04	-6.63	1.47	.86	6.37	.57			
G9.81-1.06	6.69	2.95	32.41	11.28	1.92	1.10	-4.51	-4.35	-1.68	-1.52	-6.66	-6.22	-6.66	-6.22	1.46	1.49	5.04	.62			
G353.40-0.07	8.86	4.31	46.73	4.88	2.84	.23	-	-	-1.56	-1.58	-7.54	-7.25	-7.54	-7.25	1.75	1.12	6.76	.23			
G355.75+0.65	10.17	2.52	34.22	11.29	2.71	1.49	-4.36	-4.18	-1.68	-1.47	-6.30	-5.52	-6.30	-5.52	1.83	2.21	5.18	.35			
G305.89+0.02	8.81	4.03	40.57	10.45	4.52	1.27	-3.75	-3.53	-1.18	-0.99	-5.94	-5.53	-5.94	-5.53	2.24	1.88	4.47	.40			
G326.79+0.38	12.06	5.23	37.82	13.98	6.31	.69	-3.85	-3.84	-1.15	-0.90	-5.95	-5.69	-5.95	-5.69	2.61	2.35	5.09	.44			
G359.44-0.10	6.65	3.41	33.87	11.40	7.46	.71	-3.41	-3.50	-0.89	-0.69	-5.68	-5.38	-5.68	-5.38	2.80	2.32	4.70	.34			
G343.12-0.06	12.81	4.78	36.67	7.92	8.40	.63	-3.28	-3.31	-0.75	-0.59	-5.56	-5.38	-5.56	-5.38	3.29	2.70	4.86	.22			
G332.81-0.70	17.41	4.11	42.45	9.30	5.49	1.20	-3.85	-4.01	-1.07	-0.97	-5.98	-5.75	-5.98	-5.75	2.39	2.03	4.71	.39			
G305.48-0.10	10.12	4.01	37.29	11.32	5.79	.97	-3.85	-3.78	-1.10	-1.02	-5.91	-5.76	-5.91	-5.76	2.51	2.47	4.76	.47			
G8.66-0.37	15.85	4.28	36.45	13	3.56	2.33	-4.76	-4.43	-1.35	-1.27	-5.14	-4.97	-5.14	-4.97	2.50	2.45	4.61	1.19			

(To be continued)

Table A.2 (continued)

SOURCE	χ^2	σ_{χ^2}	Av	σ_{Av}	M	σ_M	\dot{M}	$\sigma_{\dot{M}}$	M_{disk}	$\sigma_{M_{disk}}$	\dot{M}_{disk}	$\sigma_{\dot{M}_{disk}}$	L	σ_L	Age	σ_{Age}
			mag		M_{\odot}		$\log(M_{\odot} yr^{-1})$		$\log(M_{\odot})$		$\log(M_{\odot} yr^{-1})$		$\log(L_{\odot})$		$\log(yr)$	
G327.30-0.58	7.56	4.43	23.87	12.46	1.01	1.40	-4.18	-3.53	-1.65	-1.83	-4.94	-5.05	1.78	1.94	3.51	.34
G347.08-0.40	21.55	3.88	19.12	6.94	3.85	1.06	-4.15	-3.99	-1.76	-1.33	-6.76	-6.20	2.02	1.67	4.84	.33
G343.40-0.40	25.42	4.77	48.97	1.36	2.66	.32	-	-	-2.56	-2.29	-7.55	-7.11	1.71	1.44	6.82	.10
G329.07-0.31(a)	13.40	3.85	27.38	11.93	2.66	2.04	-4.89	-4.74	-1.25	-1.25	-5.14	-5.10	2.30	2.38	4.09	.95
G351.78-0.54	15.36	3.21	38.34	8.78	8.77	.87	-3.28	-3.35	-1.08	-7.7	-5.87	-5.60	3.47	3.16	4.93	.34
G358.84-0.74	9.61	3.97	26.60	11.40	2.17	1.03	-4.35	-4.07	-1.89	-1.57	-7.02	-6.45	1.46	1.17	4.94	.52
G352.52+0.77	13.34	4.29	47.06	3.77	1.66	.86	-4.86	-5.09	-1.43	-1.74	-6.49	-6.47	1.46	1.44	5.13	.46
G355.24+0.37	10.42	3.91	10.50	6.39	1.65	1.08	-4.33	-4.24	-1.40	-1.33	-6.12	-5.87	1.45	1.29	4.59	.57
G298.26+0.74	14.89	4.45	32.15	12.77	7.63	.52	-3.77	-3.84	-7.6	-6.1	-5.89	-5.71	2.83	2.35	4.61	.34
G339.95-0.54	10.08	4.59	43.96	6.81	6.01	.98	-3.81	-3.66	-1.08	-9.8	-6.16	-5.97	2.47	1.93	4.48	.43
G8.70-0.37	11.93	4.21	43.27	8.14	1.03	.73	-4.69	-4.81	-1.33	-1.45	-5.63	-5.66	1.30	.78	4.28	.52
G351.16+0.69	6.88	3.54	31.25	14.08	9.28	1.44	-3.56	-3.36	-1.05	-7.8	-5.56	-5.22	3.54	3.06	4.97	.61
G326.61+0.80(a)	9.99	3.97	45.58	4.34	2.82	1.83	-5.11	-5.11	-1.69	-1.66	-5.56	-5.22	2.35	2.39	4.85	1.11
G9.62+0.20	6.72	3.39	31.15	16.32	9.80	6.37	-3.60	-3.41	-7.3	-4.9	-5.6	-5.6	4.15	4.56	4.53	.97
G352.13-0.94	6.52	3.11	32.36	11.60	5.60	1.68	-3.81	-3.72	-1.28	-1.05	-5.63	-5.20	2.54	2.34	4.83	.95
G8.72-0.36	29.02	3.93	32.60	4.06	2.96	.96	-4.54	-4.39	-1.85	-1.55	-7.08	-6.56	1.67	1.35	5.15	.33
G298.90+0.36	9.49	4.61	39.88	8.17	3.76	1.13	-4.43	-4.44	-1.55	-1.42	-6.07	-5.75	2.01	1.60	4.83	.51
G6.19-0.36	21.18	3.54	32.36	9.48	5.93	.83	-3.88	-3.93	-1.03	-9.1	-6.09	-5.87	2.49	2.03	4.72	.52
G304.89+0.64	13.35	4.45	36.36	9.27	5.39	1.13	-3.83	-3.69	-1.06	-8.9	-6.36	-6.16	2.34	1.91	4.63	.33
G349.63-1.10(a)	7.29	2.76	21.68	11.13	2.85	1.18	-4.35	-4.06	-1.48	-1.18	-6.49	-5.83	1.75	1.97	5.18	.54
G351.02-0.86							-	-	-	-	-	-	-	-	-	-
G5.88-1	46.83	3.22	45.60	6.56	.94	.70	-5.40	-5.32	-2.54	-2.46	-8.67	-8.61	.57	.26	5.46	.50
G4.83+0.23	51.97	4.07	27.15	6.25	4.02	1.08	-4.22	-4.13	-1.71	-1.40	-6.80	-6.37	2.05	1.75	4.91	.37
G351.38-0.18	13.47	3.25	42.61	8.09	7.78	.86	-3.74	-3.85	-1.20	-9.6	-5.46	-5.16	2.97	2.65	4.43	.66
G337.16-0.39	8.24	4.11	45.04	5.34	3.12	.96	-4.33	-4.55	-1.48	-1.23	-6.22	-5.81	1.99	1.91	4.47	.51

(To be continued)

Table A.2 (continued)

SOURCE	χ^2	σ_{χ^2}	Av	σ_{Av}	M	σ_M	\dot{M}	$\sigma_{\dot{M}}$	$\log(M_{\odot} yr^{-1})$	σ_M	M_{disk}	$\sigma_{M_{disk}}$	\dot{M}_{disk}	$\sigma_{\dot{M}_{disk}}$	$\log(M_{\odot} yr^{-1})$	L	σ_L	Age	σ_{Age}
			mag		M_{\odot}		$\log(M_{\odot} yr^{-1})$				$\log(M_{\odot})$		$\log(M_{\odot} yr^{-1})$		$\log(L_{\odot})$		$\log(yr)$		
G327.40+0.44	9.07	5.23	26.46	3.45	4.67	.45	-7.83	.73	-7.39	-1.63	-1.46	-7.21	-7.12	2.59	2.15	6.57	.41		
G356.37+0.57	20.13	5.13	44	9.20	6.02	3.06	-3.42	3.06	-3.13	-1.04	-.99	-4.49	-4.42	3.27	3.56	4.33	1.24		
G329.07-0.31(b)	12.77	3.92	32.56	5.64	3.24	.54	-7.55	.52	-7.26	-2.09	-1.97	-7.60	-7.09	1.74	1.20	6.34	.39		
G352.58-0.18	8.46	4.64	42.56	10.73	.64	.52	-5.28	.41	-5.62	-2.07	-2.11	-5.28	-5.49	1.48	1.99	3.27	.29		
G344.58-0.02	11.55	3.23	40.80	11.07	5.49	1.96	-4.11	1.96	-4.26	-1.13	-.86	-5.42	-5.05	2.76	2.91	4.54	.79		
G326.61+0.80(c)	132.72	3.89	28.39	8.60	4.12	.97	-4.25	.97	-4.42	-2.05	-1.94	-7.18	-6.79	1.95	1.64	5.12	.16		
G305.82-0.11	26.05	3.37	.85	1.85	3.82	1.98	-3.53	1.98	-3.53	-1.16	-.98	-5.57	-5.08	2.17	2.18	4.67	.34		
G351.53+0.70	21.94	5.16	45.66	5.57	3.89	.99	-3.86	.99	-4.14	-1.33	-1.06	-6.66	-6.29	1.87	1.30	5.15	.16		
G351.53+0.71	9.97	4.42	33.31	15.56	.55	.24	-5.31	.24	-5.48	-1.90	-1.98	-5.20	-5.19	1.30	.78	3.22	.16		
G329.61+0.11	21.67	3.66	47.15	4.35	3.28	1.30	-5.89	1.30	-5.14	-1.83	-1.81	-7.42	-7.47	2.39	2.79	6.66	.35		
G349.62-1.11	66.89	2.69	47.78	3.70	1.35	.70	-4.90	.70	-5.37	-1.31	-1.59	-5.74	-5.77	1.46	1.06	4.44	.34		
G332.58+0.15	12.30	2.86	32	15.34	1.39	1.34	-5.59	1.34	-5.68	-2.10	-2	-5.73	-5.49	1.67	1.85	4.31	1.61		
G305.62-0.34	16.06	3.31	33.51	7.75	4.41	.87	-5.10	.87	-4.59	-1.50	-1.27	-6.42	-5.86	2.34	1.98	5.98	.61		
G332.59+0.04(a)	11.42	4.18	2.25	2.47	2.75	1.08	-4.58	1.08	-4.74	-1.74	-1.43	-7.33	-6.90	1.69	1.51	5.06	.35		
G331.71+0.60	59.75	5.57	27.03	11.73	2.93	.15	-	.15	-	-2.15	-2.36	-7.53	-7.60	1.84	1.02	6.81	.13		
G4.89-0.13	26.83	3.40	36.40	3.12	2.57	.84	-5.20	.84	-4.97	-1.66	-1.53	-7.39	-7.17	1.30	.92	5.55	.22		
G351.76-0.54	9.77	3.78	45.65	4.22	1.66	1.28	-5.33	1.28	-4.77	-2.05	-1.63	-7.68	-7.13	1.31	1.68	5.60	.37		
G8.73-0.37	6.33	3.35	37.88	11.64	2.92	3.01	-3.93	3.01	-3.40	-1.37	-1.07	-	-1.05	2.95	3.95	4.21	.86		
G348.58-0.92	9.67	3.72	21.69	8.08	2.59	1.56	-4.04	1.56	-3.88	-1.40	-1.19	-6.54	-6.15	2.10	2.72	4.73	.49		
G2.14+0.01	10.87	3.98	39.56	8.41	5.83	.89	-3.88	.89	-3.88	-1.18	-1.10	-6.15	-5.86	2.48	2.14	4.69	.46		
G9.83-1.05	88.72		8.53		10.46		-2.44		-	-	-	-	-	3.48	-	3.30			
G355.18-0.42	64.84	6.99	44.66	2.15	2.82	2.37	-5.75	2.37	-5.71	-1.30	-1.44	-4.81	-4.77	2.43	2.32	4.99	1.77		
G341.24+0.27	10.72	3.75	25.13	13.07	3.42	1.81	-3.74	1.81	-3.67	-1.60	-1.37	-5.71	-5.32	2.06	1.81	4.27	.60		
G348.17+0.46	13.48	3.93	27.99	14.05	.77	.45	-4.21	.45	-3.96	-1.73	-1.51	-5.63	-5.45	1.31	1.14	3.41	.35		
G353.46+0.56	8.27	3.94	39.32	9.01	2.50	1.15	-4.30	1.15	-4.24	-1.72	-1.42	-6.01	-5.45	1.84	1.84	4.49	.57		

(To be continued)

Table A.2 (continued)

SOURCE	χ^2	σ_{χ^2}	Av	σ_{Av}	M	σ_M	\dot{M}	$\sigma_{\dot{M}}$	\dot{M}_{disk}	$\sigma_{\dot{M}_{disk}}$	$\log(M_{\odot} yr^{-1})$	\dot{M}_{disk}	$\sigma_{\dot{M}_{disk}}$	$\log(M_{\odot} yr^{-1})$	L	σ_L	Age	σ_{Age}
			mag		M_{\odot}		$\log(M_{\odot} yr^{-1})$		$\log(M_{\odot})$			$\log(M_{\odot} yr^{-1})$		$\log(L_{\odot})$		$\log(yr)$		
G355.75-0.87	6.34	3.60	37.22	9.31	5.30	.81	-4.03	-3.93	-1.44	-1.26	-6.55	-6.16	-6.16	2.34	2.02	4.91	.53	
G332.94-0.69	36.02	4	46.12	3.28	3.30	1.12	-4.32	-4.54	-1.76	-1.54	-6.84	-6.43	-6.43	1.80	1.31	5	.40	
G349.63-1.10(b)	5.23	3.35	34.97	10.45	2.21	.96	-4.43	-4.24	-1.71	-1.54	-6.92	-6.55	-6.55	1.43	1.10	5.18	.50	
G341.23-0.27	6.36	3.46	31.30	10.28	1.37	.57	-4.33	-4.03	-1.63	-1.78	-7.10	-6.53	-6.53	1.25	1.21	5.13	.26	
G358.39-0.48	3.39	2.60	13.61	14.18	8.12	4.64	-3.63	-3.44	-99	-76		-44	-44	3.49	4.13	3.95	.77	
G351.54-0.57	8.62	3.15	19.42	9.33	2.52	.92	-4.48	-4.11	-1.64	-1.58	-6.35	-5.90	-5.90	1.55	1.37	5.66	1.13	
G341.99-0.10	17.65	3.01	33.03	15.07	4.66	.98	-4.18	-4.32	-1.31	-1.15	-6.40	-6.12	-6.12	2.21	1.89	4.86	.38	
G352.52+0.76	6.86	3.33	9.03	9.25	2.87	.95	-4.54	-4.65	-1.73	-1.52	-6.71	-6.19	-6.19	1.76	1.40	4.90	.42	
G332.36+0.60	7.73	2.87	19.22	20.27	2.85	1.99	-4.41	-4.14	-1.41	-1.35	-5.37	-5.05	-5.05	2.19	2.29	4.24	1.07	
G352.63-1.07	4.69	2.62	19.66	13.72	8.82	2.80	-3.65	-3.37	-84	-66		-49	-49	3.48	3.52	3.96	.79	
G4.63-0.67	6.37	5.15	41.28	11.34	2.82	.59	-6.30	-6.89	-2.60	-3.29	-7.31	-6.81	-6.81	1.27	1.08	5.63	.54	
G351.69+0.17	7.90	3.04	13.05	12.57	3.27	1.50	-4.19	-4.03	-1.74	-1.49	-6.47	-6.10	-6.10	1.89	1.69	4.75	.47	
G357.52+0.20	9.20	3.91	45.34	6.08	4.01	.83	-	-	-1.27	-1.36	-5.46	-5.34	-5.34	2.63	2.50	6.41	.24	
G351.80-0.45	11.01	2.08	13.14	11.58	2.41	.97	-4.35	-4.29	-1.62	-1.38	-6.92	-6.56	-6.56	1.58	1.32	5.08	.30	
G352.61-0.23	6.90	3.01	25.06	9.39	3.13	1	-4.99	-4.45	-1.51	-1.26	-6.97	-6.32	-6.32	2.02	2.51	5.74	.63	
G355.19-0.08	9.88	3.31	32.97	8.42	3.22	.57	-6.09	-5.65	-1.67	-1.42	-6.98	-6.70	-6.70	1.54	1.24	6.04	.39	
G335.43-0.24	21.99	3.02	31.88	15.15	3.11	2.56	-3.79	-3.63	-1.20	-1.10	-5.19	-5.16	-5.16	2.38	2.44	3.91	.92	
G2.54+0.20	15.18	3.02	15.37	10.89	5.43	1.07	-4.04	-3.96	-1.30	-1.07	-6.30	-5.91	-5.91	2.34	2	5.04	.35	
G355.41+0.10	3	2.60	16.69	16.25	7.47	6.19	-3.46	-3.28	-99	-88		-38	-38	3.71	4.39	3.86	.51	
G332.56-0.15	6.32	5.15	41.34	11.19	2.82	.58	-6.30	-6.90	-2.60	-3.29	-7.32	-6.82	-6.82	1.27	1.08	5.64	.53	
G305.57-0.34	8.42	3.01	6.67	7.82	2.80	1.09	-4.50	-4.46	-1.64	-1.34	-6.95	-6.54	-6.54	1.70	1.51	5.03	.38	
G328.14-0.43	4.24	1.21	1.35	1.54	3.60	.49	-4.10	-3.77	-1.76	-2.31	-7.79	-8.31	-8.31	1.68	-79	5.25	.18	
G337.30-0.87	4.44	2.59	3.43	3.27	3.66	1.26	-4.28	-3.83	-1.52	-1.39	-7.30	-7.16	-7.16	1.91	1.65	5.14	.28	
G341.20-0.26	4.41	2.56	2.24	3.11	1.10	.76	-5.99	-6.02	-2.01	-1.97	-7.70	-7.26	-7.26	.82	.68	5.47	.20	
G0.09-0.66	3.43	2.72	7.81	6.04	2.14	.96	-4.68	-4.58	-1.96	-1.73	-7.29	-6.86	-6.86	1.45	1.23	5.20	.36	

(To be continued)

Table A.2 (continued)

SOURCE	χ^2	σ_{χ^2}	Av	σ_{Av}	M	σ_M	\dot{M}	$\sigma_{\dot{M}}$	M_{disk}	$\sigma_{M_{disk}}$	\dot{M}_{disk}	$\sigma_{\dot{M}_{disk}}$	L	σ_L	Age	σ_{Age}
			mag		M_{\odot}		$\log(M_{\odot} yr^{-1})$		$\log(M_{\odot})$		$\log(M_{\odot} yr^{-1})$		$\log(L_{\odot})$		$\log(yr)$	
G350.36-0.07	5.41	2.52	4.90	7.16	2.64	1.32	-4.25	-4.28	-1.35	-1.24	-6.66	-6.25	1.81	1.65	4.68	.30
G5.62-0.08	3.63	2.82	10.69	12.65	.76	.46	-4.26	-4.18	-2.57	-2.14		-2.17	.85	2.11	4.86	.35
G326.86-0.67	3.40	2.69	9.67	7.09	1.15	.72	-5	-4.71	-2.14	-1.73	-7.24	-7.03	1.06	1.05	5.07	.36
G358.46-0.39(b)	4	2.74	9.41	11.43	1.37	.83	-5.08	-4.58	-2.19	-2.01	-7.47	-7.35	1.14	.94	5.03	.35

A.2 Figures

This supplement shows the full breadth of plots of studied sources. These are the LCs, LS periodograms, phase-folded LCs, color figures and the SEDs. These plots have been produced during the full analysis of Chap. 4. They are reproduced here for completeness.

A.2.1 LCs

The LCs of each source are reproduced here, with error bars representing $\text{MAD}(\Delta S_{i_{mjd}})$. The periodograms, along with the false alarm probability curves, and the phase-folded LC using the period which best fits them is plotted. Finally, using the Spitzer IRAC 3.6 μm , IRAC 4.0 μm , and the 24 μm MIPS band, the color figures are plotted with contours provided by ATLASGAL observations.

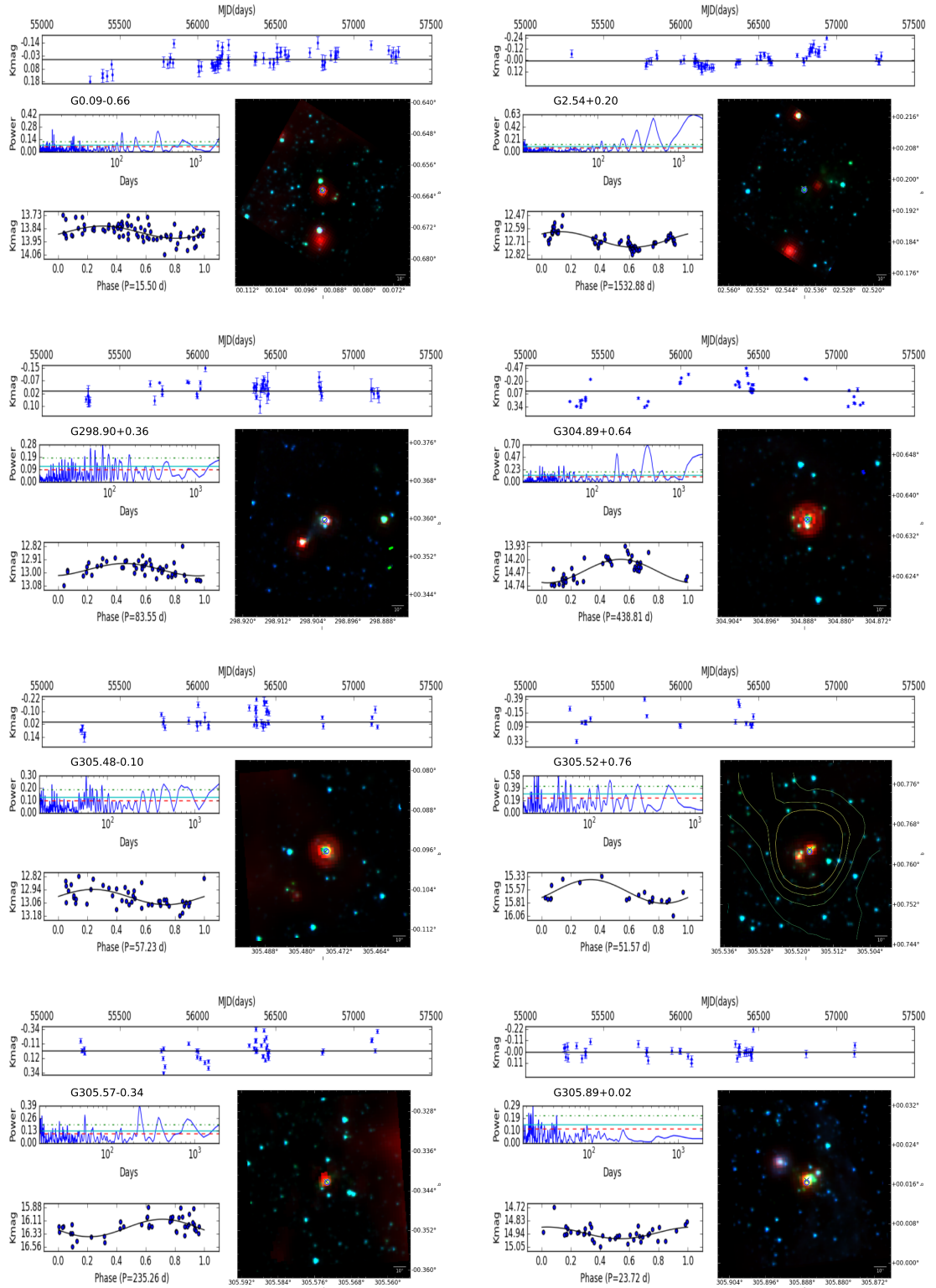


Figure A.1: LC of the source, with error bars representing $\text{MAD}(\Delta S_{i,m,j,d})$, periodograms (also plotted are the 99%, 95%, and 90% false probability levels, respectively: the green dot-dashed line, the cyan full line, and the red dashed line), the phase-folded LC using the best period fitted, the RGB image of the source using the Spitzer IRAC 3.6 μm , IRAC 4.0 μm , and the 24 μm MIPS band as blue, green and red, respectively. The VVV source is marked by the blue circle and the green cross represents the MIPS co-ordinates. The contours of the RGB are in the interval of [Peak-5 σ , Peak] from the ATLASGAL observation at 850 μm .

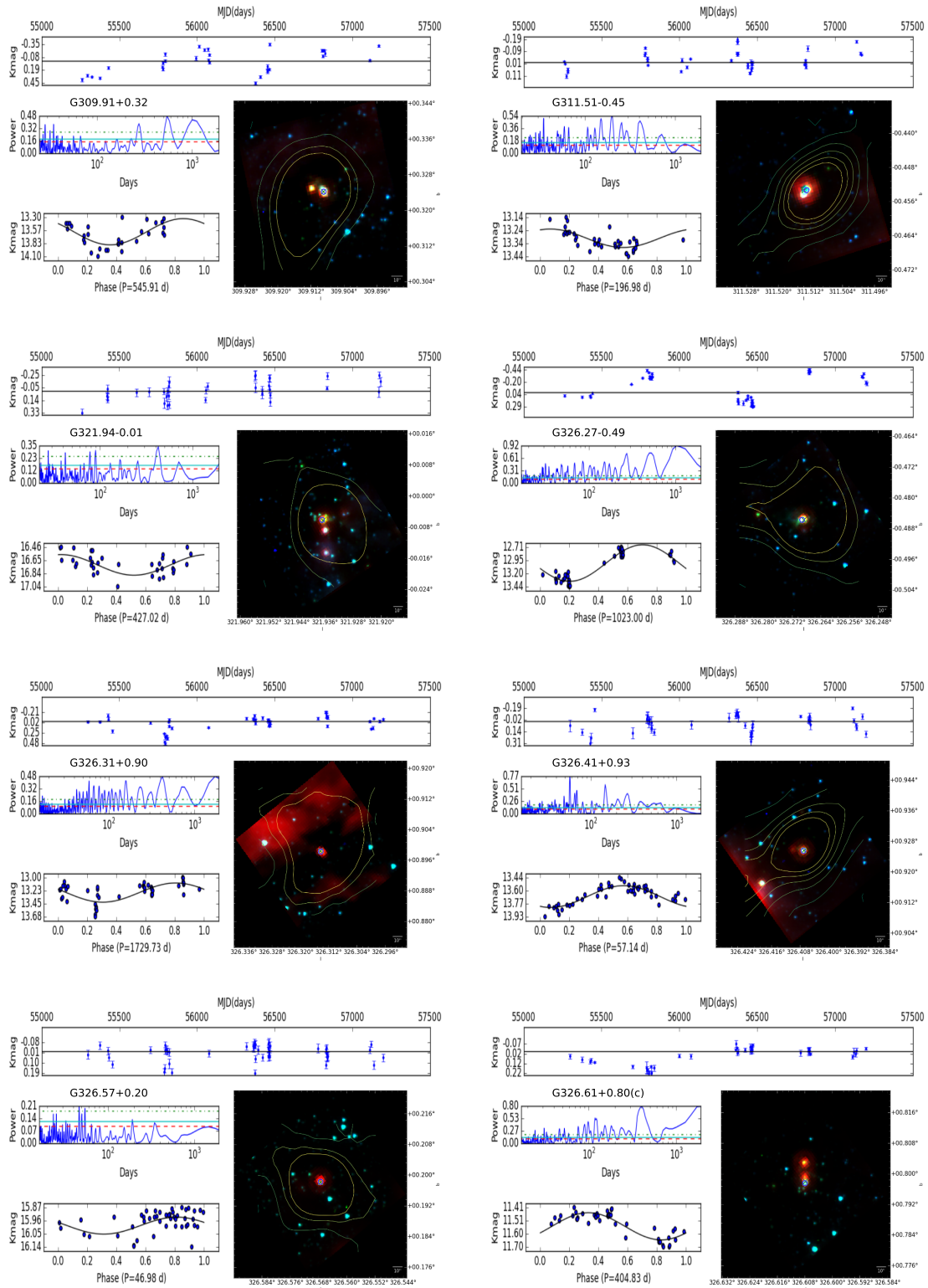


Figure A.2: Continuation of Fig. A.1.

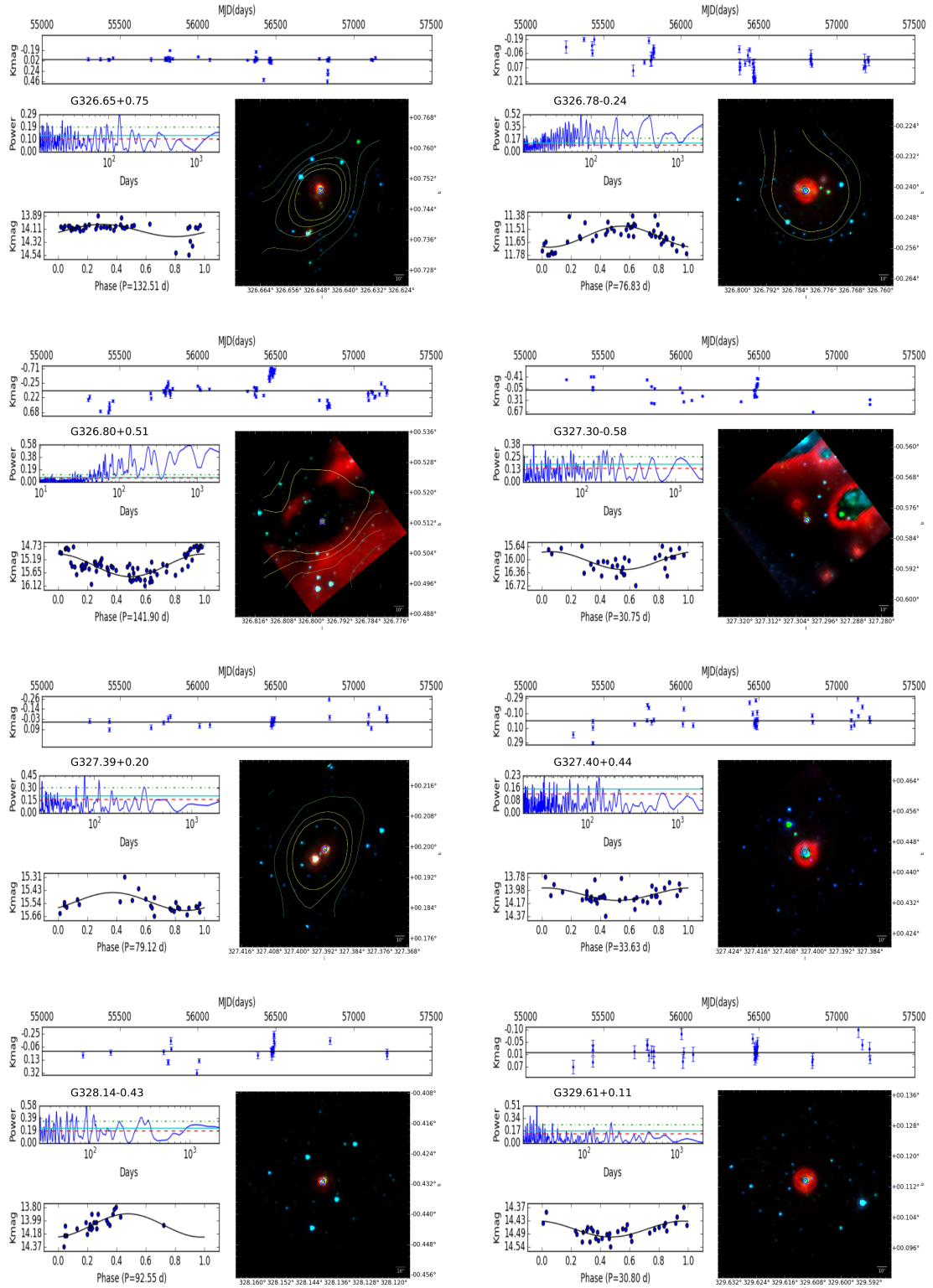


Figure A.3: Continuation of Fig. A.1.

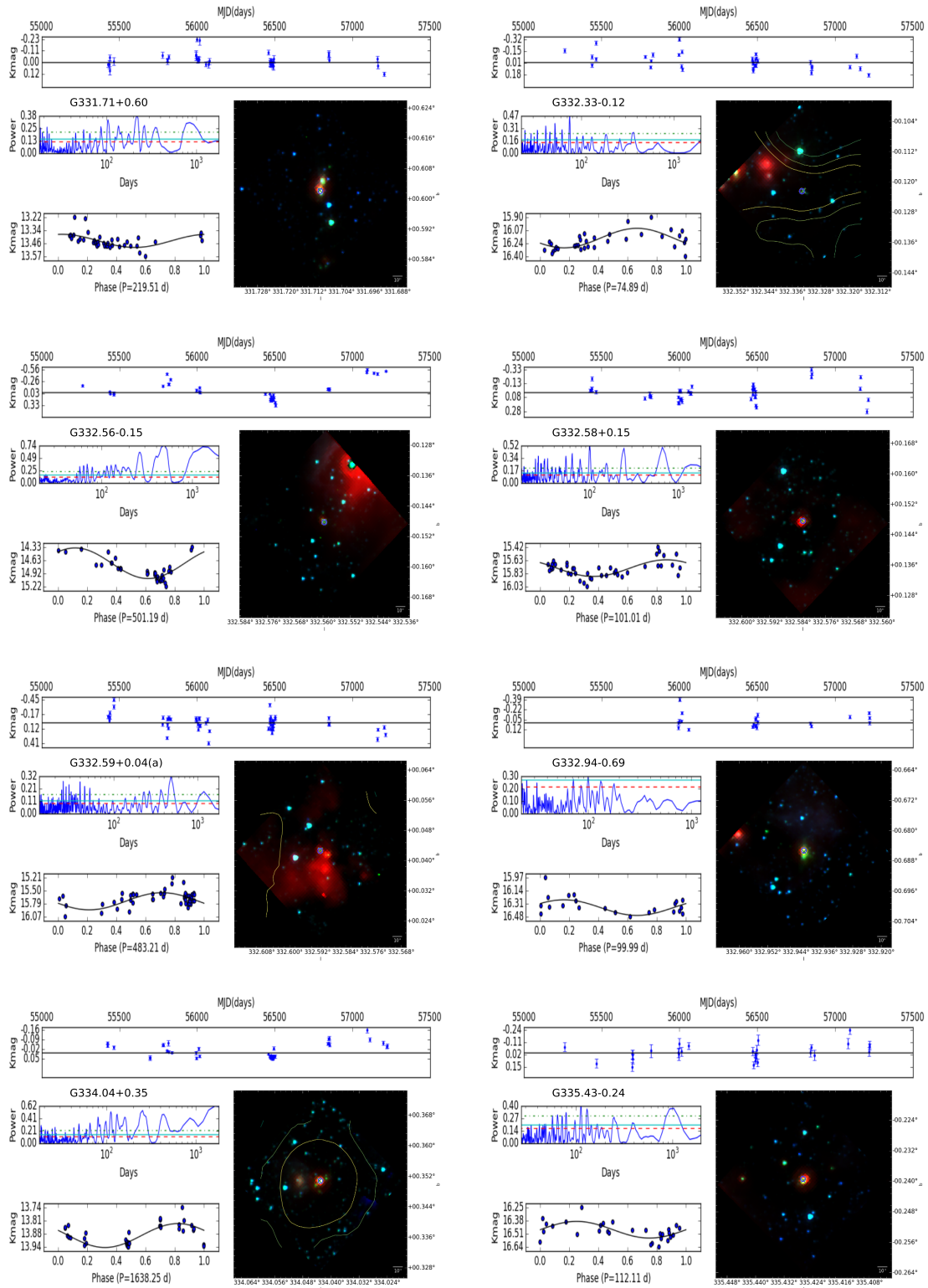


Figure A.4: Continuation of Fig. A.1.

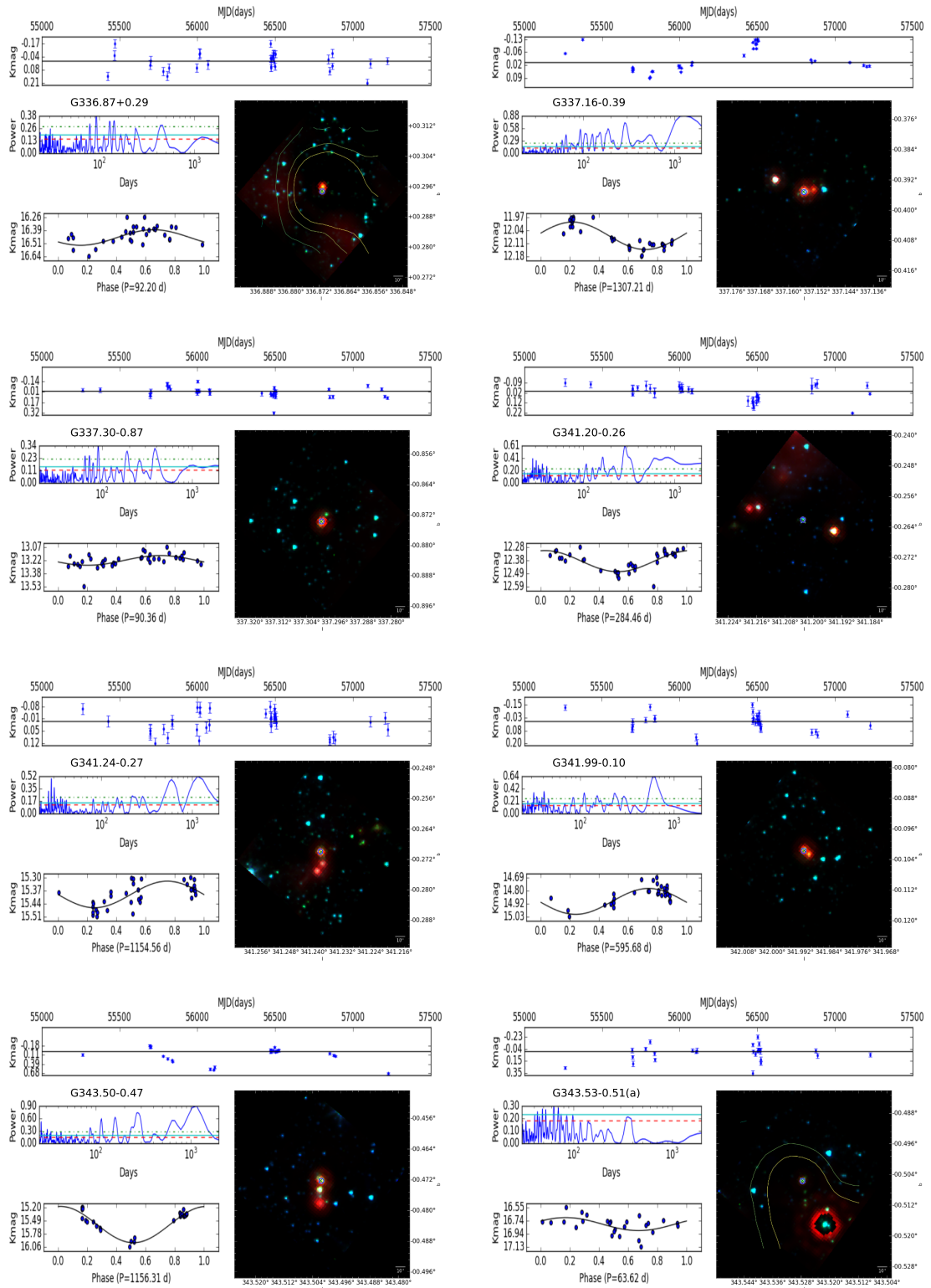


Figure A.5: Continuation of Fig. A.1.

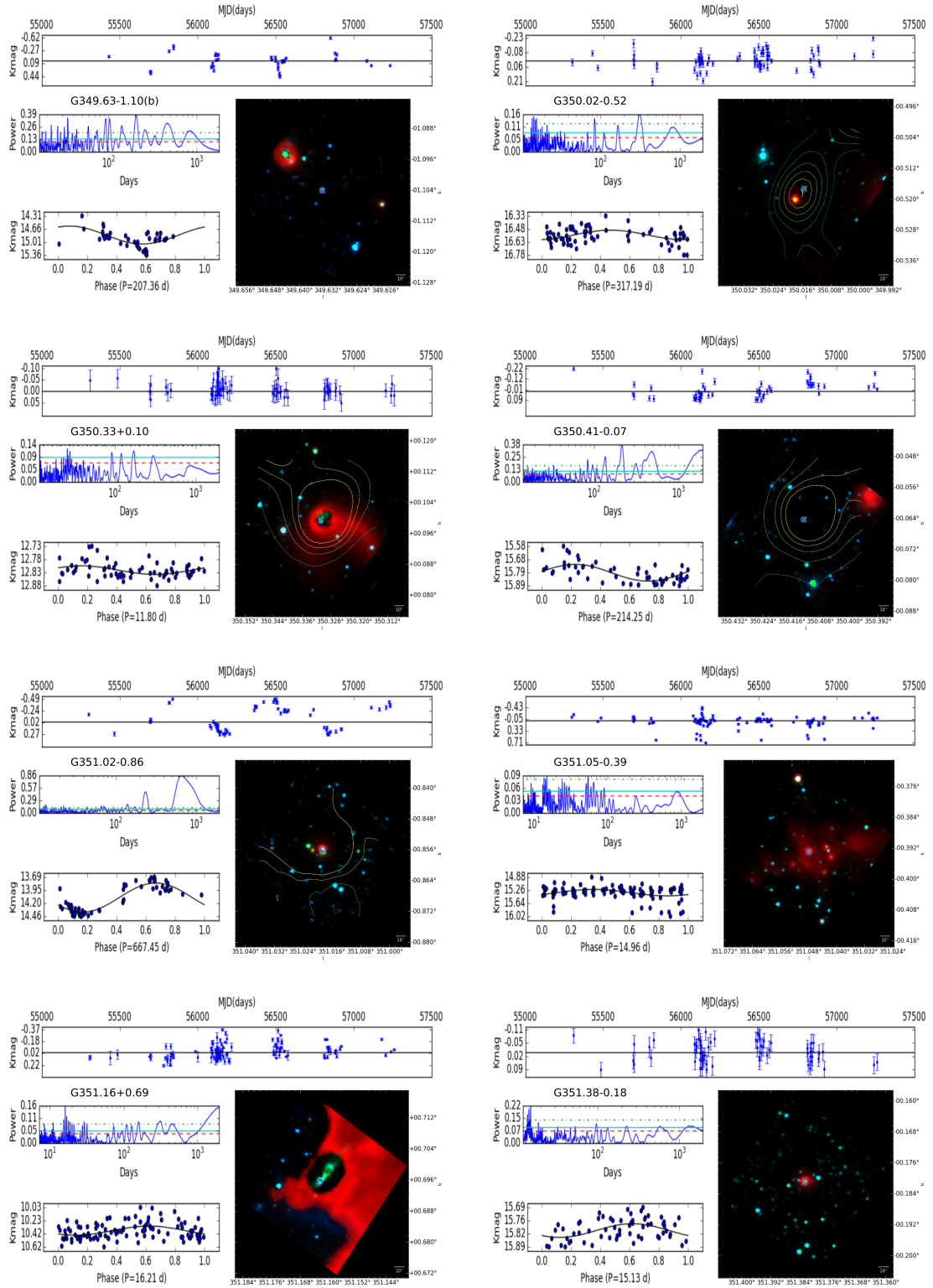


Figure A.7: Continuation of Fig. A.1.

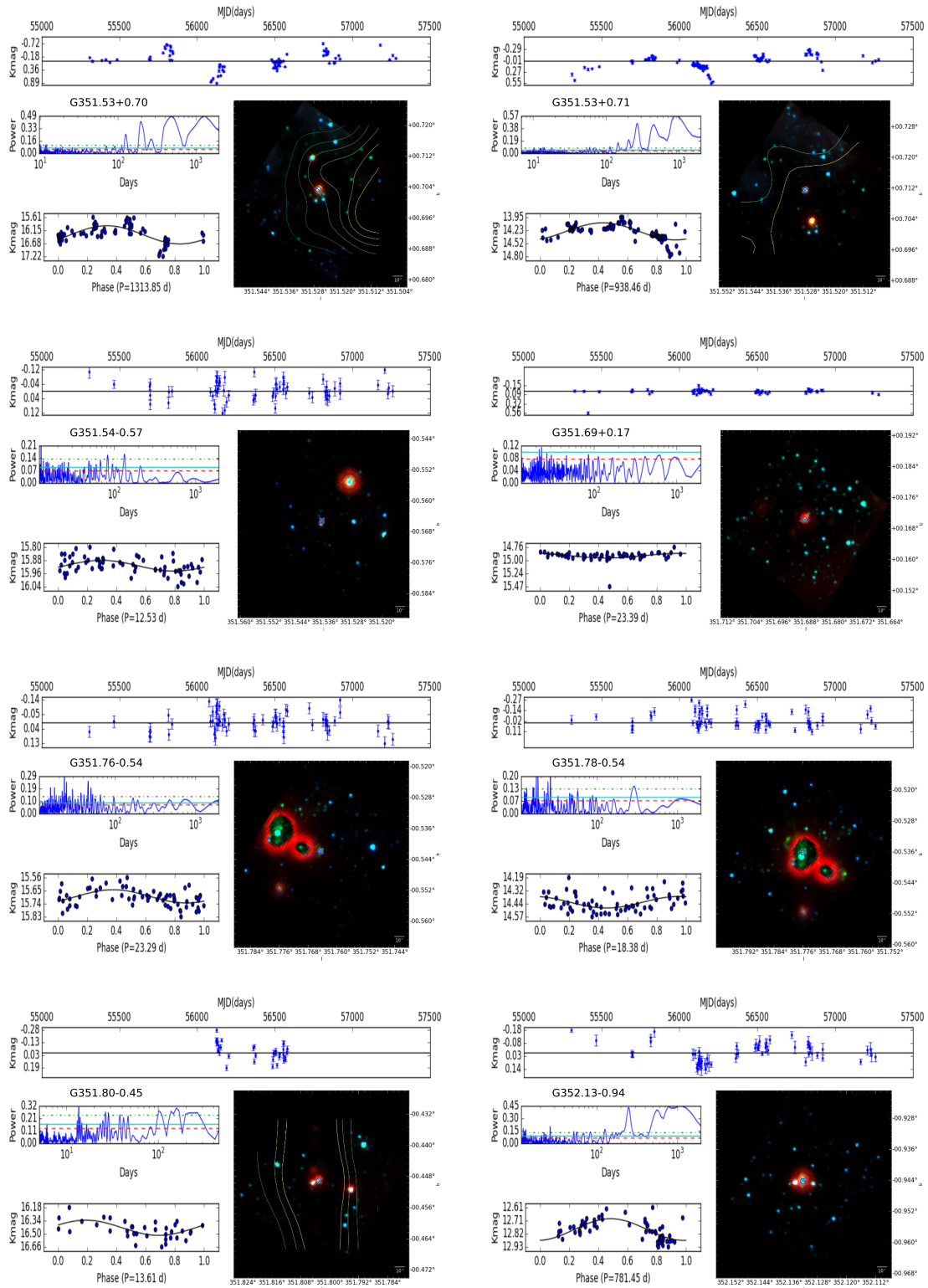


Figure A.8: Continuation of Fig. A.1.

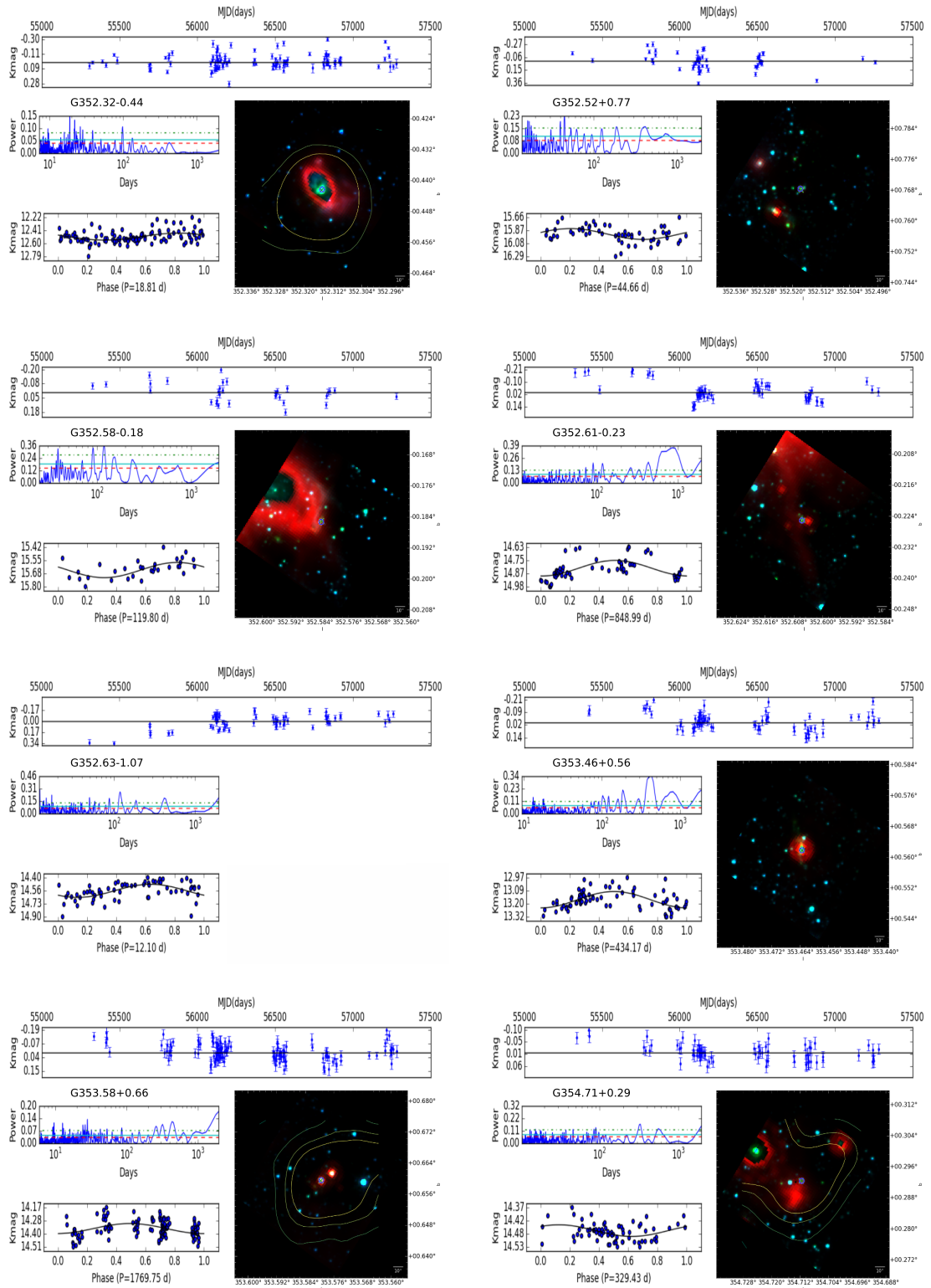


Figure A.9: Continuation of Fig. A.1.

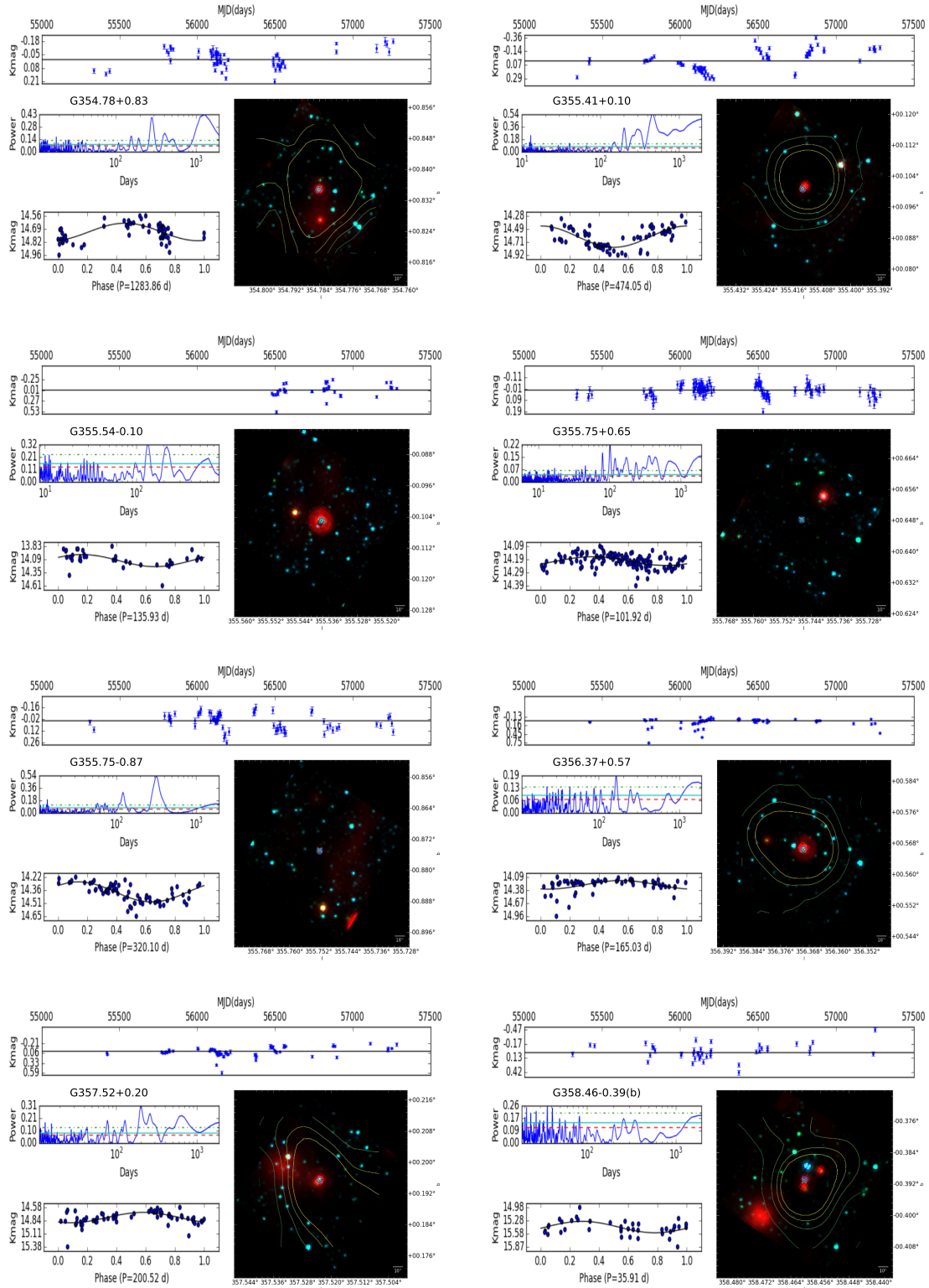


Figure A.10: Continuation of Fig. A.1.

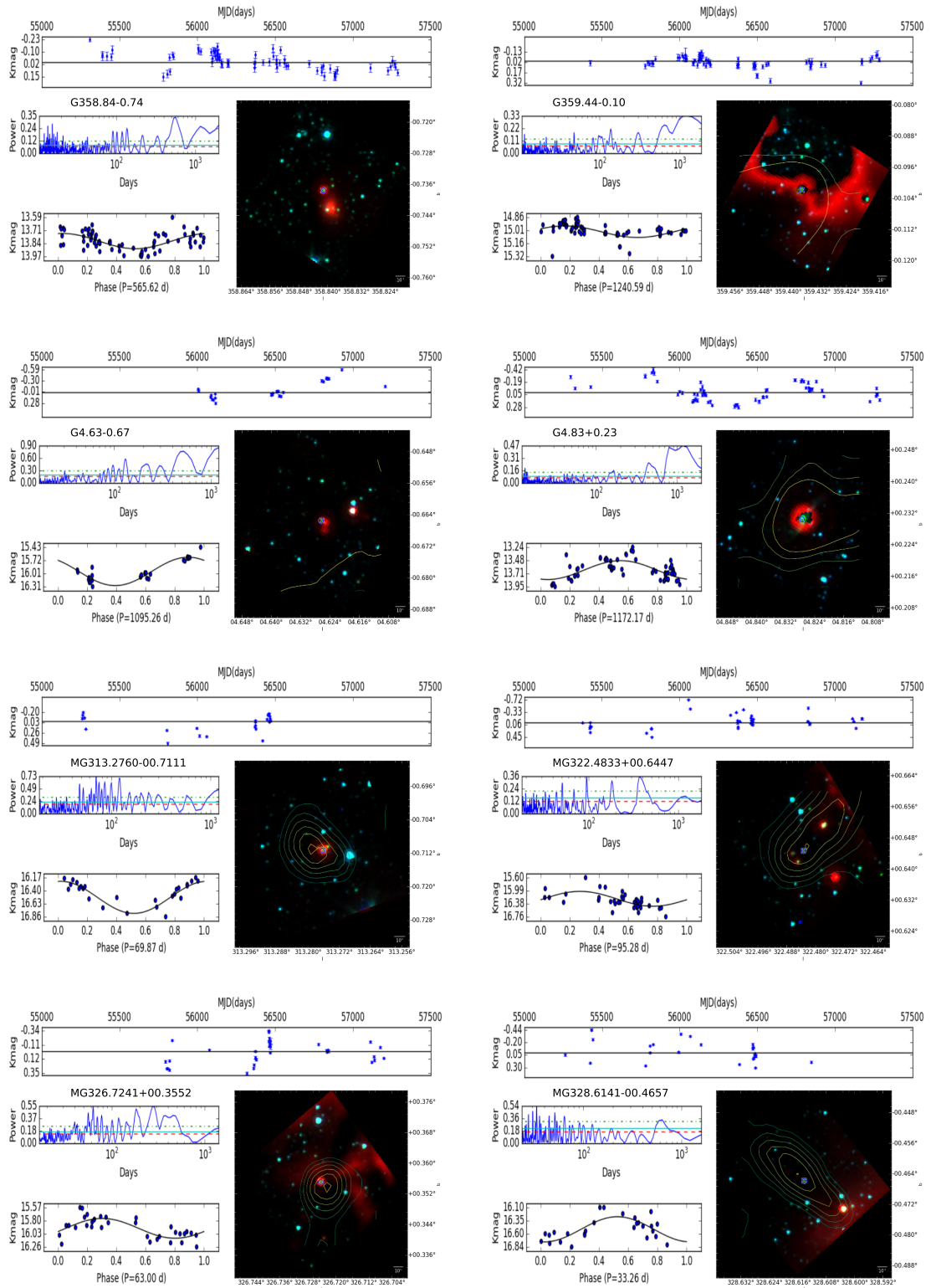


Figure A.11: Continuation of Fig. A.1.

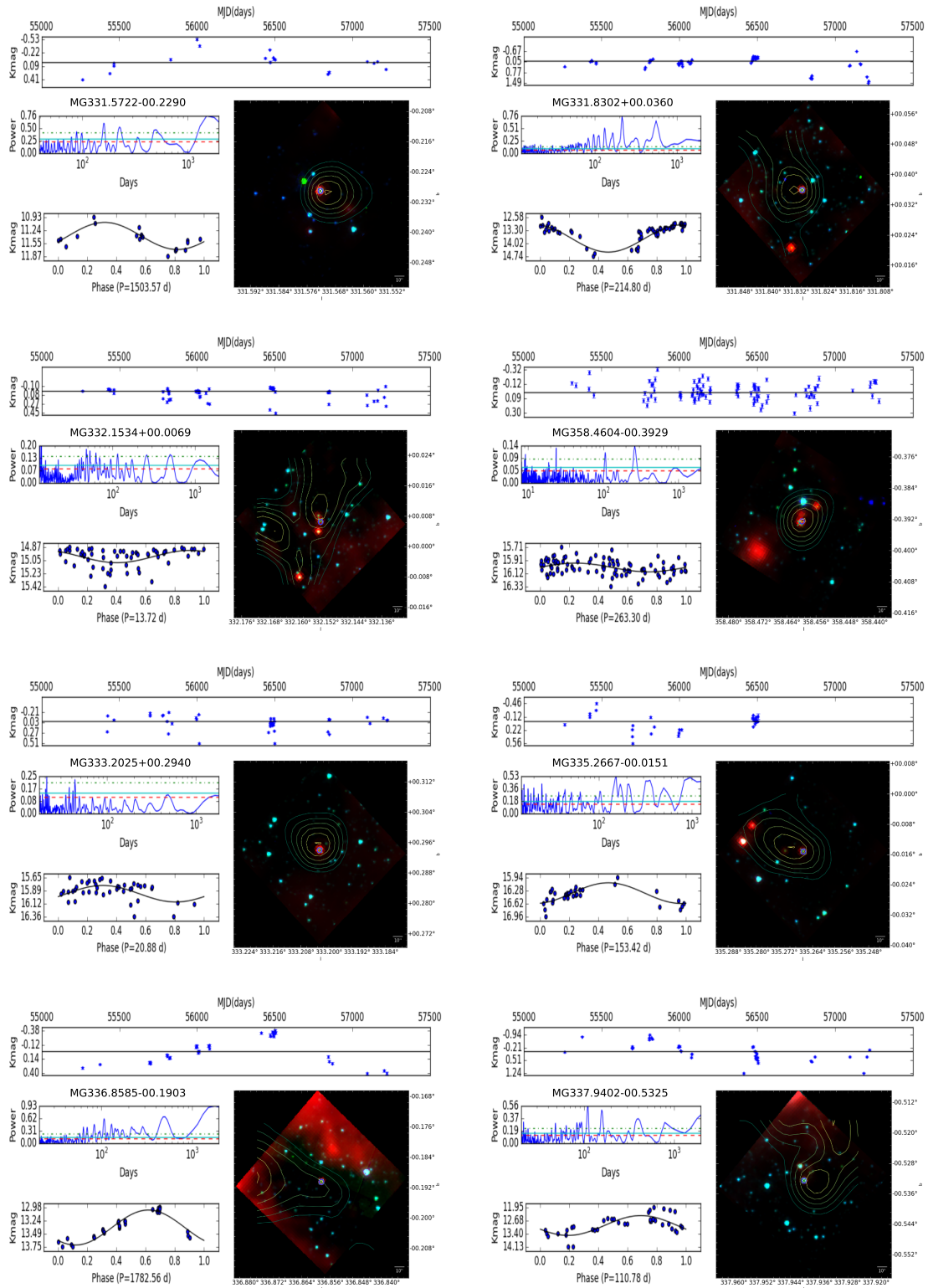


Figure A.12: Continuation of Fig. A.1.

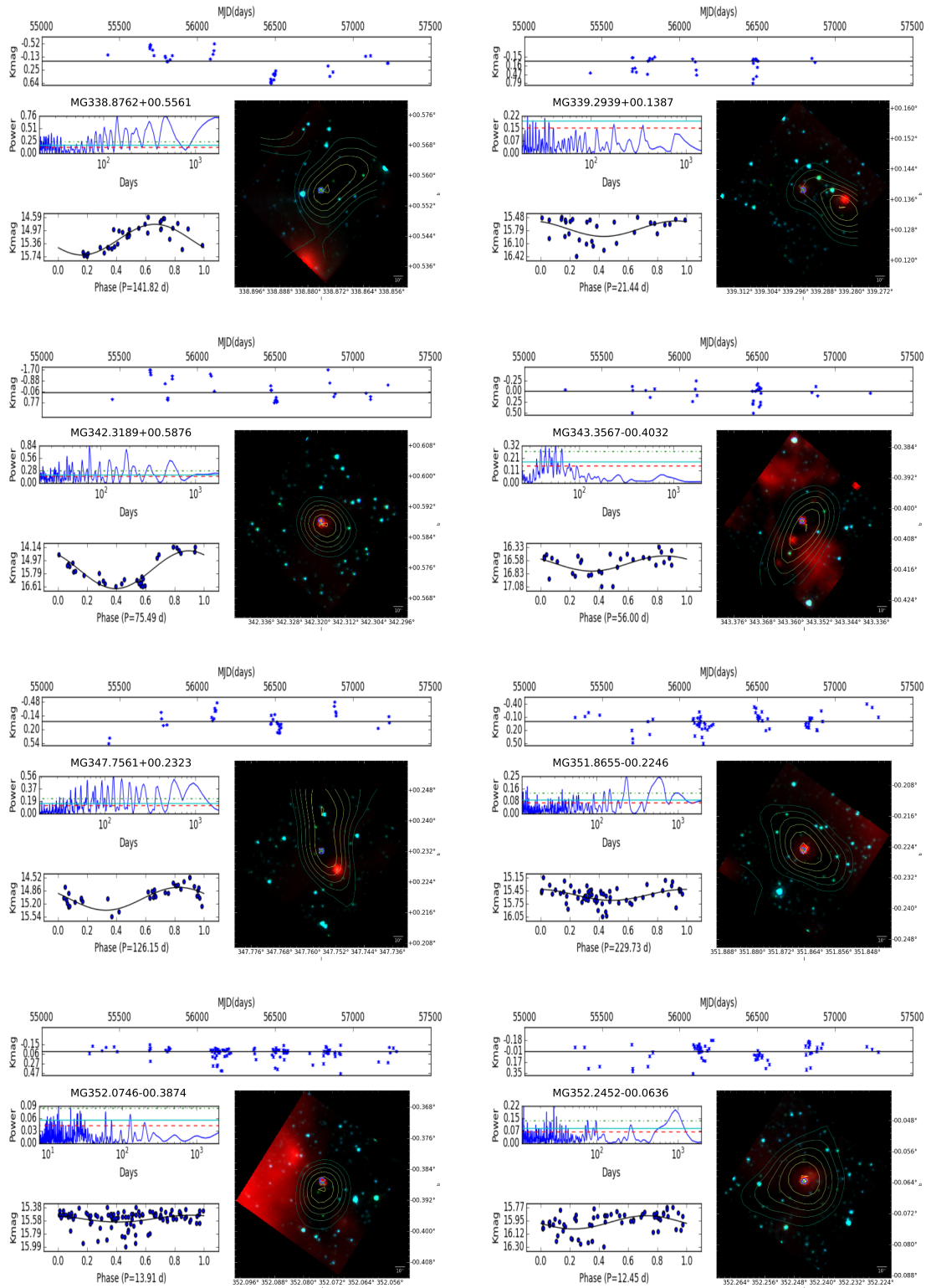


Figure A.13: Continuation of Fig. A.1.

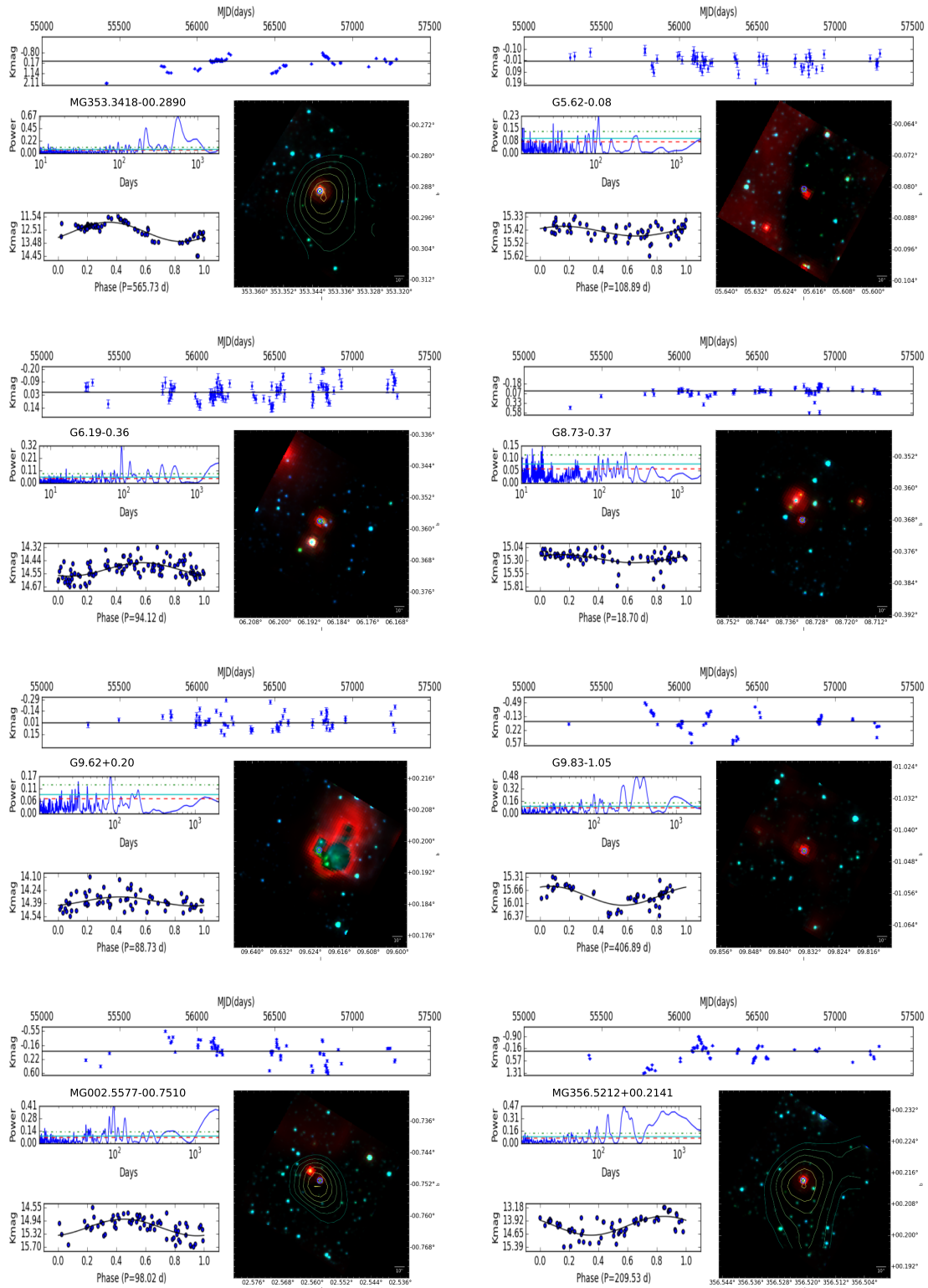


Figure A.14: Continuation of Fig. A.1.

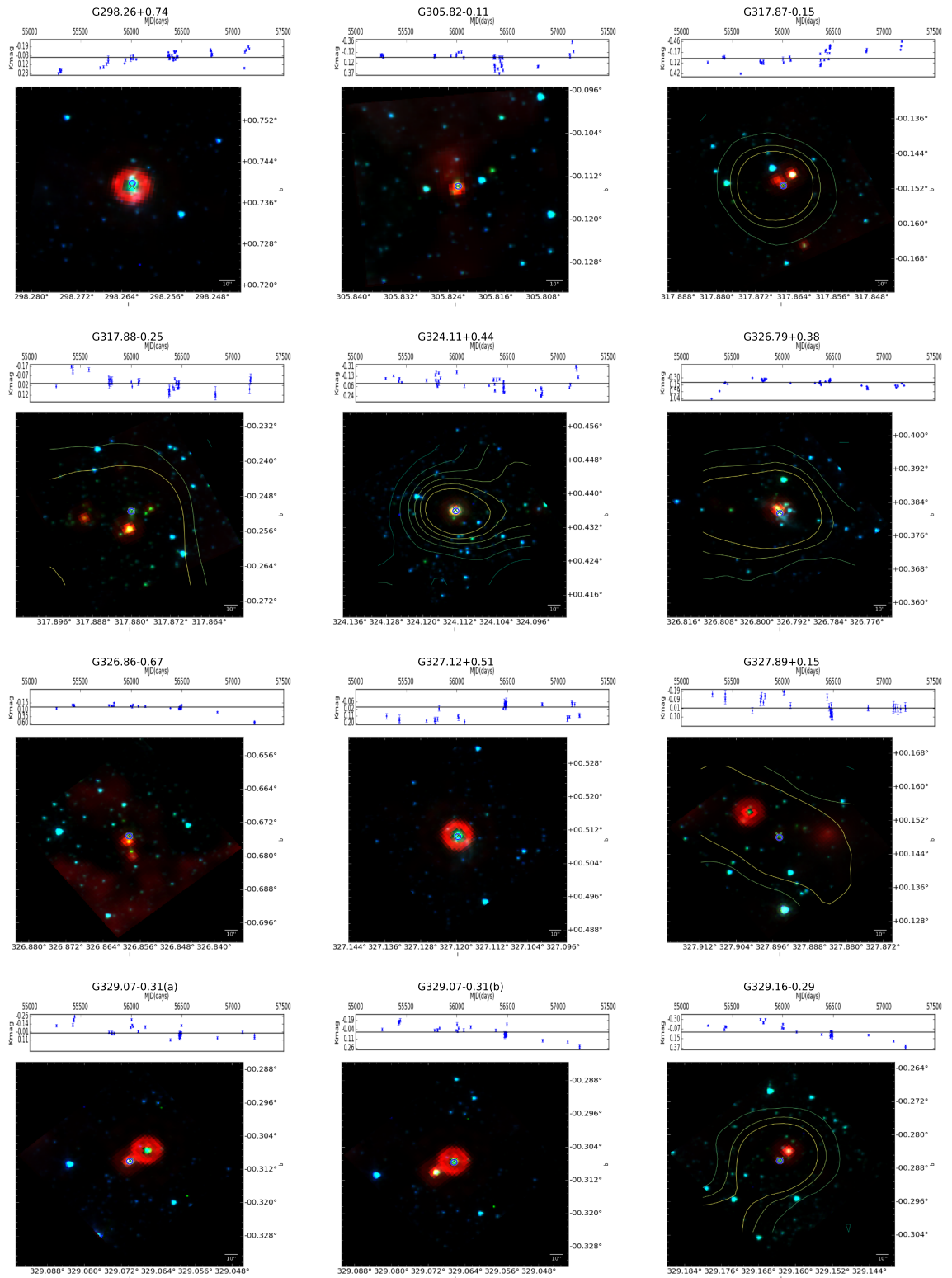


Figure A.15: Continuation of Fig. A.1.

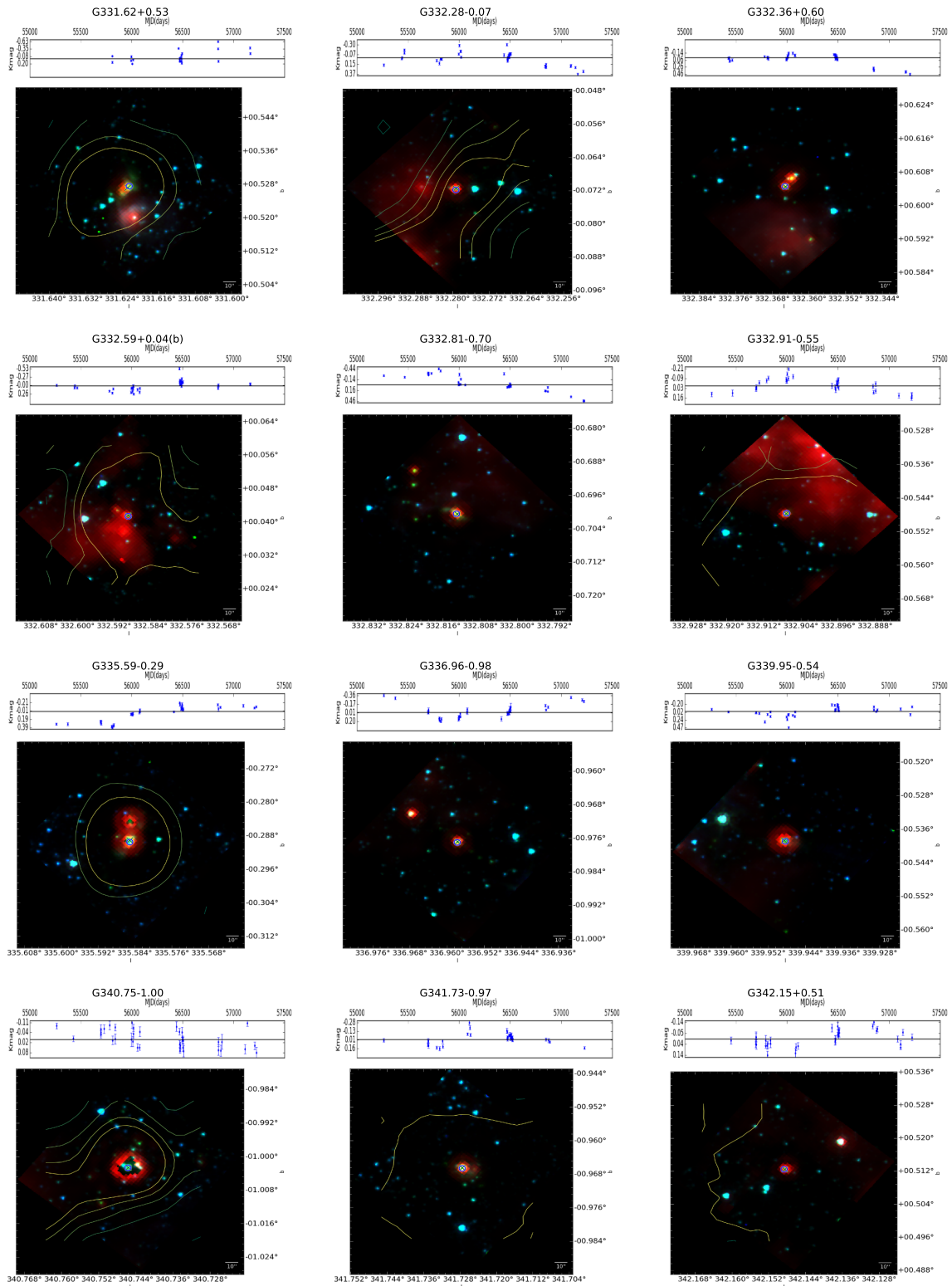


Figure A.16: Continuation of Fig. A.1.

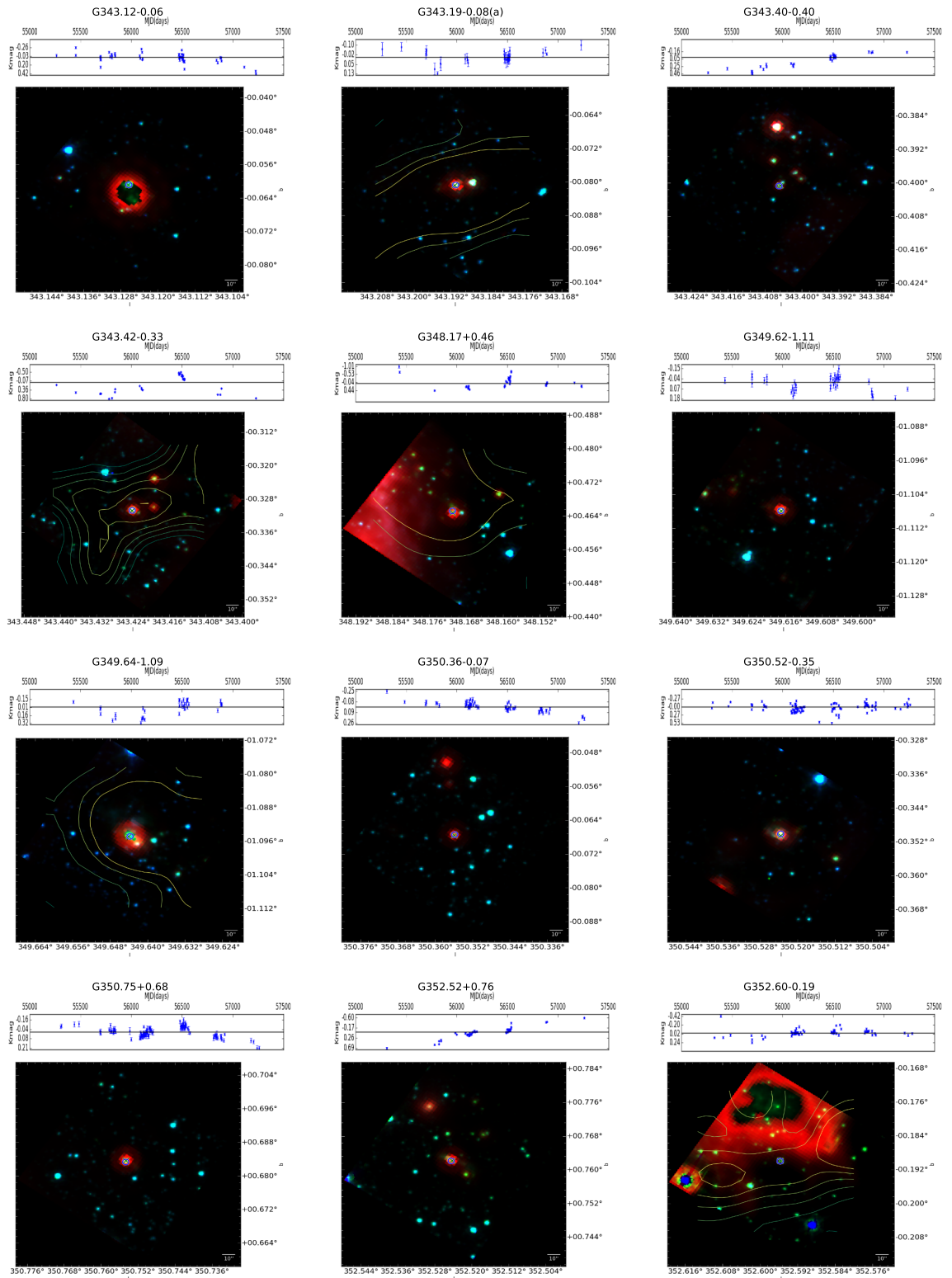


Figure A.17: Continuation of Fig. A.1.

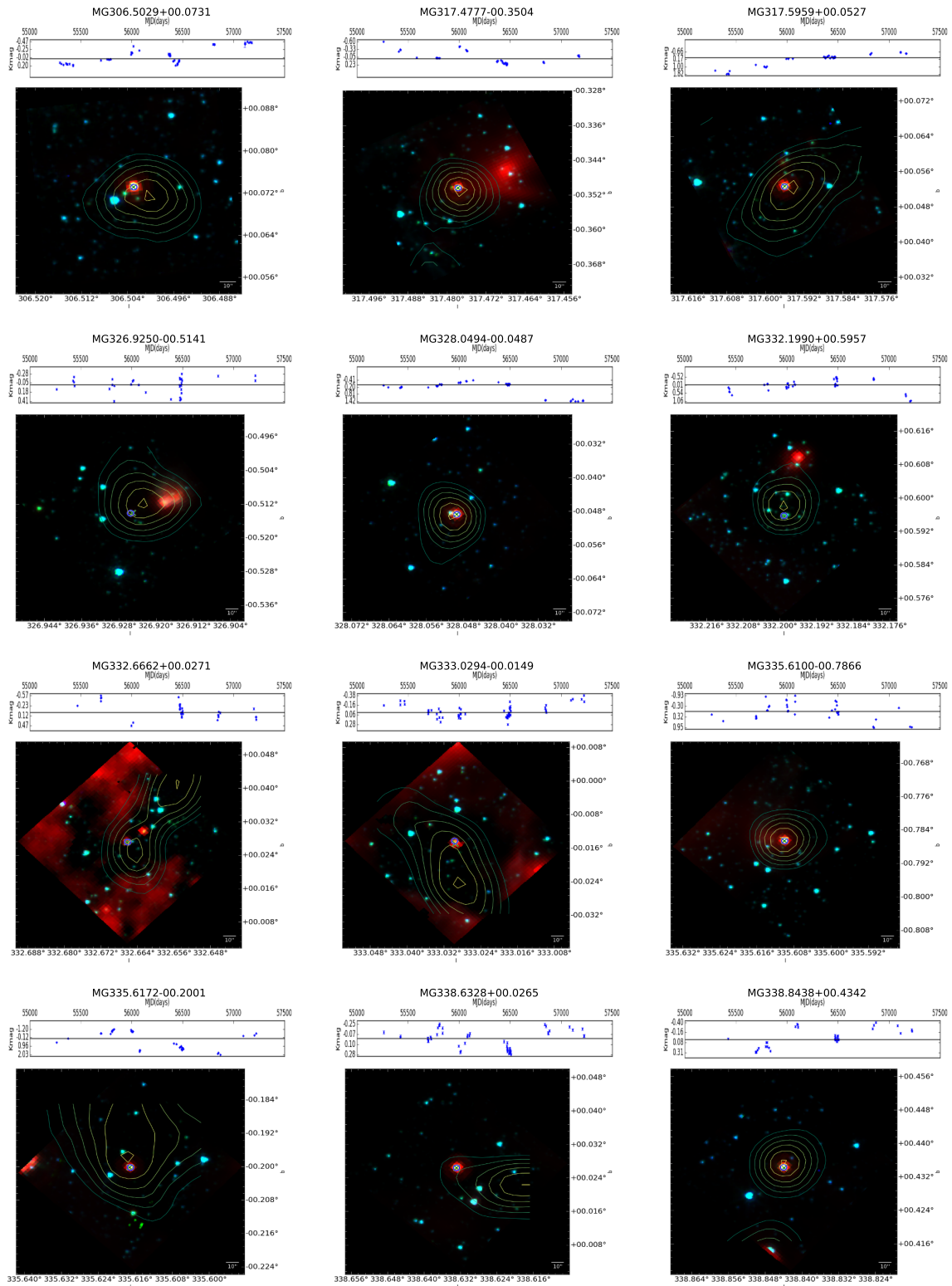


Figure A.18: Continuation of Fig. A.1.

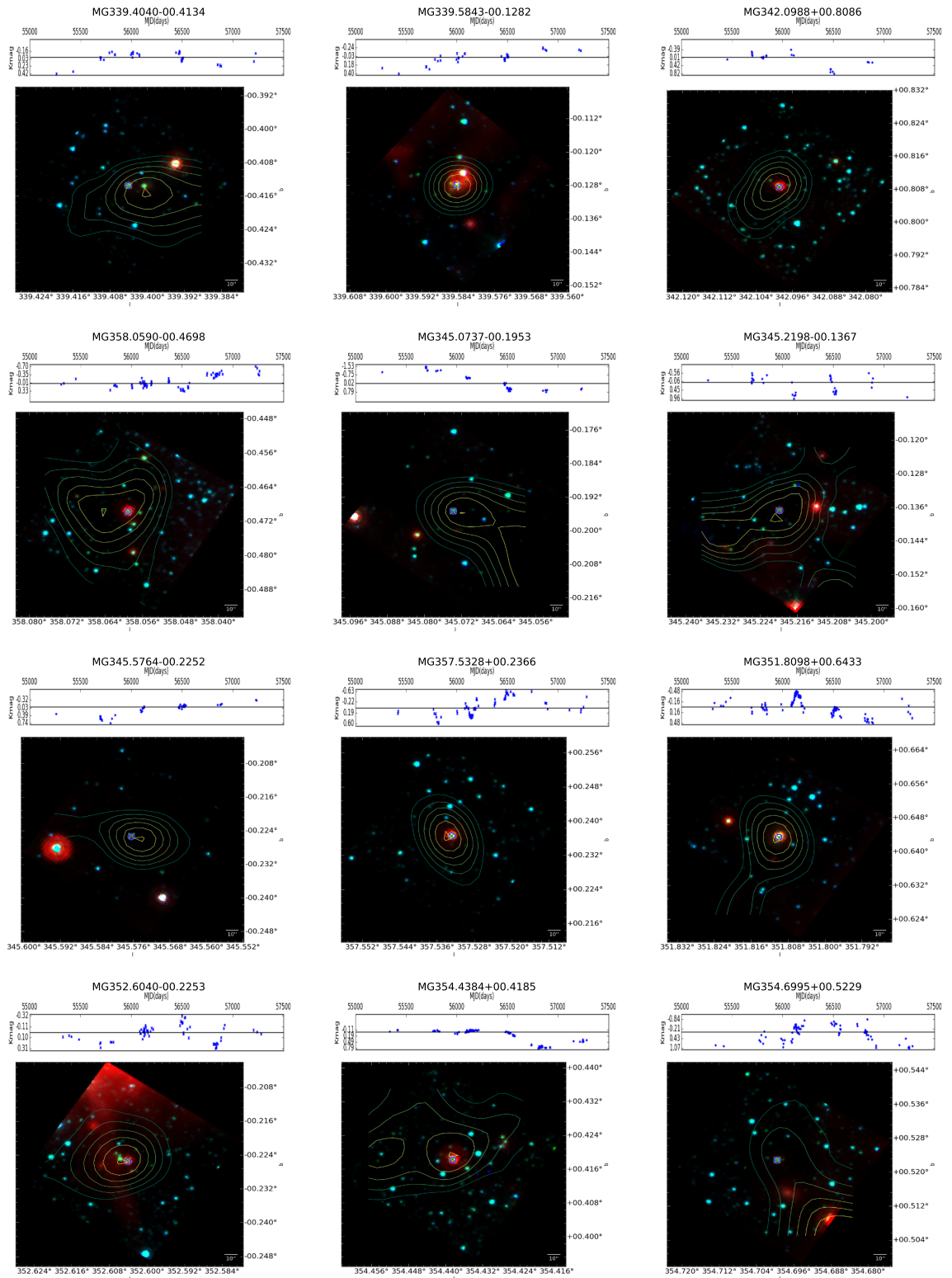


Figure A.19: Continuation of Fig. A.1.

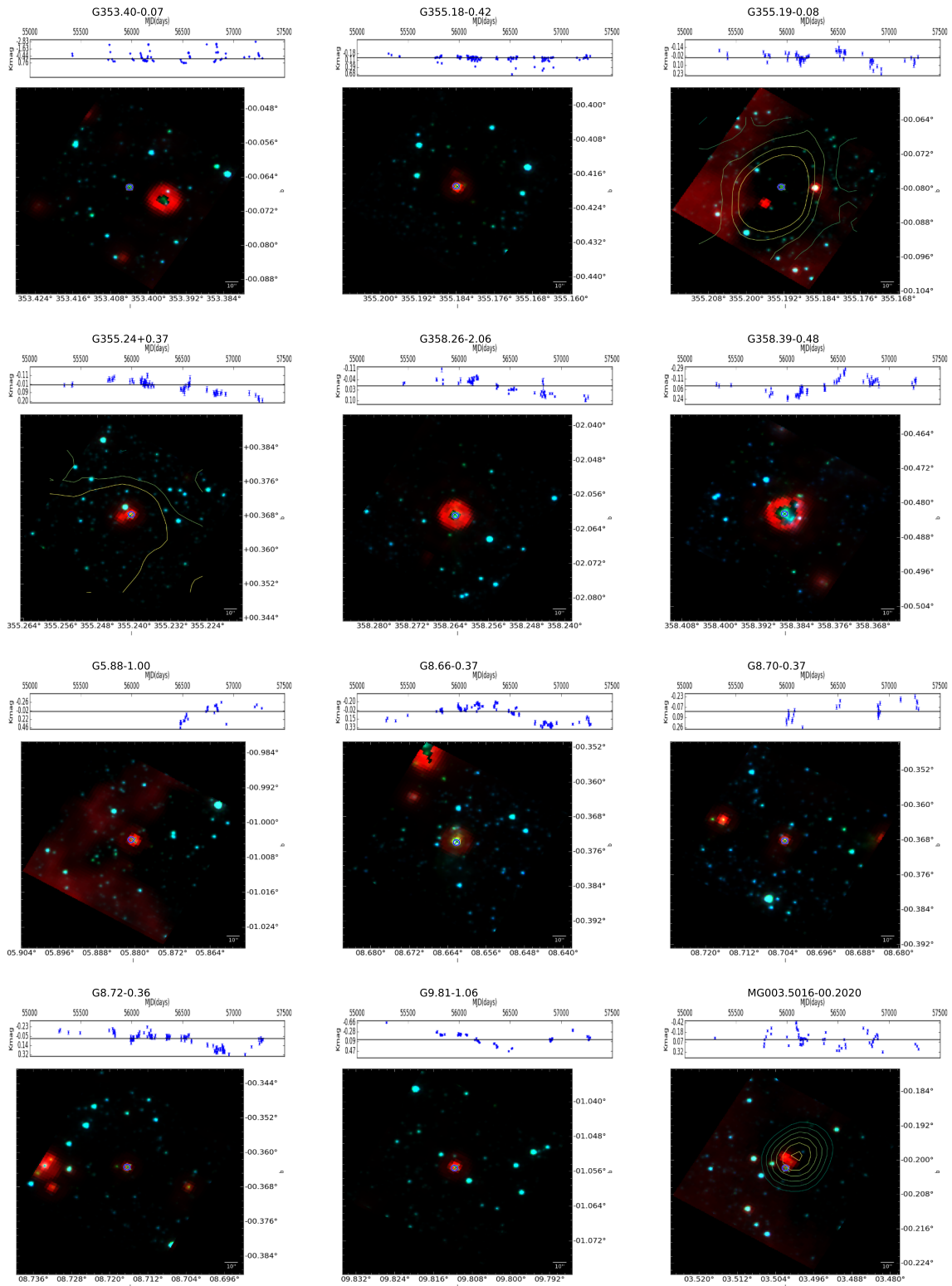


Figure A.20: Continuation of Fig. A.1.

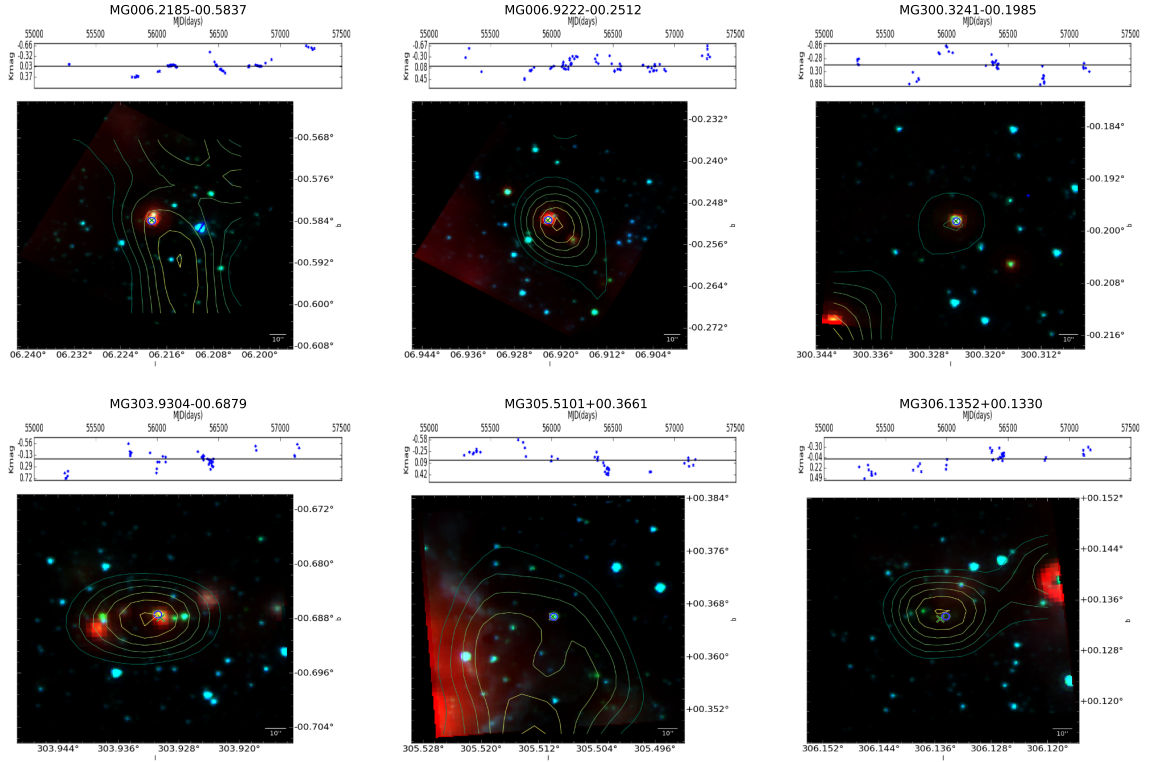


Figure A.21: Continuation of Fig. A.1.

A.2.2 SEDs

Here we present all the final SEDs produced for the variable sources, starting with Fig. A.22. These plots show the best fitted models, and the data points used to perform the fit. Finally the remained of $\chi^2 - \chi_{best}^2 < 3$ models are also shown, along the χ^2 of the best fit, and the fitted A_v .

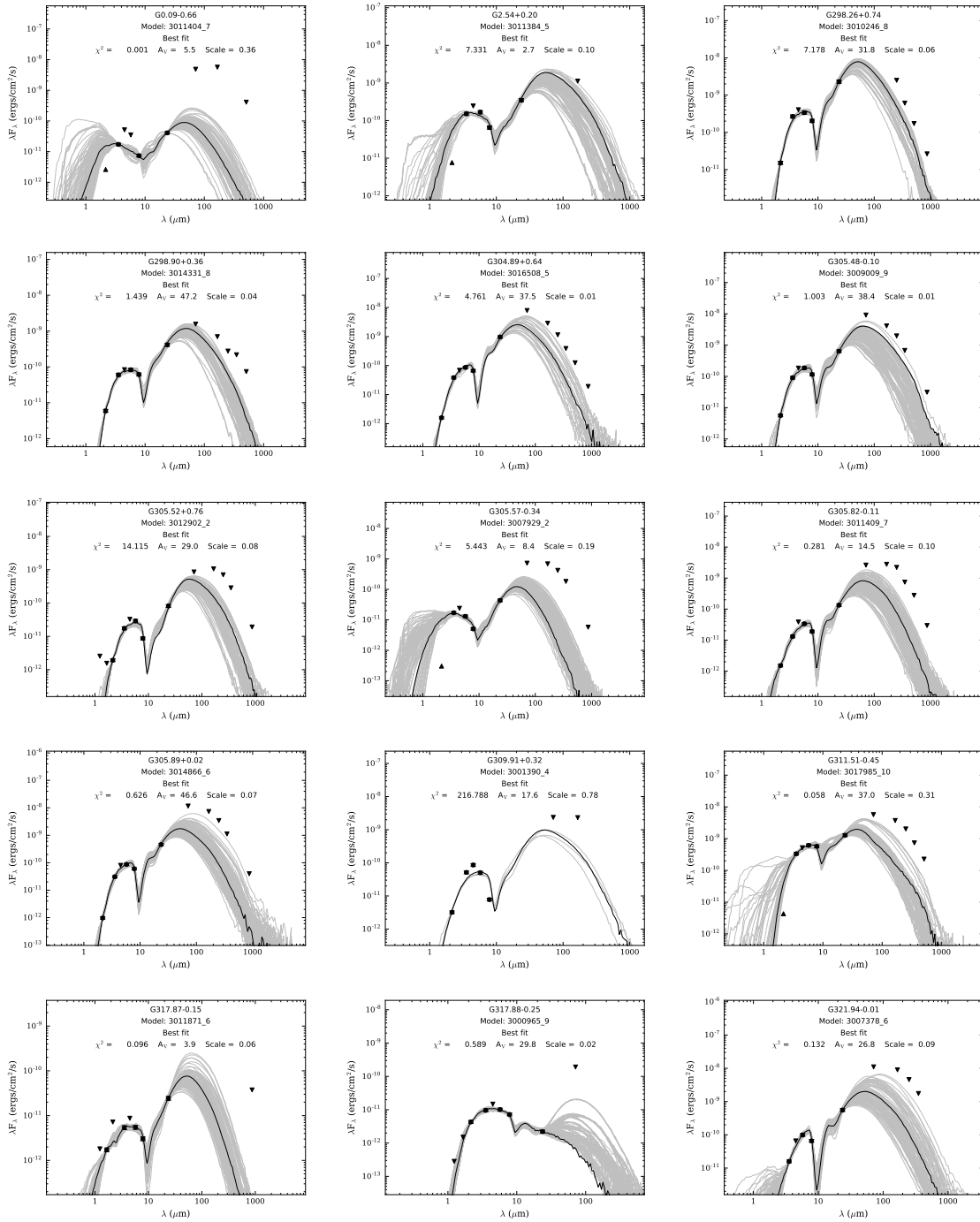


Figure A.22: The fitted SEDs with the best fit model in the black line, the grey lines are other $\chi^2 - \chi_{best}^2 < 3$ models, data points, upper, and lower limits are, respectively, circles, inverted triangles, and triangles.

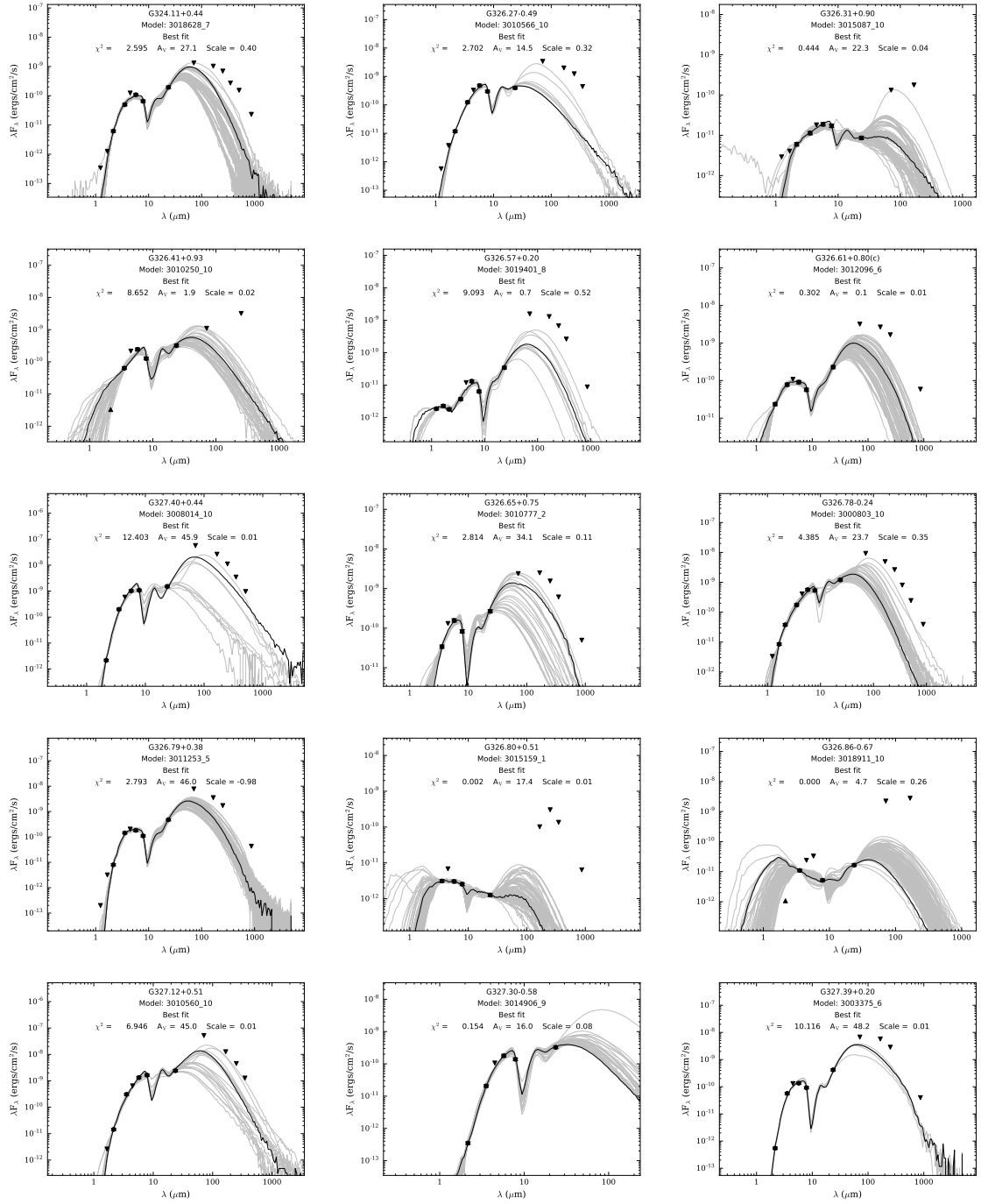


Figure A.23: Continuation of Fig. A.22.

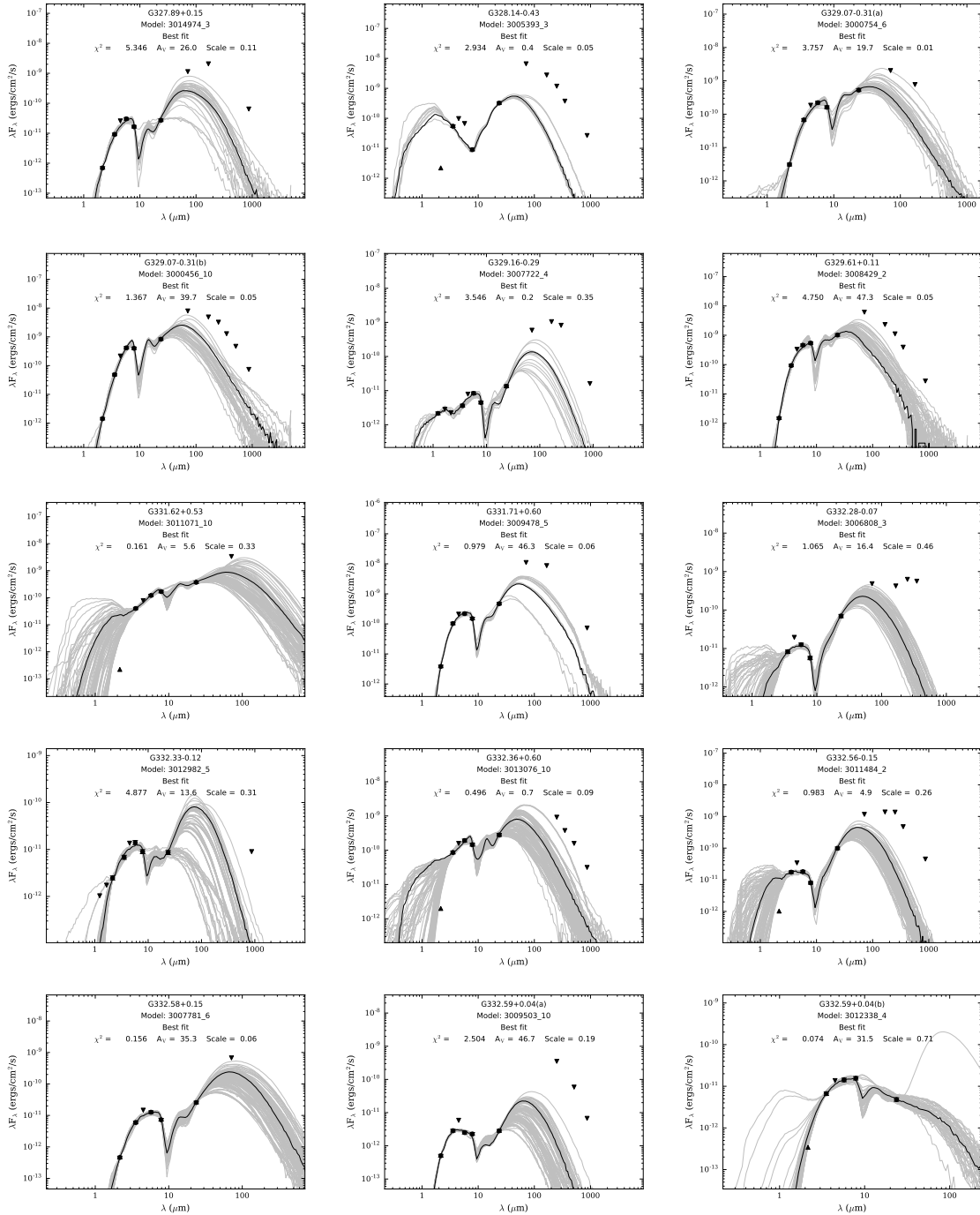


Figure A.24: Continuation of Fig. A.22.

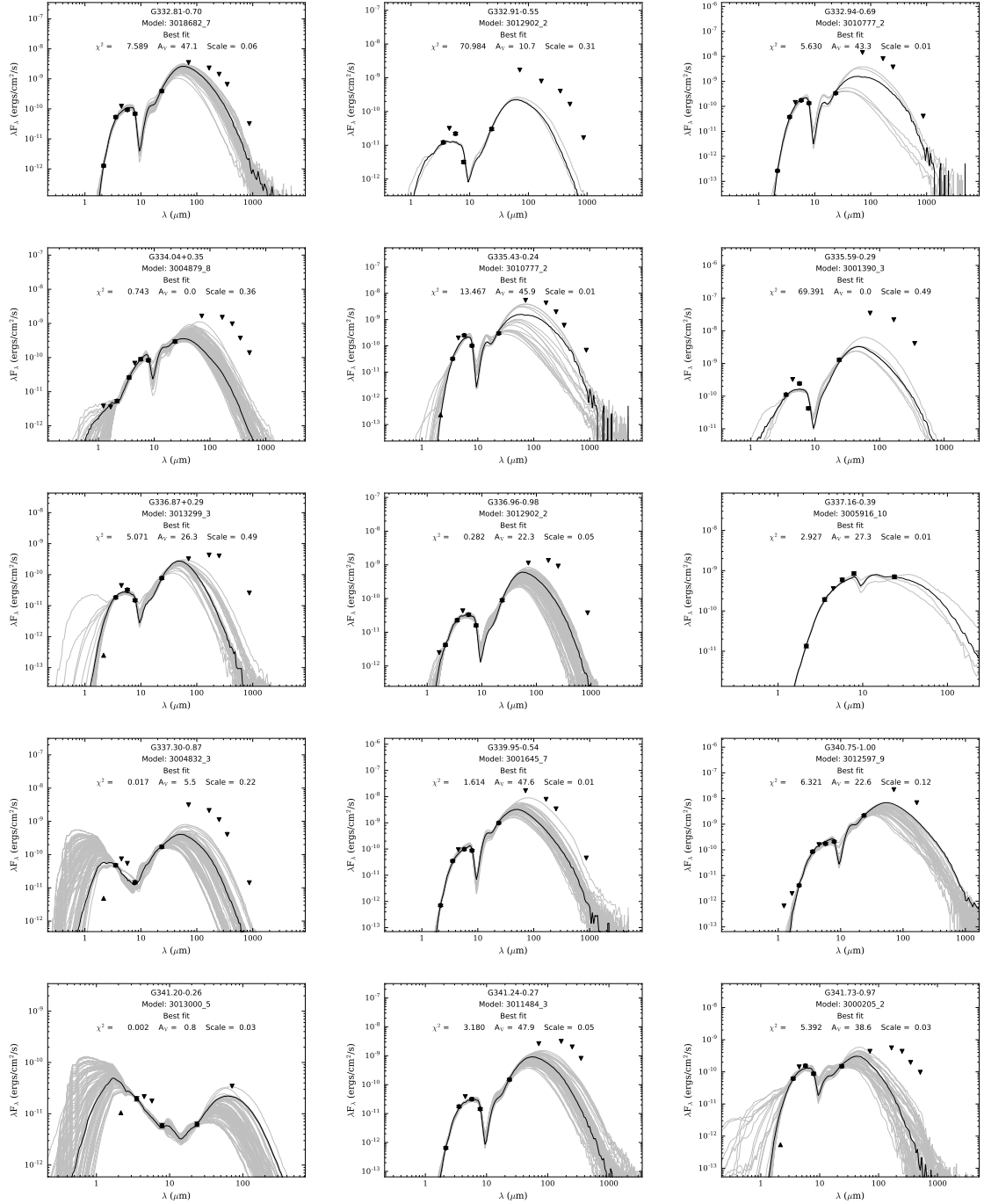


Figure A.25: Continuation of Fig. A.22.

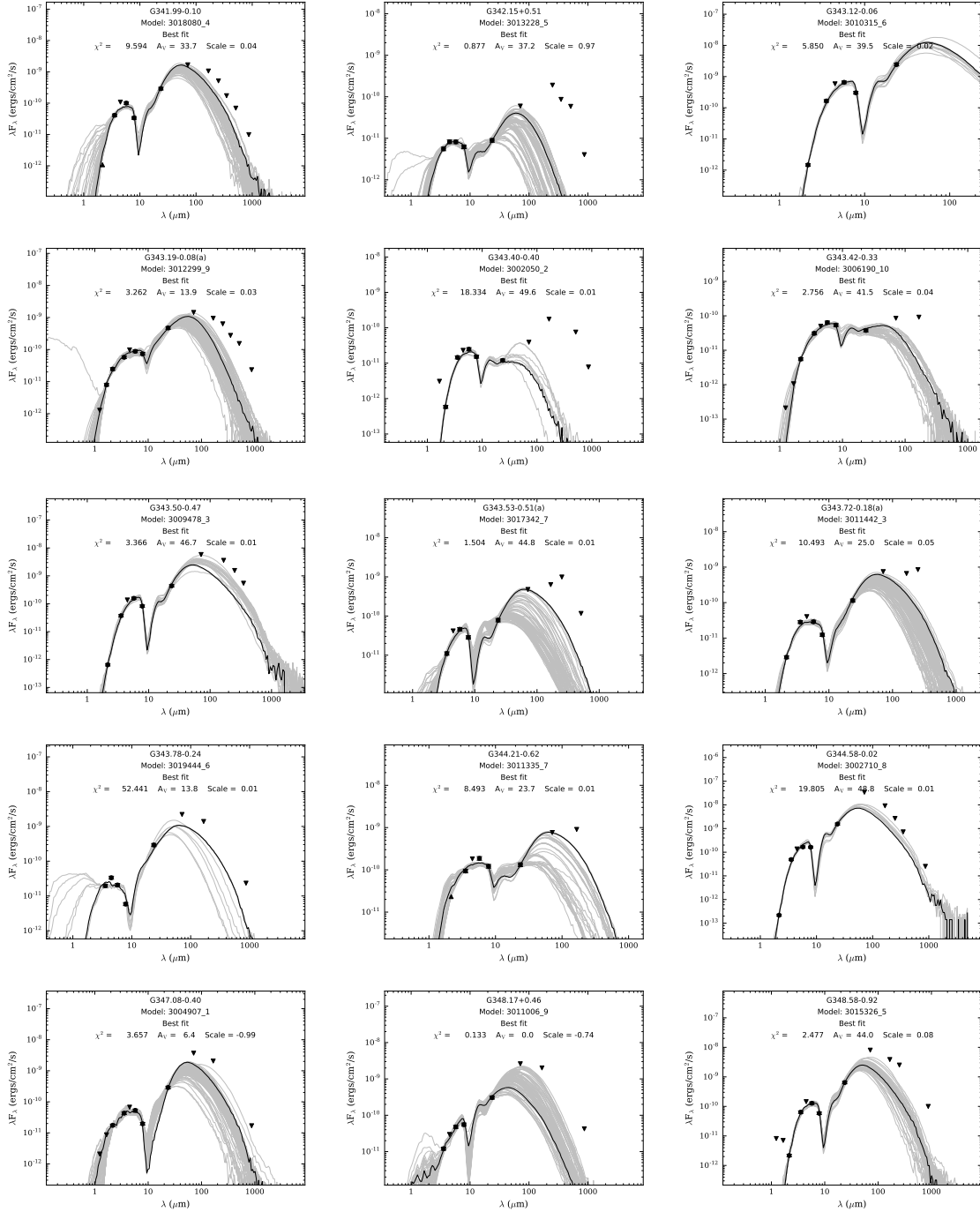


Figure A.26: Continuation of Fig. A.22.

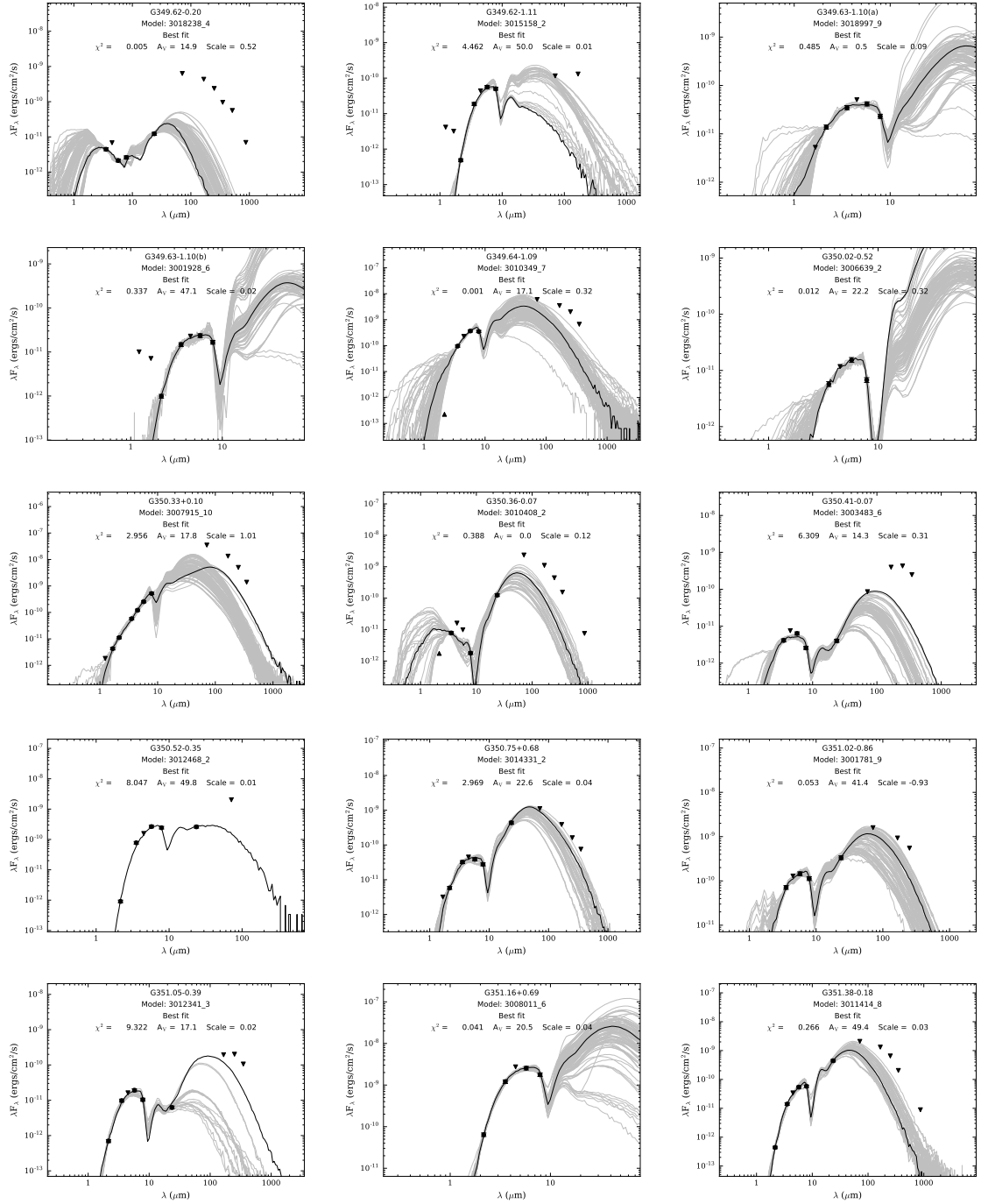


Figure A.27: Continuation of Fig. A.22.

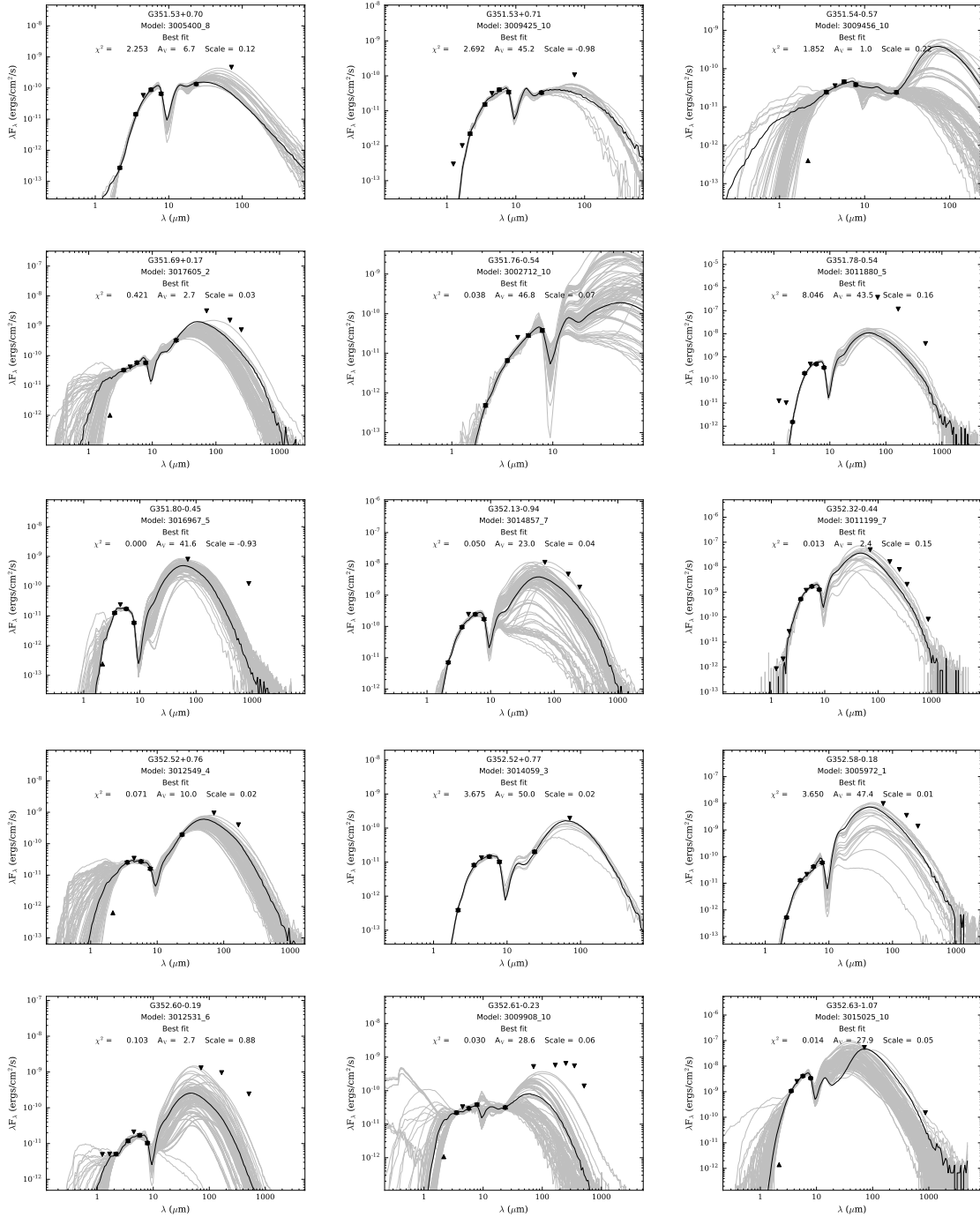


Figure A.28: Continuation of Fig. A.22.

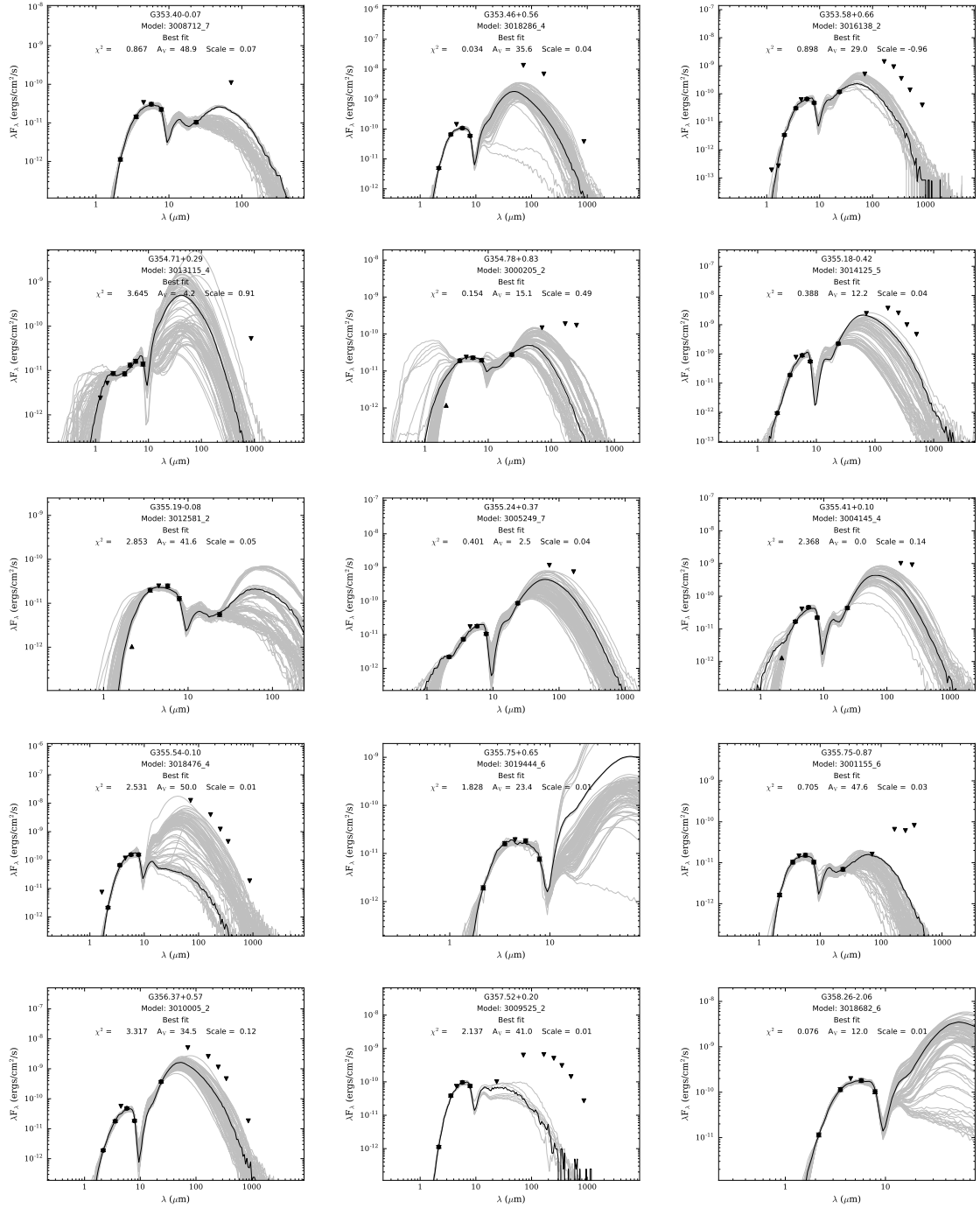


Figure A.29: Continuation of Fig. A.22.

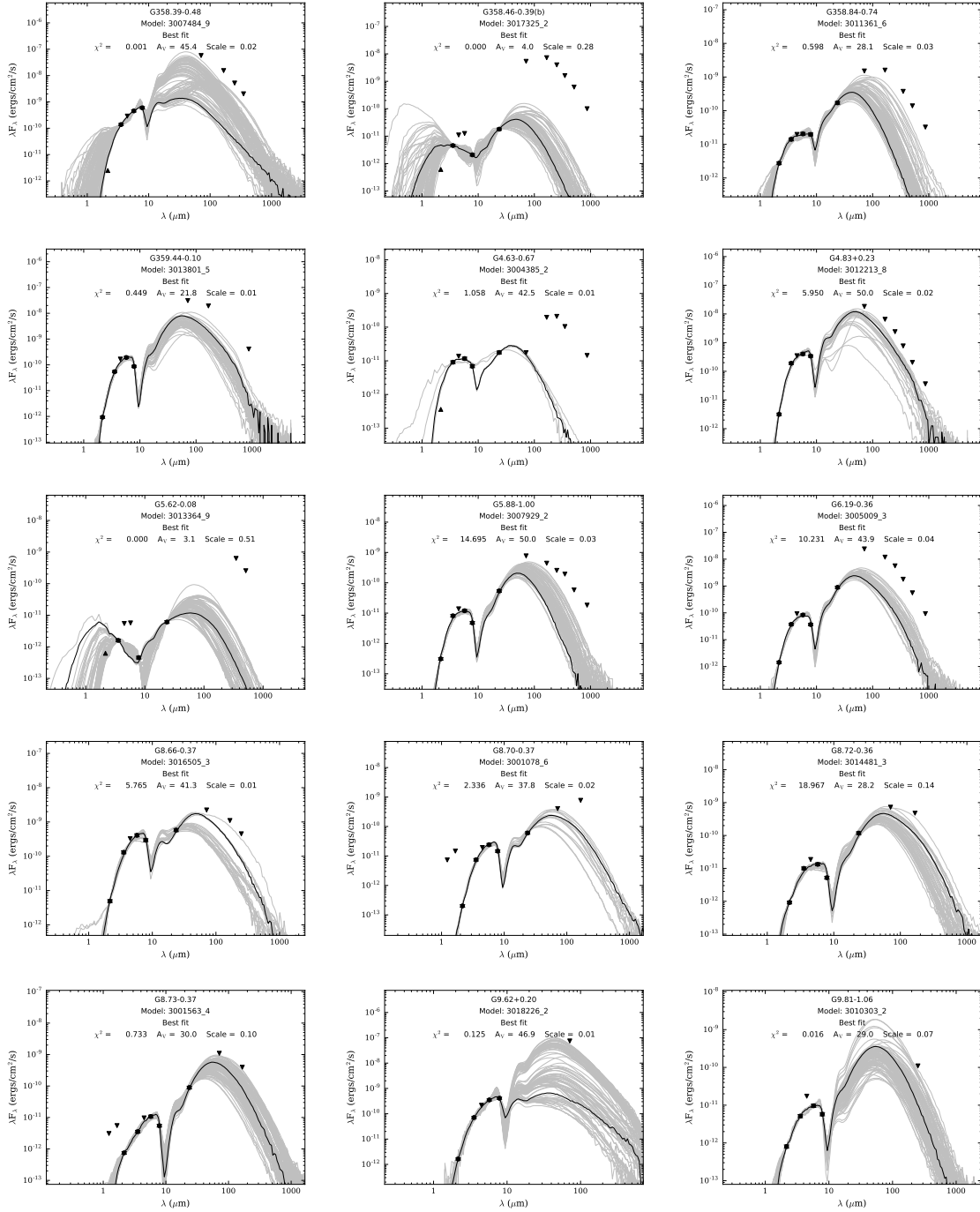


Figure A.30: Continuation of Fig. A.22.

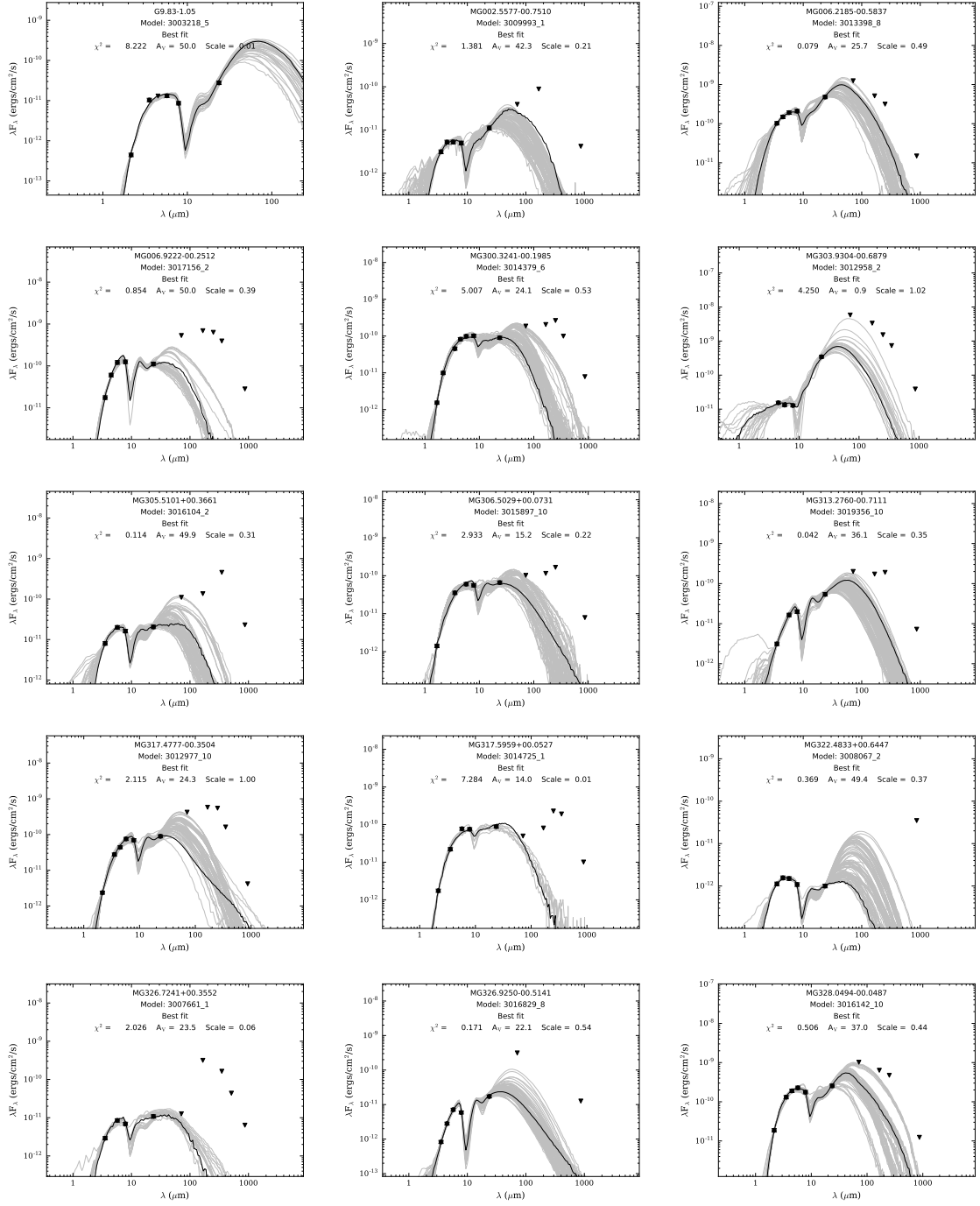


Figure A.31: Continuation of Fig. A.22.

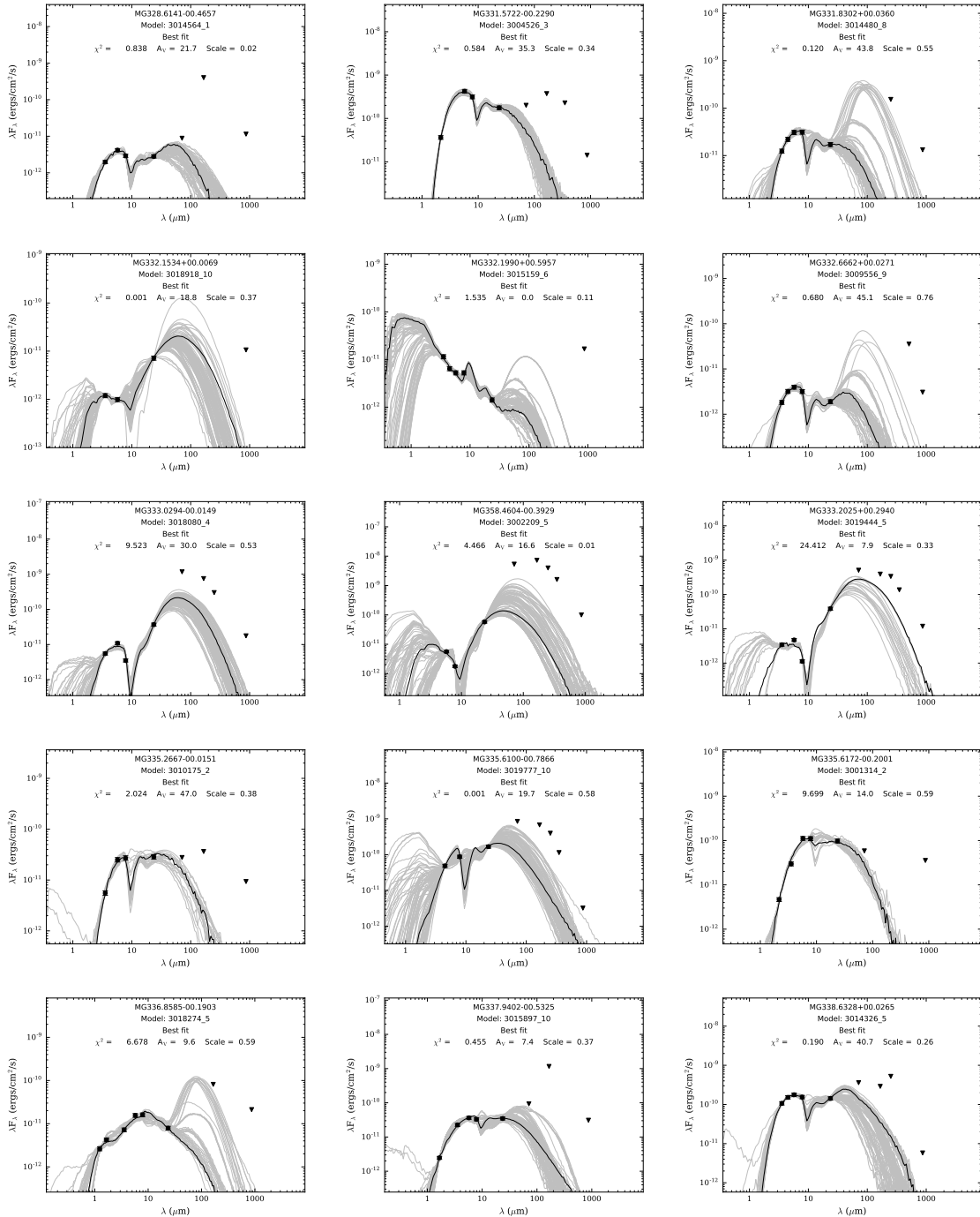


Figure A.32: Continuation of Fig. A.22.

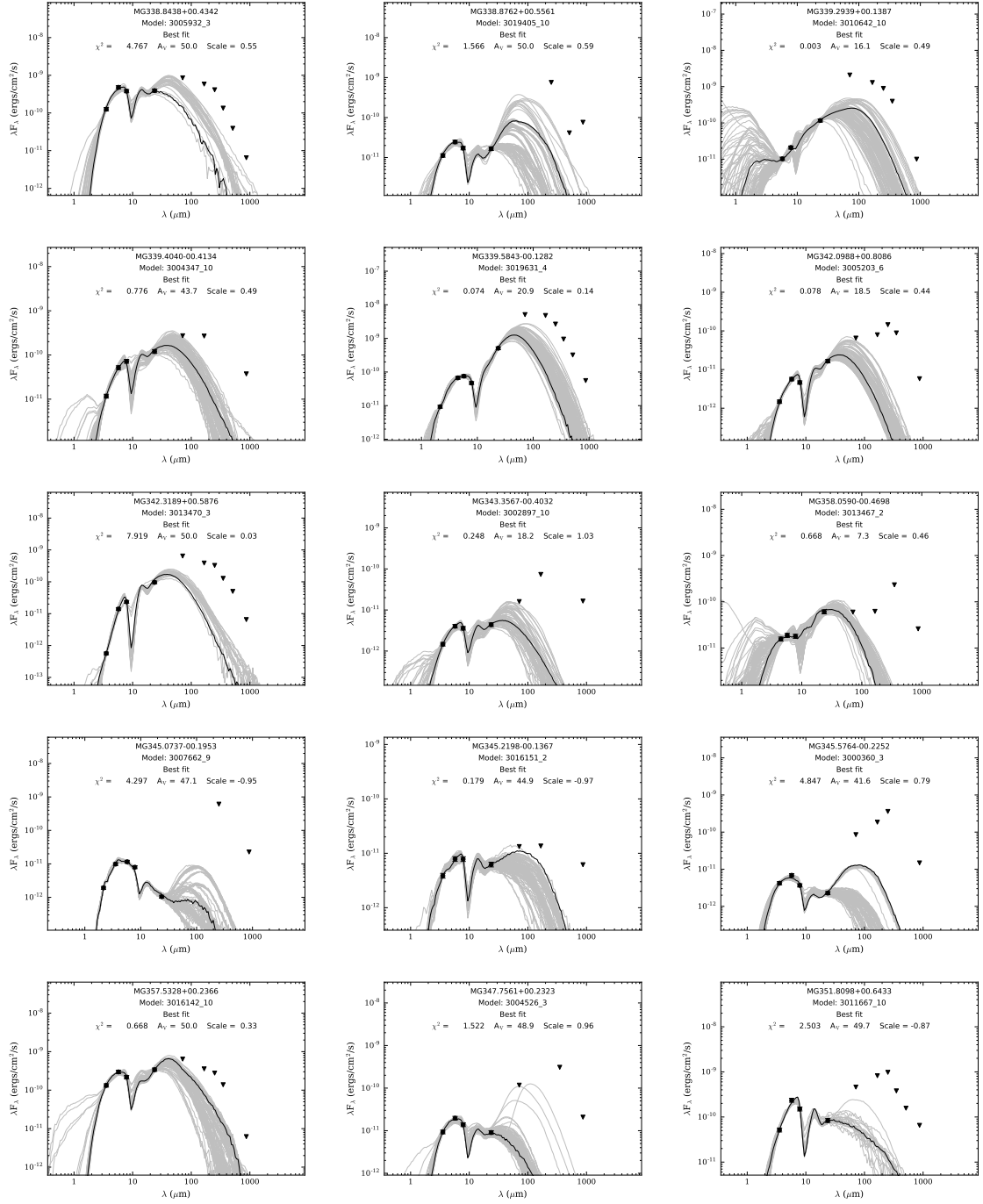


Figure A.33: Continuation of Fig. A.22.

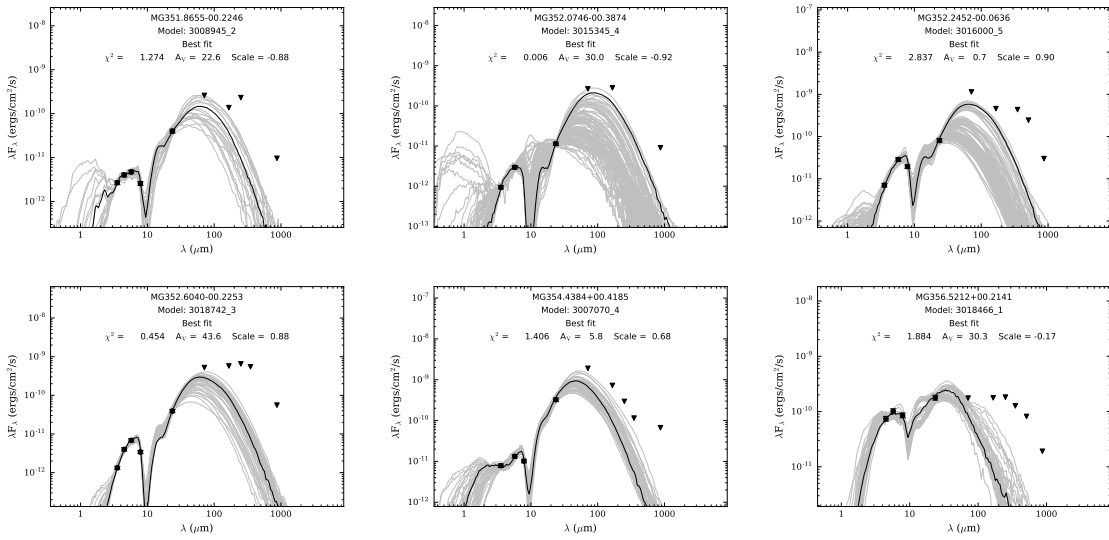


Figure A.34: Continuation of Fig. A.22.

Appendix B

Publications

The following subsections show the output of research done during this PhD. This is split into publications concerning the work presented throughout this thesis and publications that are not directly linked to the work presented above but were still performed during the PhD.

B.1 Thesis publications

B.1.1 Refereed

- Teixeira, G. D. C., Kumar, M. S. N., Smith, L., et al. 2018, *A&A*, 619, A41

B.1.2 Catalogs

- Teixeira, G. D. C., Kumar, M. S. N., Smith, L., et al. 2018, *VizieR Online Data Catalog*, 361,

B.2 Additional Publications

The following publications are the result of work while it was performed during the PhD it was not a direct result of the thesis work. Under this umbrella falls a first author paper concerning work done during the MsC thesis, which was finished and published during the PhD and several co-authored papers.

The co-authored papers were a result of collaborations started or continued during the PhD and concern the determination of stellar parameters for FGK-dwarfs and M-dwarfs. The contributions to those papers was a combination of helping to develop the software required to do parameter estimation and a strong component of data and error analysis.

B.2.1 Refereed

- Teixeira, G. D. C., Sousa, S. G., Tsantaki, M., et al. 2016, *A&A*, 595, A15
- Andreasen, D. T., Sousa, S. G., Tsantaki, M., et al. 2017, *A&A*, 600, A69
- Rajpurohit, A. S., Allard, F., Teixeira, G. D. C., et al. 2018, *A&A*, 610, A19
- Tsantaki, M., Andreasen, D. T., Teixeira, G. D. C., et al. 2018, *MNRAS*, 473, 5066
- Rajpurohit, A. S., Allard, F., Rajpurohit, S., et al. 2018, *A&A*, 620, A180

B.2.2 Proceedings

- Teixeira, G. D. C., Sousa, S. G., Tsantaki, M., et al. 2017, *European Physical Journal Web of Conferences*, 160, 01013
- Tsantaki, M., Andreasen, D. T., Teixeira, G. D. C., et al. 2018, *Astrometry and Astrophysics in the Gaia Sky*, 330, 271

B.2.3 Catalogs

- Rajpurohit, A. S., Allard, F., Rajpurohit, S., et al. 2018, *VizieR Online Data Catalog*, 362,

